Numerical methods for the simulation of continuum granular flow models

Stéphanie Riber

▶ To cite this version:

Stéphanie Riber. Numerical methods for the simulation of continuum granular flow models. Fluids mechanics [physics.class-ph]. Université Paris sciences et lettres, 2017. English. NNT : 2017PSLEM020 . tel-01737107

HAL Id: tel-01737107
https://pastel.hal.science/tel-01737107

Submitted on 19 Mar 2018

THÈSE DE DOCTORAT

de l'Université de recherche Paris Sciences et Lettres
PSL Research University

Préparée à MINES ParisTech

Numerical methods for the simulation of continuum granular flow models

École doctorale n°364

SCIENCES FONDAMENTALES ET APPLIQUÉES

Spécialité MÉCANIQUE NUMÉRIQUE ET MATÉRIAUX

COMPOSITION DU JURY :

M. Pierre-Yves Lagrée
Université Pierre et Marie Curie, Rapporteur

M. Pierre Saramito
Université de Grenoble, Rapporteur

M. Olivier Pouliquen
Université Aix Marseille, Examinateur

M. Stefan Luding
University of Twente, Examinateur

Ms. Nathalie Vriend
University of Cambridge, Examinateur

M. Laurent Lobry
Université de Nice Sophia Antipolis, Examinateur

M. Elie Hachem
Mines ParisTech, Directeur de thèse

M. Rudy Valette
Mines ParisTech, Directeur de thèse

M. Frédéric Costes
Transvalor, Invité

Soutenue par **Stéphanie RIBER**
le 03 Février 2017

Dirigée par **Elie HACHEM et Rudy VALETTE**

MINES ParisTech

PSL RESEARCH UNIVERSITY PARIS

To my grandparents, Régine and Michel Valcz...

Contents

Glossary

a	aspect ratio of the fluid column	(dimensionless)
a_c	critical aspect ratio	(dimensionless)
a_r	ratio between $h_i + h_r$ to r_i	(dimensionless)
b	bubble function	(dimensionless)
Bn	Bingham number	(dimensionless)
d	diameter of the grains	(m)
E	filtering length of the Level-Set function	(m)
E_c	kinetic energy	(J)
E_d	dissipated energy	(J)
E_m	mechanical energy	(J)
E_p	potential energy	(J)
$E_{extension}$	dissipated energy in extension	(J)
E_{shear}	dissipated energy in shearing	(J)
f	source term for Navier-Stokes equations	$(kg \cdot m^{-2} \cdot s^{-2})$
F_r	remeshing frequency	(dimensionless)
g	gravitational acceleration	$(m \cdot s^{-2})$
H	height of the computational domain	(m)
h_i	initial height of the fluid column	(m)
H_i	height of the ingot	(m)
h_m	height of liquid metal into the ingot	(m)
h_{min}	minimum mesh size	(m)
h_r	initial height of the column chute	(m)
$H(x)$	Heaviside function	(dimensionless)
I	inertial number	(dimensionless)
I_0	inertial number giving the transition between dense and collisional regimes	(dimensionless)
L	length of the computational domain	(m)
m	Papanastasiou regularization coefficient	(s)
M^i	metric tensor at node i	(m)
Nb_{Grains}	number of grains	(dimensionless)
p	pressure field	(Pa)
P	function space for the pressure field	(dimensionless)
P_h	functional space for the pressure field	(dimensionless)
P_{dissip}	dissipated power	(W)
q	test function defined in the pressure space	(Pa)
Re	Reynolds number	(dimensionless)

r_i	initial radius of the fluid column	(m)
R_i	radius of the ingot	(m)
r_f	final radius of the fluid column	(m)
s	sign of the distance function	(dimensionless)
s_{ij}	scaling factor to the edge ij	(dimensionless)
t	current time	(s)
t_f	arrest time	(s)
T_0	structuration time for thixotropic fluids	(s)
v	velocity field	$(m \cdot s^{-1})$
V	function space for the velocity field	(dimensionless)
V_h	functional space for the velocity field	(dimensionless)
V_b	volume of the powder bag	(m^3)
$V_{current}$	fluid volume at the current time increment	(m^3)
V_{gained}	gained volume	(m^3)
v_{impact}	impact velocity of the granular column onto the substrate	$(m \cdot s^{-1})$
V_{init}	initial fluid volume	(m^3)
w	test function defined in the velocity space	$(m \cdot s^{-1})$
X^i	length distribution tensor at node i	(m)
α	Level-Set function	(m)
$\hat{\alpha}$	filtered Level-Set function	(m)
Δt	time step	(s)
$\Delta\mu$	difference between the μ_F and μ_S	(dimensionless)
ϵ_g	slipping region for the granular material	(m)
η	mixing viscosity of all the fluid flowing into a specified domain	$(Pa \cdot s)$
η_{air}	viscosity of the air	$(Pa \cdot s)$
η_{eff}	effective viscosity of the fluid	$(Pa \cdot s)$
η_m	viscosity of the liquid metal	$(Pa \cdot s)$
η_{min}	minimal viscosity	$(Pa \cdot s)$
η_p	plastic viscosity	$(Pa \cdot s)$
$\dot{\gamma}$	strain rate tensor	(s^{-1})
Γ	interface between the two fluids	(dimensionless)
$\|\|\dot{\gamma}\|\|$	shear rate	(s^{-1})
$\|\|\dot{\gamma}\|\|_{min}$	minimum shear rate	(s^{-1})
λ	redistancing parameter	(dimensionless)
μ	effective friction	(dimensionless)
μ_F	dynamic friction coefficient	(dimensionless)
μ_S	static friction coefficient	(dimensionless)
Ω	computational domain	(dimensionless)
Ω_1	computational domain filled by the densest fluid	(dimensionless)
Ω_2	computational domain filled by the ambient fluid	(dimensionless)
ϕ_r	repose angle	(degrees)
Φ_a	volume fraction of air	(dimensionless)
Φ_g	volume fraction of grains	(dimensionless)
Φ_l	volume fraction of liquid	(dimensionless)
ρ	density after mixing steps	$(kg \cdot m^{-3})$
ρ_{air}	density of the air	$(kg \cdot m^{-3})$

ρ_f	density of the fluid	$(kg \cdot m^{-3})$
ρ_m	density of the liquid metal	$(kg \cdot m^{-3})$
σ	shear stress tensor	(Pa)
τ	deviatoric shear stress tensor	(Pa)
$\|\|\tau\|\|$	deviatoric shear stress	(Pa)
τ_0	yield stress	(Pa)
τ_2	stabilization parameter	(dimensionless)
τ_K	stabilization parameter	(dimensionless)

Acknowledgments

Cette thèse s'est déroulée au sein du Centre de Mise en Forme des Matériaux (Mines ParisTech). Merci à tous les membres du jury d'avoir accepté d'examiner ce travail: Olivier Pouliquen, Pierre Saramito, Pierre-Yves Lagrée, Stefan Luding, Nathalie Vriend et Laurent Lobry. C'était un réel honneur d'avoir été examinée par des chercheurs d'une telle renommée.

Ensuite, un immense remerciement va pour Elie Hachem et Rudy Valette (best thesis supervisors), sans qui rien n'aurait abouti. Merci Elie de m'avoir fait confiance jusqu'au bout et de m'avoir tant donné. Merci pour tes conseils, ton expertise en numérique, ta disponibilité et pour m'avoir "poussée" et encouragée afin que ce travail de thèse soit le meilleur possible et ait cet impact dans la communauté de mécanique numérique. Merci pour tous ces moments partagés en conférence. Si j'y suis arrivée, tu y es pour beaucoup. Rudy, merci d'avoir accepté d'encadrer ce travail de thèse en cours de route. Je ne savais pas à l'époque quel super tournant cette thèse aurait pris et que j'allais avoir en quelque sorte un deuxième "papa". Merci pour ta disponibilité, ta patience (oui oui!), tes conseils, ton expertise (Rudy alias"la bible en physique"), ta gentillesse. Merci de m'avoir intégrée dans les communautés de rhéologie et de granulaires, auxquelles j'espère appartenir pour très longtemps encore. On a vraiment passé beaucoup de temps ensemble à travailler et "bavasser", surtout dans les derniers moments. C'était un vrai plaisir et cela m'a tellement appris!

Rudy, Elie, merci pour ces 3 années magnifiques et enrichissantes. J'espère qu'on gardera contact par la suite, et qu'on continuera à travailler ensemble. Je suis maintenant reconnaissante à vie :).

Je souhaite ensuite remercier toutes les autres personnes qui ont contribué à la réussite scientifique de cette thèse. A commencer par Romain Castellani, je te remercie énormément. Merci pour ta gentillesse, ta disponibilité, et toute l'(énorme) aide apportée sur les manip'! Ensuite, un gros remerciement va au meilleur des chefs industriels, Frédéric Costes. Fred, merci pour toute l'aide apportée pendant ce travail et pour ta disponibilité. Beaucoup de résultats n'auraient pas été obtenus sans ton aide. C'était un vrai plaisir de travailler avec toi pendant ces trois années. Merci également à Youssef Mesri pour les discussions sur tous les aspects numériques du modèle. Enfin, un gros remerciement va à Prof. Malcolm Mackley, qui a gentillement accepté de me faire répeter ma soutenance et qui m'a donné de précieux conseils qui me serviront très certainement pour la suite. Thank you very much Prof. Mackley for your help and your kindness! Je remercie aussi tous les stagiaires qui ont pris part à ce travail: Florian, Jimmy, Thomas, Lamine et Oumar. Finalement, je souhaite remercier de manière générale les équipes CFL et RMP, et industriels du projet COMCEPT pour toutes les discussions, réunions et conférences partagées.

Enfin, que serait une thèse sans un super environnement de travail? Merci à tous ceux qui ont fait que cette thèse se déroule dans la bonne humeur à Sophia, où de fortes amitiés se sont nouées. A commencer par ma Laeti. Merci d'avoir été là pendant ces deux premières années (tu m'as énormément manqué par

la suite), merci pour tous ces fous rires et ces moments partagés! Tu es une des meilleures rencontres que j'ai faite pendant cette période, et j'espère qu'on gardera contact encore très longtemps. Ensuite, Jéjouille, que dire de toi? Heureusement que tu étais là pour enjouer le Cemef, et banaliser tous les petits tracas du quotidien avec ton humour décalé! Tu es une super rencontre, ne change surtout pas! Merci également à Guigou (mon copain de stade de foot!), Danai (best colleague ever), Margaux (copine de commérage), Mehdi (le grand frère), Modesar (ou plutôt Modeymar), Lucas (cours Forest!), Yasmina (copine de conf de rhéologie), Daniel, Sélim, Charbel (pour toutes les sorties ski et autres), Valentin, Maxime, Guillaume, Grégoire, Marie-Agathe, Ghalia, Wafa, Rabia, Romain M., Etienne, Christophe, Anselmo pour tous les moments partagés pendant ces 3 ans, que ce soit les soirées foots, les randos ou bien les soirées. Merci. Je n'oublie pas mes collègues de stage qui ont accompagné mes premiers pas au Cemef, et qui restent de super amis: Nicolas et Alexandre.

Ensuite, faire une thèse aux Mines ne se résume pas à cotoyer des doctorants du site de Sophia. Un gros merci à la team Dopamines, pour tous ces moments partagés pendant ces trois séjours au ski, et pour m'avoir super bien accueilli lors de mes passages parisiens. Mention spéciale pour Xavier. Merci à toi pour ton amitié et surtout pour avoir fait le déplacement le jour J. Ca m'a beaucoup touché et fait plaisir! Tu es une personne en or. Merci également à Thomas, Romain, Eva, Clémentine, Marie-Lise, Marie, Alice, Matthildi... pour m'avoir bien accueillie au sein de l'association et pour tous les moments et délires qu'on a eu pendant les séjours au ski (même à S-1 avant le jour J). Merci à eux de faire en sorte que l'environnement de travail au sein des Mines soit le meilleur possible!

Enfin, je souhaite remercier ma famille pour leur soutien: mes parents Frank et Michèle, ma soeur Jessica, et mon beau frère Jéremie. Merci à eux de m'avoir soutenue et d'avoir fait la personne que je suis devenue. Je souhaite aussi remercier mes grands parents que j'aime fort, Régine et Michel Valcz, qui nous ont brutalement quittés au milieu de mon doctorat, et qui nous ont toujours encouragés et admirés dans tous nos choix de vie... Et réciproquement. Merci pour tout ce que vous nous avez donné et appris. Papi, mamie, cette thèse est pour vous.

Chapter 1

Framework and objectives

Contents

Résumé en français

Ce chapitre a pour objectif de présenter le contexte dans lequel s'inscrit cette thèse, ainsi que les enjeux et questionnements scientifiques auxquels nous serons confrontés.

Cette thèse s'inscrit dans le cadre du projet COMCEPT, regroupant plusieurs partenaires industriels issus du domaine de la fonderie. Nous nous intéressons ici au procédé de coulée en source (appelé également coulée en lingotière). Il s'agit d'injecter du métal fondu dans un moule, permettant son remplissage progressif par le bas. Durant ce procédé, une poudre de couverture, appelée "coussin", est déposée à la surface du métal liquide, le protégeant thermiquement de l'air et évitant son oxydation. Ces poudres sont conditionnées dans des sacs, disposés suivant plusieurs méthodes (posés directement au fond du moule, suspendus par des cordes, surélevés par des cartons), et qui brûlent suite aux fortes chaleurs induites par l'entrée du métal en fusion dans le moule, permettant ainsi l'étalement de la poudre. Cependant, il arrive que l'étalement s'effectue mal, laissant des zones non recouvertes de poudre, ce qui altère la qualité finale du lingot.

Dans ce cadre, la simulation numérique apparaît comme un outil efficace pour l'optimisation du procédé, permettant ainsi la visualisation de la physique à moindre côut. L'objectif de cette thèse consiste à proposer des méthodes numériques permettant la simulation de l'écoulement de poudres, et qui seront appliquées finalement au procédé de coulée en source et intégrées dans le logiciel THERCAST, commercialisé par la société Transvalor.

Deux approches sont décrites dans la littérature pour la simulation des écoulements granulaires. Les méthodes dites "discrètes" sont les plus populaires, et consistent à décrire l'écoulement grain par grain, en considérant leurs intéractions. Cependant, ces méthodes sont très coûteuses quand le nombre de grains devient très élevé, ce qui nous amène à la simulation numérique par des approches dites "continues". Ces dernières consistent à résoudre les équations de la mécanique des fluides, et à traduire le comportement des matériaux granulaires par des lois spécifiques.

Ainsi, nous nous sommes focalisés sur certaines lois décrivant le comportement de ces matériaux, et soulevant certains enjeux numériques. Nous les avons divisés en trois catégories, suivant leur degré d'immersion. Dans un premier temps, nous nous focalisons sur les matériaux granulaires secs, qui sont caractérisés par trois régimes différents : quasi-statique (solide), dense (liquide) et collisionel (gazeux). L'association de la recherche entre communautés physique et mécanique a permis de caractériser le comportement du matériau avec un nombre adimensionnel, appelé nombre inertiel, qui correspond au rapport entre un temps microscopique lié au réarrangement des grains, à un temps macroscopique (inverse du taux de cisaillement) [1]. Par la suite, [2] ont proposé la loi de comportement $\mu(I)$, traduisant le comportement piezzo-dépendant du matériau en fonction du nombre inertiel.

Dans un second temps, nous nous sommes intéressés au comportement que présente un matériau granulaire auquel nous y ajouté une certaine quantité de liquide, créant ainsi des ponts capillaires entre les grains. Nous avons donc introduit ici les fluides à seuils. Il s'agit de fluides s'écoulant si la contrainte appliquée dépasse une certaine limite, appelée contrainte seuil. Ces fluides sont fortement non-linéaires, et spécifiquement, si un fluide ambiant est considéré. Ainsi, la simulation numérique des fluides à seuil constitue un grand enjeu, du aux grands sauts de viscosité présents aux interfaces.

Dans cette thèse, nous proposerons donc un formalisme éléments finis permettant la simulation numérique des écoulements multiphasiques de fluides non-Newtoniens, et plus particulièrement, fortement non-linéaires.

1.1 Introduction

For several centuries, metal objects are encountered everywhere in our daily life, under different shapes and usages. The oldest traces of metallurgy go back to several millennials before Christ. Indeed, the first molded objects have been elaborated with copper in 5000 years before Christ Thus, this discovery has revolutionalized the world of metallurgy, and had a great impact on the industry these days, with the diversification of employed alloys and post-processes used, such as lamination, machining or forging processes.

Casting process corresponds to the first step involved in the fabrication of metallic objects. It this process is poorly controlled, several defects appear (inclusions, porosities, rough surface ...) , leading to deteriorate surface quality and internal health of the ingot. Consequently, it is essential to control this process to obtain metal objects with optimal final features.

Internal health of final ingots represents a crucial issue for metallurgists. Indeed, characteristics of provided metals would become optimal, which would induce a decrease of waste. Three primary issues may be outlined : technological issues, as inclusions would be avoided ; then, environmental issues and finally, economical issues, due to the decrease of metal loss.

Two kinds of casting processes are found in foundry industry: continuous and ingot casting processes. In this thesis, we focus on ingot casting process.

Figure 1 illustrates geometry and purpose of ingot casting process. It consists of a tube linked to a channel, which is connected to the bottom of a mold. The process consists of injecting hot molten metal into the tube, allowing the progressive mold filling from the bottom. It is principally used for the fabrication of massive parts with large dimensions. Ingot casting processes represent a consequent worlwide market (50000 tons/year for a total cost of 500 ME).

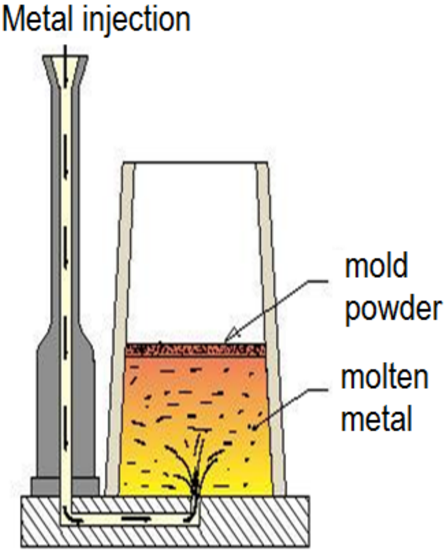

Figure 1: Ingot casting process

Many phenomena may generate inclusions, but the main source is "mold powder", corresponding to a powder layer, melting partially and aiming to cover and protect the metal during mold filling. Indeed, this powder prevents the appearance of skin defects due to its infiltration at steel/mold interface, and ensures also the steel thermal insulation from air, aiming to slow down solidification. Moreover, the liquid metal is protected of oxidation from air.

Figure 2 illustrates an overview of usual initial disposition of powders into the mold. Powders are conditioned into bags, attached mostly by ropes from the top of the mold (figure 2.a). Then, bags are burning due to the high temperatures induced by the mold filling, allowing the powder falling and spreading onto the liquid metal surface. Other industrial partners deposit the bags directly at the bottom of the ingot (figure 2.b), or raise it onto cardboard boxes (figure 2.c). After spreading, the powder phase change is occuring partially due to the contact with hot metal, turning the powder into a liquid. At the end of the process, powder has the appearance of a solid crust.

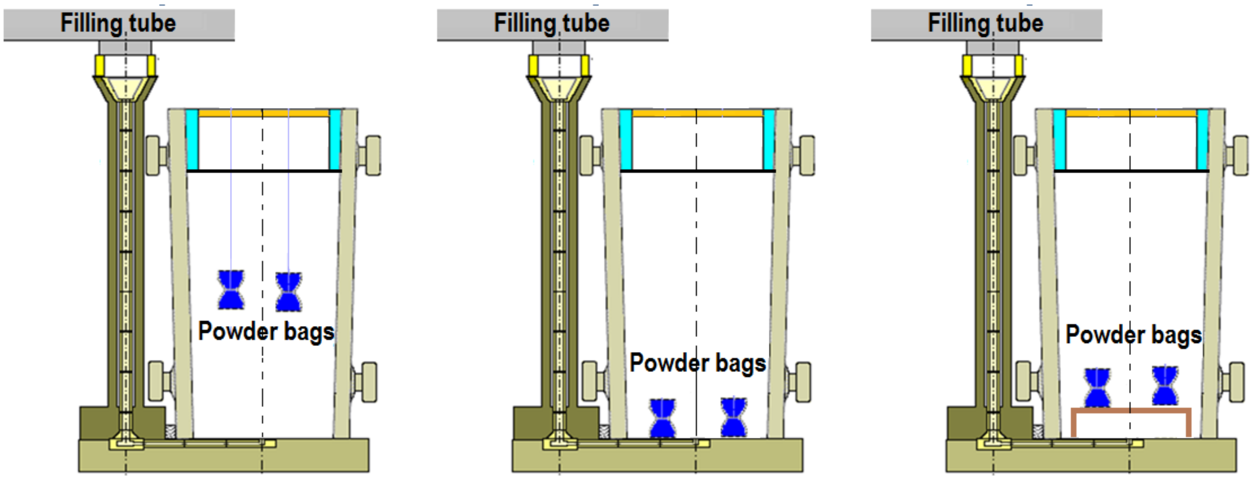

(a) (b) (c)

Figure 2: Initial disposition of powder bags into the mold : (a) bags are attached by ropes ; (b) bags are deposited at the bottom of the ingot ; (c) bags are raised onto cardboard boxes

Thus, mold powders are interesting for the optimization of internal health and surface qualities of the final ingot. However, the quoted advantages are altered if casting conditions are poorly controlled (metal overheating, powder quantities, flux rate of metal), leading to the formation of surface defects or inclusions, such as droplets extracted from powder and trapped inside the ingot.

The COMCEPT project aims to overcome these difficulties, by assisting industrial partners to ensure the most adapted powder to casting conditions. This project meets several industrial partners: Transvalor, Industeel, Arcelor Mittal, Aubert & Duval, Aperam, Sciences Computer Consultants, Ascometal, Imerys and Filab, and focuses on powder flow dynamics onto molten metal in the framework of ingot casting process. Moreover, it aims to provide a numerical tool allowing the engineers to optimize the choice of appropriate powders and best practices for the process.

1.2 Granular materials

Granular materials are defined as a collection of solid particles with size larger than ten microns [3]. We encounter them everywhere in our daily life under different shapes, dimensions, and densities. Due to the wide range of existing granular materials, they cover a wide range of fields of study, such as in geomorphology [4], and a large range of industrial processes, such as foundry, pharmaceutic, cosmetic or food industries [5]. Thus, understanding how granular materials flow may answer to several issues, from the comprehension of many natural phenomena to the optimization of several industrial processes, such as ingot casting.

Among industrial applications involving granular flows, the example of pharmaceutical industry is also relevant (figure 3.b). Indeed, a method used to manufacture pills consists of pushing a powder into cavities with a scraper. However, the scraper speed must be well chosen: indeed, for low speeds, the powder will fill the full cavities, but the process will not be well optimized due to long process times. On the other hand, increasing the scraper speed will not leave the powder to fall and thus, to fill the totality of the cavities. Therefore, it is important to find the appropriate speed for the scraper in order to optimize the process, which involves finally to determine the dynamics of the powder during its flow into the cavities.

In geophysics, issues involving granular flows problems are also encountered, for example the prediction of the avalanches run-out (figure 3.a).

Figure 3: Omnipresence of granular materials in nature and industry

In conclusion, the determination of granular dynamics is necessary for several physical and industrial issues. Since several years, numerical simulation appeared as a powerful tool to simulate several physical and industrial processes, and consists nowadays of an inevitable step for engineers to optimize it. Thus, the goal of this work consists of proposing a numerical tool, that simulates granular flows and free-falls in the industrial framework, taking into account its specific dynamics.

In the literature, two approaches exist for the numerical simulation of granular flows : the most used, called Discrete Numerical Simulation (DNS), consists of the flow description at the microscopic scale, by simulating directly the collisions between grains using basic physical interactions (non-penetration, friction, elasticity). In the past, this method helped to understand some key features related to the dynamics of granular materials, and to answer to several physical questions [1].

However, computational costs may increase drastically if one wants to simulate the granular flow at the industrial scale. Indeed, one powder bag may cover a total volume of $1dm^3$. By considering the coarsest powder (whose grain diameter is equal to $0.2mm$) and by assuming that the packing is maximum (percentage of the total volume that is occupied by grains, usually maximal at 0.64), 80 millions of grains are contained into this volume. Consequently, simulating powder spreading with a discrete method becomes irrelevant, and may give rise to huge computational costs. Indeed, the usual limitation for the number of grains by the use of discrete method is one million of grains. Thus, the idea consists of simulating powder flows using a continuum approach, which aims to solve momentum equations. The definition of appropriate constitutive model used to describe granular dynamics after a fall must then be chosen.

In this work, we will thus develop a continuum model for the simulation of granular flows. The next parts give an overview and discussion on the usual constitutive laws that are relevant for the description of granular dynamics.

1.3 Rheology of granular materials

In this section, we introduce a crude and intentionally naive classification of rheological behaviors according to the relative volume fractions Φ_g, Φ_l and Φ_a, respectively, solid (grains), liquid and gas (air) of the total fluid. This classification involves three categories : dry granular ($\Phi_l = 0$), wet (non-zero Φ_g, Φ_l and Φ_a) and immersed granular ($\Phi_a = 0$) systems.

This classification avoids many physical processes, some being still an active research field, that could provide accurate macroscopic rheological models, but we will underline their main features that are challenging for numerical simulation, typically strong nonlinear formulations. The proposed models shall them be seen as generic nonlinear behaviors for granular materials.

Dry dense granular systems, illustrated on figure 4.a exhibit a pressure-dependent behavior, due to frictional interactions. For a given deviatoric stress, they behave as solid in highly pressure regions, and grains velocity becomes higher as pressure tends to zero.

If a slight amount of liquid added into the granular material leads to the creation of capillarity bridges between grains, as shown on figure 4. b for wet granular systems. A very crude approach is now to consider that the pressure-dependent behavior of the granular material turn then into a yield stress behavior. Thus, a new constant parameter is introduced, called the yield stress, below which the fluid does not flow anymore. For immersed granular systems (figure 4.c), the behavior is assumed to be Newtonian at first approximation. For low Φ_g, the material may exhibit eventually nonlinear behavior (appearance of a yield stress, a frictional dynamics) or for high Φ_g and high strain rates $||\dot{\gamma}||$, but we will not study such systems.

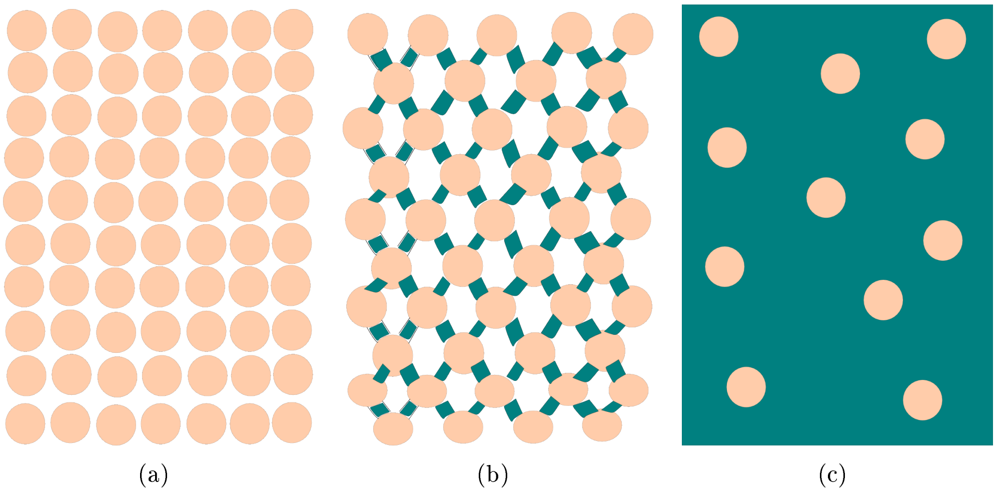
(a) (b) (c)

Figure 4: Pictures of granular microstructures with respect to the amount of interstitial fluid : (a) Dry granular material ; (b) Creation of capillarity bridges ; (c) Immersed granular material

1.3.1 Dry granular materials

During the ingot process, powder bags burn, fall and spread onto the metal surface. As introduced before, the flow is split in two parts : the fall of the granular material, and its spreading. Then, the phase change of the powder starts, turning it eventually into a liquid. In the industrial process, it has been shown that the granular flow takes less than one second. Thus, the powder does not have the time to turn significantly into a liquid (phase change takes several minutes). Thus, the powder is assumed to be dry during the spreading.

Three regimes describe dry granular flows. Figure 5 represents the distribution of these regimes in a granular flow. In the center of the flow (highly pressured regions), grains arrangements do not deform. This regime is called quasi-static. Approaching the free surface leads to higher velocities, and a liquid-like behavior. This regime is called dense. Finally, velocity of grains in a thin layer, located at the free-surface of the pile, are higher than grains size, and deconstruct the granular flow by creating several collisions between grains. Thus, this regime is called collisional.

In the literature, we may find some attempts to determine dry granular constitutive laws [6, 7]. Particularly, a CNRS GdR on granular materials has been created early 2000. Thus, [8] proposed an overview of their research on the behavior of dense granular flows. Figure 6 illustrates the six different configurations for the study of granular dynamics, where early simple shear is achieved : plane shear, annular shear, vertical-chute flows, flow onto an inclined plane, heap flow and flow into a rotating drum. For each case, they reported yields, the kinematic properties but also the rheological behavior of the flow. All the results obtained by these measurements are then interpreted.

Da Cruz *et al.*[1] determined the relevant parameters that describe the mechanical dynamics of the granular flow, by investigating all the mechanisms occurring at each scales (microscopic scale, grain scale, and geometrical scale). Particularly, they discussed the mechanisms occurring at the grain level, and determined dimensionless parameters that may describe relevantly the granular dynamics.

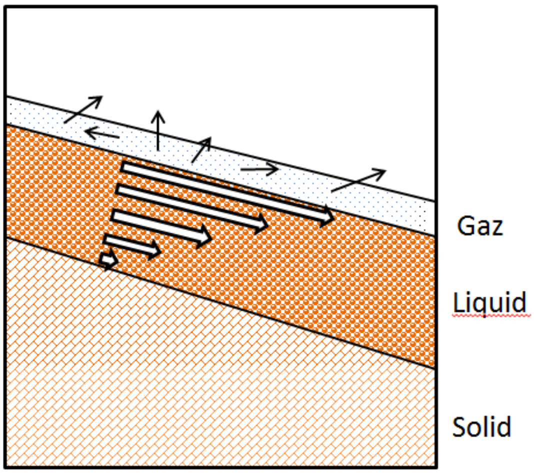

Figure 5: Representation of the three regimes (solid, liquid, gas) occurring in a granular flow

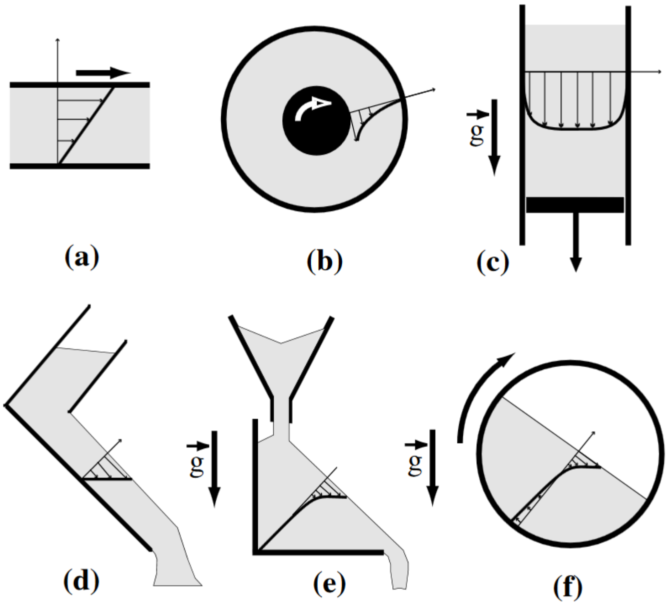

Figure 6: Study configurations of granular flows [8] : (a) plane shear, (b) annular shear, (c) vertical-chute flows, (d) inclined plane, (e) heap flow, (f) rotating drum

Particularly, they show that a dimensionless number, called the inertial number and denoted I, is able to describe the transition of regimes. This rheology describes the dry granular dynamics (pressure-dependent behavior) and the transition between the different regimes.

Consequently, the quasi-static regime is approximated by a macroscopic expression which traduces microscopic friction effects. Moreover, [2] proposed a pure plasticity constitutive law, which is pressure-dependent:

$$\tau = \frac{\mu p}{\| \dot{\gamma} \|} \dot{\gamma} \tag{1.1}$$

where μ is a friction coefficient. $\dot{\gamma}$ and τ are respectively the strain rate and shear stress tensors. $\| \dot{\gamma} \|$ corresponds to the norm of the strain rate tensor and is defined as:

$$\| \dot{\gamma} \| = 2\dot{\gamma} : \dot{\gamma} \tag{1.2}$$

For large domains (with a huge number of grains), dimensional analysis shows that a time constant t_{micro} exists, which may be considered as the time for a grain to fall into a hole of size d (diameter of the grains) under the confinement pressure p. Indeed, following [3], the following expression is obtained if the Newton law is formulated following the ordinate axis:

$$m\frac{d^2y}{dt^2} = F_y \tag{1.3}$$

where the mass m of a grain with density ρ and diameter d is approximated by $m = \rho d^3$, where its acceleration is estimated as $\frac{d^2y}{dt^2} = \frac{d}{t^2_{micro}}$ and where the applied force F_y is computed as the confinement pressure p multiplied by the grain surface ($F_y = pd^2$). Thus, we obtain the following expression for t_{micro}:

$$t_{micro} = \frac{d}{\sqrt{\frac{p}{\rho}}} \tag{1.4}$$

If the time $t_{macro} = \frac{1}{\|\dot{\gamma}\|}$ (time for a grain to move to a distance equal to its diameter) is small, it means that the strain rates are important and that the grains do not have the time to rearrange. Da Cruz *et al.*[1] showed that in this case, the volume fraction decreases, whereas the apparent friction coefficient μ increases. Inversely, if $t_{macro} > t_{micro}$, the strain rates are very small and the behavior will tend to a quasi-static regime, described by the equation 1.1.

The inertial number I, defined as t_{micro}/t_{macro}, corresponds to the qualitative transition between the quasi-static and collisional regimes:

$$I = \frac{\| \dot{\gamma} \| d}{\sqrt{\frac{p}{\rho}}} \tag{1.5}$$

Figure 7 illustrates the different regimes of a granular flow, according to the value of the inertial number I. For very small inertial numbers ($I <\approx 10^{-3}$), the regime is assumed to be quasi-static. Between 10^{-3} and a material parameter I_0, defined as the inertial number transition between dense and collisional regimes, the regime is dense. Beyond I_0, the regime is collisional.

Then, the tensorial constitutive law of the $\mu(I)$ rheology is thus formulated such as [2] :

$$\tau = 2\mu(I)p\frac{\dot{\gamma}}{\| \dot{\gamma} \|} \tag{1.6}$$

where the effective friction depends on the inertial number such as:

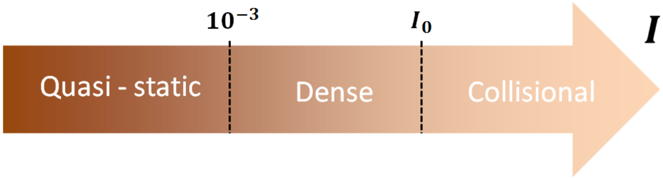

Figure 7: Determination of the flow regime according to the inertial number

$$\mu(I) = \mu_S + \frac{\mu_F - \mu_S}{\frac{I_0}{I} + 1} \tag{1.7}$$

where μ_S and μ_F correspond, respectively, to static and dynamic friction coefficient of the granular material.

Figure 80 illustrates the evolution of effective friction μ according to I. For low I (quasi-static regime), it shows that the effective friction μ tends to the static friction coefficient μ_S, which defines the repose angle ϕ_r of the granular material ($\phi_r = atan(\mu_S)$). When I increases, μ tends to the dynamic friction coefficient μ_F. At $I = I_0$, the friction is equal to $\frac{\mu_S+\mu_F}{2}$. Up to I_0, the flow regime is collisional.

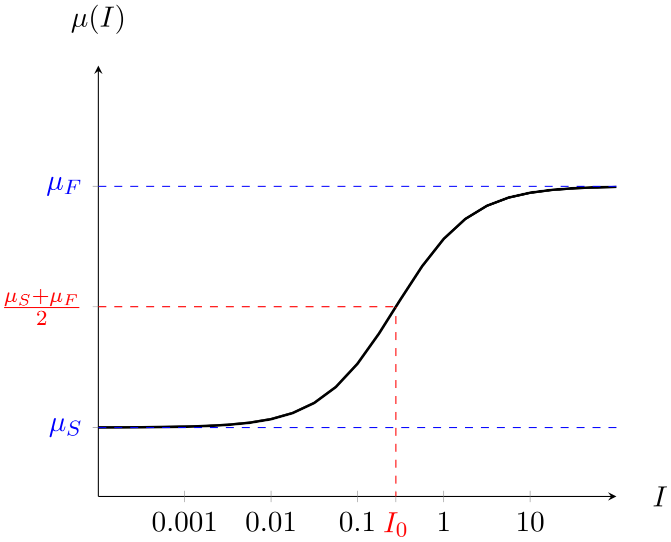

Figure 8: Effective friction μ according to the initial number I

During the last few years, $\mu(I)$ rheology has been well understood by physicist and gave rise to several studies [8]. However, the physical parameters describing granular cohesion and glassy state are still badly understood. Generic model are thus considered for the moment before physicists give keys to understand these phenomena.

1.3.2 Dense suspensions

P. Coussot performed a review on dense suspension rheophysics [9]. He defines it as materials made of a sufficiently high concentration of soft elements into a liquid, in order to form a continuous network of interactions which may be assimilated to a jammed structure. Moreover, the concentration of soft elements must be larger than a certain critical value, in order that the behavior is governed by the soft phase.

Furthermore, dense suspensions have the particularity to hold a given shape. Several studies outlined that pastes correspond to materials with a constant yield value below which they do not flow anymore. They belong thus to the wide category of yield stress fluids.

Focusing on the numerical simulation of yield stress flows is thus interesting as a dynamic yield exists for $\mu(I)$ rheology, which depends on the pressure. Consequently, the numerical simulation of yield stress fluids may appear as a first step before the one of $\mu(I)$ rheology fluids. Indeed, the purpose consists first of developing numerical tools, validating it onto yield stress fluids, and studying the overcoming limitations. Thus, the extension and the validation of these tools to $\mu(I)$ rheology fluids will be possible.

Yield stress fluids represent a class of complex fluids, and are encountered in many fields of study. These fluids flow only if the applied shear stress is larger than a constant τ_0, called the yield stress. Several yield stress fluids are encountered in the dairy life: mud, mayonnaise, gels and toothpaste for instance.

In [10], a review of simple yield stress fluids is performed. The usual one that describes suspensions dynamics is called a Herschel-Bulkley fluid. Constitutive equations are defined such as :

$$\begin{cases} \tau = 2\left(\eta_p + \frac{\tau_0}{||\dot{\gamma}||^n}\right)\dot{\gamma} & \text{if } \ ||\ \tau\ || > \tau_0 \\ \dot{\gamma} = 0 & \text{if } \ ||\ \tau\ || \leq \tau_0 \end{cases} \tag{1.8}$$

$||\ \dot{\gamma}\ ||$ corresponds to the shear rate and has been defined in equation 1.2. η_p defines the plastic viscosity, and corresponds to the viscosity limit at high shear stress. As mentioned previously, τ_0 denotes the yield stress. n corresponds to an exponent that describes the rheology of the fluid.

Equation 1.9 gives the normalized formulation of Herschel-Bulkley constitutive equations :

$$\begin{cases} ||\ \tau\ || = \eta_p\ ||\ \dot{\gamma}\ ||^n + \tau_0 & \text{if } \ ||\ \tau\ || > \tau_0 \\ ||\ \dot{\gamma}\ || = 0 & \text{if } \ ||\ \tau\ || \leq \tau_0 \end{cases} \tag{1.9}$$

$||\ \tau\ ||$ corresponds to the norm of the stress tensor, defined as:

$$||\ \tau\ || = \frac{1}{2}\tau : \tau \tag{1.10}$$

The apparent viscosity of a fluid is defined as the ratio between the shear stress to the shear rate, and is denoted η. When the applied shear stress is above τ_0 ($||\ \tau\ || > \tau_0$), it may be shown that $\eta = \eta_p + \frac{\tau_0}{||\dot{\gamma}||^n}$. It also appears in the tensor formulation such as : $\tau = 2\eta\dot{\gamma}$. However, the apparent viscosity remains non defined in unyielded regions, as $\dot{\gamma} = 0$. For numerical simulations, a special focus on this point must be done.

Two categories of Herschel-Bulkley fluids are defined, and depend on the value of the exponent n. Indeed, if n is lower than one, the apparent viscosity tends to decrease with the applied shear rate, as illustrated on figure 9(a). It represents the typical behavior for some polymer suspensions or mud. On the other hand, if n is greater than one, we then talk about shear-thickening behavior. As the applied shear rate increases, the grains may get in contact with each other and consequently, the apparent viscosity increases.

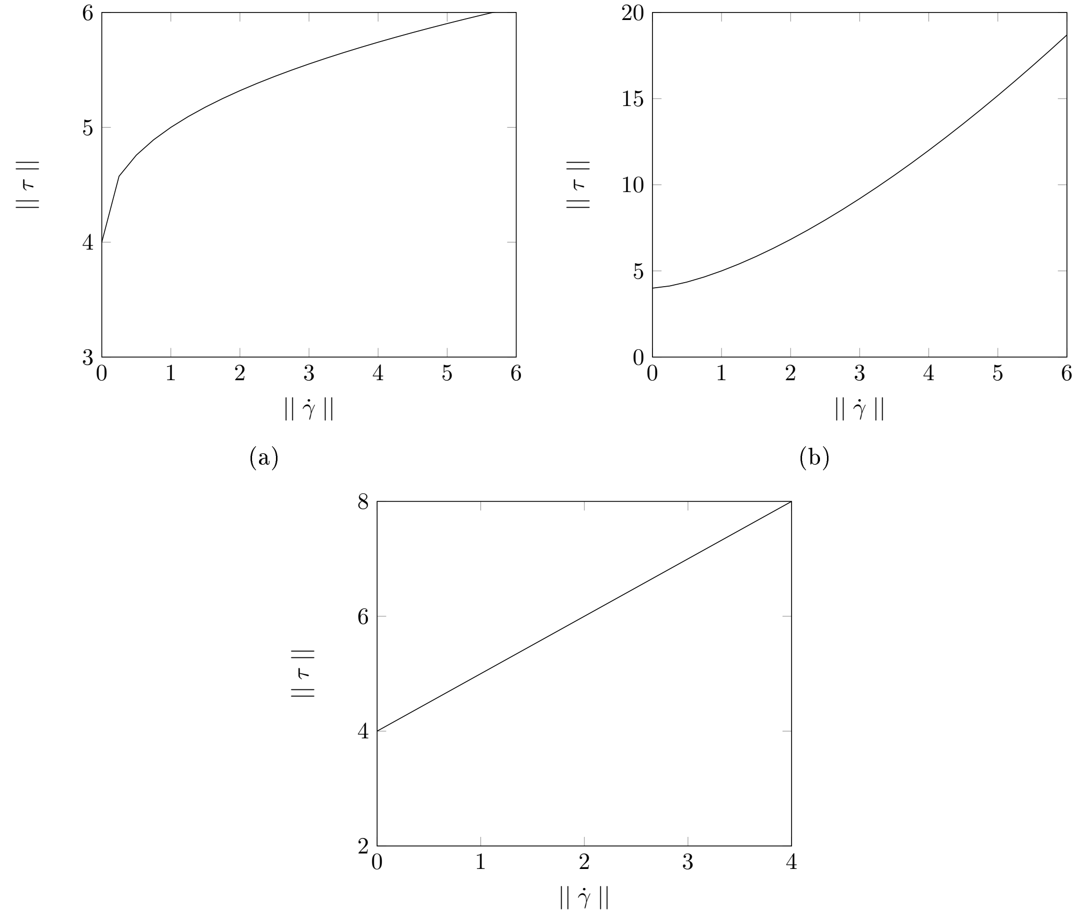

(a) (b)

(c)

Figure 9: Shear stress according to shear rate for Herschel-Bulkley fluids : (a) Shear-thinning fluids ($n < 1$) ; (b) Shear-thickening fluids ($n > 1$) ; (c) Bingham fluids ($n = 1$)

Bingham fluids represent a particular case of Herschel-Bulkley fluid, as the exponent n is fixed to 1. They are very common in industry : mayonnaise, gels or toothpaste for instance. Particularly, the behavior corresponds to the transition between shear-thinning and shear-thickening ones: they flow as Newtonian fluids above the yield stress. It means that the shear stress is proportional to the shear rate, and the proportionality coefficient corresponds to the plastic viscosity η_p. Constitutive equations of such fluids are thus formulated such as:

$$\begin{cases} || \tau || = \eta_p || \dot{\gamma} || + \tau_0 & \text{if } || \tau || > \tau_0 \\ || \dot{\gamma} || = 0 & \text{if } || \tau || \leq \tau_0 \end{cases} \tag{1.11}$$

Figure 9.(c) illustrates the rheological curve of Bingham fluids, which plots the shear stress according to the shear rate. As observed into the constitutive law, the shear stress is defined as an affine function according to the shear rate. The slope of this curve corresponds thus to the plastic viscosity η_p, and the ordinate at origin, to the yield stress τ_0.

1.3.3 Immersed granular materials

If the volume fraction occupied by the interstitial fluid is important compared to the one occupied by the grains (Φ_g and Φ_a are negligible compared to Φ_l), it is assumed here that grains have a small influence on the fluid flow. Indeed, this configuration may arise when the powder is totally melt. Consequently, a basic approach to describe the behavior of this melting mixture consists of neglecting the influence of grains, and to consider the behavior of the interstitial fluid predominate the granular behavior. Thus, the mixture may be described as a Newtonian fluid.

Newtonian fluids represent the most usual fluids found in Nature: water, oil and air for example. The apparent viscosity that describes the behavior of such fluids is constant. It is defined as the resistance for the fluid to flow uniformly (without any turbulence). Dynamically, it may be seen as the ratio between the shear stress to velocity gradients, as for Herschel-Bulkley fluids. The tensor formulation for the constitutive law is thus:

$$\tau = 2\eta\dot{\gamma} \tag{1.12}$$

1.4 Conclusion

The study of granular dynamics is thus interesting and useful for the optimization of a wide range of industrial applications. In this work, the optimization of mold powder flow onto molten metal during ingot casting process is considered. Numerical simulations appear to be an inevitable step and a powerful tool for engineers in order to control and optimize several processes. Thus, this thesis will focus on the numerical simulation of granular flows in order to understand its dynamics. Due to the needs for simulating granular flows at the industrial scale, it is irrelevant to use discrete methods. Thus, granular flows are solved as a continuum, with the resolution of mass balance and momentum equations, which need to be coupled with relevant constitutive laws adapted to the industrial configuration for the description of granular dynamics.

During ingot casting process, powder spreads onto the molten metal before a phase change occurs. Thus, it has been assumed that the dry powder obeys a $\mu(I)$ rheology, well-understood constitutive law for the description of granular dynamics. After the spreading and due to the interaction with molten metal, the powder is assumed to turn into a Newtonian fluid.

For the sake of numerical simulation, it is necessary to develop numerical methods for the resolution of granular flows. In order to perform it, the idea consists of proposing first a general framework for the resolution of Newtonian flows (constant viscosity), and thus, for the resolution of Navier-Stokes equations. The limitations of chosen numerical methods will then be discussed. Then, the extension to yield stress fluids, and especially to Bingham fluids, will be performed. Particularly, a special focus on methods used to treat the discontinuity between yielded and unyielded regions will be outlined. Then, the formulation will be extended to $\mu(I)$ rheology flows and sensitivity analysis to rheological and geometrical parameters in the framework of ingot casting will be investigated. Finally, the numerical framework will be extended to free surface flows.

Chapter 2

Finite element framework for multiphase flows

Contents

Résumé en français

Ce chapitre a pour objectif de présenter le modèle numérique permettant la résolution des écoulements multiphasiques, qui consiste en l'écoulement de deux ou plusieurs fluides dans un domaine.

Dans un premier temps, nous avons introduit les manières de décrire numériquement un problème multiphasique. Tout d'abord, les méthodes Lagrangiennes consistent à faire coincider le maillage considéré avec l'interface. Enfin, les méthodes Eulériennes consistent à décrire l'interface indépendamment du maillage, en utilisant ensuite des méthodes d'interpolation. Nous avons choisi d'utiliser une description Eulérienne pour sa plus grand flexibilité. De plus, une formulation basée sur la méthode des éléments finis a été choisie pour discrétiser le problème, puisque permettant des changements topologiques plus complexes.

La résolution des écoulements multiphasiques est composée ici de trois étapes. Dans un premier temps, il s'agit de choisir une méthode permettant de décrire et suivre l'interface au cours du temps. Ensuite, les équations de la mécanique des fluides stabilisées doivent être résolues. Enfin, nous adaptons le maillage de manière anisotrope afin que nos calculs soient très précis.

Pour capturer l'interface, une méthode Level-Set, basée sur le calcul des distances signées à l'interface, a été choisie pour son faible temps de calcul. Puis, la fonction Level-Set a été filtrée autour de l'interface, évitant les oscillations numériques loin de l'interface. Enfin, les étapes de réinitialisation et de convection de la Level-Set ont été couplées afin de gagner en précision et en rapidité.

Ensuite, les équations de la mécanique des fluides (Navier-Stokes) sont résolues et stabilisées grâce à une méthode variationelle multi-échelles. Il s'agit ici de décomposer les champs vitesse et pression en petites et grandes échelles, et d'injecter les effets des petites échelles dans le problèmes grandes échelles.

Finalement, une technique de maillage adaptatif anisotrope à nombre d'éléments fixe est employée. La métrique est basée sur le calcul du tenseur de distribution des arêtes, qui donne ainsi l'orientation et l'étirement de chaque arête. Dans les régions à fortes variations de gradients d'un vecteur, contenant les critères suivant lesquels adapter, les mailles seront très étirées dans la direction considérée. Sinon, le maillage sera déraffiné.

Ces outils numériques sont finalement testés sur un cas d'écroulement de barrage (effondrement d'une colonne de fluide sous gravité). L'influence des paramètres de remaillage (fréquence d'adaptation, nombre d'éléments) sur la précision et la conservation de masse est enfin analysée.

2.1 Introduction

This chapter is devoted to the the numerical framework used for the simulation of multiphase flows. They are encountered in nature and in several industrial processes (figure 10), such as in ingot casting, with the interaction between liquid metal, air and powder. Consequently, the numerical simulation of multiphase flows represents an inevitable step for the comprehension of many physical and industrial processes. In this chapter, we focus only on two-fluid flows problem.

Figure 10: Examples of multiphase flows in nature and industry

Figure 11 illustrates the problem statement of a two-fluid flow problem. The computational domain Ω is split into two subdomains Ω_1 and Ω_2, occupied by different fluids. Γ corresponds to the interface.

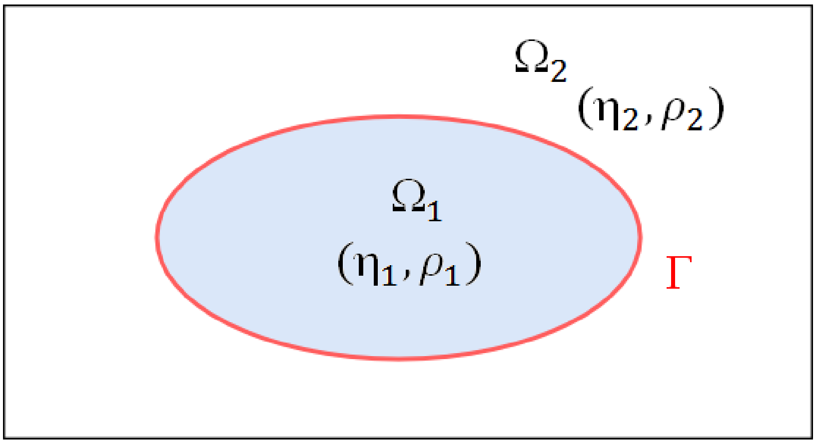

Figure 11: Computational domain of a multiphase problem

The numerical simulation of multiphase flows needs three steps: first, the problem is described by the choice of an appropriate discretization method for the resolution. Then, we need to solve the fluid mechanics equations, which are defined by momentum and mass equations (Navier-Stokes for Newtonian fluids). Finally, we need to capture and follow the interface during the simulation.

In this chapter, we discuss the choice of the problem description. Then, numerical tools are proposed to capture and follow interfaces between two different fluids. Then, the mechanical equations are solved. Furthermore, additional tools allowing to increase the solution accuracy are then proposed. Finally, the model is validated using a well-known multiphase benchmark.

2.2 Discretization method

A numerical simulation can be described according to two ways. First, there are Lagrangian methods (figure 12). At any instant of the simulation, the mesh fits with the interface. These descriptions are advantageous as the interface is tracked and followed without any additional algorithm to solve, explaining that there are very used for the simulation of free-surface flows.

Among Lagrangian methods, we find Smoothed Particles Hydrodynamics (SPH) methods, corresponding to meshfree methods [11]. It consists in splitting the domain into several particles, and following it during the simulation. These methods allow the accurate tracking of highly physical regions and phenomena, such as vorticies or interfaces.

However, Lagrangian descriptions lead to several drawbacks, leading to a high number of remeshing steps, that generate high computational times. Moreover, a larger number of particles is needed to solve accurately the flow. Finally, the extension to complex problems with high topology changes remains complicated.

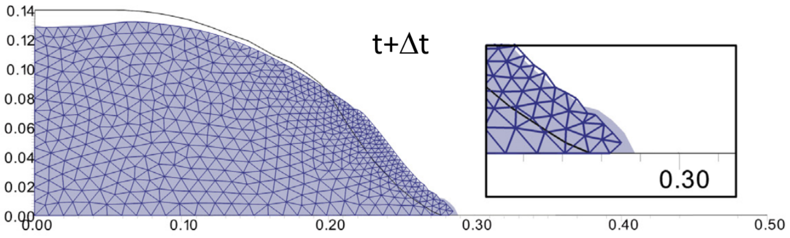

(a) time t

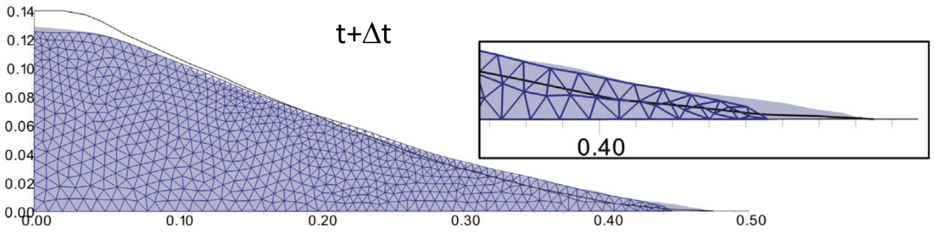

(b) time $t + \Delta t$

Figure 12: Lagrangian description of a multiphase problem [12]

Then, there are Euleurian descriptions (figure 13). Contrary to Lagrangian descriptions, the mesh does not fit the interface, whose location is computed by the use of approximation methods.

These methods have several advantages, such as lower computational times (remeshing steps are not required at every time steps) . Moreover, complex topology changes are better handled. However, these descriptions remain less used for free-surface flows problems with turbulence, as the tracking of interfaces, vorticities and other small phenomena (droplets, bubbles) are difficult to catch, if additional numerical tools are not introduced to improve computational costs. Indeed, the discretization step in space must be very low to capture these small details, leading to high computational times.

In this work, we chose to describe the problem by using an Eulerian framework, due to its better flexibility to handle complex problems. Moreover, an advanced remeshing method is used to improve the solution accuarcy.

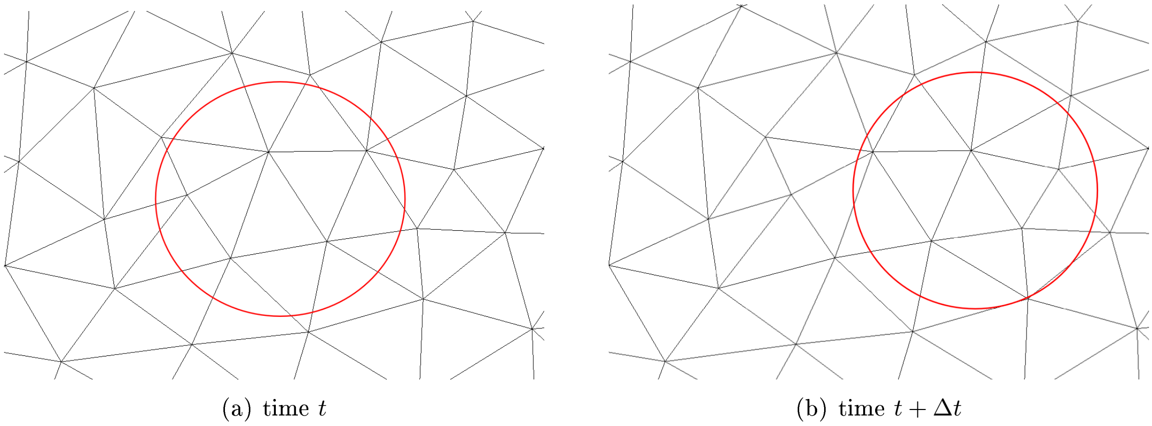
(a) time t (b) time $t + \Delta t$

Figure 13: Eulerian description of a multiphase problem

Three discretization methods are found in the literature for the resolution of multiphase flows in an Eulerian framework. First, there are finite difference methods. It consists in discretizing the computational domain in each direction, and in solving the equations using numerical approximation schemes. These methods are simple, efficient to implement, and appropriate for the flow resolution with high order schemes. However, there are several drawbacks, especially when numerical applications involve complex geometries. Indeed, the mesh must be regular and boundary conditions may be difficult to implement. Thus, we need to use an other discretization method.

The finite volume method is often found for the resolution of fluid mechanics problems [13]. It consists in splitting the fluid domain into control volumes, and in performing energy balances, that lead in the end to the resolution of integrals in each cell. This method has the advantage to be very conservative: all the energies leaving from one control volume go to another one. Thus, it gives good approximations for the verification of conservation laws, that explain the method popularity for fluid mechanics problems. However, this method may become harder to implement for problems with complex geometries, such as ingot casting. Moreover, computational times increase fastly for multiphase problems, due to the reconstruction of interfaces.

The finite element method is also used for the resolution of flows problems. It consists of splitting the fluid domain into a mesh, composed of several elements and associated nodes, which define the discretized required fields. Then, the flow resolution leads to the resolution of the variational formulation of the problem over the domain, corresponding to an energy minimization problem. Finally, it leads to the resolution of a linear system and to the determination of the problem unknowns. This method has the powerful advantage to be able to consider problems with complex geometries, and thus, to easily fix the required boundary conditions. However, it has several drawbacks. We can quote non conservation of the problem, for which some additional treatments are necessary.

In this work, the finite element method is chosen for the resolution of multiphase flows, due to its better flexibility to handle problems with complex geometries. In this chapter, the numerical method for the resolution of multiphase Newtonian flows will be introduced. First, we will introduce the capturing method for the interface. Then, the resolution and the stabilization will be presented. Then, we will talk about anisotropic mesh adaptation, allowing to a better accuracy of the final solution. All the numerical tools introduced in this work are implemented in the finite element library CIMLib-CFD, developed by the Computing & Fluids (CFL) team in CEMEF.

2.3 Multiphase tool

2.3.1 Properties mixing

As show in figure 11, the computational domain Ω is occupied by two fluids corresponding to Ω_1 and Ω_2 domains. Properties of fluids 1 and 2 are taken as ρ_1, ρ_2 for density fields, and η_1, η_2 for viscosity. Thus, we must take into account properly the several fluids features for the resolution of fluid mechanics. Consequently, a linear mixing law is used, leading to the final expression for density and viscosity as follows:

$$\left\{ \begin{array}{l} \rho = \rho_1 H(x) + \rho_2 \left(1 - H(x)\right) \\ \eta = \eta_1 H(x) + \eta_2 \left(1 - H(x)\right) \end{array} \right. \tag{2.1}$$

where $H(x)$ corresponds to the Heaviside function:

$$H(x) = \left\{ \begin{array}{ll} 1 & \text{if } x \in \Omega_1 \\ 0 & \text{if } x \in \Omega_2 \end{array} \right. \tag{2.2}$$

2.3.2 Literature review on interfaces descriptions

After taking into account the several properties features into single density and viscosity fields, a method allowing to describe properly the interface between the two fluids must be proposed. Interfaces description may be performed by two approaches: tracking and capturing methods.

Tracking methods are defined as Lagrangian methods. By using this method, the mesh is adapting as the interface moves. Marker particles methods have been also extensively used to track and follow the interface during the time [14]. The specificity of this method consists in describing interfaces with particles, moving with the flow velocity. Then, these methods have the advantages to be very accurate, but it requires a huge number of elements or particles. Moreover, marker particles methods need a huge storage capacity because all datas must be stored independently at each of them [14]. Moreover, we may find difficulty to evaluate gradients at corners properly.

Capturing methods consist of another way to describe the interface between two fluids. During the simulation, the mesh doesn't fit with the boundaries, and the exact location is obtained by performing interpolations. At we mentioned before, we prefer these methods due to the more reasonable computational times it induces. In the literature, several capturing methods are found for interfaces description.

Firstly, Volume of Fluid (VOF) methods have been introduced by Hirt et al. [14]. The purpose consists in localizing the interface by the volume fraction occupied by the several fluid into the control volumes.

Then, the interface is reconstructed by using numerical schemes, as performed by Mosso et al. [15]. This method is very popular in multiphase flows problems, as it is well conservative. However, it presents some limitations. Particularly, the interface is not smooth but fragmented, which makes normal and curvature computation very challenging. By the way, it remains not well adapted to handle problems with complex topology changes.

Among Eulerian methods, we find also in the literature diffuse interface methods [16]. The purpose consists in choosing an appropriate smoothed field that describes the interface. Two diffuse interface methods are found in the literature: phase field and Level-Set methods. Phase field methods are often used for interfaces description in applications with solidification phenomena, but are not now appropriate for the resolution of fluid mechanics problems. In an other hand, Level-Set methods are commonly found for the resolution of flow problems, and is chosen in this work for its ability to handle complex problems with high topology changes. However, they are not conservative, and additional treatments must be performed to overcome this limitation.

2.3.3 Introduction to the Level-Set method

The Level-Set method has been formulated for the first time by Osher et al. and was applied to the modeling of front flame propagation [17]. For interface capturing, the purpose consists in computing the signed distance function to the interface α, also called Level-Set function. As shown in figure 14, this function is positive in Ω_1 and negative in Ω_2. Th zero value corresponds to the interface between the two subdomains.

$$\alpha(x) = \begin{cases} \quad d(x,\Gamma) & , x \in \Omega_1 \\ - \quad d(x,\Gamma) & , x \in \Omega_2 \\ \quad 0 & , x \in \Gamma \end{cases} \tag{2.3}$$

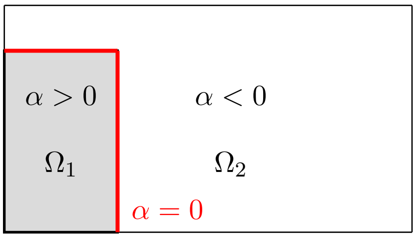

Figure 14: Computation of the signed distance function α

After capturing the interface, we need to follow it during the numerical simulation. Thus, the transport equation of the Level-Set function is solved, giving the new interface location:

$$\begin{cases} \frac{\partial \alpha}{\partial t} + v.\nabla\alpha = 0 \\ \alpha(t=0,x) = \alpha_0(x) \end{cases} \tag{2.4}$$

This method is often applied in phase transformation and multiphase flows [18, 19]. Indeed, it allows to describe a wide range of problems, as it can handle problems where the surface evolves in fairly complex ways, with high topology changes, and to be flexible to extend from two to tree dimensions problems. Then, intrinsic geometric properties of the interface, such as normal vectors or curvatures, are determined from the

Level-Set field. However, it does not appear to be fully-conservative, leading to the loss of small phenomena (droplets, bubbles). Consequently, some additional treatments are necessary to improve it.

In the next part, we will overview the existing extension of Level-Set methods in the literature, used to overcome the encountered problems, such as mass loss. Then, we will discuss of the chosen Level-Set method for the flow resolution.

2.3.4 Improvement of Level-Set methods

For treating the occurring limitations due to mass conservations, several works have been performed during the last few years. In the literature, several methods consist in coupling Level-Set with other conservative interface methods.

In [20], a new formulation is proposed, combining the Level-Set with the mass conservation properties of Volume of Fluid method. The purpose consists in capturing the interface by using the Level-Set method, and also in computing the volume fraction of fluid in elements. Then, both Level-Set and volume fraction fields are convected, followed by a redistancing step of the Level-Set function. Finally, Volume of Fluid acts to shift the zero-isovalue of the Level-Set function to a location leading to good mass properties.

In [21], an other method, called Particle Level-Set, is proposed. The purpose consists in placing the particles at each side of the interface, allowing to reconstruct interface regions with bad mass conservation.

Thus, the coupling of Level-Set method with an other interface description method appears to be a powerful alternative to decrease the mass loss which may occur during the simulation. However, it may generate high computational costs if the method is not well-adapted, and especially, for large systems. Thus, the proposed Level-Set method in this work is not coupled with other interface methods. In the next section, details on the considered convective Level-Set method will be introduced.

2.3.4.1 Redistancing step

After the resolution of the transport equation (2.4), many oscillations may appear close to the interface, polluting the interface quality. Indeed, the iso-contours of the Level-Set function are not smoothed anymore, leading to the loss of distance function property: $\| \nabla\alpha \| \neq 1$. Thus, the numerical scheme stabilization consists of giving back this property to the Level-Set function computed in (2.4). Consequently, this reinitialization is performed by the resolution of Hamilton-Jacobi equation:

$$\begin{array}{l} \frac{\partial\alpha}{\partial t} + v \cdot \nabla\alpha = 0 \\ \alpha(t = 0, x)) = \alpha_0(x) \end{array} \tag{2.5}$$

2.3.4.2 Filtering of the Level-Set function

During the convection of the Level-Set function, high gradient changes may occur, giving rise to instabilities and then polluting the final solution. The transport equation stabilization is performed by regularizing the Level-Set function, keeping it constant far from the interface. Thus, a filtering function $\hat{\alpha}$ is defined, equal to zero at the interface, approaching α close to the interface, and keeping constant value far from the interface. Several filtering functions are found in the literature [22, 23]. In this work, a hyperbolical tangential filter is used [24]. Thus, the new filtered Level-Set function $\hat{\alpha}$ is computed such as:

$$\hat{\alpha} = Etanh\left(\frac{\alpha}{E}\right) \tag{2.6}$$

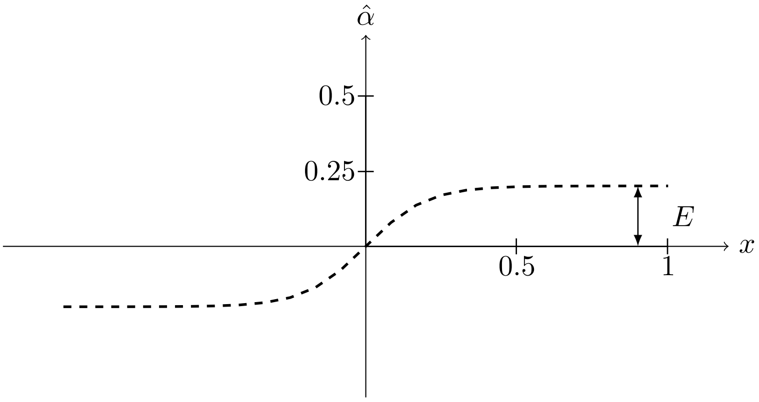

Figure 15: Filtering curve for the Level-Set function

E corresponds to the interface thickness with high variations of the gradient of $\hat{\alpha}$. The curve illustrating the evolution of $\hat{\alpha}$ is shown in figure 15. As expected, $\hat{\alpha}$ approaches to E as α increases.

Thus, the reinitialization equations are solved using the filtered Level-Set function $\hat{\alpha}$. Consequently, the gradient of $\hat{\alpha}$ is computed such as:

$$\nabla\hat{\alpha} = 1 - tanh^2\left(\frac{\alpha}{E}\right) \tag{2.7}$$

and is formulated with respect to $\hat{\alpha}$:

$$\nabla\hat{\alpha}(\hat{\alpha}) = 1 - \left(\frac{\hat{\alpha}(\alpha)}{E}\right)^2 \tag{2.8}$$

Then, a new fictive time space step, called τ_f, is introduced. The purpose consists in finding a new parametric function β where reinitialization step must be performed, and having the same isovalue α such as:

$$\mid \nabla\beta \mid = 1 \tag{2.9}$$

The Hamilton Jacobi equations are then formulated such as:

$$\begin{cases} \frac{\partial\beta}{\partial\tau_f} + s(\beta)(|\nabla\beta| - 1) = 0 \\ \beta(\tau = 0, x) = \alpha(t, x) \end{cases} \tag{2.10}$$

where $s(\alpha)$ corresponds to the sign function of α. However, the filtered Level-Set function is always positive.

By working now with the filtering Level-Set function $\hat{\alpha}$, the Hamilton Jacobi equations becomes:

$$\begin{cases} \frac{\partial\beta}{\partial\tau} + s(\hat{\alpha})\left(|\nabla\hat{\alpha}| - \left(1 - \left(\frac{\hat{\alpha}}{E}\right)^2\right)\right) = 0 \\ \beta(\tau_f = 0, x) = \alpha(t, x) \end{cases} \tag{2.11}$$

By transforming equations (2.11) as a transport equation, the problem is rewritten such as:

$$\begin{cases} \frac{\partial\beta}{\partial\tau} + U.\nabla\hat{\alpha} = s(\hat{\alpha}) \cdot \left(1 - \left(\frac{\hat{\alpha}}{E}\right)^2\right) \\ \beta(\tau_f = 0, x) = \alpha(t, x) \end{cases} \tag{2.12}$$

with:

$$U = \frac{s(\hat{\alpha})\nabla\hat{\alpha}}{\mid \nabla\hat{\alpha} \mid}$$

.

2.3.4.3 Coupling transport and redistancing steps

For improving computational costs, the goal is to couple transport and Hamilton Jacobi equations [22, 25]. Thus, we define λ such as the ratio between fictive and real time steps:

$$\lambda = \frac{\partial\tau}{\partial t} \tag{2.13}$$

Then, by chosing $\lambda = \frac{h}{\Delta t}$, we obtain:

$$\frac{\partial\beta}{\partial t} = \lambda\frac{\partial\beta}{\partial\tau} \tag{2.14}$$

By replacing (2.14) in (2.12), the new convection-reinitialization equation is obtained:

$$\frac{\partial\beta}{\partial t} + \lambda U.\nabla\hat{\alpha} = \lambda s(\hat{\alpha}) \cdot \left(1 - \left(\frac{\hat{\alpha}}{E}\right)^2\right) \tag{2.15}$$

Moreover, $\hat{\alpha} \approx \beta$ throughout the interface. Therefore, the equation that couples the transport and the reinitialization steps is formulated as follows:

$$\frac{\partial\hat{\alpha}}{\partial t} + (v + \lambda U).\nabla\hat{\alpha} = \lambda s(\hat{\alpha}) \cdot \left(1 - \left(\frac{\hat{\alpha}}{E}\right)^2\right) \tag{2.16}$$

This new equation leads to the appearance of a new convection term: $(v + \lambda U) \cdot \nabla\hat{\alpha}$. Then, the associated variational formulation is: find $\hat{\alpha} \in \mathcal{L}^2(\Omega)$ such that:

$$\left(\frac{\partial\hat{\alpha}}{\partial t}, \Phi\right)_\Omega + ((v + \lambda U) \cdot \nabla\hat{\alpha}, \Phi)_\Omega = \left(\lambda s(\hat{\alpha}) \cdot \left(1 - \left(\frac{\hat{\alpha}}{E}\right)^2\right), \Phi\right)_\Omega \tag{2.17}$$

for all $\Phi \in \mathcal{L}^2(\Omega)$.

The problem is then discretized with respect to the time by using a BFD2 [24]. Thus, the discretized problem turns into:

$$\left(\frac{3\hat{\alpha}^{n+1} - 4\hat{\alpha}^n + \hat{\alpha}^{n-1}}{2\Delta t}, \Phi\right)_\Omega + \left((v + \lambda U) \cdot \nabla\hat{\alpha}^{n+1}, \Phi\right)_\Omega = \left(\lambda s(\hat{\alpha}^n) \cdot \left(1 - \left(\frac{\hat{\alpha}^n}{E}\right)^2\right), \Phi\right)_\Omega \tag{2.18}$$

2.3.5 Conclusion

In this section, we introduced multiphase numerical tools for describing two-fluids flows, by overviewing methods of interfaces description. Thus, the proposed Level-Set method has been introduced, and consists in a convective reinitialization method, allowing to reduce computational times and avoiding several oscillations. The next stage of the multiphase flow resolution consists in solving mass and momentum equations, defined by the Navier-Stokes equations.

2.4 Navier-Stokes equations

2.4.1 Weak formulation

The numerical simulation of flows leads to the resolution of fluid mechanics equations. They are defined by the Navier-Stokes equations for Newtonian fluids. The multiphase flow is assumed to be incompressible. The computational fluid domain is defined such as $\Omega \subset \mathbb{R}^n$ (where n corresponds to the number of space dimensions), at time $t \in [0, T]$.

Incompressible Navier-Stokes equations consist in finding velocity and pressure fields (v and p), defined respectively in the spaces $V = \mathbb{R}^n$, $P = \mathbb{R}$, such that:

$$\begin{cases} \rho \frac{\partial v}{\partial t} + \rho v . \nabla v - \nabla \cdot \sigma = f & \text{in } \Omega \times [0, T] \\ \nabla \cdot v = 0 & \text{in } \Omega \times [0, T] \end{cases} \tag{2.19}$$

σ and f correspond respectively to the shear stress tensor and the source term.

By replacing σ by $-pI_d + \tau$ in equations (2.19) (with τ defined as the deviatoric shear stress tensor), the Navier-Stokes equations are formulated such that:

$$\begin{cases} \rho \frac{\partial v}{\partial t} + \rho v \cdot \nabla v + \nabla p - \nabla \cdot \tau = f \\ \nabla \cdot v = 0 \end{cases} \tag{2.20}$$

Velocity and pressure functional spaces are defined respectively such that:

$$\begin{array}{l} V = \{v(x,t) | v(x,t) \in H^1(\Omega)^n\} \\ P = \{p(x,t) | p(x,t) \in \mathcal{L}^2(\Omega)\} \end{array} \tag{2.21}$$

Then, the test functions w and q are defined in the same space as v and p. By multiplying the Navier-Stokes equations by the couple test functions (w, q), and integrating over the computational fluid domain Ω, the weak formulation consists in finding $v : [0, T] \to V$, $p : [0, T] \to P$ such that:

$$\begin{cases} \left(\rho \frac{\partial v}{\partial t}, w\right)_\Omega + (\rho v \cdot \nabla v, w)_\Omega - (p, \nabla . w)_\Omega + (\nabla \cdot \tau, w)_\Omega = (f, w)_\Omega & \forall w \in V \\ (\nabla . v, q)_\Omega = 0 & \forall q \in Q \end{cases} \tag{2.22}$$

where $(\cdot, \cdot)_\Omega$ corresponds to the scalar product in $\mathcal{L}^2$:

$$(a, b)_\Omega = \int_\Omega (a \cdot b) d\Omega \tag{2.23}$$

For Newtonian fluids, $\tau = 2\eta\dot{\gamma}(v)$. Thus, it is obtained finally that:

$$\left\{ \begin{array}{l} (\rho \frac{\partial v}{\partial t}, w)_\Omega + (\rho v \cdot \nabla v, w)_\Omega - (p, \nabla . w)_\Omega - (\nabla \cdot (2\eta\dot{\gamma}(v)), w)_\Omega = (f, w)_\Omega \\ (\nabla . v, q)_\Omega = 0 \end{array} \right. \tag{2.24}$$

Then, the computational domain is decomposed into a mesh Ω_h. Subscript h is used here and in the following to denote the finite element component. The functional spaces with finite dimension for the velocity and pressure fields V_h and P_h are defined as:

$$\begin{array}{l} V_h = \{u_h \in C^0(\Omega)^n, u_{h|K} \in P^1(\kappa)^n; \forall \kappa \in \tau_h\} \\ P_h = \{p_h \in C^0(\Omega), p_{h|\kappa} \in P^1(\kappa), \forall \kappa \in \tau_h\} \end{array} \tag{2.25}$$

Navier-Stokes weak formulation turns then into: find $(v_h, p_h) \in (V_h, P_h)$ such that, $\forall (w_h, q_h) \in (V_h, P_h)$:

$$\left\{ \begin{array}{l} \left(\rho \frac{\partial v_h}{\partial t}, w_h\right)_\Omega + (\rho v_h \cdot \nabla v_h, w_h)_\Omega - (p_h, \nabla . w_h)_\Omega + (2\eta\dot{\gamma}(v_h) : \dot{\gamma}(w_h))_\Omega = (f, w_h)_\Omega \\ (\nabla \cdot v_h, q_h)_\Omega = 0 \end{array} \right. \tag{2.26}$$

2.4.2 Variational MultiScale Methods

As it is well known, the stability of this discrete formulation depends on appropriate compatibility restrictions for the choice of finite element spaces. In this section, a Variational MultiScale (VMS) method is introduced, and initially proposed by Hugues et al. [26, 27, 28], which enables the use of equal order continuous interpolations, apart from preventing from oscillations due to convection dominated flows. Indeed, it offers an ideal framework to deal accurately with different physics such as Darcy [29], fluid-structure interaction [30], hydrodynamics [31], non-Newtonian fluids [32] and more. For more details on the proposed VMS method for this work, we can refer to [33].

The Variational MultiScale method consists in decomposing pressure and velocity spaces as $P_h \oplus P'$ and $V_h \oplus V'$. Subscript h is used to denote the finite element (coarse) component, and the prime is used for the so called subgrid scale (fine) component. According to that, the problem unknowns v and p are split likewise:

$$\begin{array}{ll} v = v_h + v' & \in V_h \oplus V' \\ p = p_h + p' & \in P_h \oplus P' \end{array} \tag{2.27}$$

According to that, the weak formulation of Navier-Stokes problem, defined in equation (2.26) turns then into: find $(v_h + v', p_h + p') \in V_h \oplus V' \times P_h \oplus P'$ such that:

$$\left\{ \begin{array}{ll} (\rho\partial_t(v_h + v'), w_h + w') & + (\rho(v_h + v') \cdot \nabla(v_h + v'), w_h + w') - (p_h + p', \nabla \cdot (w_h + w')) \\ & +(2\eta\dot{\gamma}(v_h + v') : \dot{\gamma}(w_h + w')) = (f, w_h + w') \\ (\nabla \cdot (v_h + v'), q_h + q') = 0 & \end{array} \right. \tag{2.28}$$

for all $(w_h + w', q_h + q') \in V_h \oplus V' \times P_h \oplus P'$.

The purpose consists now in modeling the small scales and in replacing its effects into the large scales. Even though the subgrid scales could be approximated and inserted into the previous equations (see [34]), three assumptions are made to simplify the fine scale problem:

- Interpolation functions are linear (P1 functions), leading to zero second derivatives.
- The subscales are not tracked in time.
- The convective velocity of the non-linear term may be approximated using only its large scales part. Thus:

$$(v_h + v')\nabla \cdot (v_h + v') \approx v_h \nabla \cdot (v_h + v') \tag{2.29}$$

Finally, the large scales problem is formulated such as: find $(v_h, p_h) \in V_h \times P_h$ such that:

$$\left\{ \begin{array}{ll} (\rho \partial_t v_h, w_h) & +(\rho v_h \cdot \nabla(v_h + v'), w_h) - (p_h + p', \nabla \cdot w_h) \\ & +(2\eta\dot{\gamma}(v_h + v') : \dot{\gamma}(w_h)) = (f, w_h) \\ (\nabla \cdot (v_h + v'), q_h) = 0 & \end{array} \right. \tag{2.30}$$

for all $(w_h, q_h) \in V_h \times P_h$.

The small-scales problem is obtained with the same process as the large scales one: find $(v', p') \in V' \times P'$ such that:

$$\left\{ \begin{array}{ll} (\rho \partial_t v_h, w') & +(\rho v_h \nabla \cdot (v_h + v'), w') - (p_h + p', \nabla \cdot w') \\ & +(2\eta\dot{\gamma}(v_h + v') : \dot{\gamma}(w')) = (f, w') \\ (\nabla \cdot (v_h + v'), q') = 0 & \end{array} \right. \tag{2.31}$$

for all $(w', q') \in V' \times P'$.

2.4.2.1 Small scales problem

By rearranging the terms into the small scales problem, the system (2.31) turns then into: find $(v', p') \in V' \times P'$ such that:

$$\left\{ \begin{array}{l} (\rho v_h \cdot \nabla v', w') + (\nabla p', w') + (2\eta\dot{\gamma}(v') : \dot{\gamma}(w')) = (\mathcal{R}_1, w') \\ (\nabla \cdot v', q') = (\mathcal{R}_2, q') \end{array} \right. \tag{2.32}$$

for all $(w', q') \in V' \times P'$.

The residuals $\mathcal{R}_1$ and $\mathcal{R}_2$ depend only on the large scales fields:

$$\begin{array}{l} \mathcal{R}_1 = f - \nabla \cdot (2\eta\dot{\gamma}(v_h)) - \nabla p_h - (\rho v_h \cdot \nabla v_h) - \rho \partial_t v_h \\ \mathcal{R}_2 = -\nabla v_h \end{array} \tag{2.33}$$

According to [35], v' and p' are defined such that:

$$\left\{\begin{array}{l} v' = \sum_{K\in\tau_h} v'_K b_K \\ w' = \sum_{K\in\tau_h} w'_k b_k \end{array}\right. \tag{2.34}$$

with b_K corresponding to the bubble shape function.

Following [27], the expression of p' is obtained as follows:

$$p' = \tau_2 \mathcal{R}_2 \tag{2.35}$$

where τ_2 corresponds to a stabilization coefficient, defined in Codina et al. [36]:

$$\tau_2 = \left(\left(\frac{\eta}{\rho}\right)^2 + \left(\frac{c_2}{c_1}\frac{\| u \|_K}{h}\right)^2\right)^{1/2} \tag{2.36}$$

c_1 and c_2 correspond to independent constants of the characteristic size of the element h. Finally, equation (1.3.2) can be written as:

$$\textstyle\sum_K (\rho v_h \cdot \nabla(v'_K b_K), w_K b_K)_K + 2\sum_K (\eta\dot{\gamma}(v'_k b_k) : \dot{\gamma}(v'_k b_k))_K = \sum_K (\mathcal{R}_1, w'_k b_k)_K \tag{2.37}$$

It allows us to extract the expression of v':

$$v'_{|K} = \tau_K \mathcal{R}_1 \tag{2.38}$$

where τ_K is a stabilization parameter, obtained in a natural way from the small scales problem:

$$\tau_K = \frac{(1, b_K)_K}{(\rho v_h \cdot \nabla b_K, b_K)_K + 2(\eta\dot{\gamma}(b_K) : \dot{\gamma}(b_K))_K} \tag{2.39}$$

A particular attention should be made on the choice of the test bubble function.

In this part, the modeling of fine scales has been performed, by defining v' and p' with stabilization terms. Now, the idea consists in injecting these fields into the large scales problem, leading to the formulation of stabilized Navier-Stokes equations.

2.4.2.2 Large scales problem

Recall that the large scale problem is formulated such as:

$$\left\{\begin{array}{ll} (\rho\partial_t v_h, w_h) & +(\rho v_h \cdot \nabla(v_h + v'), w_h) - (p_h + p', \nabla \cdot w_h) \\ & +(2\eta\dot{\gamma}(v'_h), \dot{\gamma}(w_h)) = (f, w_h) \\ (\nabla \cdot (v_h + v'), q_h) = 0 & \end{array}\right. \tag{2.40}$$

By integrating by part and injecting v' and p' in (2.40), the problem turns then into:

$$\left\{\begin{array}{ll} (\rho\partial_t v_h, w_h) & +(\rho v_h \cdot \nabla(v_h + \tau_K \mathcal{R}_1), w_h) - (p_h + \tau_2 \mathcal{R}_2, \nabla \cdot w_h) \\ & +(2\eta\dot{\gamma}(v_h), \dot{\gamma}(w_h)) = (f, w_h) \\ (\nabla \cdot (v_h + \tau_K \mathcal{R}_1), q_h) = 0 & \end{array}\right. \tag{2.41}$$

2.5 Mesh adaptation

In multiphase flows, it is important to obtain the most accurate interface description during the simulation.The mesh adaptation strategy presented in this work relies on the *a posteriori* definition of a unit metric able to, in some specified sense, minimize the interpolation error on the finite element solution. It relies on a statistical representation of the distribution of edges sharing an extremity, a quantity we call length distribution tensor. In order to relate the length distribution tensor to the interpolation error, following [37], we define an edge based error estimator based on a gradient recovery procedure. Once the optimal metric has been obtained, the mesh generation and adaptation procedure described in [37], based on a topological representation, is applied to obtain the new mesh.

2.5.1 Definition of the length distribution tensor: a statistical representation

Let $\Omega \in R^d$ be a polynomial domain, we consider a discretization $\Omega = K$ where K is a simplex such as a triangle or tetrahedron. Let $\Gamma(i)$ be the "patch" associated to a vertex x^i of the mesh defined as the set of nodes which share one edge with x^i, and let us denote by x^{ij} the edge connecting x^i tp x^j. The problem of finding a unitary metric M^i associated to the i^{th} node can be formulated as the least squares problem [37]:

$$M^i = \underset{M \in R^{d\times d}_{sym}}{\text{argmin}} \left(\sum_{j\in\Gamma(i)} M x^{ij} \cdot x^{ij} - \mid \Gamma(i) \mid \right)^2 \tag{2.42}$$

Provided that the vertices of $\mid \Gamma(i) \mid$ form at least d non-colinear edges with vertices x^i, then an approximate solution of (2.42) is given by

$$M^i = \frac{1}{d} \left(X^i \right)^{-1} \tag{2.43}$$

where, denoting by $\otimes$ the tensor product between two vectors, we have introduced the *length distribution tensor*

$$X^i = \frac{1}{\mid \Gamma(i) \mid} \left(\sum_{j\in\Gamma(i)} x^{ij} \otimes x^{ij} \right) \tag{2.44}$$

whose purpose is to give an "average" representation of the distribution of edges in the patch.

2.5.2 Gradient recovery error estimator

Let v_h be a P1 finite element approximation obtained by applying the Lagrange interpolation operator to a regular function $v \in C^2(\Omega)$. At node x^i, we seek the recovered gradient g^i defined by:

$$g^i = \underset{g \in R^d}{\text{argmin}} \sum_{j\in\Gamma(i)} \mid (g - \nabla v_h) \cdot x^{ij} \mid^2 = \underset{g \in R^d}{\text{argmin}} \sum_{j\in\Gamma(i)} \mid g \cdot x^{ij} - (v_h(x^j) - v_h(x^i)) \mid^2 \tag{2.45}$$

The solution to (2.45) can be expressed in terms of the length distribtuion tensor introduced before as

$$g^i = \frac{1}{\mid \Gamma(i) \mid} \left(X^i \right)^{-1} \sum_{j\in\Gamma(i)} \left(v_h(x^j) - v_h(x^i) \right) x^{ij} \tag{2.46}$$

It can be shown [38] that the quantity $| g^{ij} \cdot x^{ij} |$ gives a second order accurate approximation of the second derivative of v along the edges x^{ij}. Motivated by the fact that, for P1 finite elements on anisotropic mesh, residuals dominate a posteriori errors, as proved in [39], it is therefore suitable to define an error indicator function associated to the edges x^{ij} as:

$$e^{ij} = | g^{ij} \cdot x^{ij} | \,. \tag{2.47}$$

Moreover, this quantity can be easily extended to account for several sources of error, instead of just the scalar field v_h, by applying formula (2.47) to each component separately.

2.5.3 New metric construction

In order to relate the error indicator defined in (2.47) to a metric suitable for a mesh adaptation procedure, we introduce the concept of stretching factors s^{ij} defined as the ratio between the length of the edges x^{ij} after the adaptation procedure and before the adaptation procedure. The new metric, denoted by $\tilde{M}^i$, will then given by

$$\tilde{M}^i = \tfrac{1}{d}\left(\tilde{X}^i\right)^{-1} \quad ; \quad \tilde{X}^i = \tfrac{1}{|\Gamma(i)|}\left(\textstyle\sum_{j\in\Gamma(i)} (s^{ij})^2 x^{ij} \otimes x^{ij}\right) \tag{2.48}$$

To relate the metric to the interpolation error, following [38], we set a target total number of nodes N. Because of the quadratic behaviour of the error as a function of the scaling factor, denoting by $\tilde{e}^{ij}$ the quantity defined in (2.47) computed after the mesh adaptation process we have

$$s^{ij} = \left(\frac{\tilde{e}^{ij}}{e^{ij}}\right)^{1/2} \tag{2.49}$$

Moreover, the number of nodes in the new mesh after applying the scaling factors s^{ij} to the edge will be roughly equal to

$$N^{ij} = \frac{1}{s^{ij}}, \tag{2.50}$$

so that the total contribution of node i (in the old mesh) to the number of nodes in the new mesh will be given by

$$N^i = \det\left(\left(X^i\right)^{-1} \sum_{j\in\Gamma(i)} N^{ij} x^{ij} \otimes x^{ij}\right) \tag{2.51}$$

By combining (2.49) and (2.50), it is possible to see that (2.51) is a function of $\tilde{e}^{ij}$. If we assume that the total error is equidistributed among all edges such that each edge contributes a constant error e to the total, we can see that $N^{ij} = \left(\frac{e^{ij}}{e}\right)^{1/2}$, which yields the relation

$$N^i(e) = e^{-\frac{d}{2}} N^i(1). \tag{2.52}$$

By summing over all the nodes of the old mesh, we get an expression for the total error as a function of the number of nodes in the new mesh. By inverting this equality, we obtain

$$e = \left(\frac{\sum_i N^i(1)}{N} \right)^{\frac{2}{d}} \tag{2.53}$$

and injecting this into (2.49) yields an expression for the scaling factors

$$s^{ij} = \frac{\left(\sum_i N^i(1)\right)^{\frac{1}{d}}}{N^{\frac{1}{d}}(e^{ij})^{\frac{1}{2}}} \tag{2.54}$$

2.6 Validation on a two-dimensional Newtonian collapse

2.6.1 Introduction to the dam-break problem

In this section, we will validate the numerical tools introduced previously on a well-known multiphase flow benchmark. Thus, we chose to simulate the dam-break problem and to compare our results with the one of [40].

The dam-break problem consists of the collapse of a fluid column due to gravity. The two-dimensional problem statement is illustrated on figure 81. A computational domain with height H and length L, is filled with two different fluids: the first one is a rectangular column (height h_i and length r_i) filled with a denser newtonian fluid, and the second one is air. Slip boundary conditions are applied at the bottom wall, and symmetric conditions ($\nabla \cdot \tau = 0$), at the left wall.

For dam-break problems, a dimensionless parameter is defined, called aspect ratio a, and corresponds to the ratio between initial height h_i and length r_i of the column:

$$a = \frac{h_i}{r_i} \tag{2.55}$$

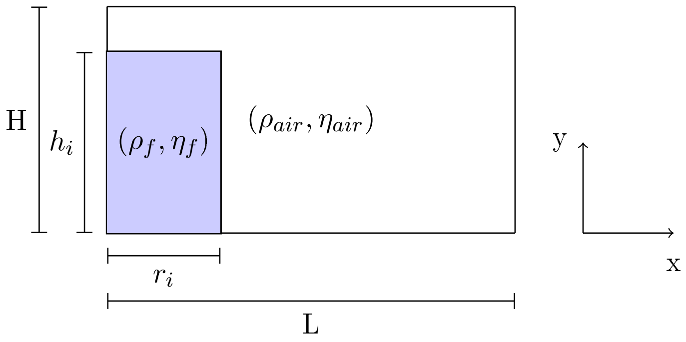

Figure 16: Problem statement of a two-dimensional dam-break problem

In the literature, several works have been conducted on Newtonian dam-breaks. For the model validation, we will focus on the work performed by [40], where experimental and numerical dam-breaks have been conducted and validated. A rectangular box, with dimensions $H = 0.44m$ and $L = 0.42m$, is considered. Initial lengths of the fluid column are taken as $h_i = 0.114m$, and $r_i = 0.114m$ (aspect ratio equal to

1). Consequently, the purpose of this section consists in validating the proposed numerical tools onto a Newtonian dam-break problem described in [40].

In this work, two different fluids are considered with $\rho_f = 10^3 kg \cdot m^{-3}$, $\rho_{air} = 1 kg \cdot m^{-3}$ as denser fluid and air density, and $\eta_f = 1 Pa \cdot s$, $\eta_{air} = 10^{-3} Pa \cdot s$ as viscosity. Concerning the Level-Set features, the reinitializing parameter λ is set to 1, imposing the same weight for convection and reinitialization steps. Moreover, the filtering length E is taken twice larger than minimum mesh size h_{min}.

2.6.2 Computational initialization

Thus, the purpose consists in simulating the dam-break problem introduced previously, for the validation of the multiphase numerical tools. Before solving the flow problem, the computations need to be initialized by taking into account the different fluid properties and by preparing the geometry of the problem.

Thus, the computational domain is meshed, followed by its splitting into two subdomains corresponding to the location of the different fluids (leading to the Level-Set function computation). Then, the filtered Level-Set function is computed, allowing the properties mixing. These steps correspond to computations initialization. However, the mesh is fixed, and by looking to the interface (figure 17), several oscillations appear which deteriorate the interface quality. The purpose consists now of preadapt the mesh close to the interface.

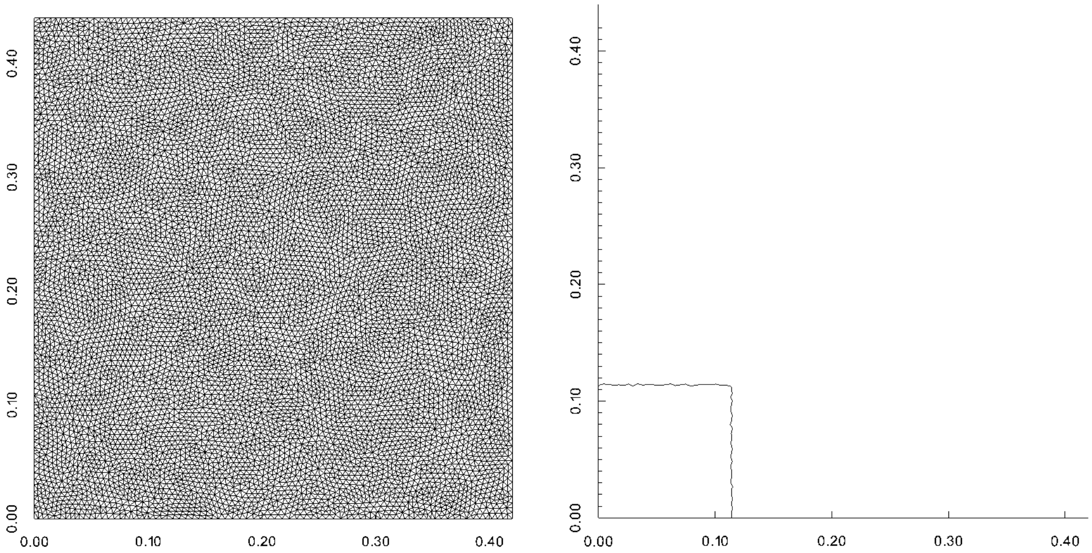

Figure 17: Fixed mesh with 20000 elements and the associated interface

Thus, the mesh must be adapted with respect to $\hat{\alpha}$. Thus, remeshing steps are performed several times until obtaining a smooth interface before the computations. The mesh and the interface are shown in figure 18. It is composed of 20000 elements. In this work, the minimum mesh size is set to $h_{min} = 5 \cdot 10^{-4} m$.

Moreover, it is interesting to adapt also the mesh according to velocity fields during the simulation. Thus, the idea consists in introducing a muti-criteria vector, as in Coupez and Hachem [41], containing the velocity norm, velocity components in each direction, and Level-Set function.

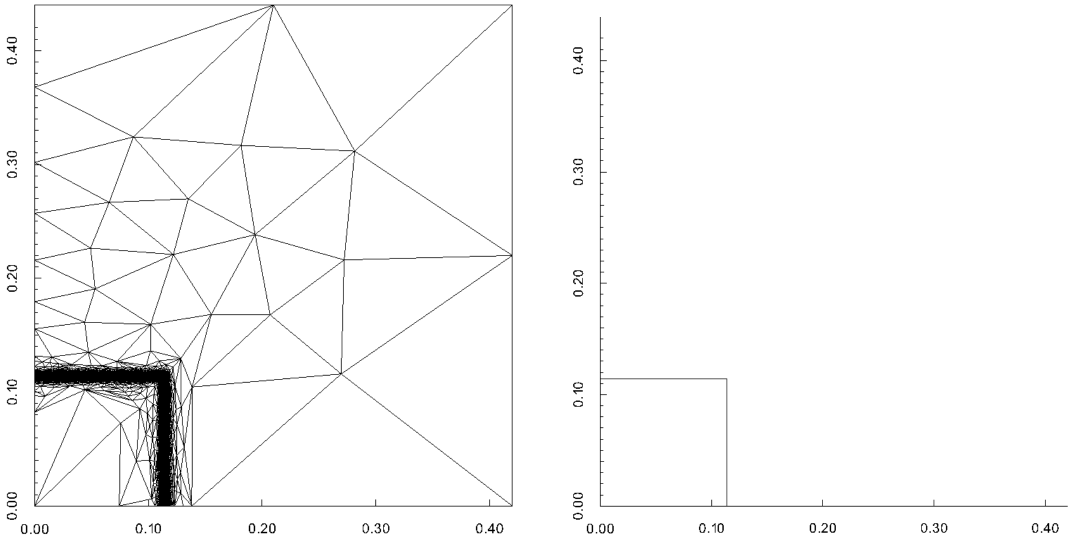

Figure 18: New adaptive mesh with 20000 elements and the obtained interface after five remeshing steps

Algorithm 19 summarizes the different required steps for computations initialization, as explained previously.

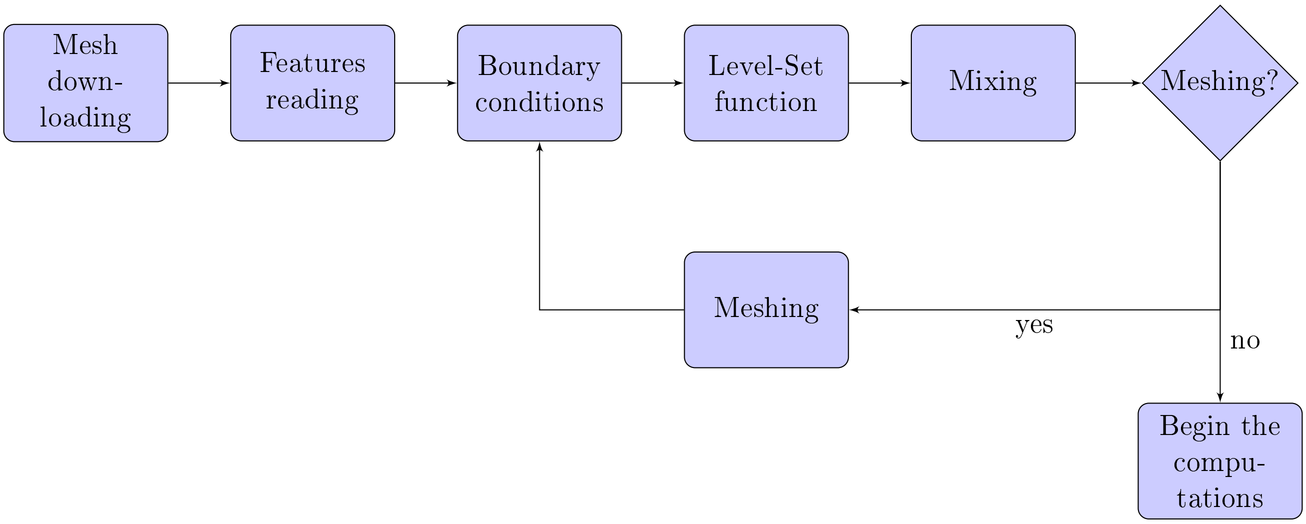

Figure 19: Initialization before the resolution of multiphase flows

2.6.3 Run-out and height analysis

Figure 20 illustrates the interface between the two fluids, at $t = 0.1s$. At this stage, the fluid does not reach the right wall yet. The power of mesh adaptation is outlined here, allowing an accurate capturing of the interface and small phenomena during the simuation.

Figure 21 illustrates the interface between the two fluids, at $t = 0.4s$. At this stage, the fluid impacts the right wall. Furthermore, kinetic energy induced by the dam-break begins to transform into potential energy (close to the right wall), leading to a wave formation.

At $t = 1s$, the fluid impacts the left wall (figure 22), leading to the creation of bubbles and droplets (figure 23).

Figure 24.a illustrates the dimensionless front position of the flow with respect to the time. The obtained results are compared with Cruchaga *et al.*[40]. The same flow dynamics is observed for the run-out, but the front goes faster in the numerical simulations than in the experimental work. These differences are generated by the boundary conditions applied at the bottom surface (slip-boundary conditions) and thus, to the abscence of friction law.

Figure 24.b illustrates the dimensionless height on the left wall according to the time. Now, the first wave occurring at the left wall is closer to the experimental work [40].

Figure 24.c illustrates the evolution of dimensionless height measured on the right wall. Around $t = 0.8s$, the impact with the right wall is observed as the measured height increases. However, we observe the same note as in the simulations of [40] for the second wave (small delay).

Figure 24.d illustrates the dimensionless height at $x = 0.27m$ according to the time. The obtained results are in a very good agreement with [40].

These results show us the interest of the coupling between anisotropic mesh adaptation, VMS and the Level-Set method for the simulation of multiphase flows. First, we observed in figure 23 that it is possible to accurately capture very small phenomena, such as bubbles or droplets, and to follow it according to the time. Moreover, run-out and height positions of the fluid show the same trend as observed in the experiments of [40]. Consequently, the numerical tools introduced previously seem to be adequate for the simulation of multiphase problems. In the next parts, sensitivity analysis will be performed in order to determine some limitations of the model.

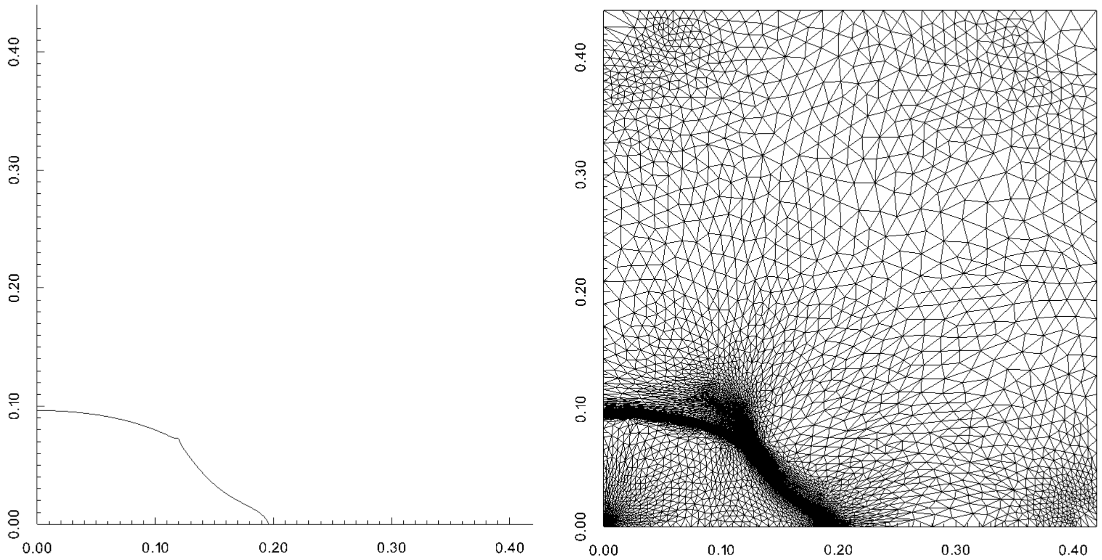

Figure 20: The interface and the associated mesh at $t = 0.1s$

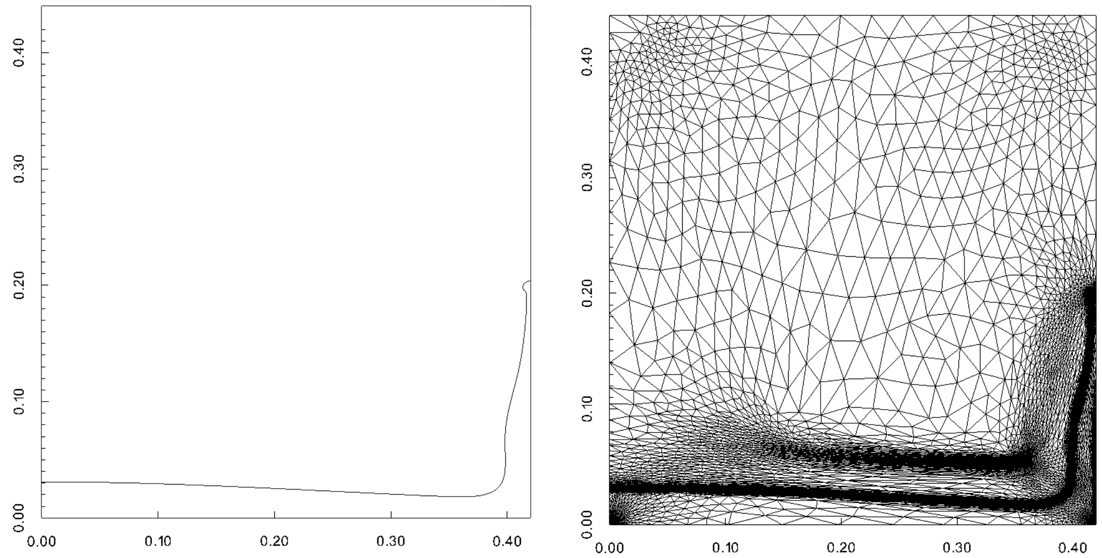

Figure 21: The interface and the associated mesh at $t = 0.4s$

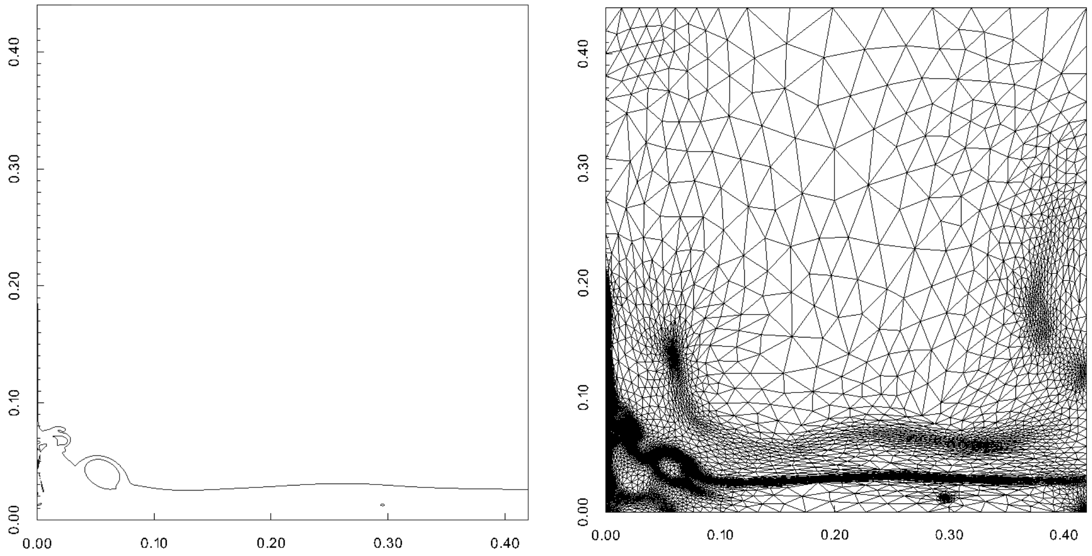

Figure 22: The interface and the associated mesh at $t = 1s$

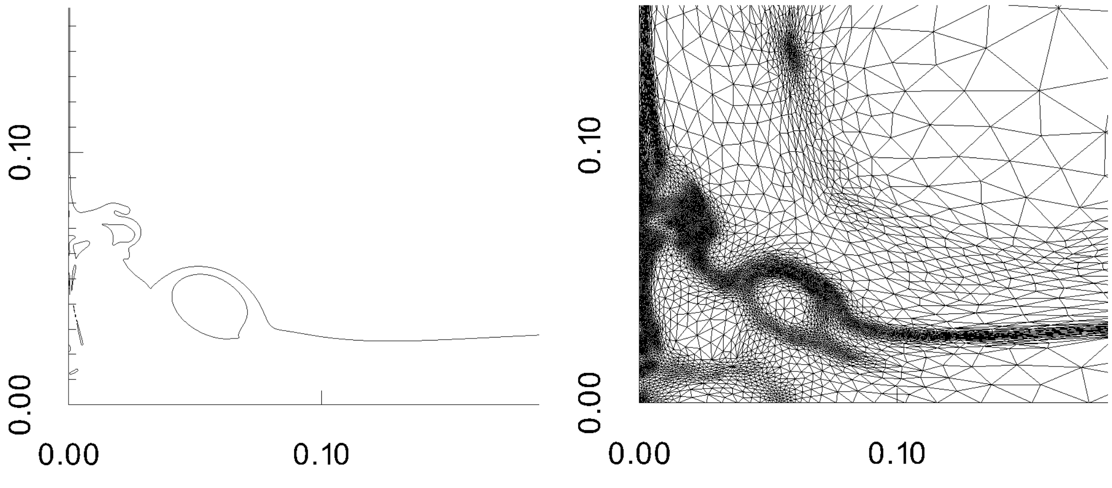

Figure 23: Zoom on the interface and associated mesh at $t = 1s$

Figure 24: Interface locations according to the time for a Newtonian dam-break with aspect ratio $a = 1$ (a) Dimensionless position of the front; (b) Dimensionless height on the left wall ; (c) Dimensionless height on the right wall ; (d) Dimensionless height at $x = 0.27m$

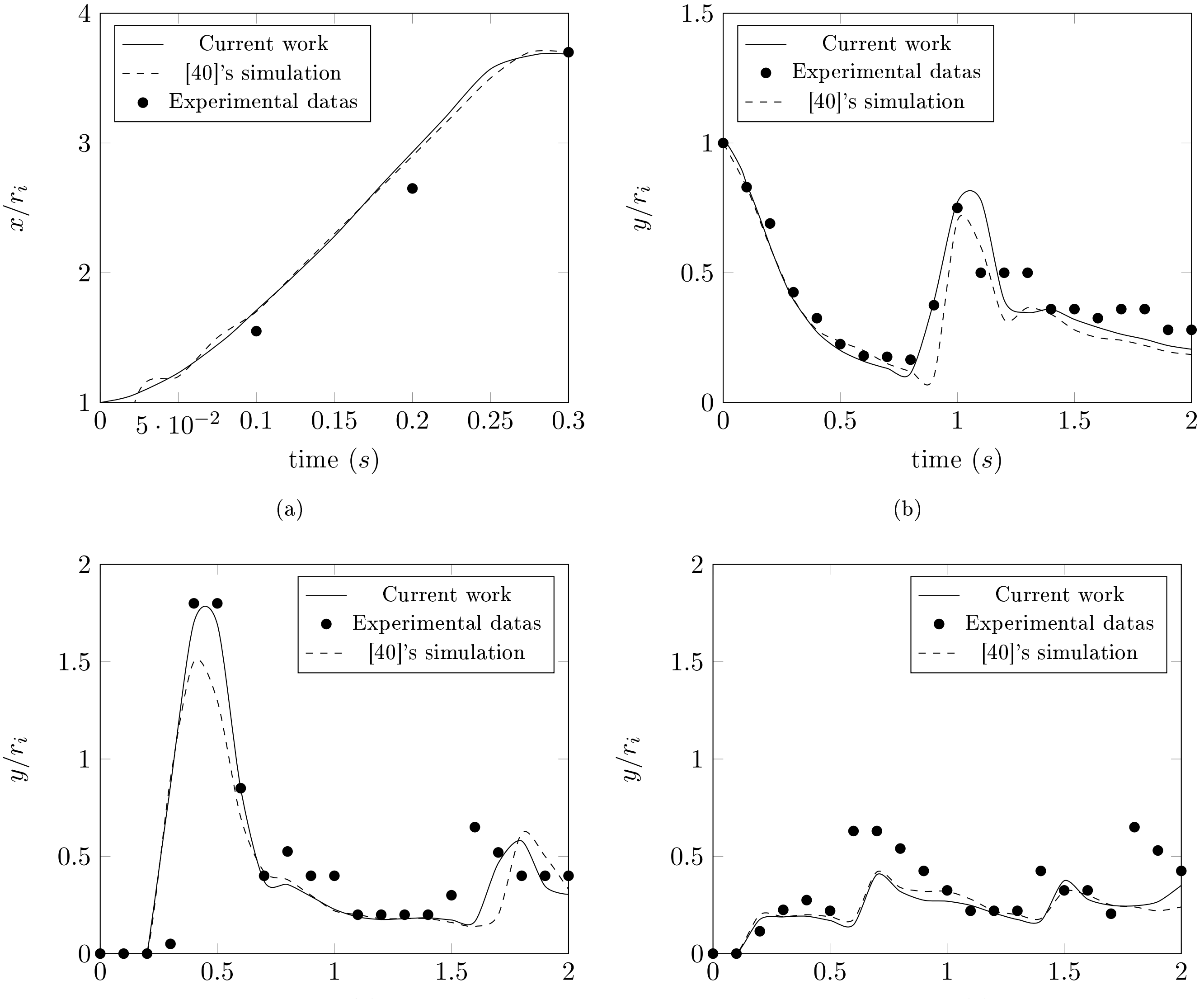

(a)

(b)

(c)

(d)

2.6.4 Sensitivity analysis to mesh parameters

In this part, the influence of several remeshing parameters onto the height and run-out position is discussed.

Thus, this work focus on the interface position during the simulation on lateral walls, by changing several remeshing parameters. The minimum mesh size is fixed to $h_{min} = 10^{-3}$. The parameter that control the thickness of the filtering of the Level-Set function is set to $E = 2 \cdot 10^{-3}$.

2.6.4.1 Influence of the mesh adaptation

In this part, we focus on the influence of the use of mesh adaptation. Figures 25 and 26 measure the interface position on both left and right walls respectively, and study the influence of the mesh adaptation on the solution quality.

These curves show that the use of mesh adaptation improves the accuracy of interface locations onto the two lateral walls. Indeed, the results measured on the left wall show that mesh adaptation better describes the wall impact. Particularly, the use of a coarse mesh (5000 elements) leads to a larger height for the first wave as described in the experiments [40], and reaches a closer value with [40] experiments, as the mesh is refined.

The results obtained onto the right wall, show the same trend. By increasing the number of elements, the maximum height reached by the fluid onto the right wall decreases as the mesh is coarsered, and fits better with experimental datas as the mesh size decreases. Moreover, the impact with the right wall occurs later for a mesh with a lower number of elements. Thus, it is crucial to perform the numerical simulations on a mesh sufficiently fine, to get relevant results.

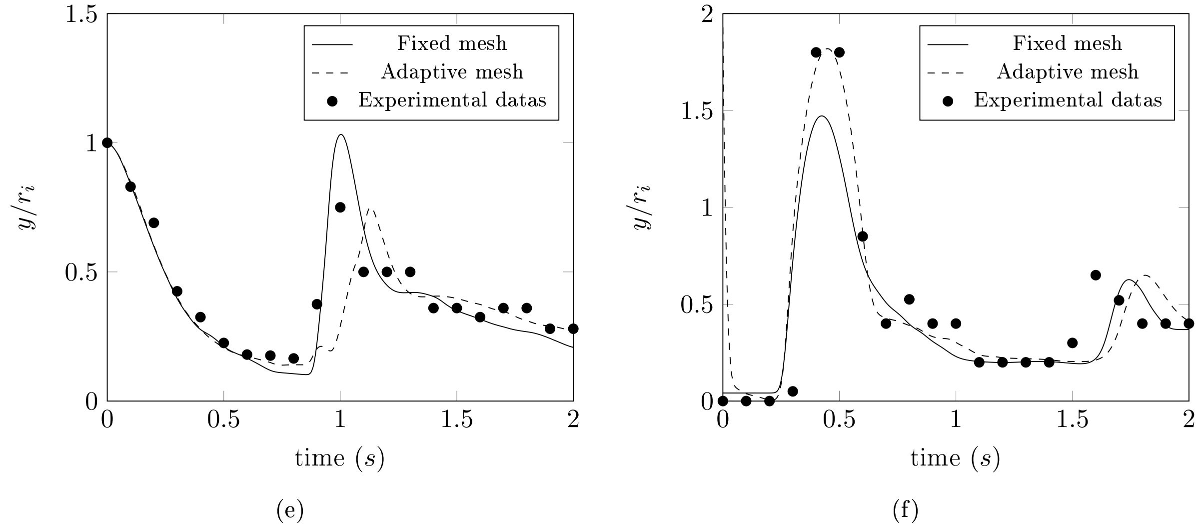

(e)

(f)

Figure 25: Influence of mesh adaptation on the height position of the water onto lateral walls for a mesh with 5000 elements: (a) Dimensionless height position measured on the left wall ; (b) Dimensionless height position measured on the right wall

Then, we focus on the influence of mesh adaptation onto the solution quality. Figure 25 illustrates the comparison between numerical simulations performed onto a fixed and adaptive mesh, with the same number of elements (set to 5000). Figure 26 illustrates the same comparison for a mesh with 10000 elements. It is observed that the use of mesh adaptation leads to a very good agreement with the experiments of [40]. Thus, the computations remain very accurate without using a mesh with high number of elements, leading to the decrease of computational times.

2.6.4.2 Number of elements

Figures 27.a and 27.b measure the interface position onto the left and right walls, and discuss the influence of number of elements on the solution accuracy. Now, the mesh adaptation is used for all the simulations.

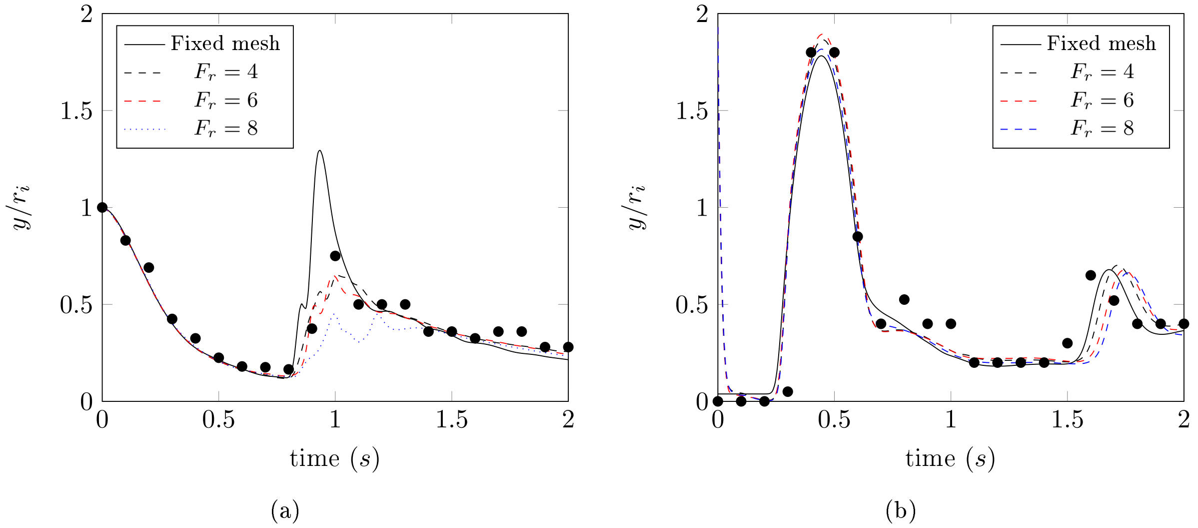

(a)

(b)

Figure 26: Influence of mesh adaptation frequency on the height position of the water onto walls by considering a mesh with 10000 elements: (a) Dimensionless height position measured on the left wall ; (b) Dimensionless height position measured on the right wall

We may observe the influence of the number of elements on the solution quality: by considering a mesh with 10000 elements, the interface location on the two lateral walls is closer to the experimental points extracted from [40], especially for the maximum height measured on the left wall.

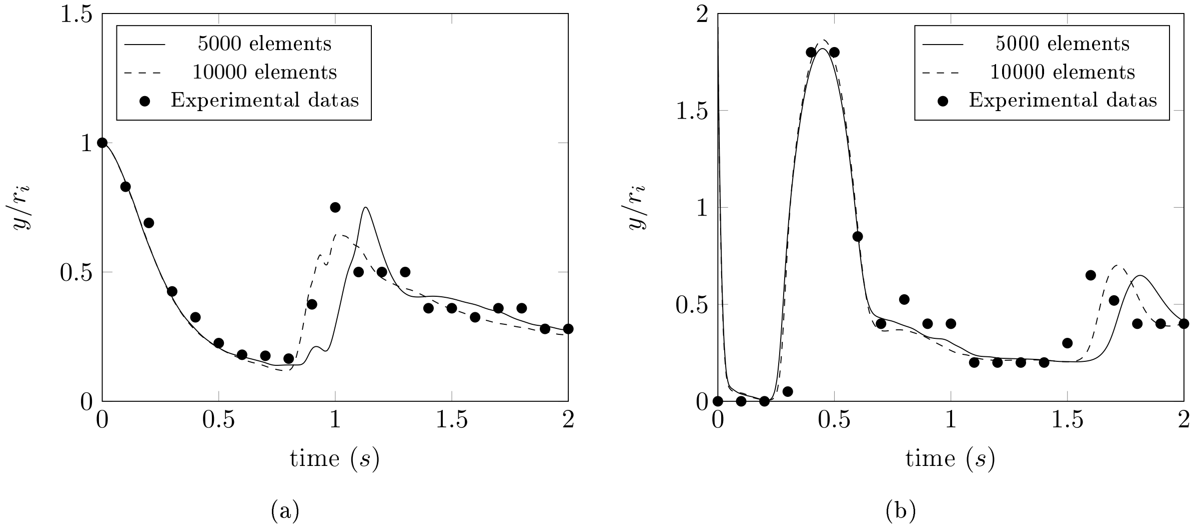

(a)

(b)

Figure 27: Influence of the number of elements on the height position onto lateral walls: (a) Dimensionless height position measured on the left wall ; (b) Dimensionless height position measured on the right wall

To conclude, it is outlined here the importance of chosing the appropriate number of elements to perform mesh adaptation. Indeed, more phenomena are able to be captured for a huge number of elements. However, a compromise must be chosen in order to increase the accuracy, without increasing the computational times.

2.6.5 Mass conservation analysis

In this section, we focus on the volume conservation of the dense Newtonian fluid, called V_f. First, we discuss on the remeshing frequency, denoted as F_r, onto mass loss. As outlined previously, the time step Δt is set to $1 \cdot 10^{-3}s$ and the remeshing frequency is first set to $F_s = 5$. The percentage of gained volume is computed at each time increment i such that:

$$V^i_{gained} = \frac{V^i_f - V^0_f}{V^0_f} \tag{2.56}$$

Figure 28 illustrates the percentage of gained volume during the simulation, by using a mesh with 10000 elements. Now, the influence of mesh adaptation frequency is discussed. It is observed that the percentage of gained volume increases as F_r increases. However, it is acceptable, as it does not overcome 0.5% .

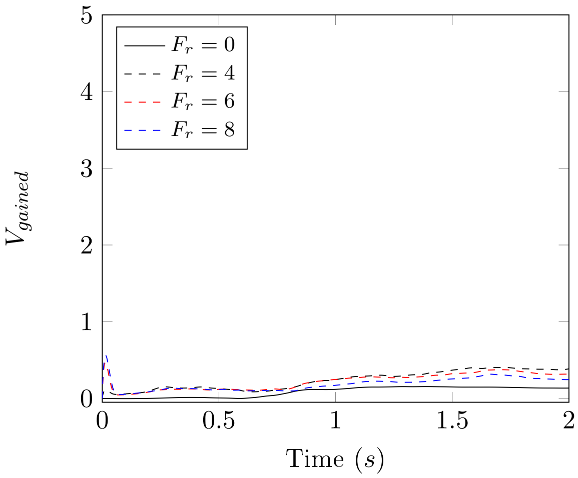

Figure 28: Percentage of gained volume of densest fluid according to the time and influence of the remeshing frequency

In conclusion, a compromise on the choice of the remeshing frequency must be performed. Indeed, the mass loss is more important as F_r increases, but the accuracy is better as observed in the previous section. Thus, chosing $F_r = 6$ in this simulation is relevant.

2.7 Conclusion

In this part, we introduced some specific numerical tools to investigate multiphase flow problems. Thus, three different steps are needed: first, we need to perform the mechanical resolution (Navier-Stokes equations for Newtonian fluids). Then, we need to capture and convect the interface between the two different fluids, and finally, remeshing methods are performed for increasing the computations accuracy.

The flow resolution is performed by using the finite element method, and by considering P1 elements. A variational multiscale method (VMS) is used to solve these types of flows. The interface is captured by defining a signed distance function (Level-Set method), and the transport equation of this function is coupled with the reinitialization step, in order to reduce computation times. Then, the remeshing method consists of an anisotropic mesh adaption, with a fixed number of elements.

These tools have been validated with a two-dimensional Newtonian dam-break. The influence of several remeshing parameters has also been discussed, and the mass conservation of the multiphase model has been studied. Thus, the coupling between Variational MultiScale, Level-Set and anisotropic mesh adaptation methods is very powerful as the flow front is well-captured, and small phenomena are able to be captured. Moreover, a good mass conservation is observed for the model applied on dam-break problems.

Consequently, the purpose of the further work will consists in extending this accurate formulation to strongly non-linear fluids, such as yield stress fluids or dry granular flows.

Chapter 3

Numerical simulation of Bingham flows

Contents

Résumé en français

Ce chapitre a pour objectif de simuler numériquement les écoulements de fluides de Bingham dans un contexte éléments finis.

Comme pour les écoulements de fluides Newtoniens, les équations de conservation des moments et de la masse (mécanique des fluides) doivent être résolues. Cependant, tout l'enjeu consiste à prendre en compte les équations constitutives des fluides de Bingham dans la mécanique des fluides, et plus particulièrement, de traduire numériquement les zones non-déformées (contrainte de cisaillement non défini en dessous du seuil). Dans la littérature, deux approches existent. Tout d'abord, des méthodes dites exactes existent et consistent à calculer la contrainte de cisaillement en dessous du seuil en résolvant un problème de minimisation de l'energie du système. Généralement, la méthode du Lagrangien augmenté est utilisée, et couplée avec un algorithme d'Uzawa, comme effectué par Roquet *et al.*[42]. Enfin, des méthodes de régularisation sont plus communément trouvées dans la littérature, et consistent à traduire le comportement du fluide de Bingham par le calcul d'une viscosité effective.

Dans le cadre de ce travail de thèse, nous avons choisi une méthode de régularisation. Ainsi, la première partie de ce chapitre s'intéresse à des écoulements de Bingham monophasiques hautement plastiques (cavité entraînée, expansion planaire et écoulement autour d'un cylindre). Comme pour les fluides Newtoniens, la résolution des équations de conservation des moments et de la masse sont résolues et stabilisées par une méthode variationelle multi-échelles. De plus, le maillage est adapté de manière anisotrope dans les régions à fortes variations de gradients des champs Level-Set, vitesse, mais également du champ viscosité effective afin de bien caractériser la transition entre zones cisaillées et non-cisaillées. Il a été observé que ces méthodes permettent de traiter des cas hautement plastiques (et donc, à très grands nombres de Bingham), puisque permettant des grands sauts de viscosité entre chaque élément du maillage, et sont ainsi très intéressantes dans notre contexte.

La deuxième partie de ce chapitre est dédiée à la simulation numérique de l'écoulement multiphasique de fluides de Bingham. Les résultats obtenus ont été comparé à ceux de Liu *et al.*[43], et une bonne concordance entre les deux modèles a été trouvée. De plus, nos résultats montrent encore une fois la puissance des outils numériques pour la résolution des écoulements de fluides de Bingham hautement plastiques.

3.1 Introduction

Numerical simulation offers a very flexible tool to model yield stress fluids, and remains an inevitable step to study these complex fluids behavior. The remaining challenge is to construct efficient methods to capture such flow patterns in a robust and accurate way. In the literature, the computational domain may be discretized by different techniques in order to solve Bingham flows. In [44], a finite volume method is employed to discrete the equations which leads to approximate continuity and momentum equations on each control volumes. In [45], a Smoothed Particle Hydrodynamics (SPH) approach is applied, which can be viewed as a numerical scheme where the fluid flow is decomposed into discrete particles. The most common used method in the literature is the finite element formulation (see [42] and [46] for details). Nevertheless, the stability of the discrete formulation depends on appropriate compatibility restrictions on the choice of the finite element spaces [47]. The lack of stability manifests in uncontrollable oscillations that pollute the solution, in particular for high Bingham and Reynolds numbers.

On the other hand, we highlight another issue in the numerical simulation of a viscoplastic flow and is connected to the singularity of relations 3.1 and impossibility to determine stresses in the domains where the rate of deformation equals zero. In order to overcome these difficulties, various modifications, known as regularization methods have been introduced. We note two approaches, Bercovier-Engleman [48] and Papanastasiou [49], where the term $\eta_p + \tau_0 / \parallel \dot{\gamma} \parallel$ in relations 3.1 is replaced with $\eta_p + \tau_0 / \sqrt{\parallel \dot{\gamma} \parallel^2 + (1/m)^2}$ (Bercovier-Engleman) or $\eta_p + \tau_0 (1 - e^{-m \parallel \dot{\gamma} \parallel}) / \parallel \dot{\gamma} \parallel$ (Papanastasiou) for an arbitrarily large regularizing parameter m. The performance and comparisons between these methods are summarized and analyzed in [50].

Despite the simplicity of implementing these models, some limitations still exist. The resolution is strongly dependent on the regularizing parameter m. Indeed, taking high values of this parameter encounters convergence issues whereas small values limit the flow prediction and the flow arrest is not controlled. One must find a compromise for choosing this parameter, in order to ensure reasonable computation time and good accuracy of the solution.

Several techniques have been developed aiming to increase this coefficient. One consists in applying a continuation method, which means to select dynamically m and to keep it smaller during all the simulation. Another one found in the literature consists in performing a number of Picard iterations, and switch to the Newton method when a sufficiently good approximation to the solution is found [51]. One may also consider multiplier methods as alternatives for regularized models. It consists in computing the extra-stress tensor directly using minimization algorithms. The most useful way consists in employing Augmented Lagrangian method, coupled with Uzawa algorithm. This kind of methods reveals to be more accurate to determine flow arrests, but convergence may be slow, which can lead to unreasonable computational times.

In this chapter, we derive an adaptive Variational MultiScale (VMS) method for Bingham flows combined with a regularization method. In fact, we adapt the numerical tools introduced previously and used to solve Newtonian flow, to Bingham flows. The main reasons for this choice of adaptive variational approach are stability, robustness and computational efficiency, as proven before in Newtonian benchmarks. Indeed, mesh adaptation reveals to be a useful tool to improve accuracy, without reaching high computational times. In [52], an isotropic mesh adaptation is proposed and is based on the subdivision of a quadrilateral grid into subvolumes, each of them with the same mesh size. However, isotropic adaptation lacks in accuracy when the flow presents specific directional properties. We combine here the VMS formulation with an a posteriori error estimator for dynamic anisotropic mesh adaptation. It involves building a mesh based on a metric map. It provides both the size and the stretching of elements in a very condensed information data. Consequently, due to the presence of high gradients when using high values for the regularization coefficient, it provides highly stretched elements at the inner and the boundary layers, and thus yields an accurate modeling framework for Bingham flows as explained in [42]. The obtained system is then solved using a stabilized finite element method designed to handle the discontinuity on shear stress field. Indeed, it consists on the decomposition for both the velocity and the pressure fields into coarse/resolved scales and fine/unresolved scales, needed to deal with both high Bingham and Reynolds numbers.

We assess the behavior and accuracy of the proposed formulation in the simulation of three time-dependent challenging numerical examples, aiming for the first time to deal with high regularizing parameter (up to 10^6), high Bingham (up to 2000) and Reynolds (up to 10000) numbers.

Finally, we apply these tools to multiphase Bingham flows.

3.2 Constitutive equations

As introduced in the first chapter, the constitutive equations of Bingham fluids are defined such as:

$$\begin{cases} \tau = 2\left(\eta_p + \frac{\tau_0}{||\dot{\gamma}||}\right)\dot{\gamma} & \text{for } \ || \ \tau \ || > \tau_0 \\ \dot{\gamma} = 0 & \text{for } \ || \ \tau \ || \leq \tau_0 \end{cases} \tag{3.1}$$

In this formulation, the apparent viscosity is defined above the yield stress such as:

$$\eta_a = \eta_p + \frac{\tau_0}{||\dot{\gamma}||} \tag{3.2}$$

The resolution of momentum equations leads thus to a problem as the apparent viscosity is not defined in the unyielded areas. Consequently, the main challenge consists in taking into account the constitutive law into motion and mass equations. In this work, we use a regularization method, aiming to compute effective viscosity of the fluid. When the fluid is flowing, this viscosity must approach the plastic viscosity and when no deformations occur, it must be the maximum possible. Regularization methods aim to control and limit the maximum viscosity, in order to avoid convergence problems due to viscosity jumps.

Papanastasiou proposed a regularization which consists of expressing effective viscosity as an exponential function of shear rate [49]. Thus, we find the following expression for the effective viscosity η_{eff} of the fluid:

$$\eta_{eff} = \eta_p + \frac{\tau_0}{|| \ \dot{\gamma} \ ||}[1 - exp(-m \ || \ \dot{\gamma} \ ||)] \tag{3.3}$$

m corresponds to the Papanastasiou coefficient designed to control the yield limit: the larger m, the better we approach the classical Bingham model. However, as mentioned before, it may manifest in uncontrollable oscillations and a non-convergent solution, in particular for high Bingham and Reynolds numbers.

3.3 Mesh adaption criteria

In viscoplastic flows, the yielded and unyielded regions are not a priori known and may vary in time, thus it is difficult to pre-adapt the mesh around these regions. This motivates again the use of implicit strategy that imposes a dynamic mesh adaptation that changes the mesh frequently and minimizes as possible the prescribed error. Consequently, it requires a criterion based solely on the solution.

The common way to adapt a mesh to several variables, such as the velocity and the viscosity, is to compute the metrics corresponding to each of them and then to produce a unique metric by an operation known as the intersection of metrics. In this work, we simplify this operation and we use one metric that account for different variables, as introduced in chapter 2. In the following numerical experiments, the adaption accounts for the velocity, its magnitude and also the viscosity η_{eff} by defining the following vector of sources of error

$$\mathbf{v}(\mathbf{x}^i) = \left\{ \frac{v^i}{||v^i||}, \frac{||v^i||}{\max\limits_j ||v^j||}, \frac{\eta_{eff}}{\max(\eta_{eff})} \right\} \tag{3.4}$$

3.4 Model validation

In order to validate the proposed methods, three time-dependent numerical test cases are presented in this section. The results obtained with the proposed approach are compared with those obtained by other approaches that can be found in the literature. Some test cases cannot be handled using classical model in particular for high Bingham and Reynolds numbers using high regularizing parameter (up to 10^6) attest of the benefit of adaptive VMS formulation.

Recall first the two dimensionless parameters used in the test cases: the Reynolds number characterizes the flow regime, such as laminar or turbulent, and is defined as the ratio of inertial forces to viscous forces [53].

$$Re = \frac{\rho v_c L_c}{\eta_p} \tag{3.5}$$

where L_c and v_c correspond respectively to the characteristic length and velocity.

Bingham number is defined as the ratio between yield stress and viscous stresses:

$$Bn = \frac{\tau_0}{\eta_p \mid\mid \dot{\gamma} \mid\mid_c} \tag{3.6}$$

where $\mid\mid \dot{\gamma} \mid\mid_c$ corresponds to the characteristic shear rate.

3.4.1 Flow in a lid-driven cavity

The flow inside a lid-driven square cavity of length unity is investigated and the performance of the mesh adaptation is examined. Figure 29 illustrates the problem statement. No-slip velocity boundary conditions are imposed at the left, right and bottom walls of the cavity. A horizontal uniform velocity $v_{lid} = 1$ is prescribed at the top. Characteristic values of length, velocity and shear rate are given by L, v_{lid}, and v_{lid}/L.

Several test cases with increasing complexity will be presented using different Reynolds and Bingham numbers and Papanastasiou regularizing coefficients. Comparisons with the literature and new results will be proposed. Moreover, the mesh has been adapted according to the velocity norm, to each component of the velocity vector and to the obtained viscosity.

In figure 30, yield stress effects on viscoplastic fluid dynamics are analyzed, plotting extra-stress isobands of very-low-inertia Bingham flows. In this case, we fixed $Re = 0$ and $m = 1000$ and we let the Bingham number varies from 1 to 1000. The number of elements is fixed to 10000. Yielded (liquid-like) and unyielded (solid-like) regions may be observed respectively in white and black color. Two different kinds of rigid areas

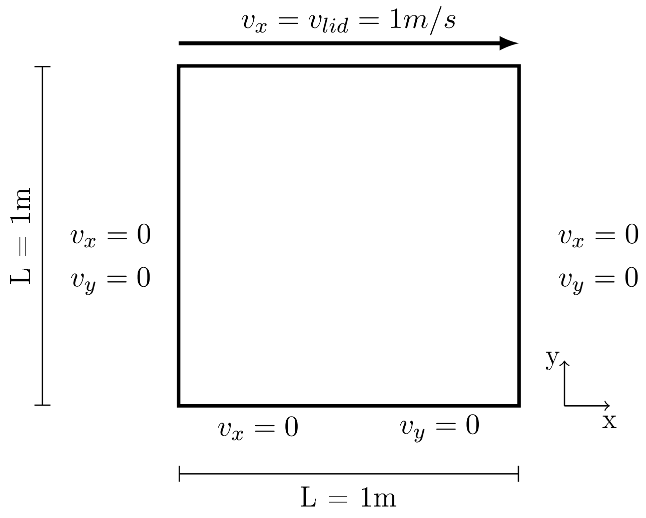

Figure 29: Lid-driven cavity flow: problem statement

may be distinguished: one close to the bottom wall which corresponds to an almost stagnant flow (very low velocities) and another one at the upper zone in which the fluid is performing a nearly rigid body motion. We can observe that yielded and unyielded proportions in the cavity are strongly influenced by the Bingham number. Indeed, increasing of unyielded regions is observed as Bingham number increases, as it was noticed in [54, 53].

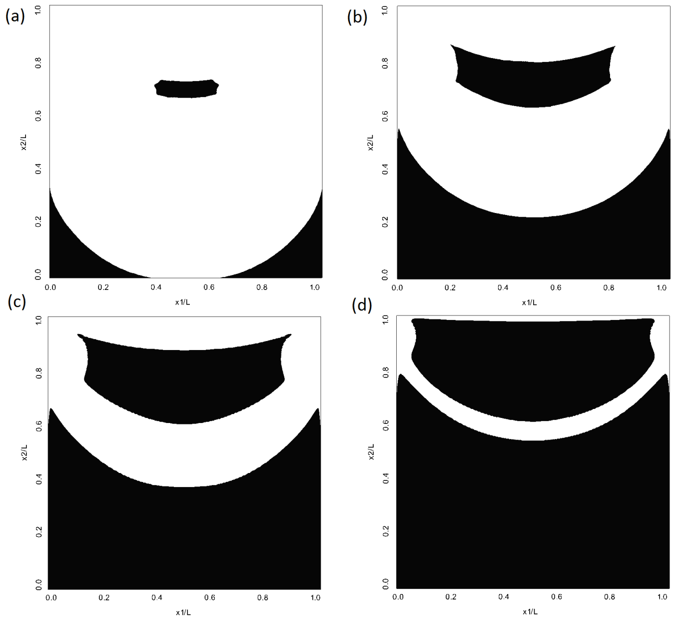

Figure 30: Yielded and unyielded regions in a lid-driven cavity, for Re=0: (a) Bn=1, (b) Bn=5, (c) Bn=20, and (d) Bn=1000

Horizontal and vertical velocity profiles are proposed in [54]. Therefore, to assess the accuracy of the adaptive VMS method, we repeated the same cases using two different number of elements: 2000 and 1000 and we plotted the results in Figures 31 and 32. We recall that Re is equal to 100 and two values of Bingham number were used: Bn= 0.1 and 1.

As expected, the fluid behavior may be recognized with low velocity values at the bottom of the cavity (unyielded areas) and with high velocities at the top (yielded areas). Moreover, the efficiency of using adaptive anisotropic meshing is well highlighted with the use of very low number of elements. It decreases considerably the computational times without loss of accuracy.

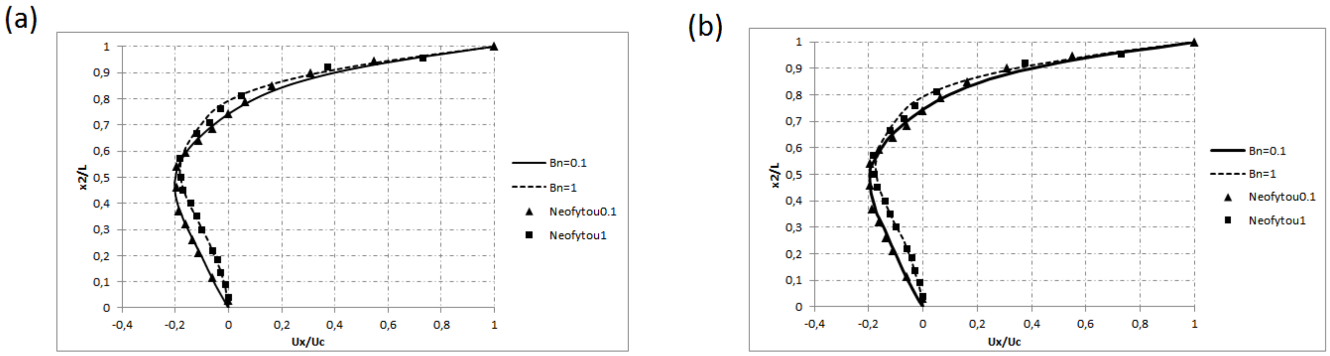

Figure 31: Horizontal velocity, for Re = 100 and Bn = 0.1 - 1: (a) Mesh with 10000 elements, (b) Mesh with 2000 elements

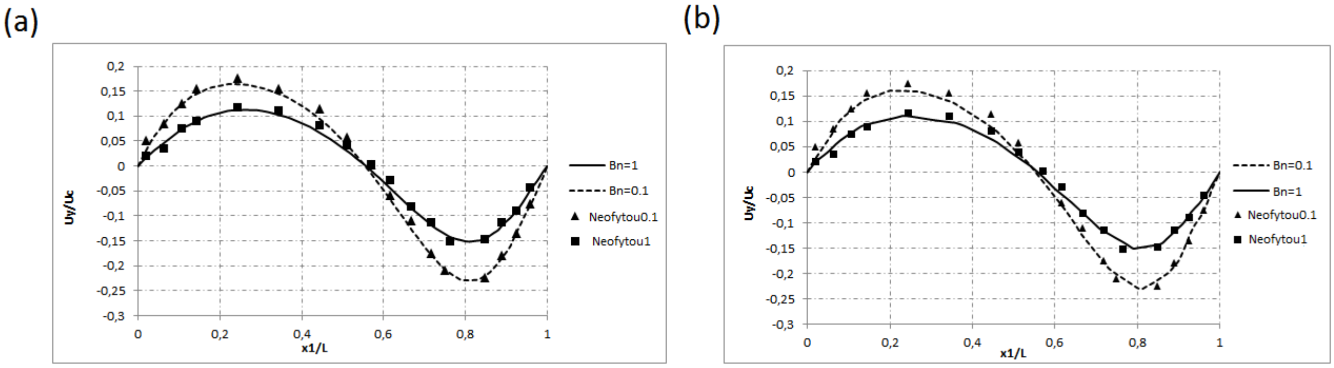

Figure 32: Vertical velocity, for Re = 100 and Bn = 0.1 - 1: (a) Mesh with 10000 elements, (b) Mesh with 2000 elements

From a theoretical point of view, increasing the Papanastasiou regularization parameter involves a more realistic Bingham model. Figure 33 clearly shows the influence of using high values of m up to 10^6. The interfaces between yielded and unyielded regions are clearer and are capture better using anisotropic mesh adaptation. This phenomenon is due to the increasing viscosity of the fluid in order to get unyielded regions with more rigidity, but also to approach to a realistic Bingham fluid.

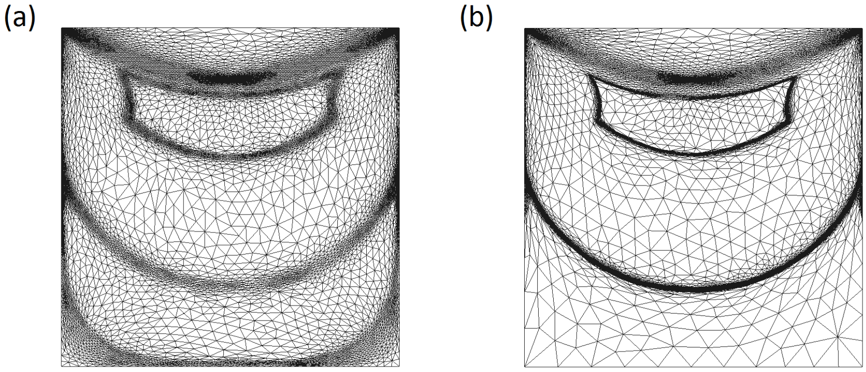

Figure 33: Mesh adaptation according to velocity and viscosity fields, for Re = 0 and Bn = 5: (a) $m = 10^3$, (b) $m = 10^6$

Finally, to assess the performance of the proposed VMS adaptive framework and its ability to solve very complex yield stress flows, we repeated the same numerical test using higher Reynolds numbers (1000 and 10000) and varying the Bingham number up to 2000. The Papanastasiou regularizing parameter is set to 10^6 and the number of elements in all the simulations is fixed to 10000. The adaptive process always starts from a uniform mesh and is iterated every five time step. The results on the respective converged meshes can be seen in Figures 34 and 35. Note the concentration of the resolution not only along all the boundary layers but also at the detachment regions. This reflects well the anisotropy of the solution caused by the discontinuity of the boundary conditions and the nature of the flow. The elements far from the discontinuities are mostly isotropic and increase in size as the Reynolds number increases. Again, this reflects and explains how, for a controlled number of nodes, the mesh is naturally and automatically coarsened in that region with the goal of reducing the mesh size around the discontinuities.

As Reynolds and Bingham numbers increases, the flowing regions decreases and the fluid in the cavity becomes totally rigid. At this level, it is important to highlight how sharply the layers can be captured. It shows the correct orientation and deformation of the mesh elements (longest edges parallel to the boundary). This yields a great reduction of the number of triangles. This results give confidence that the proposed framework allows to deal for the first time with extreme cases.

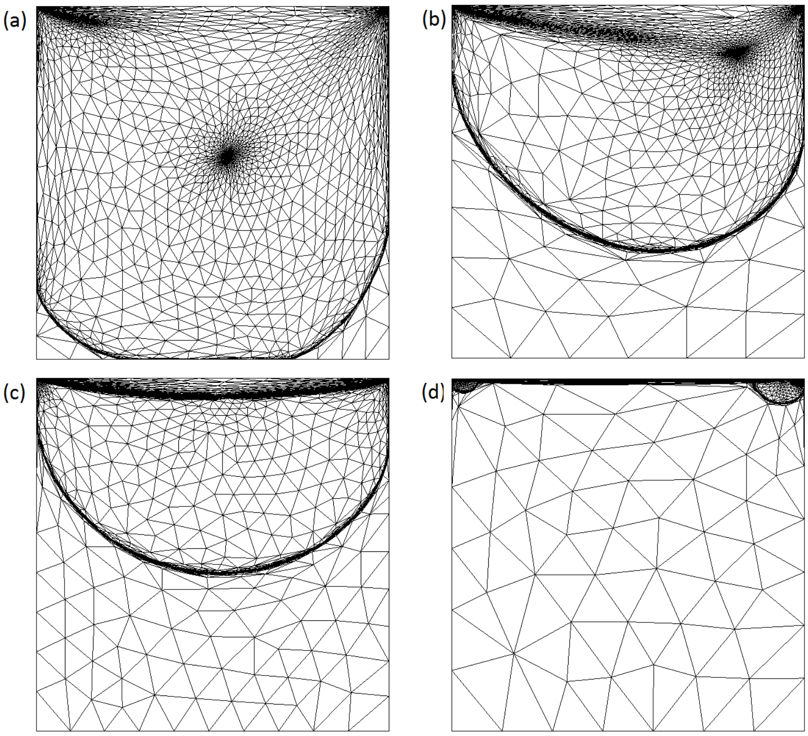

Figure 34: Mesh adaptation following velocity field, for Re=1000 and m = 10^6: (a) Bn = 1, (b) Bn = 100, (c) Bn = 1000, (d) Bn = 2000

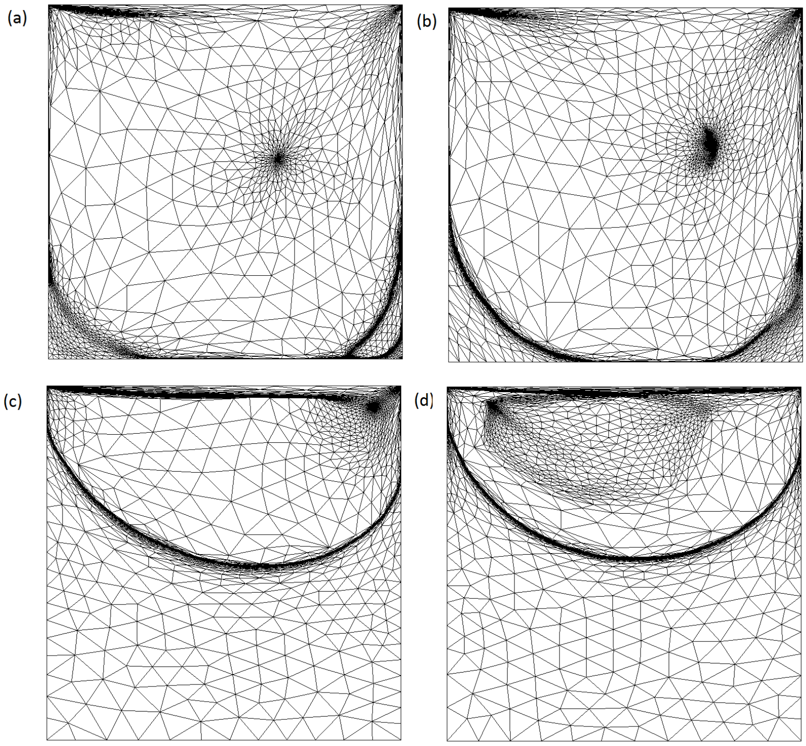

Figure 35: Mesh adaptation following velocity field, for Re=10 000 and m = 10^6: (a) Bn = 1, (b) Bn = 100, (c) Bn = 1000, (d) Bn = 2000

3.4.2 Flow through a sudden planar expansion

In this example, we study a Bingham flow through a sudden planar expansion as illustrated in Figure 36. A new dimensionless number is introduced as the ratio β between higher and smaller channels ($\beta = H_2/H_1$). On both channel walls, no-slip and impermeability boundary conditions are applied. At the inlet, a parabolic velocity profile $V_x(y)$ is applied. The characteristic values of length, velocity and shear rate are given by H_1, the average inlet velocity $\overline{V}_1$ and $\| \dot{\gamma} \|_c = \overline{V}_1/2H_1$.

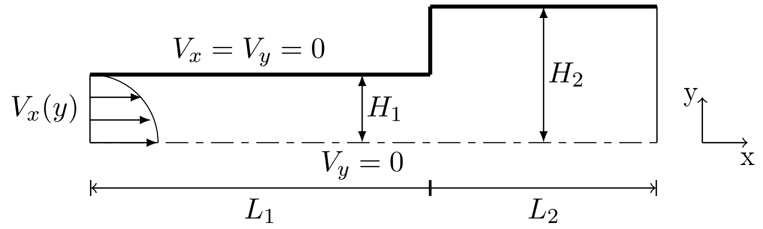

Figure 36: Problem statement of the flow through a sudden planar expansion

In this example, we consider a ratio β of 2 with a smaller channel height of 1. In addition, the Papanastasiou regularizing coefficient is assumed to be equal to 10^6 in order to obtain the most realistic Bingham model.

Figure 37 illustrates the distribution of yielded and unyielded regions in the computational domain. Unyielded zones (black ones) may be sorted into two distinct zones: non-moving regions (dead zones) at expansion corner and moving regions (plug-flows) around the center-line. The more Bingham number Bn increases and the more unyielded regions expand, as being noticed for the lid-driven cavity case. This is the consequence of material yield limit increasing.

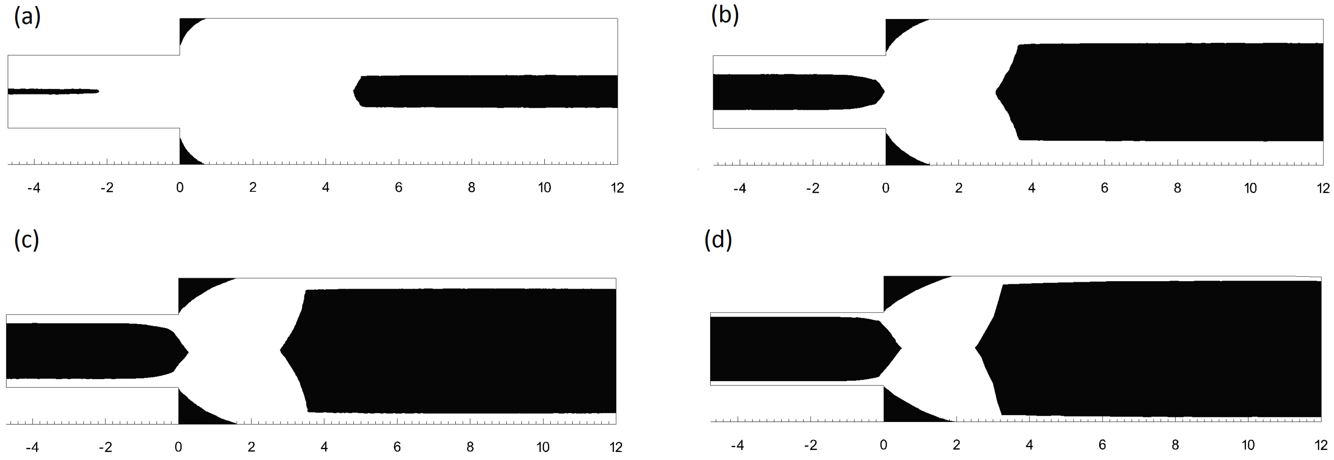

Figure 37: $\| \tau \|$ iso-bands for Re=0: (a) Bn=0.2, (b) Bn=3.9, (c) Bn=27 (d) Bn=127

Figure 38 shows the obtained horizontal velocity profiles at a fully developed region of larger channel and for three different Bingham numbers. Solutions of this test case obtained in [53] agree very well with our results. The influence of Bingham number on the plug-flow is quite relevant in these plots: the more the Bingham number increases, the more the velocity profile becomes flatter - plug-flow zones with $\| \tau \| \leq \tau_0$ - and subjected to severe boundary-layers near the wall - shear zones with $\| \tau \| > \tau_0$.

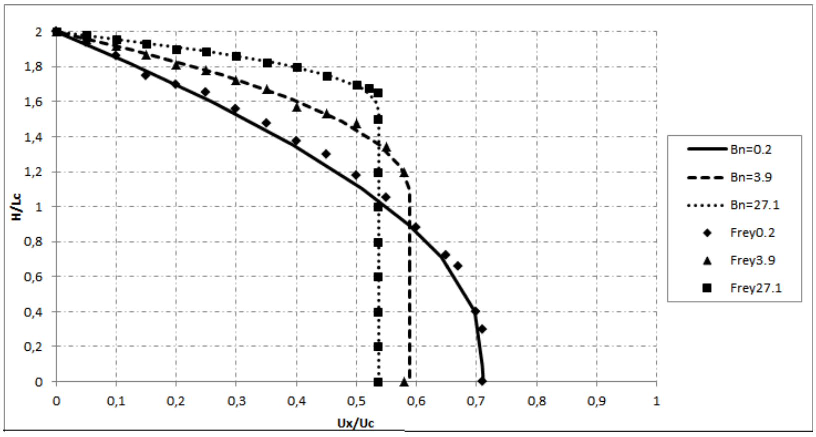

Figure 38: Horizontal velocity profile at a fully developed region of larger channel for Re=0

Figure 39 shows the obtained anisotropic adaptive meshes. The number of elements was set here to $20,000$. We notice that the viscosity computation becomes more accurate, especially in unyielded zones located at the center of both channels, where the mesh captures the underlying physics of such flows. Again, this reflects and explains how, for a controlled number of nodes, the mesh is naturally and automatically coarsened in yielded regions with the goal of reducing the mesh size near the discontinuities.

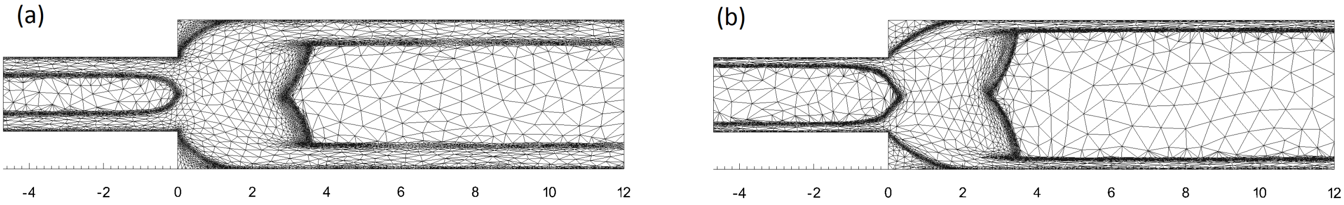

Figure 39: Anisotropic adaptive meshes, for $Re = 0$ and $m = 10^6$: (a) Bn=3.9 (b) Bn=27.1

3.4.3 Flow around a cylinder

We consider a circular unity cylinder of an incompressible Bingham plastic fluid with a uniform free stream velocity V_0. The problem statement is illustrated in Figure 40. In order to make the problem of unconfined flow numerically feasible, the cylinder is placed in a rectangular fictitious domain characterized by upstream length L_l, downstream length L_r, and lateral height H. As proposed in [55], we set $L_l = 20$, $L_r = 25$ and $H = 30$. At the surface of the cylinder, no-slip condition is assumed ($V_x = 0$, $V_y = 0$). At outlet, zero diffusion condition for all dependent variables (except pressure, which is zero at the outlet).

Figure 41 illustrates the distribution of yielded and unyielded regions for two different Bingham numbers (Bn=10 and Bn=100) and for a low Reynolds number (Re=1). We observe three different unyielded subdomains: two regions located at both extremities of the cylinder, which represent front stagnation points, and undergo rigid-body like rotations; two small unyielded zones, known as polar caps, which are static in nature; but also a solid-like region moving like a plug without deforming. We can observe in the same figure that polar caps and front stagnation points are still present. However, the area occupied by the other yielded regions decreases as the Bingham number increases.

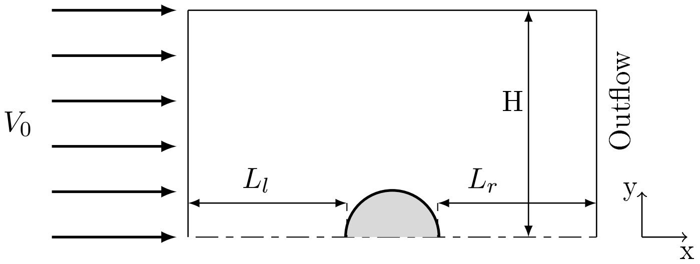

Figure 40: Problem statement of a Bingham flow around a cylinder

Figure 41: $\| \tau \|$-Isobands, for Re = 1: (a) Bn=1 , (b) Bn=100

In figures 42 and 43, we plot the horizontal velocity profiles measured in regions close to the cylinder. The obtained results agree very well with the ones in [55]. We notice that the higher the Bingham number the faster the velocity converges to 1. This is especially due to the reduction of solid-like regions which enclose the cylinder when Bn increases too fast. According to y-components, two observations may be added. First, the appearance of front stagnation points can be noticed on all the curves. The more the Bingham number, the larger the velocity gradients in these zones. Second, the zones located after the front stagnation points are studied. We notice that with a low value of Bn, the velocity approaches slowly to 1, in contrary to what was observed using high Bingham numbers. This is the consequence of a larger yielded region.

Finally, figure 44 shows the obtained anisotropic adaptive mesh. As expected, the refinement is important close to the polar caps, where higher viscosity and velocity gradients are noted. Again, the developed Navier-Stokes VMS solver combined with anisotropic mesh adaptation shows to be very efficient and robust to deal with yield stress fluid flows.

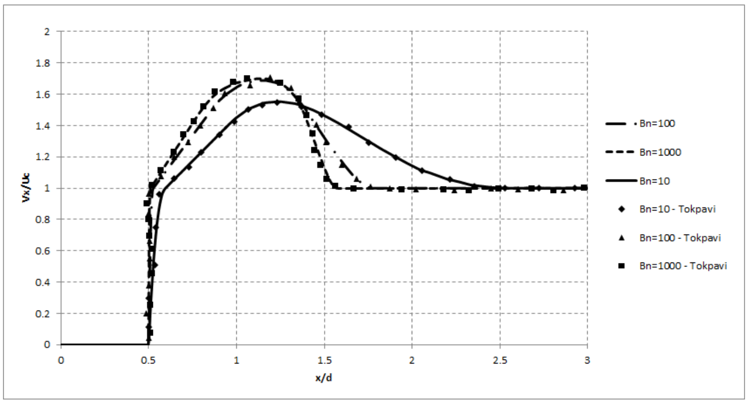

Figure 42: Horizontal velocity according to y-coordinate, Re = 1, Bn=10, 100, 1000

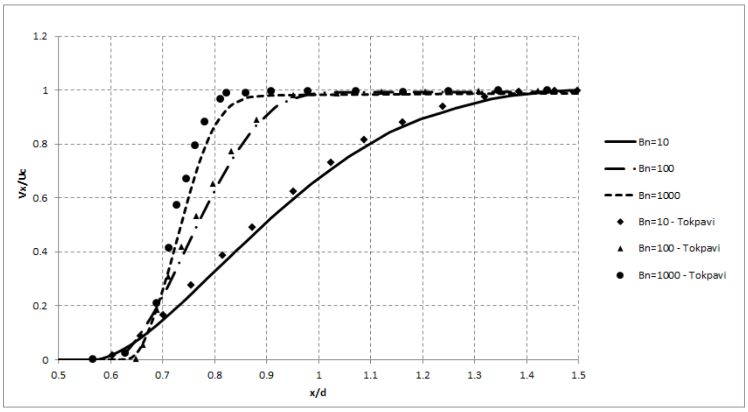

Figure 43: Horizontal velocity according to x-coordinate, Re = 1, Bn = 1, 10, 100, 1000

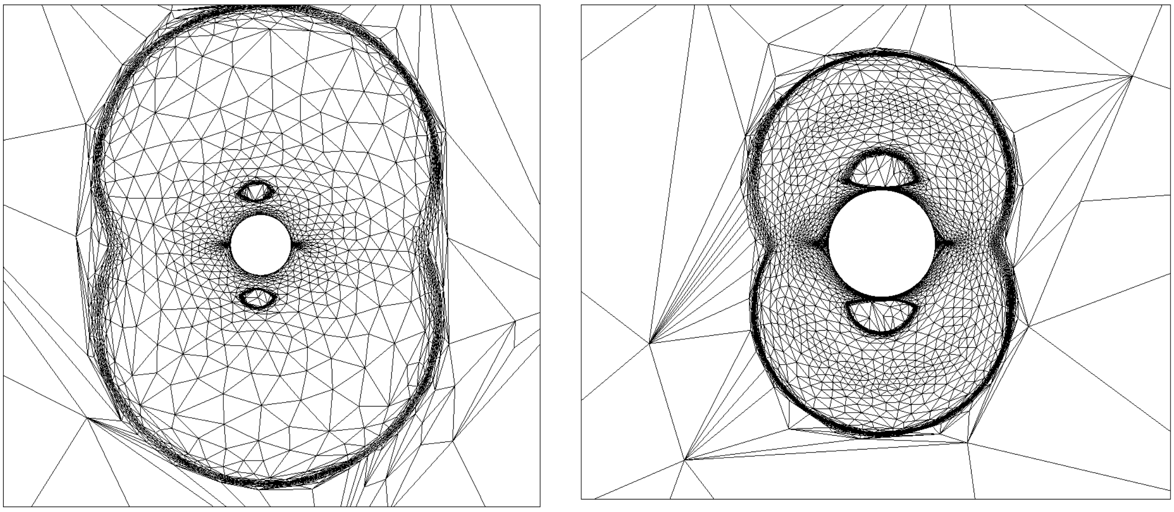

Figure 44: Anisotropic mesh adaptation according to velocity and viscosity fields, for Re = 1: (a) Bn = 1, (b) Bn = 100

3.4.4 Conclusion

We have shown in this section that the Variational MultiScale method combined with anisotropic adapted meshes with highly stretched elements can be used to compute high Reynolds and Bingham number flows [56]. All the meshes are obtained by solving an optimization problem under the constraint of a fixed number of edges in the mesh. We demonstrated the efficiency of this framework to be capable of automatically producing boundary layers and capturing the interfaces between yielded and unyielded regions. The numerical results show that the flow solvers based on stabilized finite element method is able to exhibit good stability and accuracy properties using very high values of the Papanastasiou coefficient up to 10^6. This is an important novelty for Bingham fluids study. Indeed, the maximum value reached for Papanastasiou coefficient is found in the literature around 10^3.

We validated the proposed model for the simulation of Bingham flows in a monophase framework. Now, the purpose consists in simulating multiphase Bingham flows, and specifically, in adapting the multiphase tools previously validated for two Newtonian fluids flows. This point will be the purpose of the next section.

3.5 Multiphase framework: the dam-break problem

In this section, we will focus on the simulation of mutiphase Bingham flows. Previously, the Level-Set method has been introduced, and aim to capture and follow the position of the interface between two fluids during the simulation. Particularly, we introduced the convective auto-reinitializing Level-Set method, which couples both transport and reinitialization steps of the signed distance function. Now, this section is devoted to the numerical simulation of multiphase Bingham flows.

3.5.1 Problem statement

The dam-break problem consists of the collapse of a fluid column due to gravity. The problem statement is illustrated in figure 81. We consider a computational domain of height H and length L, filled with two fluids: the first one is a rectangular column (height h_i and length r_i) of Bingham fluid, and the second one is air. No-slip boundary conditions are applied on the bottom wall, and symmetric conditions, at the left wall.

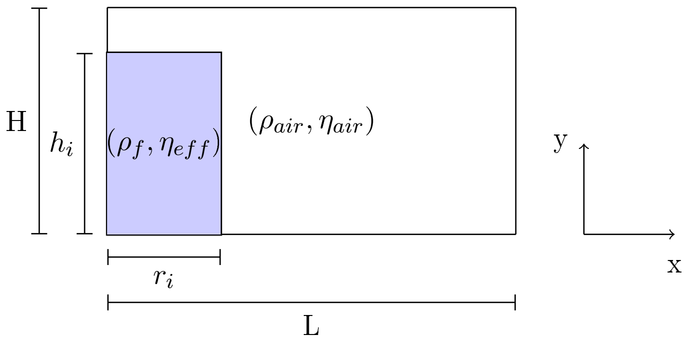

Figure 45: Problem statement of a Bingham dam-break problem

3.5.2 Literature review

Previously, we simulated monophase Bingham flows. An overview of existing challenging and difficulties has been established. Particularly, the main difficulty for the resolution of Bingham flows comes from the jump of viscosity induced by the regularization method. However, the extension to multiphase flows induces additional difficulties, as the ambient fluid viscosity (generally very low) must be taken into account. Indeed, properties mixing between Bingham and ambient fluids leads to higher viscosity jumps than observed for monophase flows.

Some works on the simulation of multiphase Bingham flows are found in the literature. First, shallow water models are found, and consider that the height of the flow is negligible compared to the run-out distance. Several works deal with free-surface yield stress flow, by using this method. For instance, [57] and [58] used such an approach for the spreading of a Herschel-Bulkley fluid down a slope. In [57], unyielded areas are thus defined such that zero velocity in the height direction is applied. In [58], the critical height, which defines the transition height between unyielded and yielded areas, is estimated. Then, the velocity in the height direction is computed by integrating momentum equations separately in yielded and unyielded areas. This approach is interesting, but is limited for flows high Bn.

[59] performed two-dimensional Bingham collapses, by using the finite element method in a Lagrangian framework. Momentum equations are solved only in the flowing (yielded) area, avoiding the use of any regularization methods. This method consists in expressing the problem of potential energy minimization and in solving it with Uzawa algorithm. The interface is tracked at each time step, and is then reconstructed after its convection by using polygonal curves. They performed non-Newtonian collapses on a slope, and compared the shape of the flow between several rheological models (Bingham, Herschel-Bulkley, Power-law). This method is able to simulate flow arrests, as no effective viscosity is computed. However, it leads to higher computational times as an additional loop is needed.

[60] performed two-dimensional Bingham collapses, by using a volume of fluid method (VOF). The constitutive equations are taken into account into the momentum equations by using a regularization method. Specifically, they chose to limit the viscosity by introducing directly a maximum viscosity η_{max}. Thus, the viscosity field is thought discontinuous which may generate numerical difficulties. Moreover, the ratio between maximum viscosity and plastic viscosity is only taken to 10^2. Following [60], this choice for η_{max} does not affect the results. However, they have not extended their formulation to highly viscous flows (high Bingham numbers), for which flow arrests can be difficult to determine.

[43] performed also two-dimensional Bingham collapses by using VOF method. However, they used the simple regularization method. Properties of the ambient fluid have been chosen such that the ratio with the Bingham fluid properties is 10^{-3}. Moreover, the regularization parameter m has been chosen as 10^7, allowing the simulation of Bingham dam-breaks with high Bn.

The purpose of the next section consists in validating first our model with the results of [43], for analyzing the model robustness to flows with high Bn. Then, sensitivity analysis will be performed.

3.5.3 Dimensionless constitutive equations

As in [43], dimensionless momentum and mass equations are solved. Each length is non-dimensionalized by dividing it by a characteristic value, determined by the flow problem. For the dam-break problem, characteristic height and velocity are thus chosen such as $L_c = h_i$ and $v_c = \frac{\rho_f g h_i^2}{\eta_p}$. Characteristic time and stress are defined such as $t_c = \frac{h_i}{v_c}$ and $\tau_c = \rho_f g h_i$.

Thus, characteristic density is $\rho_c = \frac{\rho_f}{Re}$ where Re corresponds to the Reynolds number, defined such as:

$$Re = \frac{\rho_f v_c h_i}{\eta_p} \tag{3.7}$$

Consequently, characteristic viscosity is $\eta_c = \eta_p$ and characteristic acceleration, $g_c = gRe$.

By scaling each lengths by the appropriate characteristic value, dimensionless momentum equations are expressed formulated such that:

$$\begin{cases} \bar{\rho} Re \left[\frac{\partial \bar{u}}{\partial t} + (\bar{u} \cdot \nabla \bar{u})\right] = -\nabla \bar{p} + \nabla \cdot \bar{\tau} + \rho \\ \nabla \cdot \bar{u} = 0 \end{cases} \tag{3.8}$$

In [43], the Bingham number Bn is defined as the ratio between yield stress and viscous stress, defining dimensionless yield stress from which the fluid begins to flow:

$$Bn = \frac{\tau_0}{\rho_f g h_i} \tag{3.9}$$

Thus, dimensionless constitutive equations of Bingham fluids are:

$$\begin{cases} \| \bar{\tau} \| = Bn + \| \bar{\dot{\gamma}} \| & \text{for } \| \bar{\tau} \| > Bn \\ \| \bar{\dot{\gamma}} \| = 0 & \text{for } \| \bar{\tau} \| \leq Bn \end{cases} \tag{3.10}$$

Finally, dimensionless effective viscosity of the fluid is computed in all the domain such as:

$$\bar{\eta}_{eff} = 1 + \frac{Bn}{\| \bar{\dot{\gamma}} \|} \left(1 - exp(-\bar{m} \| \bar{\dot{\gamma}} \|)\right) \tag{3.11}$$

where $\bar{m}$ corresponds to the dimensionless regularization parameter, which must be chosen as large as possible.

Figure 46 illustrates the rheological curve of Bingham fluids (logarithmic scale), after the use of Papanastasiou regularization. It is observed the existence of a critical shear rate, denoted $\dot{\gamma}_c$, which corresponds to the transition between unyielded and yielded regions. Theoretically, finding $\dot{\gamma}_c$ corresponds to find the zero of the function $x - Bn \cdot exp(-\bar{m}x)$.

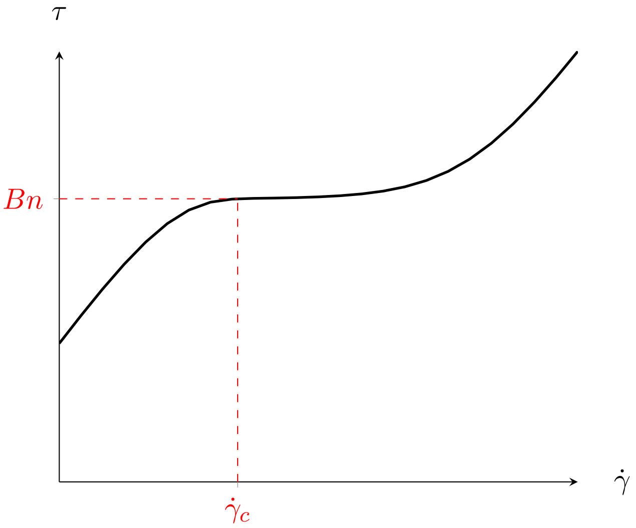

Figure 46: Rheological curve for Bingham fluid by the use of Papanastasiou regularization

Now, the purpose consists in simulating the Bingham dam-break problem, and in validating with the results obtained by [43]. As for monophase flows, momentum and mass equations are solved, and coupled with the Papanastasiou regularization method. However, no-slip boundary conditions are applied on the bottom surface. Consequently, the wetting of the Bingham is not performed as a fine air layer is present at the bottom surface. In the following part, a method will be proposed to ensure the Bingham wetting onto the bottom surface.

3.5.4 Wetting

As explained before, the dynamic wetting of the Bingham fluid must be ensured onto the bottom surface. Thus, a thin layer ϵ_g, of the order of the minimum mesh size h_{min}, is computed at each time increment. On ϵ_g, the Bingham fluid is able to slip, allowing the air to escape.

To compute ϵ_g, the first step consists in localizing the zero-isovalue position on the bottom wall. Then, we compute the signed distance function on the bottom surface nodes. When it is positive, no-slip boundary conditions ($v = 0$) is thus applied and when it is negative, the air is able to slip ($v_y = 0$). Then, the coordinates of the nearest node to the zero-isovalue, localized both on the bottom wall and inside the Bingham domain, are determined. At this node, the boundary conditions are changed, to slip conditions. Figure 47 illustrates how to determine the slipping region.

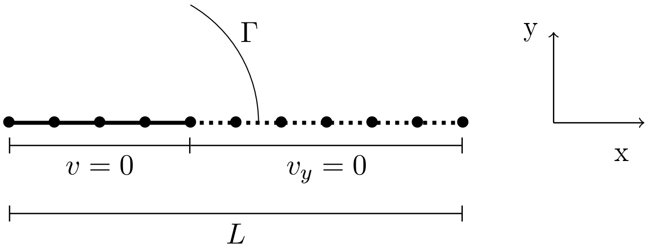

Figure 47: Boundary conditions at the bottom surface for a Bingham dam-break

3.5.5 Model validation

In this part, the model proposed for Bingham flows is validated by comparing the obtained results with the ones of [43]. A Bigham dam-break is studied, with aspect ratio $a = 1$.

Two dimensionless parameters control the flow: the Reynolds number Re, and the Bingham number Bn. For the validation, the Reynolds number is fixed to $Re = 10^{-3}$, and Bn varies from 0.01 to 0.2.

Dimensionless viscosity and density of air are chosen such that its ratio with Bingham properties is 10^{-3}, in order to be negligible. Thus, $\bar{\eta}_{air} = 10^{-6}$ and $\bar{\rho}_{air} = 10^{-3}$. For instance, a Bingham fluid with density $\rho_f = 1000 kg/m^3$ and plastic viscosity $\eta_p = 100 Pa \cdot s$ will be surrounded by a Newtonian fluid with density $\rho_{air} = 1 kg/m^3$ and viscosity $\eta_{air} = 10^{-1} Pa \cdot s$. The initial height of the column h_i is equal then to $20 cm$. Yield stress are thus taken in a range from 2 to 40 Pa.

3.5.5.1 Computations initialization

Figure 48 illustrates adaptive mesh and iso-zero value of the Level-Set function, which corresponds to the interface between the Bingham fluid and the air. Computations initialization has been performed in the same way as for Newtonian fluid: the mesh is adapted several times until the obtention of the finest possible mesh close to the interface.

3.5.5.2 Numerical results

Figures 49, 50, and 51 show the height profile during a Bingham collapse with $Bn = 0.03$, and illustrate dimensionless velocity (a), shear rate (b), shear stress (c) and effective viscosity (d) fields at several instants

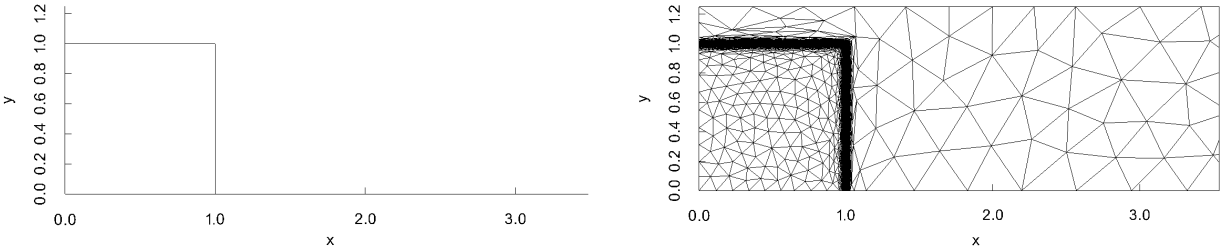

(a) (b)

Figure 48: Computations initialization of a Bingham dam-break problem: (a) Interface ; (b) Initial adaptive mesh

of the simulation ($\bar{t} = 10, 100$ and 1000). At time $\bar{t} = 10$, the results illustrated in figure 49 show a velocity increase as approaching the flow front. Moreover, unsheared regions are localized at the center of the flow, but also at the corner, still kept at this stage. Thus, effective viscosity is larger and maximal in these areas.

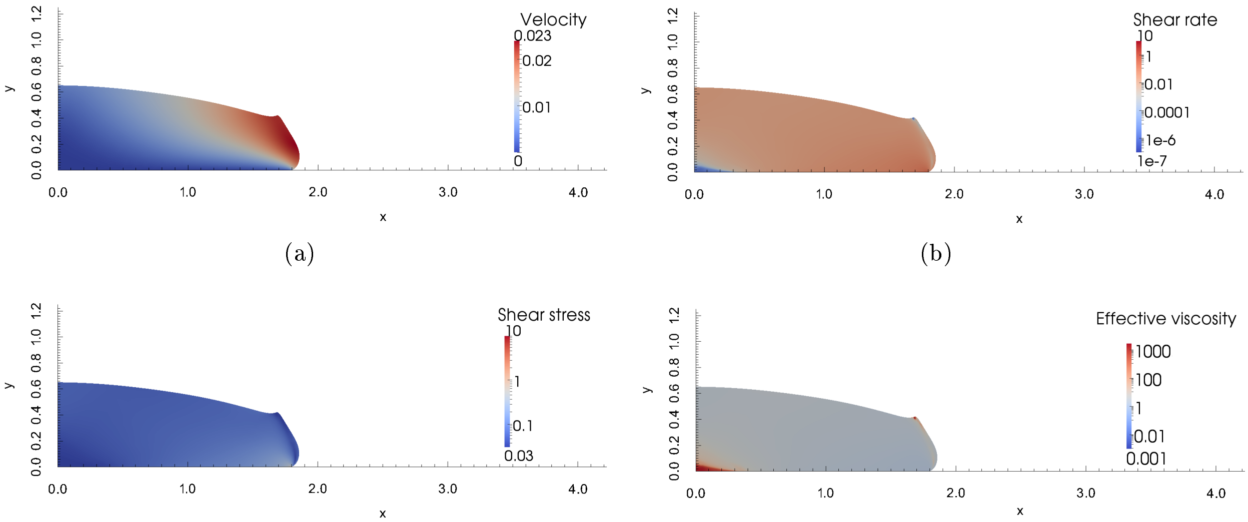

(a) (b)

(c) (d)

Figure 49: Dam-break of a Bingham fluid with $Bn = 0.03$ at $\bar{t} = 10$: (a) Velocity $\bar{v}$; (b) Shear rate $\bar{\dot{\gamma}}$; (c) Shear stress $\bar{\tau}$; (d) Effective viscosity $\bar{\eta}_{eff}$

Figures 50 illustrates the Bingham profile at $\bar{t} = 100$. At this stage, the corner has totally vanished. The unsheared region, located at the center of the flow, has grown.

At time $\bar{t} = 1000$, as illustrated in figure 51, the maximum velocity is very low, and the fluid seems to be stopped since $t = 100$.

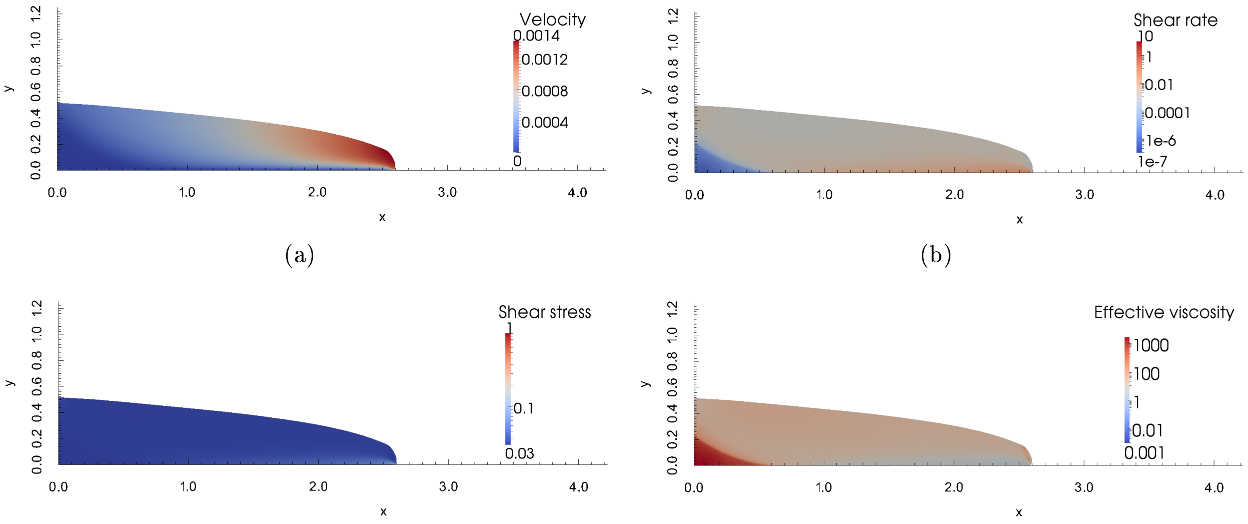

(a) (b)

(c) (d)

Figure 50: Dam-break of a Bingham fluid with $Bn = 0.03$ at $\bar{t} = 100$: (a) Velocity $\bar{v}$; (b) Shear rate $\bar{\dot{\gamma}}$; (c) Shear stress $\bar{\tau}$; (d) Effective viscosity $\bar{\eta}_{eff}$

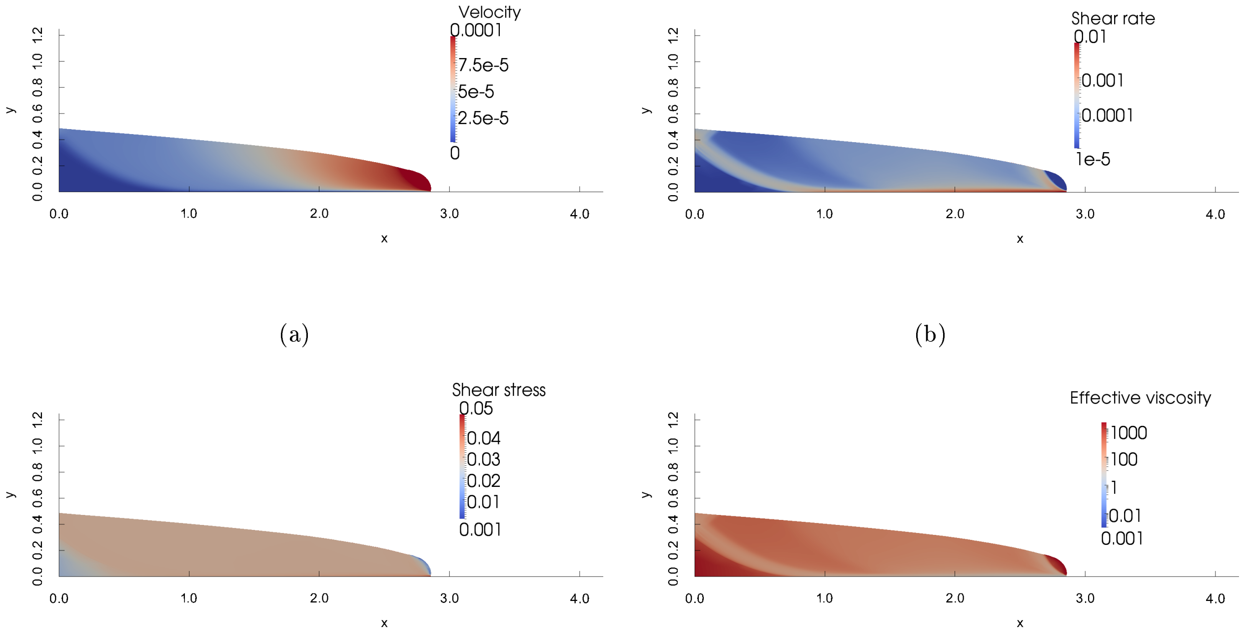

(a) (b)

(c) (d)

Figure 51: Bingham dam-break with $Bn = 0.03$ at $\bar{t} = 1000$: (a) Velocity $\bar{v}$; (b) Shear rate $\bar{\dot{\gamma}}$; (c) Shear stress $\bar{\tau}$; (d) Effective viscosity $\bar{\eta}_{eff}$

Figures 52 and 54 show the height profile during Bingham dam-break with larger Bn ($Bn = 0.1$. Now, unsheared regions are larger than previously. Particularly, an other unyielded region located at the flow front, has grown. Furthermore, the fluid is more resistant to the flow, leading to a better corner conservation. At $\bar{t} = 1000$, effective viscosity is very large and the fluid seems to be stopped.

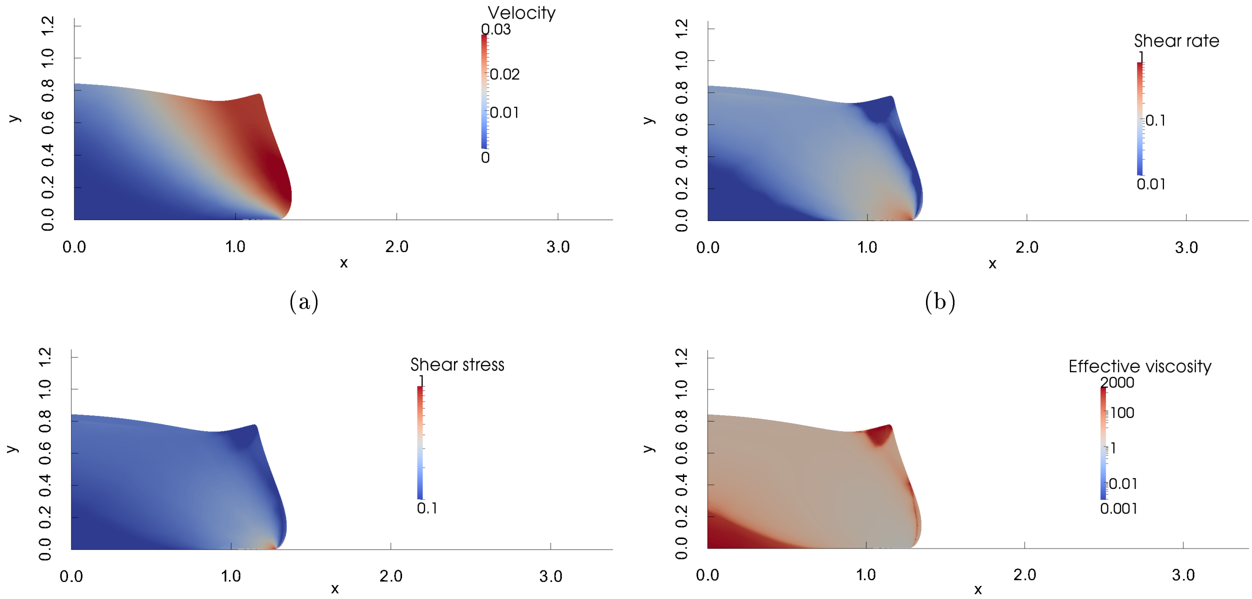

(a) (b)

(c) (d)

Figure 52: Dam-break of a Bingham fluid with $Bn = 0.1$ at $\bar{t} = 10$: (a) Velocity $\bar{v}$; (b) Shear rate $\bar{\dot{\gamma}}$; (c) Shear stress $\bar{\tau}$; (d) Effective viscosity $\bar{\eta}_{eff}$

3.5.5.3 Yielded and unyielded regions

Figures 55, 56 and 57 illustrate yielded (white) and unyielded (black) regions during a Bingham dam-break with $Bn = 0.03$, at several instants ($\bar{t} = 10, 100, 1000$). At the flow beginning (figure 55, i.e. $\bar{t} = 10$), an unyielded region, located at the flow center and corresponding to a dead zone, is observed. We observe also a smaller unyielded area located at the column corner, tending to vanish as the fluid is flowing (figure 56). Moreover, the associated mesh captures very accurately yielded and unyielded transition. During the collapse, the dead zone grows onto the Bingham domain, and the corner vanishes completely. At the end of the simulation ($\bar{t} = 1000$), the flow stabilizes and seems to be stopped.

Then, a Bingham dam-break with $Bn = 0.1$ is performed, and influence of Bn is analyzed. At $\bar{t} = 10$, unyielded areas located both at corner and column center, are larger. Moreover, an other small unyielded region appears at the front, giving a curved front shape.

To conclude, the model allows the simulation of highly viscoplastic flows, and the accurate capture of small unyielded regions, such as the column corner. Particularly, the mesh adapation allows an accurate description of the transition unyielded/unyielded areas.

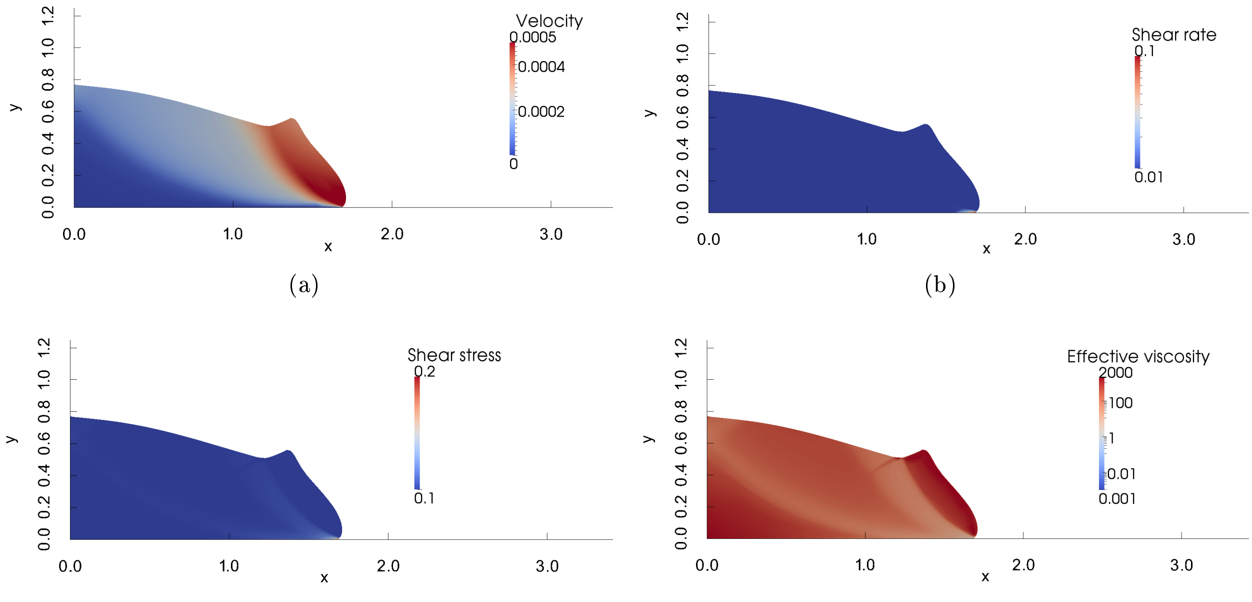

(a) (b) (c) (d)

Figure 53: Dam-break of a Bingham flow with $Bn = 0.1$ at $\bar{t} = 100$: (a) Velocity $\bar{v}$; (b) Shear rate $\bar{\dot{\gamma}}$; (c) Shear stress $\bar{\tau}$; (d) Effective viscosity $\bar{\eta}_{eff}$

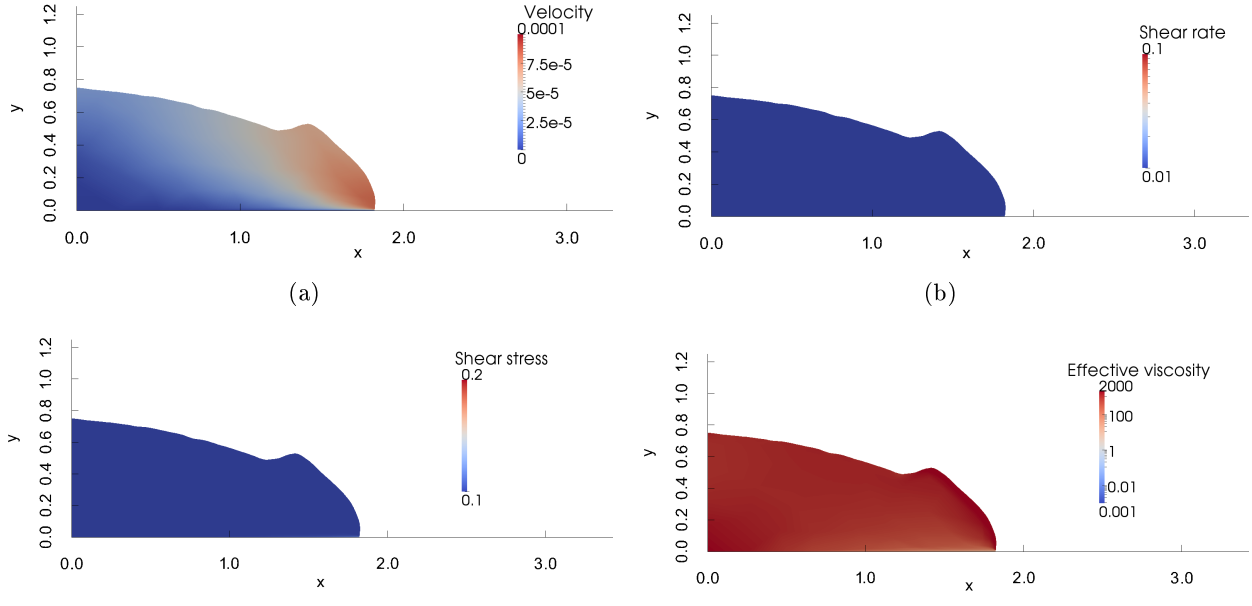

(a) (b) (c) (d)

Figure 54: Dam-break of a Bingham flow with $Bn = 0.1$ at $\bar{t} = 1000$: (a) Velocity $\bar{v}$; (b) Shear rate $\bar{\dot{\gamma}}$; (c) Shear stress $\bar{\tau}$; (d) Effective viscosity $\bar{\eta}_{eff}$

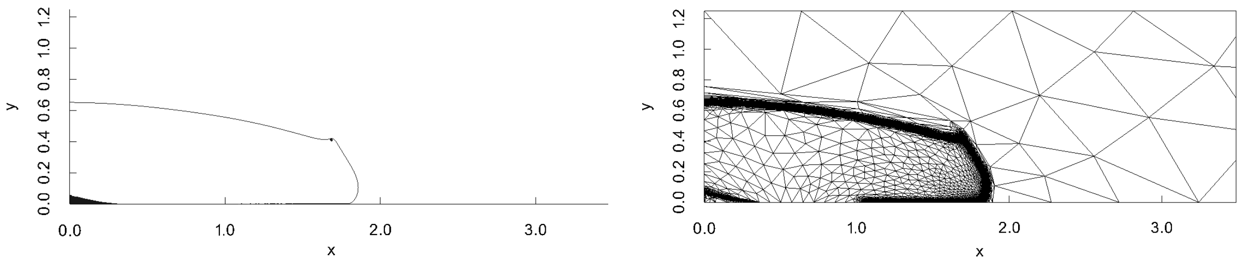

(a) (b)

Figure 55: Bingham dam-break with $Bn = 0.03$ at $\bar{t} = 10$: (a) Inteface and yielded/unyielded areas ; (b) Adaptive mesh

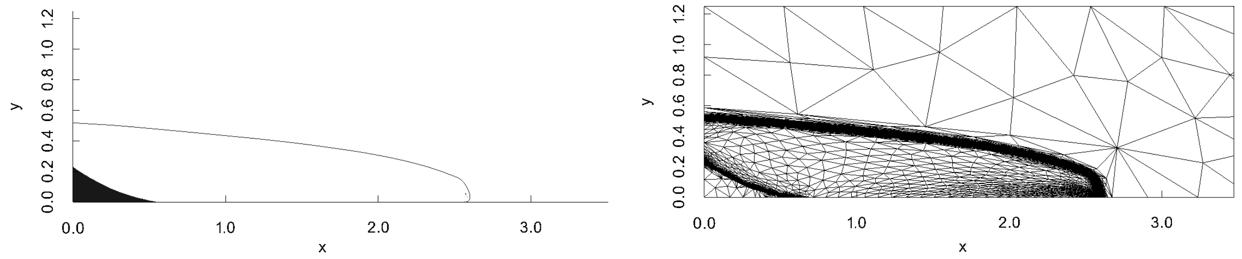

(a) (b)

Figure 56: Bingham dam-break with $Bn = 0.03$ at $\bar{t} = 100$: (a) Inteface and yielded/unyielded areas ; (b) Adaptive mesh

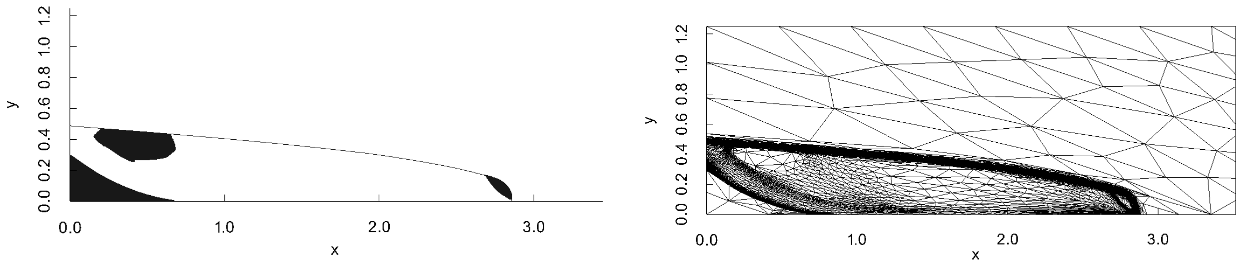

(a) (b)

Figure 57: Bingham dam-break with $Bn = 0.03$ at $\bar{t} = 1000$:(a) Inteface and yielded/unyielded areas ; (b) Adaptive mesh

3.5.5.4 Run-out and height analysis

Now, run-out distance and height profile are determined with respect to the time, and are compared with Liu *et al.*[43].

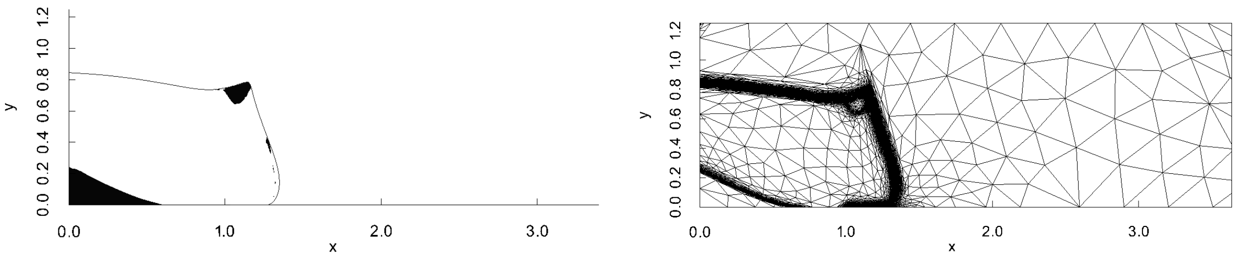

(a) (b)

Figure 58: Bingham dam-break with $Bn = 0.1$ at $\bar{t} = 10$: (a) Interface and yielded/unyielded regions ; (b) Adaptive mesh

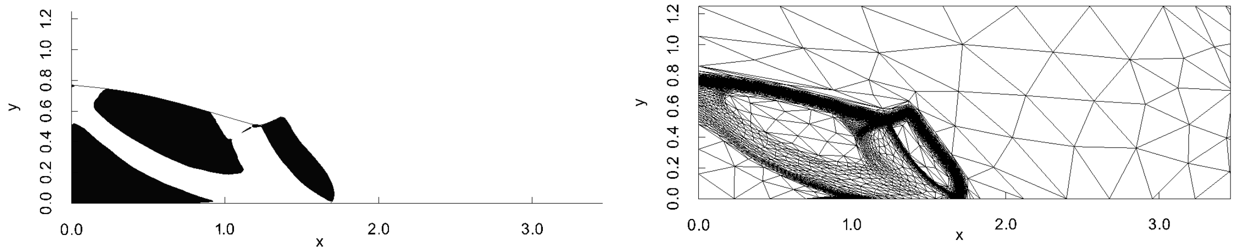

(a) (b)

Figure 59: Bingham dam-break with $Bn = 0.1$ at $\bar{t} = 100$: (a) Interface and yielded/unyielded regions ; (b) Adaptive mesh

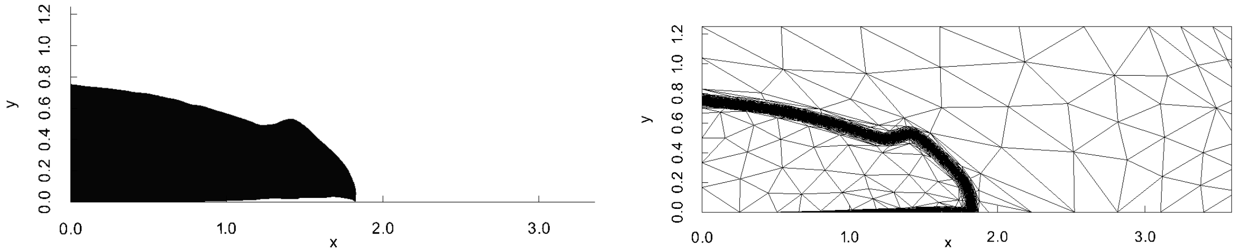

(a) (b)

Figure 60: Bingham dam-break with $Bn = 0.1$ at $\bar{t} = 1000$: (a) Interface and yielded/unyielded regions ; (b) Adaptive mesh

Figure 61 illustrates the Bingham run-out distance, for dam-breaks with different Bn: $Bn = 0.03, 0.06$ and 0.1. The larger Bn, the further the run-out distance, and consequently, the sooner the final run-out distance.

Figure 62 illustrates the Bingham height, measured on the left wall for dam-breaks with different Bn. First, the larger Bn, the larger the final Bingham height. Moreover, the final Bingham height is minimum

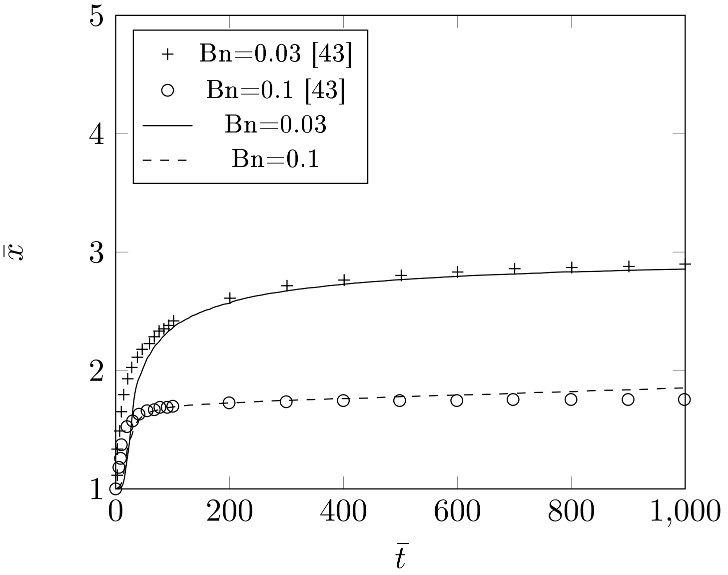

Figure 61: Run-out distance during dam-breaks with different Bn and comparison with Liu *et al.*[43]

sooner for larger Bn. Finally, our results fits the ones of Liu *et al.*[43].

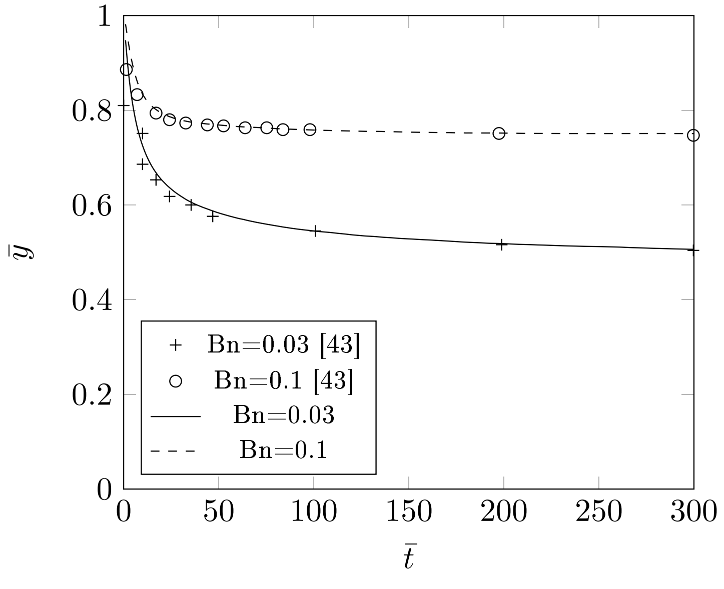

Figure 62: Bingham height, measured on the left wall, during dam-breaks with different Bn

3.5.5.5 Energy analysis

Now, an energy analysis is performed. First, kinetic energy is computed such as:

$$E_c = \frac{1}{2}\rho \parallel v \parallel^2 \tag{3.12}$$

Potential energy corresponds to the energy able to be transformed into kinetic energy, and is computed such as:

$$E_p = \rho g z \tag{3.13}$$

where z corresponds to the height coordinate.

Mechanical energy corresponds to the sum of both energies. In the absence of friction (for instance, in the case of a chute), the total potential energy is transformed into kinetic energy, inducing constant mechanical energy.

$$E_m = E_p + E_c \tag{3.14}$$

Moreover, dissipated power is defined such as:

$$P_{dissip} = \eta_{eff} \parallel \dot{\gamma} \parallel^2 \tag{3.15}$$

The analysis of energy evolution with respect to the time, is performed, by computing the mean energy over the Bingham domain:

$$\begin{array}{l} E_c = \frac{1}{2V_tot} \int_{\Omega_f} \rho \parallel v \parallel^2 d\Omega_f \\ E_p = \frac{1}{V_tot} \int_{\Omega_f} \rho g z d\Omega_f \\ P_{dissip} = \frac{1}{V_tot} \int_{\Omega_f} \eta \parallel \dot{\gamma} \parallel d\Omega_f \end{array} \tag{3.16}$$

Figure 63.a illustrates kinetic energy evolution during two Bingham dam-breaks with $Bn = 0.03$ and $Bn = 0.1$. We observe that kinetic energy decreases drastically between $\bar{t} = 0$ to 20, and stabilizes slowly to a very low value for the two dam-breaks. The difference deals with kinetic energy value during the first instants: when Bn is larger, kinetic energy is slightly lower.

Figure 63.b illustrates potential energy evolution. A brutal decrease is observed at the first instants. However, a larger time is needed to stabilize to a final value for low Bn. Indeed, figure 62 shows that final height is larger for a Bingham fluid with higher Bn. Moreover, we notice that kinetic energy is negligible compared to potential energy. Thus, all the variation of potential energy is transformed into power dissipation as the Reynolds number is very low. Thus, the flow is quasi-static.

Figure 63.c illustrates mechanical energy evolution. As mentioned before, we find here the negligibility of kinetic energy compared to potential energy, traducing the quasi-static flow.

Figure 63.d illustrates the variation of power dissipation. The same trend as kinetic energy curve 63.a is observed. First, a decrease is observed until $\bar{t} = 20$, leading to the stabilization at a low value, as observed before. Moreover, the flow dissipates more power for a low Bn.

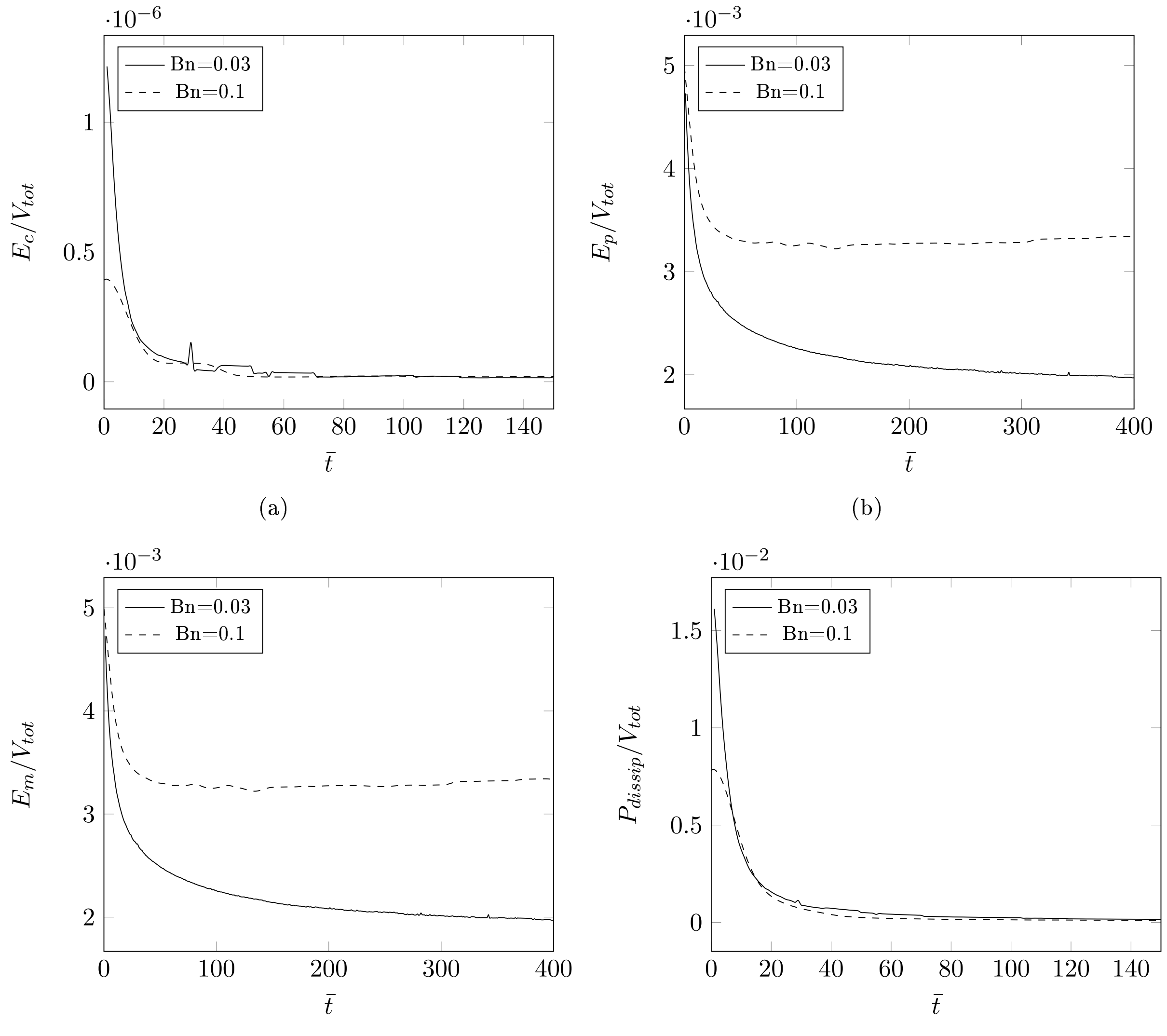

(a)

(b)

(c)

(d)

Figure 63: Energy analysis during Bingham dam-breaks with $Bn = 0.03$ and $Bn = 0.1$: (a) Kinetic energy ; (b) Potential energy ; (c) Mechanical energy ; (d) Dissipated power

3.5.5.6 Mass conservation

Now, the evolution of Bingham fluid loss is discussed, by computing the relative gained volume of Bingham fluid:

$$V_{gained} = \frac{V_{current} - V_{init}}{V_{init}} \tag{3.17}$$

Figure 64.a illustrates Bingham volume during a Bingham dam-break with $Bn = 0.03$. A larger volume gain is observed between $\bar{t} = 0$ and 200.Indeed, figure 61 shows clearly it corresponds to the flowing times until almost reaching the final profile. It is observed that the Bingham fluid gains 1.5% of its initial volume.

Up to $\bar{t} = 200$, we notice that the gained volume stabilizes around 0.5% of the initial one.

Figure 64.b illustrates the gained volume of Bingham fluid V_{gained} according to the time $\bar{t}$ for a Bingham dam-break with $Bn = 0.1$. Thus, V_{gained} increases also during a certain period (until $\bar{t} = 100$ approximately), corresponding almost to the time until almost reaching the final profile. However, the volume conservation is worse, due to the computation stiffness (higher Bn). Up to $\bar{t} = 100$, the gained volume is more stable, but continue as well to increase.

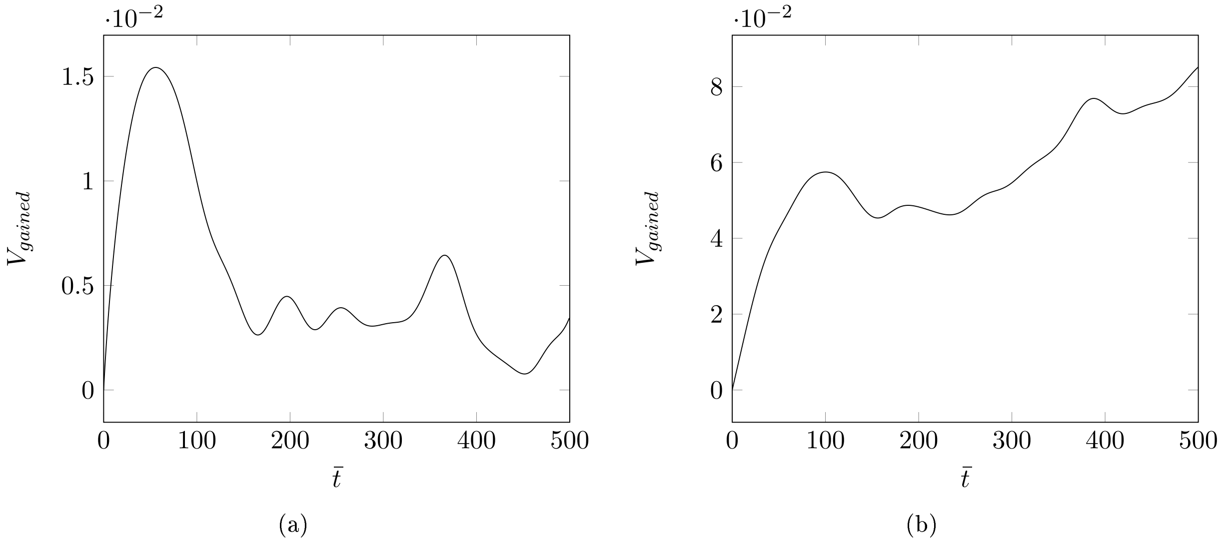

Figure 64: Volume conservation of Bingham fluid according to the time for a dam-break problem: (a) $Bn = 0.03$; (b) $Bn = 0.1$

3.5.5.7 Determination of arrest times

Regularization methods are not able to simulate flow arrests. Thus, we need to propose a method capable to determine time arrests. The purpose consists in proposing a arrest criterion based on the mean shear rate value.

To correlate our criterion to values of the shear rate field, the shear rate integral $|| \dot{\gamma} ||$ is first computed. Figure 65.a illustrates the evolution of $\int_{\Omega_f} || \dot{\gamma} || \, d\Omega_f$ according to the dimensionless time, during a Bingham collapse with $Bn = 0.03$. This curve leads to the observation of two trends. Before $\bar{t} = 200$, the mean shear rate computed into the fluid domain is decreasing drastically. Up to this value, it decreases in a constant power-law regime. At this stage, even if the front advances very slowly, the mean shear rate continues to decrease and does not stabilize to a small value, as the fluid continues to creep (see figure 57). The flow stop criterion is then reached for time $\bar{t} \approx 1840$ and corresponds to $|| \dot{\gamma} || = 1.29 \cdot 10^{-4}$, which is approximately the creep rate of a Newtonian fluid of viscosity $\bar{\eta}_{eff} = 1 + \bar{m}Bn$.

By denoting $n+1$ as the current time step, we plotted the speed of descent (difference between successive mean shear rates) in figure 65.b. We observe that the difference decreases quickly during the first iterations, and tends to stabilize after by oscillating at very low values.

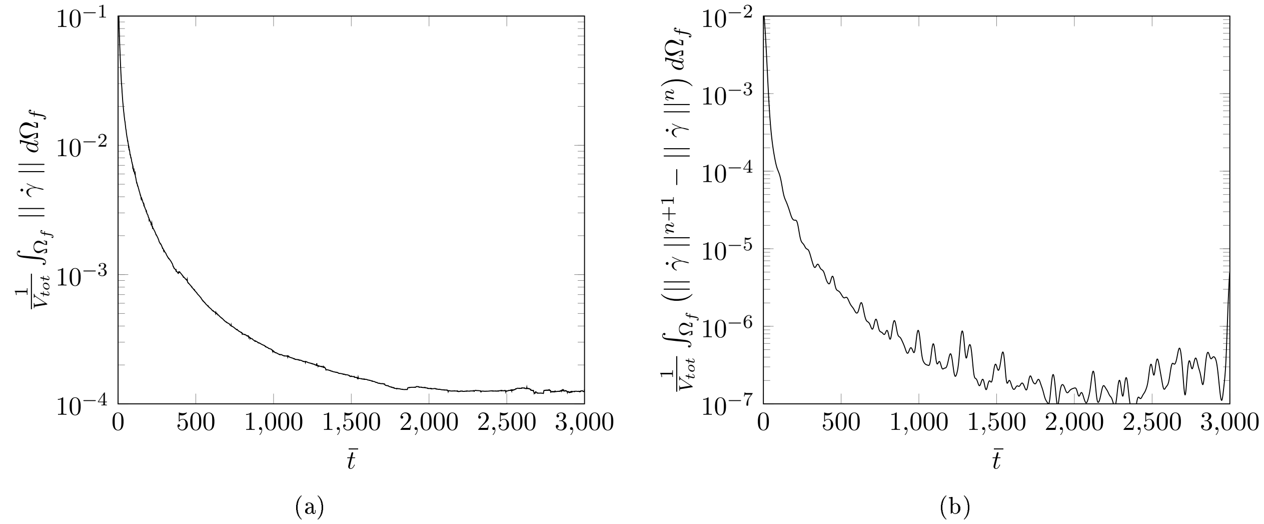

Figure 65: Mean shear rate evolution during a dam-break with Bn=0.03: (a) Mean shear rate ; (b) Speed of descent

Figure 66.a illustrates the evolution of $\frac{1}{V_{tot}} \int_{\Omega_f} || \dot{\gamma} || \, d\Omega_f$ with respect to the time, during a dam-break with $Bn = 0.1$. Before a certain time $\bar{t} \approx 200$, the mean shear rate decreases a lot. The flow stop criterion is then reached for time $\bar{t} \approx 310$ and corresponds to $|| \dot{\gamma} || = 2 \cdot 10^{-4}$, which is approximately the creep rate of a Newtonian fluid of viscosity $\bar{\eta}_{eff} = 1 + \bar{m}Bn$.

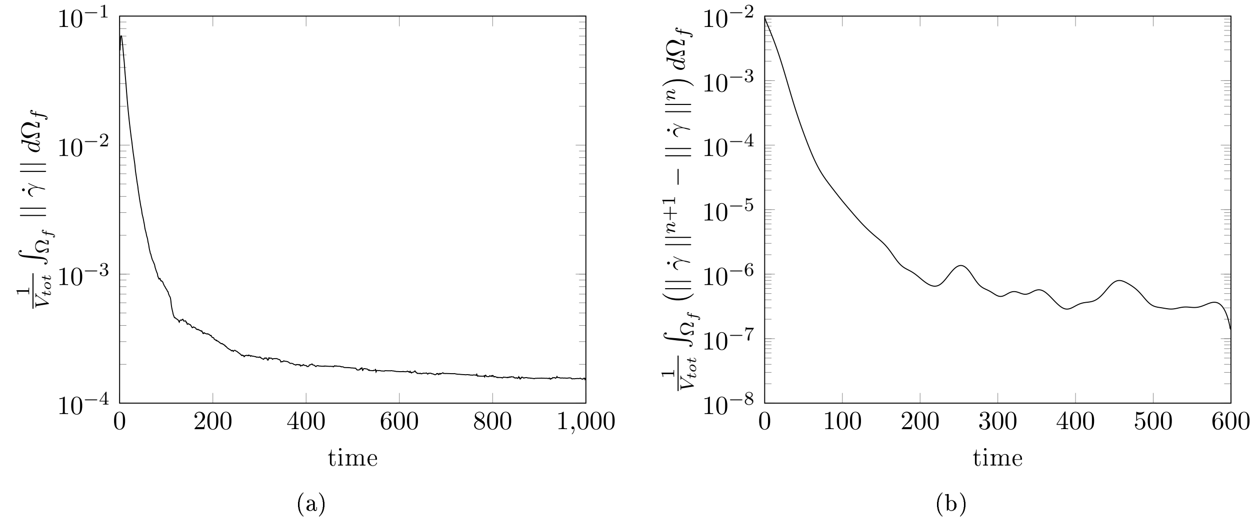

Figure 66: Mean shear rate evolution during a dam-break with Bn=0.1: (a) Mean shear rate ; (b) Speed descent

To conclude, regularization methods have several limitations due to the difficulty to simulate flow arrests. We proposed a criterion based on shear rate value. However, some incertainties remain for the determination for the time arrest, which stays a crude approximation.

3.5.5.8 Influence of boundary conditions

Now, the influence of the applied boundary conditions at the bottom surface is analyzed.

Figure 67 illustrates yielded/unyielded regions during Bingham dam-breaks with different boundary conditions: figure 67.a represents the flow shape with no-slip boundary conditions, and figure 67.b with slip boundary conditions. In the first flow, dead regions are observed at the flow center, making slow down the fluid. In the second flow, no-dead zones are noticed. However, two unyielded zones, moving enmasse, are observed: the first one is located at the front. The second one is located close to the corner, inducing its conservation during the flow.

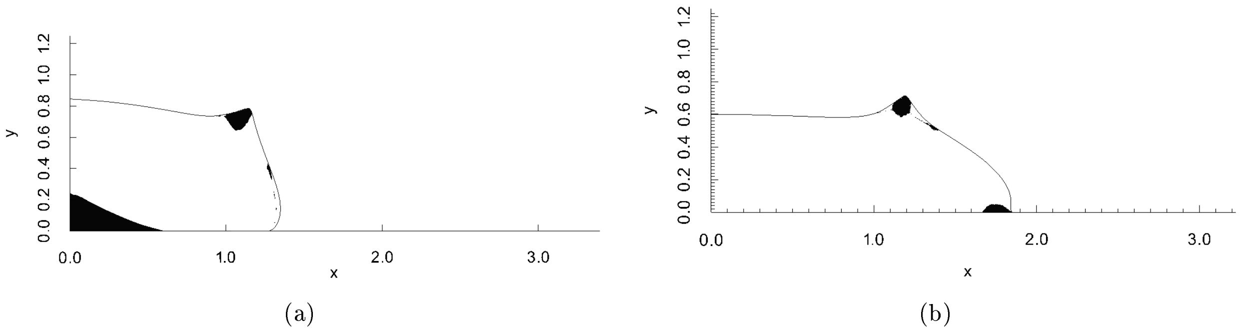

(a) (b)

Figure 67: Yielded/unyielded regions during a dam-break with $Bn = 0.1$ at $\bar{t} = 10$: (a) No-slip boundary conditions ; (b) Slip boundary conditions

Figures 68 and 69 compare run-out distance and height at the left wall. Changing the boundary conditions at the bottom surface induces a totally different dynamics and shape of the flow. In the case of slip boundary conditions applied at the bottom surface ($\nabla \cdot v = 0$), the flow stops approximately twice further, and the height position of the interface on the left wall is twice lower.

Run-out distance of Bingham collapses are thus different by changing the applied boundary conditions at the bottom surface. However, both flows have the same dynamics : an acceleration phase, leading to the motion of the column, followed by a deceleration phase leading to the flow stabilization. As observed in the energy analysis section, a very small part of potential energy E_p is dissipated into kinetic energy, leading to a quasi-static flow.

The dissipated energy of the fluid is defined such as:

$$E_d = \frac{1}{2V_{tot}} \int_{\Omega} \tau : \dot{\gamma} d\Omega \tag{3.18}$$

Thus, shear dissipated energy E_{shear} is computed such as tangential contribution of E_d:

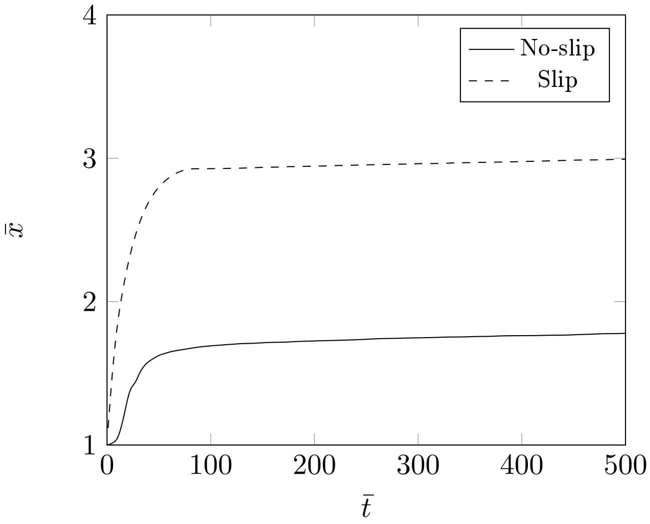

Figure 68: Run-out distance of dam-breaks with $Bn = 0.1$ with no-slip and slip boundary conditions

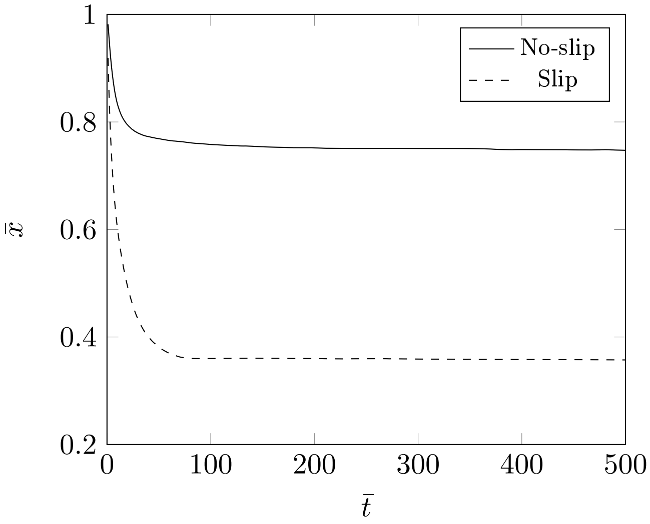

Figure 69: Height measured on the left wall of a dam-break with $Bn = 0.1$ with no-slip and slip boundary conditions

$$E_{shear} = \frac{1}{2V_{tot}} \int_{\Omega} \tau_{xx} \cdot \dot{\gamma}_{xx} + \tau_{yy} \cdot \dot{\gamma}_{yy} d\Omega \tag{3.19}$$

Figure 70 illustrates dissipated energy in shear according to the dimensionless time for two Bingham collapses with different boundary conditions applied at the bottom surface (slip and no-slip). A large dissipated energy in shear at the beginning of the flow is observed, which corresponds to the setting into motion of the flow. Indeed, a larger dissipated energy in shear is observed for a column collapse with no-slip boundary conditions at the bottom surface as observed in curves 70 (twice more dissipation initially). When the flow is arrested, there is no more energy to dissipate.

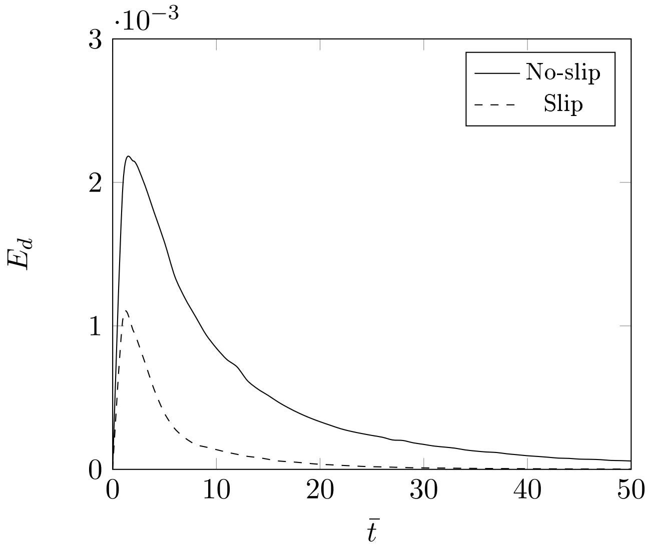

Figure 70: Comparaison of the dissipative energy in shear $E_d = 2\int_{\Omega}\tau_{xy}\dot{\gamma}_{xy}d\Omega$

In the same manner, the extensional dissipated energy $E_{extension}$ is computed such as tangential contribution of E_d:

$$E_{extension} = \frac{1}{V_{tot}}\int_{\Omega}\tau_{xy}\cdot\dot{\gamma}_{xy}d\Omega \tag{3.20}$$

Figure 71 illustrates dissipated energy in extension according to the dimensionless time for two Bingham collapses with different boundary conditions applied at the bottom surface. For collapses with no-slip boundary conditions, dissipative energy in extension increases slowly (the sticky substrate retains the flow), until reaching a maximum value, corresponding to the time at maximum velocity. Then, it decreases slowly until no more energy is dissipated (arrest of the flow). For collapses with slip boundary conditions, dissipated energy in extension is much larger. Indeed, only the yield stress retains the front to advance on the slipped substrate. Thus, the dissipative energy in extension reaches its maximum at the very beginning of the flow. Finally, as for a flow with no-slip boundary conditions, the fluid stabilizes (dissipative energy equal to 0).

In conclusion, the choice of appropriate boundary conditions at the bottom surface is essential and can affect drastically the way for the fluid to flow, and can impact the final shape of the Bingham fluid.

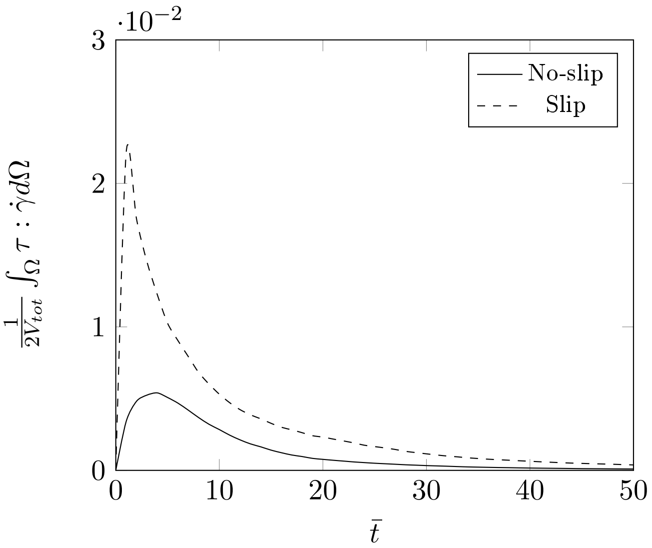

Figure 71: Comparaison of the dissipative energy in extension $E_d = \int_\Omega \tau_{xx}\dot{\gamma}_{xx} + \tau_{yy}\dot{\gamma}_{yy} d\Omega$

3.5.6 Conclusion

This section was devoted to multiphase Bingham flows. A regularization method has been used to take into account the constitutive law into momentum and mass equations. This is a multiphase problem (Bingham/air): we use the convective auto-reinitialization Level-Set method to capture and follow the interface between the two fluids. Anisotropic mesh adaptation has been used, in order to catch all the physics occurring during the flow. Finally, as for monophase flows, a Papanastasiou regularization method is used for the coupling between the constitutive law and momentum equations.

Then, Bingham dam-break problems with different Bn are performed and compared with Liu *et al.*[43]. First, the results show a good agreement with the work of Liu *et al.*[43]. Then, the robustness of the numerical methods has been studied. Particularly, mass conservation studies show that the loss remains reasonnable (several percents of volume loss of Bingham fluid) during the flow.Finally, an appropriate choice for the boundary conditions applied onto the bottom surface is crucial, and may affect drastically the dynamics and shape of the final Bingham profile.

In the multiphase framework, the limitations of the regularization method have been also observed. By using this method of resolution, the fluid will continue to flow slightly even when it was supposed to stop, altering mass conservation.

3.6 Conclusion

In this chapter, numerical simulations of Bingham flows have been performed by the use of a regularization method, coupled with anisotropic meshing. The coupling between the different numerical tools, mostly introduced in chapter 2, leads to the simulation of highly plastic flows, and to take stiff regularization parameters, allowing high jumps of effective viscosity. Even if regularization methods have some limitations, it appears to be an interesting method leading to relevant results due to its coupling with VMS and the anisotropic meshing.

Now, future work will consist in proposing a method to extend this finite element formulation to $\mu(I)$ rheology, in order to simulate dry granular flows. Indeed, unyielded regions exist also in these flows (quasi-static areas). Thus, it would be interesting to solve these flows with the numerical tools able to simulate Bingham flows. However, we need to take into account the pressure-dependency of dry granular material.

Chapter 4

Modeling of dry granular flows using a continuum approach

Contents

Résumé en français

Ce chapitre est consacré à la simulation numérique de l'écoulement des matériaux granulaires secs par une approche continue en deux et trois dimensions.

Nous nous focalisons ici sur la dynamique de l'effondrement de colonnes granulaires en deux et trois dimensions. Dans un premier temps, une étude bibliographique expérimentale est menée. La forme finale du dépôt nous mène à l'existence de deux régimes d'écoulements suivant le rapport d'aspect de la colonne a: forme de cône tronqué quand a est faible, forme de "chapeau mexicain" quand a est grand, et une forme conique obtenue à un a critique, noté a_c. De plus, la courbe illustrant la distance parcourue adimensionnée du matériau en fonction de a, conforte cette hypothèse, avec un régime linéaire pour $a < a_c$, un régime en loi puissance pour $a > a_c$ (exposant $\simeq 0.7$ pour des écoulements 2D et $\simeq 0.5$ pour des écoulements 3D). De plus, il a été observé que la dynamique des matériaux granulaires serait indépendante des propriétés rhéologiques. En effet, la distance parcourue adimensionnée en fonction du temps adimensionné suit une même courbe maîtresse.

Dans un second temps, la résolution des écoulements granulaires secs, décrits par la rhéologie $\mu(I)$, a été effectuée. Afin de prendre en compte les équations constitutives du comportement dans les équations de la mécanique des fluides, une méthode de régularisation de type Bercovier-Engelman a été utilisée, qui revient au calcul de la viscosité effective du matériau granulaire. Comme pour les fluides de Bingham, le maillage est adapté suivant les champs Level-Set, vitesse et viscosité effective.

Le modèle a été validé tout d'abord sur des cas d'effondrements de colonnes granulaire en deux dimensions. Les deux régimes (linéaire et loi puissance) caractérisés par la littérature expérimentale sont bien retrouvés avec la simulation numérique. De plus, une étude de sensbilité aux différents paramètres rhéologiques du matériau a été menée. Il a été ainsi observé que le coefficient de frottement statique est le paramètre le plus influant sur la distance parcourue du matériau.

Par la suite, le modèle a été étendu à des cas d'effondrements de colonnes en trois dimensions. Les deux régimes correspondant aux différentes formes des dépôts finaux ont été également retrouvés. Cependant, la transition s'effectue à plus grand a_c que dans les travaux expérimentaux de Lajeunesse *et al.*[61]. Les mêmes analyses de sensibilité aux paramètres rhéologiques sont menées, et les mêmes constats que pour des écroulements en deux dimensions sont effectués. Additionnellement, l'influence de la hauteur initiale de la colonne h_i sur l'écoulement a été analysée, montrant que la dynamique dépend du nombre inertiel.

Finalement, la modélisation en trois dimensions a été étendue à des cas de chute de colonnes de granulaire. Un nouveau nombre adimensionnel a_r a été défini, et correspond au rapport entre hauteur maximale de la colonne (somme entre h_i et hauteur de lâcher h_r) et rayon initial r_i. Il a tout d'abord été observé que la distance parcourue suit une courbe en loi puissance, en fonction de a_r, et qui se rapproche de la courbe loi puissance d'exposant 0.54 (courbe obtenue pour les effondrements de colonnes de grains) au plus la colonne est élancée. Enfin, il a été souligné qu'à même a_r (même hauteur maximale de la colonne), la colonne contenant plus de grains, et donc FBla plus élancée, s'étalera plus loin.

In the previous chapters, a numerical framework for the numerical simulation of multiphase Newtonian and Bingham flows has been proposed and validated. Particularly, the developed numerical tools allow the treatment of highly viscoplastic fluids. Now, the extension of the formulation to the simulation of $\mu(I)$ rheology flows is investigated. The physical flow features, where the yield stress and plastic viscosity depend now on the pressure, shear rate, and other rheological parameters defining the granular material, will be then analyzed and the limitations of the employed approach will be outlined.

This chapter is split into two sections. First, a literature review on granular collapses is performed. Then, the finite element formulation is extended to two and three-dimensional $\mu(I)$ rheology flows. A parametric sensitivity analysis will be finally conducted in order to show the relevance of $\mu(I)$ rheology to describe dry granular flows.

4.1 Experimental granular collapses

For the last past years, several works focused on the dynamics of granular collapses, leading to determine the impact of rheological and geometrical features on the dynamics. This section will be devoted to the literature review on experimental collapses, leading to the determination of several features describing the granular dynamics.

Granular collapses consist of an initial cylindrical column of height h_i and radius r_i filled with a granular material, which collapses by gravity. As defined in the previous chapters, the aspect ratio a corresponds to the ratio between initial height h_i and radius r_i of the column:

$$a = \frac{h_i}{r_i} \tag{4.1}$$

In 2004, Lajeunesse *et al.*[61] performed three-dimensional granular collapses with glass beads and studied the influence of a and the substrate on the final deposit.

Figure 72 illustrates the experimental setup used to perform three-dimensional granular collapses. A tube, with radius r_i and height h_i, is set onto a plane surface, and is filled with glass beads. A lifting system, linked to the tube, has been used in order to release the column. This step must be done very quickly in order to be negligible compared to the acceleration phase of the flows.

Figure 73 illustrates the column shape at several instants, for three granular collapses with different initial aspect ratios a. This picture leads to the observation of two flow regimes. For small aspect ratios (figure 73.a), they observed that the final profile has a truncated cone shape. For high aspect ratios (figure 73.c), there is a grains chute phase, that leads to considerable grains spreading and a final profile that looks like a Mexican hat. Moreover, a critical aspect ratio, denoted a_c exists, and gives the transition between these two regimes. For a granular collapse with $a = a_c$, the shape of the final deposit is conic (figure 73.b).

Figure 74 illustrates the two regimes for granular column collapses of several materials, performed by Lube *et al.*[62]. In their experiments, Lajeunesse *et al.*[61] found that for small aspect ratios ($a < 1.7$), the run-out distance varies linearly according to a (final shape of truncated cone in figure 73), and for higher a, the dimensionless run-out distance follows a power-law curve with exponent 0.5 according to a (final

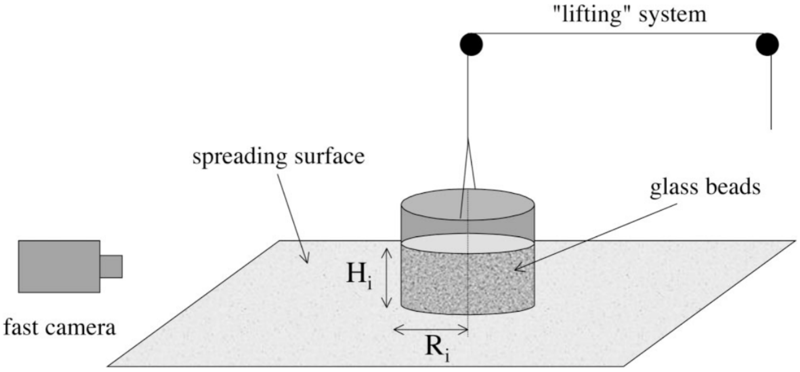

Figure 72: Experimental procedure to perform granular collapses [61]

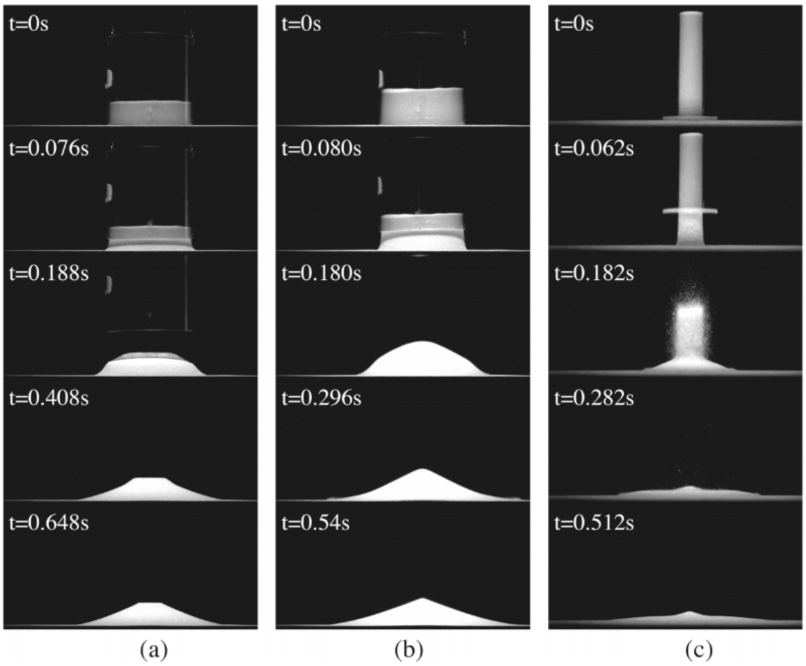

(a) (b) (c)

Figure 73: Profiles of granular collapses with different aspect ratios [61]

shape looking like a Mexican hat in figure 73). Moreover, the intersection of the two curves is found at $a_c = 1.7$. This value corresponds to the critical aspect ratio that defines the transition between the two regimes (conical final profile observed in figure 73). Finally, they concluded that the substrate (sandpaper, erodible bed, smooth wooden surface) and initial radius r_i do not influence the granular dynamics, which remains controlled by the geometrical properties.

Contrary to Lajeunesse *et al.*[61], Lube *et al.*[62] performed granular collapses with different granular materials (sand, salt, rice, couscous and sugar). By plotting the dimensionless run-out distance according to the aspect ratio (figure 74), they conclude that the rheological properties of the granular material do not influence the flow dynamics. Moreover, the same trends as observed in LAjeunesse *et al.*[61] are outlined. Indeed, dimensionless run-out distance follows a linear regime for $a < a_c$ (figure 74.a) and a power-law regime with 0.5 exponent for $a > a_c$, with the same critical aspect as Lajeunesse *et al.*[61] ($a_c = 1.7$).

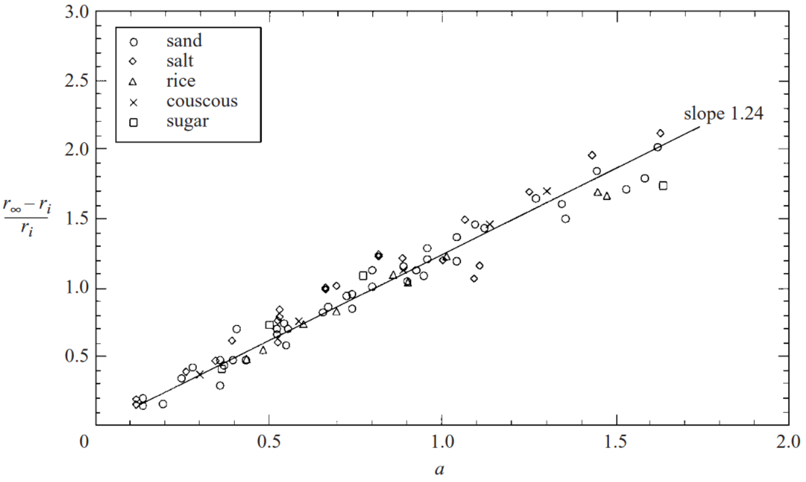

(a)

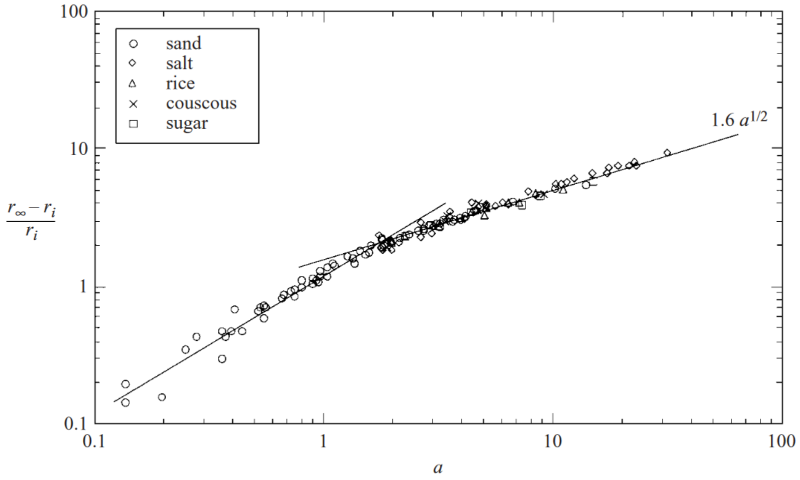

(b)

Figure 74: Dimensionless run-out distance according to the aspects ratios [62]: (a) Linear curve for low aspect ratios collapses ; (b) Power-law curve for high aspect ratios collapses

In the several conducted experiments of granular collapses, the existence of a transition between two regimes, corresponding to a final conic profile was outlined , as illustrated in figure 73b. Moreover, Lube *et al.*[62] shown, using columns with three initially concentric zones of different colors (see figure 75) that the kinematics suggests that the run-out is achieved by the initially top external grains, at least for low aspect ratios. At this stage, we can propose crude arguments to retrieve the linear dependency of dimensionless run-out distance with respect to initial aspect ratio. Indeed, using an energetic analysis of a quasi-static collapse, we could assume that only friction (no rolling or bouncing) is occurring during the collapse, and then the loss of potential energy of any granular column of mass m_c is equal to the dissipated work of radial (in 3D collapses) or axial (in 2D) friction forces. Assuming no slip on the substrate, the friction force is simply μ times the weight of the column. Equaling the two energies for the grains reaching the final run-out gives:

$$m_c g h_i = \mu m_c g \Delta r \tag{4.2}$$

where $\Delta r = r_f - r_i$ is the run-out distance. Consequently, the dimensionless version of this equation becomes:

$$\frac{a}{\mu} = \frac{r_f - r_i}{r_i} \tag{4.3}$$

An other argument could also consider the final pile obtained for a_c as a simple static pile, so that $\mu = tan(\phi_r) = h_i/r_f$ (see figure 76), which gives finally:

$$\frac{a}{\mu} - 1 = \frac{r_f - r_i}{r_i} \tag{4.4}$$

which is close to the previous energetic argument. Both confirm the linear experimental dependency in the first regime, but suggests a spreading proportional to μ^{-1}, contrarily to the experiments of Lube *et al.*[62]. Further experiments from Balmforth and Kerswell [63] have shown indeed a material dependency that suggests a negative influence of static friction.

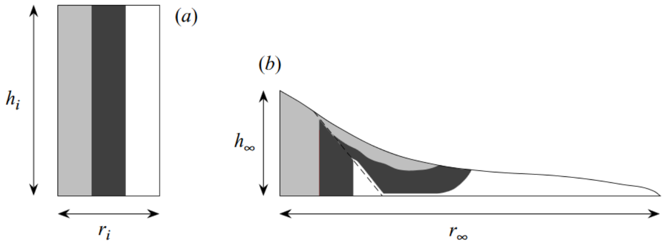

Figure 75: (a) vertical section of the deposit (b) of a granular column with three initially concentric zones [62]

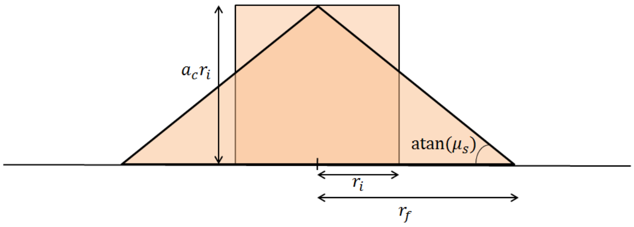

Figure 76: Final profile shape after a granular collapse with $a = a_c$

In 2005, Lube *et al.*[64] focused on two-dimensional granular collapses. Figure 77 illustrates the two experimental set-ups used to perform granular collapses. The first one consists of the symmetric granular spreading along a channel with a constant width (Series A in figure 77). The second one consists of an unidirectional spreading and has been performed in a tank of 20cm width (Series B in figure 77). For all the investigated setups, the gate that retains the granular material, are removed in the fastest possible way.

Several granular collapses, with several granular materials (rice, sugar, coarse and fine quartz sands) and with several aspect ratios, are performed.

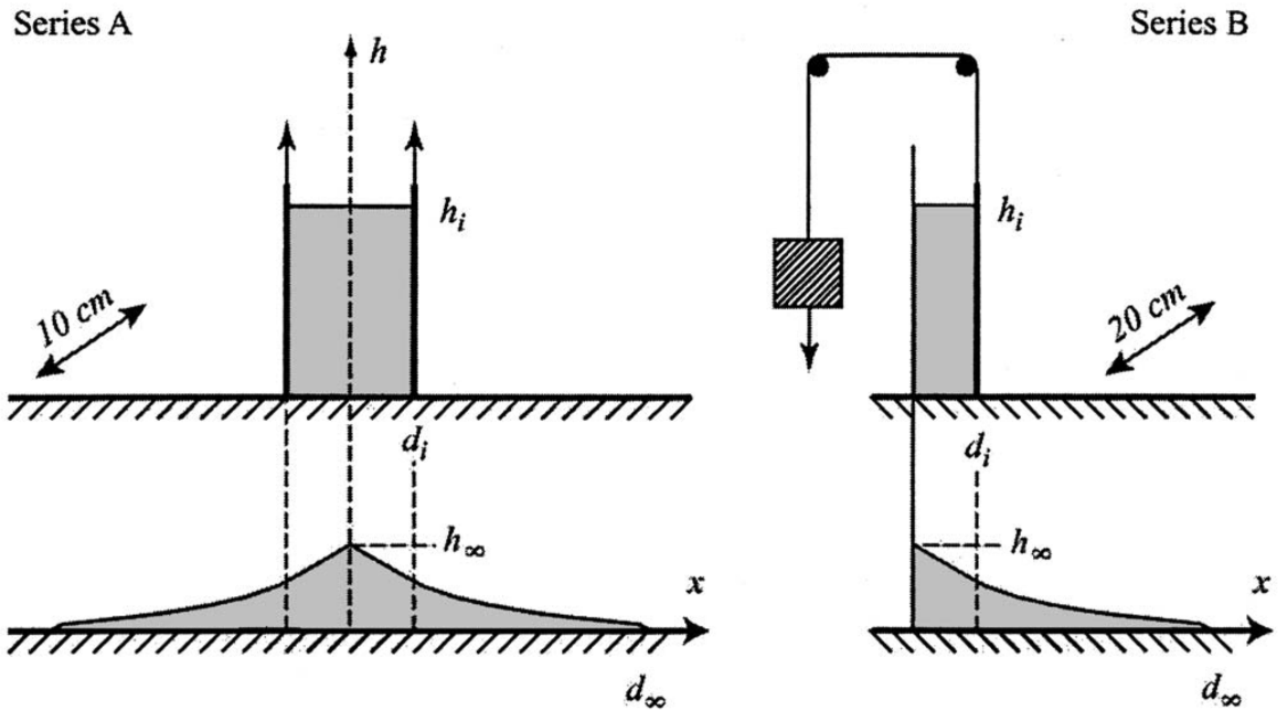

Figure 77: Initial set-up of the two series of 2D granular collapses

Here also, as noticed in three-dimensional granular collapses, experiments show that 2D granular dynamics depends on the aspect ratio [64, 61], but not on the type of material [64]. More precisely, as shown on figure 78, the dimensionless run-out distance varies linearly for small aspect ratios ($a < a_c$), and as $a^{2/3}$ for $a > a_c$, a_c being of the same order as in 3D collapses.

Finally, for large aspect ratios, Lube *et al.*experiments [64] show that the total collapse time t_f varies as $\sqrt{h_i/g}$, which is the time scale of a free fall. Here also, this value was not found to be dependent on the type of material. Interestingly, the relative distance-time plot $(r(t)/r_f, t/t_f)$ falls into a single master curve (see figure 79) that shows an initial acceleration of the front flow, followed by a constant velocity phase that lasts almost 80% of the flow, and ended by a short deceleration phase. According to all these results, one could wonder what governs the spreading in the general case: aspect ratio only, rheological constants, etc...

In the next section, numerical simulations of granular collapses will be performed by the use of $\mu(I)$ rheology. Then, the results observed in Lajeunesse *et al.*[61] and Lube *et al.*[64] will be discussed in the light of a sensitivity analysis that could validate this model for such complex flows.

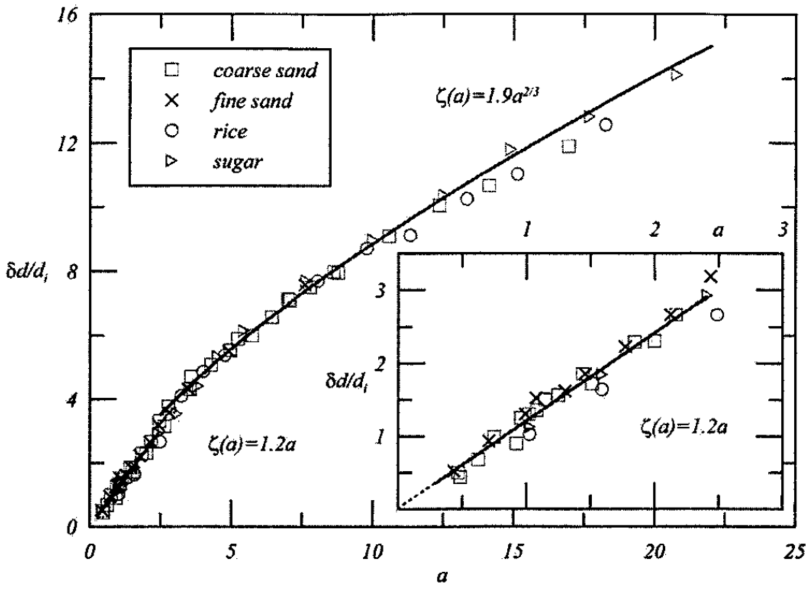

Figure 78: Final dimensionless run-out distance of the front according to the initial aspect ratio a for two-dimensional granular collapses [64]

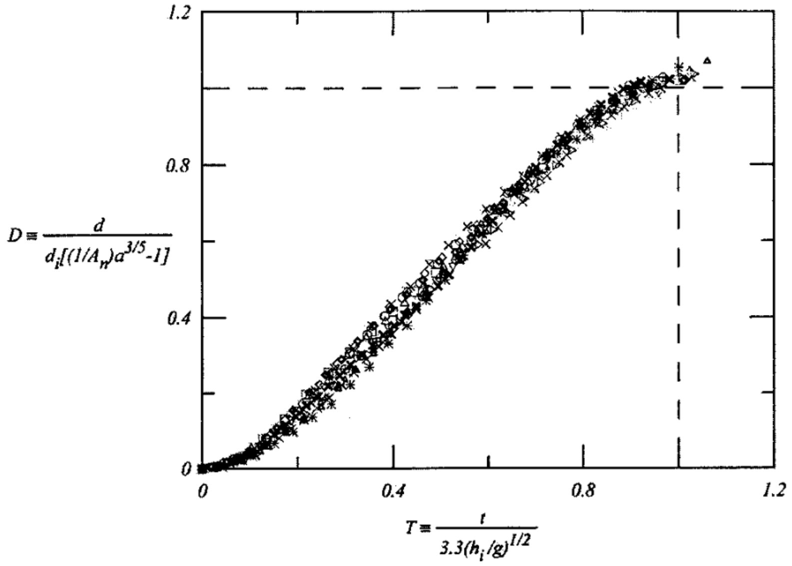

Figure 79: Final dimensionless run-out distance according to the dimensionless time [64]

4.2 Continuum model for granular materials flows

4.2.1 The $\mu(I)$ rheology

As for Newtonian and Bingham flows, a continuum approach is used for the simulation of granular flows. It is based on the resolution of momentum and mass equations of the flow, and not on the modeling of granular materials as an assembly of solid particles. As described in the first chapter, the $\mu(I)$ rheology has the powerful feature to be able to describe the transition between the granular flow regimes (quasi-static, dense, collisional) with a dimensionless number, called inertial number.

The inertial number I is defined as the ratio between the time for grains rearrangement (microscopic time) to the inverse of the shear rate (macroscopic time):

$$I = \frac{|| \dot{\gamma} || \, d}{\sqrt{\frac{p}{\rho_f}}} \tag{4.5}$$

The tensorial constitutive law of the $\mu(I)$ rheology is thus formulated such as [2]:

$$\tau = 2\mu(I)p \frac{\dot{\gamma}}{|| \dot{\gamma} ||} \tag{4.6}$$

where the effective friction depends on the inertial number such as:

$$\mu(I) = \mu_S + \frac{\mu_F - \mu_S}{\frac{I_0}{I} + 1} \tag{4.7}$$

Figure 80 illustrates the variation of the effective friction μ according to I.When the inertial number is low (quasi-static regime), it shows that the effective friction μ tends to the static friction coefficient μ_S, which defines the repose angle ϕ_r of the granular material ($\phi_r = atan(\mu_S)$). When I increases, μ tends to the dynamic friction coefficient μ_F. At $I = I_0$, the friction is equal to $\frac{\mu_S+\mu_F}{2}$. Up to I_0, the flow regime is collisional.

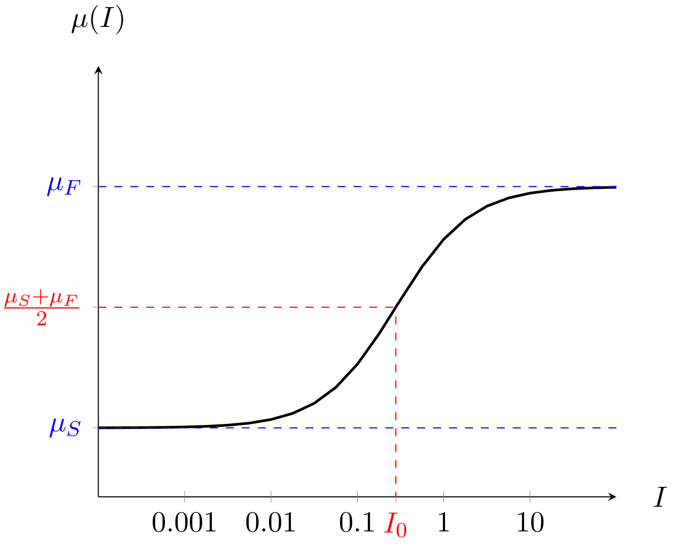

Figure 80: Effective friction μ according to the initial number I

The constitutive law that describes the $\mu(I)$ rheology, may also be formulated like a Bingham constitutive equation:

$$\begin{cases} \tau = 2\left(\eta_f(p, \| \dot{\gamma} \|) + \frac{\tau_0(p)}{\|\dot{\gamma}\|}\right)\dot{\gamma} & \text{if } \| \tau \| > \tau_0 \\ \| \dot{\gamma} \| = 0 & \text{if } \| \tau \| \leq \tau_0 \end{cases} \tag{4.8}$$

where $\tau_0(p)$ and $\eta_f(p, \| \dot{\gamma} \|)$ represent the yield stress (pressure dependent) and the plastic viscosity (pressure and shear rate dependent) of the granular material. These quantities are defined as follows:

$$\tau_0(p) = \mu_s p \tag{4.9}$$

$$\eta_f(p, \| \dot{\gamma} \|) = \frac{(\mu_F - \mu_s)p}{\sqrt{\frac{p}{\rho}}\frac{I_0}{d} + \| \dot{\gamma} \|} \tag{4.10}$$

By analogy with Bingham flows, unyielded (quasi-static) areas are defined when the shear stress is lower than a yield value $\mu_S p$. Thus, the larger the pressure, the larger the yield criterion, and the larger the unyielded regions. The term $\eta_f(p, \| \dot{\gamma} \|)$ corresponds to the plastic viscosity of the fluid, and depends both on the pressure and shear rate fields. It increases with pressure and decreases with shear rate.

4.2.2 Literature review on numerical models of granular flows

As for Bingham fluids, the difficulty lies in the coupling between the constitutive law and the fluid mechanics. In the literature, some studies that simulate continuum $\mu(I)$ rheology flows may be found, and the two existing coupling methods are based on the same principle that those introduced for Bingham fluids. Thus, regularization (mostly used) and multiplier methods are also found in the literature for the resolution of dry granular flows.

In a first hand, several works deal with the numerical simulation of granular collapses in a Lagrangian framework.

Recently, Dunatunga and Kamrin [65] proposed a new model based of the $\mu(I)$ rheology when the fluid is dense, and as disconnected, stress-free media when the material is deemed to separate. A Material Point Method (MPM) is used for the simulation. The mechanics is first solved in a finite element framework, and information are then projected to a set of Lagrangian points, which are advected. This approach leads to avoid the use of any regularization methods.

Minatti and Paris [66] proposed a SPH model for the simulation of $\mu(I)$ rheology flows. It consists of a meshless method, in which the fluid domain is discretized into a set of particles. Chambon *et al.*[67] proposed also a model based on the SPH method.

However, numerical simulation of granular collapses in an Eulerian framework remains less explored, even if some attempts have been performed during the last few years.

In 2013, Chauchat and Medale [68] investigated numerical simulations of $\mu(I)$ rheology flows, and performed a comparison between several kinds of regularization methods. In their work, they proposed to regularize the shear rate in unyielded regions, by introducing a minimum shear rate. Moreover, they also regularize the pressure, as it tends to zero close to the free-surface. The model has been validated onto a Bagnold profile. However, this paper did not treat free surface flows.

Lagrée *et al.*[13] proposed a finite volume method, coupled with a regularization method for the simulation of $\mu(I)$ rheology. A Volume of Fluid method (VOF) is used to track and follow the interface air/granular material. They compared their model with discrete simulations for different 2D granular collapse simulations, and found a good agreement between both models and also the experimental regimes and scaling with aspect ratio. These results were the first confirmation of the validity of the $\mu(I)$ rheology in 2D.

Finally, the coupling between the $\mu(I)$ model and fluid mechanics may be performed by using a multiplier method. In the literature, a 2D study is proposed by Ionescu *et al.*[12] using a finite element method, based on an Augmented Lagrangian/decomposition-coordination method where the principle remains the same as for the Bingham analogy explained previously. An arbitrary Langrangian-Eulerian method is used to compute the free surface position. The authors show that the $\mu(I)$ and Drucker-Prager (constant viscosity) models give very similar height profiles.

In this section, we propose a new continuum model to simulate granular materials flows, following the $\mu(I)$ rheology constitutive law. The multiphase resolution is performed by using the numerical tools introduced in the previous chapter. Finally, the model will be validated with two-dimensional and three-dimensional granular collapses, and comparisons with experimental works will be investigated. Moreover, the formulation will be extended to the simulation of granular chutes, and will try to determine a general dynamics for the granular flow in this geometrical configuration.

4.2.3 Regularization method for $\mu(I)$ rheology flows

In this work, granular flows are solved by using a continuum approach. Thus, momentum and mass equations must be solved and are defined such as:

$$\begin{cases} \rho\left(\partial_t v + v \cdot \nabla v\right) + \nabla p - \nabla \cdot \tau = f & \text{in } \Omega \times [0,T] \\ \nabla \cdot v = 0 & \text{in } \Omega \times [0,T] \end{cases} \tag{4.11}$$

However, granular flows are described by the $\mu(I)$ rheology constitutive law, which must be traduced into these equations. Thus, as for Bingham flows, the difficulty deals with the way to introduce the specific constitutive law into momentum and mass equations (4.11). In the literature, two ways are found for the coupling of $\mu(I)$ rheology law and fluid mechanics: regularization and multiplier methods. In this work, a regularization method is privileged. Indeed, it would be able to predict accurately unyielded areas as we observed that high plastic Bingham flows may be described with this method. Moreover, as the mold powder spreading onto liquid metal will be integrated in the future into a commercial software, the computational times induced by the resolution must not be too large. Thus, a regularization method seems to be more appropriate in this framework.

From the constitutive law introduced in equation (4.8), the apparent viscosity of $\mu(I)$ rheology fluids, denoted as η_a, is defined such as (in the case where $|| \dot{\gamma} || \neq 0$):

$$\eta_a = \eta_f(p, || \dot{\gamma} ||) + \frac{\tau_0(p)}{|| \dot{\gamma} ||} \tag{4.12}$$

The constitutive equations (4.8) of $\mu(I)$ rheology, written in a Bingham analogy, show that the shear stress is not defined below the dynamic yield stress $\tau_0(p)$, and thus, leads to the divergence of apparent viscosity as the shear rate $|| \dot{\gamma} ||$ tends to zero. Consequently, as for Bingham flows, the maximum apparent viscosity must be limited in order to allow the resolution of $\mu(I)$ rheology flows in unyielded regions. In this framework, a Bercovier-Engelman regularization method is employed, and consists of the introduction of the minimum shear rate $|| \dot{\gamma} ||_{min}$, which corresponds to the regularization parameter. The effective viscosity of the fluid becomes then:

$$\eta_{eff} = \eta_f(p, || \dot{\gamma} ||) + \frac{\tau_0(p)}{\sqrt{|| \dot{\gamma} ||^2 + || \dot{\gamma} ||^2_{min}}} \tag{4.13}$$

However, the yield stress and plastic viscosity tends to zero as the pressure field tends to zero, which leads to a zero effective viscosity, which naturally is outside the validity window of the physical $\mu(I)$ model. Thus, an additional treatment must be done in order to control the viscosity in high Reynolds number regions. Consequently, an additional regularization parameter is added, and corresponds to the minimum viscosity of the fluid. Generally, it is taken as the viscosity of the ambient fluid (air). The effective viscosity for $\mu(I)$ rheology fluids is thus defined such that:

$$\eta_{eff} = min \left(\eta_{air}, \eta_f(p, || \dot{\gamma} ||) + \frac{\tau_0(p)}{\sqrt{|| \dot{\gamma} ||^2 + || \dot{\gamma} ||^2_{min}}} \right) \tag{4.14}$$

Finally, the numerical resolution of $\mu(I)$ rheology flows requires the resolution of mass and momentum equations, defined in (4.11). The constitutive law is thus taken into account by the definition of the shear stress tensor such as $\tau = 2\eta_{eff}\dot{\gamma}$.

4.2.4 Mesh adaptation criteria

As for Bingham flows, yielded and unyielded regions evolve during the simulation. Thus, it is difficult to preadapt the mesh around these regions. This motivates again the use of implicit strategy that imposes a dynamic mesh adaptation that minimizes as much as possible the prescribed error.

The adaptivity accounts for the effective viscosity η_{eff} and the velocity norm $| \ v \ |$ in order to catch accurately the transition between yielded and unyielded areas. It also accounts for the filtered Level-Set function $\hat{\alpha}$ in order to describe accurately the interface evolution. These fields are described in the following vector V, containing all the adaptation criteria:

$$V(\mathbf{x}^i) = \left\{ \frac{v^i}{||v^i||}, \frac{||v^i||}{\max\limits_j ||v^j||}, \frac{\eta_{eff}}{\max(\eta_{eff})}, \frac{\hat{\alpha}}{\max(\hat{\alpha})} \right\} \tag{4.15}$$

Here also, mesh adaptation is supposed to improve the conditioning and then helps the convergence of the regularization algorithm.

4.3 Application to granular collapses

In this section, $\mu(I)$ rheology flows are solved in the finite element framework, leading to validate first the proposed modeling. Then, the relevance of $\mu(I)$ for the description of granular dynamics, is discussed, by performing two and three-dimensional granular collapses. Finally, the obtained results will be compared to the experimental results of Lajeunesse *et al.*[61] and Lube *et al.*[64].

4.3.1 Two-dimensional granular collapses

4.3.1.1 Introduction of the problem

First two-dimensional granular collapses are investigated. As for Newtonian and Bingham flows, it consists of a granular column of height H_i and radius R_i which flows only due to gravity (figure 81). This is a multiphase problem, as the air is considered as the ambient fluid. Moreover, height H and length L of the computational domain are taken sufficiently large so that the run-out does not reach the end of the domain.

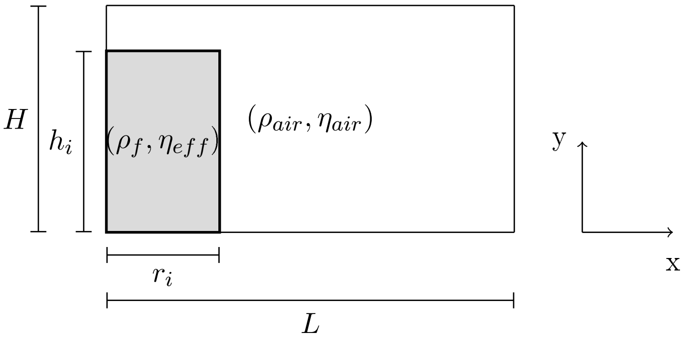

Figure 81: Problem statement of the granular collapse problem

In our simulations, no-slip boundary conditions are applied at the bottom surface. However, the dynamic wetting of this surface with the granular material must be ensured. To do so, a perfect slip is imposed on a thin layer, which length is of the order of the minimum mesh size h_{min} (set as a few grains diameters) upstream the granular front (see figure 82).

To compute the position of this layer, the first step consists in localizing the zero-isovalue position on the bottom wall. Then, the signed distance function of the nodes located on the bottom surface, are computed. When it is positive, no-slip boundary conditions ($v = 0$) is thus applied and when it is negative, the air is allowed to slip ($v_y = 0$). Then, the thin slipping layer at the granular front is computed. Thus, the coordinates of the nearest node from the zero-isovalue, localized both on the bottom wall and inside the granular material, are determined. At this nodes, the boundary conditions are changed, and the granular material is allowed to slip. In practice, this method avoids the occurrence of stress singularities at the flow front.

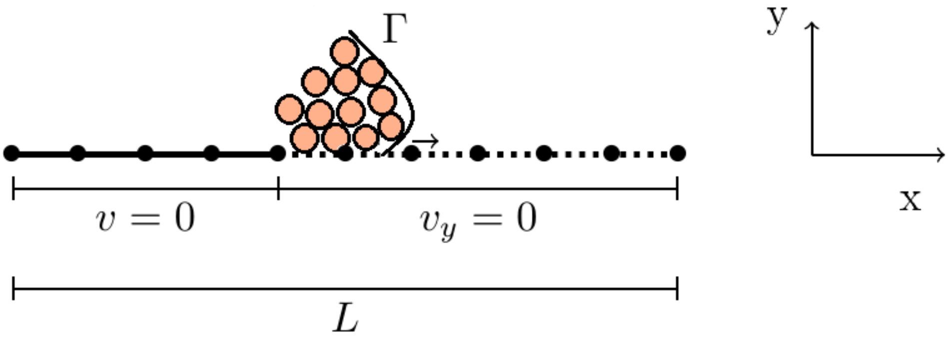

Figure 82: Boundary conditions applied on the bottom surface for two-dimensional granular collapses

4.3.1.2 Validation of the model

This work aims to simulate two-dimensional granular collapses in the finite element framework. After introducing the numerical tools, we need to validate the model. Lagrée *et al.*[13] performed two-dimensional granular collapses by using the finite volume method, and validated the model by comparing the obtained results with discrete simulations. These discrete simulations were set using grains of average diameter d, aspect ratio a and a total number of grains Nb_{Grains}. To deduce an estimate for the height h_i and width r_i, we assume a simple cubic compacity and get $h_i = d\sqrt{aNb_{Grains}}$ and $r_i = d\sqrt{Nb_{Grains}/a}$. The continuous problem turns then into a dimensionless formulation as performed in Lagrée *et al.*[13]: the characteristic length, velocity, time and density are taken respectively as h_i, $\sqrt{gh_i}$, $\sqrt{h_i/g}$ and ρ_f. In this new dimensionless problem, five dimensionless numbers control the system: the number of grains Nb_{grains}, the initial aspect ratio of the column a, and the dimensionless rheological parameters μ_S, $\Delta\mu$ and I_0.

Consequently, the inertial number computation involves the dimensionless grain diameter $\bar{d} = 1/\sqrt{aNb_{Grains}}$ and granular density $\bar{\rho_f} = 1$. The dimensionless geometries become: initial column radius $\bar{r_i} = 1/a$, initial column height $\bar{h_i} = 1$.

By considering dimensionless shear rate and pressure fields, the inertial number turns then to:

$$I = \frac{|| \bar{\dot{\gamma}} ||}{\sqrt{\bar{p} a Nb_{Grains}}} \tag{4.16}$$

Three granular collapses with different aspect ratios $a = 0.5, 1.42$ and 6.26 are performed, respectively with $Nb_{grains} = 3407, 6041$ and 6036. The same rheological parameters as Lagrée *et al.*[13] are considered: $\mu_S = 0.32$, $\Delta\mu = 0.28$ and $I_0 = 0.4$. The regularization parameters are taken as $|| \bar{\dot{\gamma}} ||_{min} = 10^{-3}$ and $\bar{\eta}_{air} = 10^{-4}$. As mentioned previously, the mesh is adapted according to the effective viscosity, velocity norm and filtered Level-Set fields, and the number of elements is set to $4 \cdot 10^4$.

Figures 83.a, 83.b and 83.c illustrate the height profiles at different instants, $t = 0, 1, 2$ and 4 respectively. For $a = 0.5$ (figure 83.a), we observe that the granular deposit corresponds to a truncated cone, leading to a maximum height on the left wall (equal to 1). For $a = 1.42$ (figure 83.b), a larger spreading is observed, leading to the granular collapse on the left side. Thus, the run-out distance is larger as a increases, leading to a wide final deposit (figure 83.c).

Figures 84, 85, 86 and 87 illustrate several fields during a granular collapse with $a = 1.42$, at several dimensionless instants: $\bar{t} = 1, 2, 4$ and 6. As observed in the screen-shots, the velocity is larger as approaching the free-surface, and is maximal at the front. Moreover, unyielded regions are characterized by a very low shear rate (close to $|| \dot{\gamma} ||_{min}$), a large effective viscosity η_{eff}, but also by a negative $\tau - \mu_S p$. In the screen-shots, they are close to the flow center, and get closer to the free-surface as the granular material flows. At the end of the simulation (figure 87), it is observed that unyielded regions cover the full fluid, as it stopped.

Figures 88.a, 88.b and 88.c illustrate the dimensionless front position according to the dimensionless time, and compare the obtained results with the ones of Lagrée *et al.*[13]. It is observed that our simulations get closer to the discrete simulations, than the continuum method of Lagrée *et al.*[13], probably due to mesh adaptation that improves accuracy.

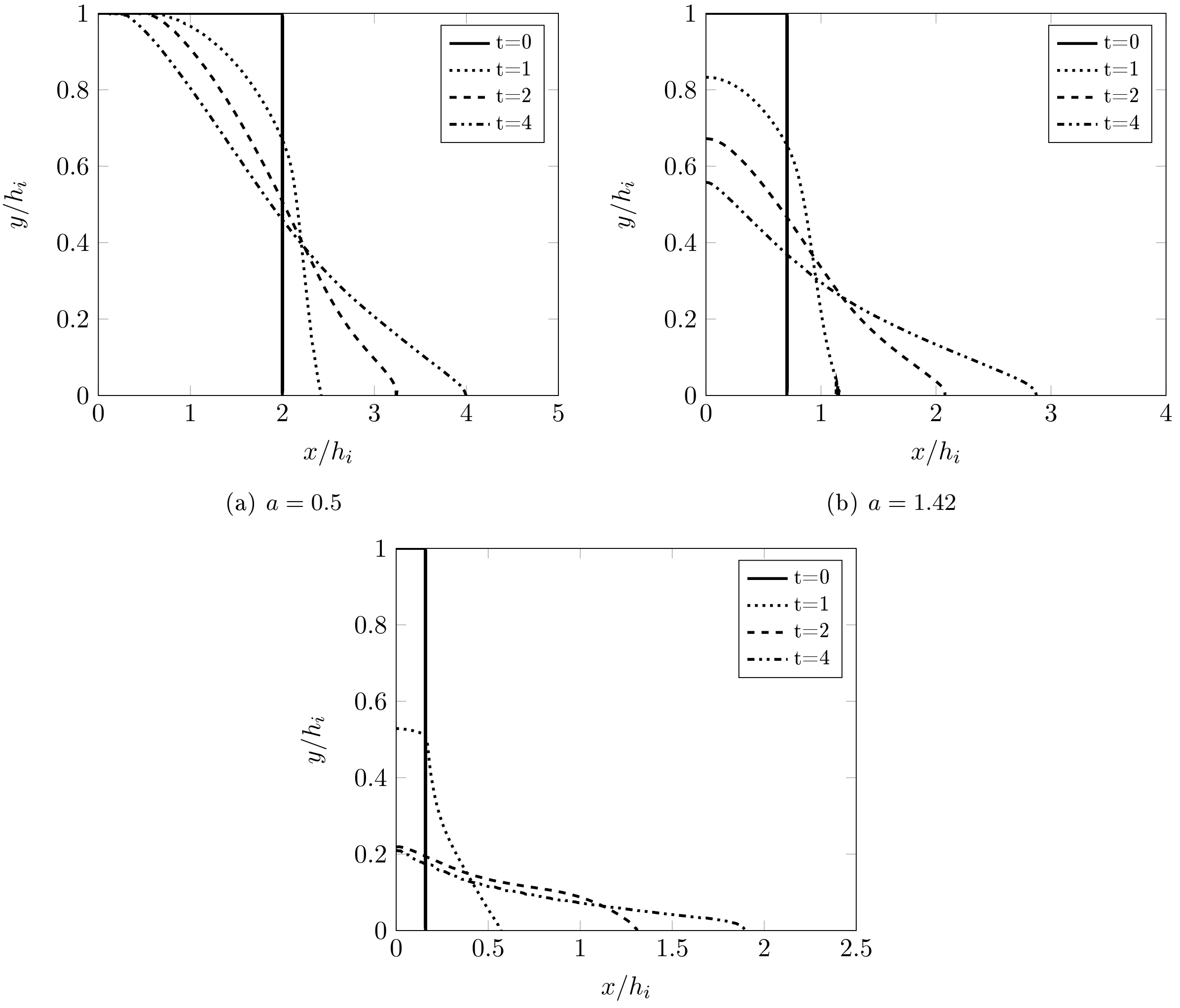

(a) $a = 0.5$

(b) $a = 1.42$

(c) $a = 6.26$

Figure 83: Height profiles after granular collapses with different aspect ratios ($a = 0.5, 1.42$ and 6.26) at several instants $t\sqrt{g/h_i} = 0.1, 2$ and 4

Figure 89 illustrates the adaptive mesh for a granular collapse with aspect ratio $a = 1.42$ at different instants. It is observed that the mesh follows very accurately the interface and the transition regions delimiting the three regimes: quasi-static at the left corner, collisional at the flow front, and dense elsewhere. Finally, the quasi-static regime dominates in the full granular material, leading to a extreme mesh refinement close to air/granular interface.

4.3.1.3 Sensitivity to regularization parameters

As introduced previously, two numerical parameters are defined for regularizing $\mu(I)$ flows: $|| \dot{\gamma} ||_{min}$ (minimum shear rate) used to limit the viscosity into unyielded areas, and η_{min} (minimum granular viscosity) used to limit the Reynolds areas. This subsection will give a sensitivity analysis leading to the best choice for these parameters.

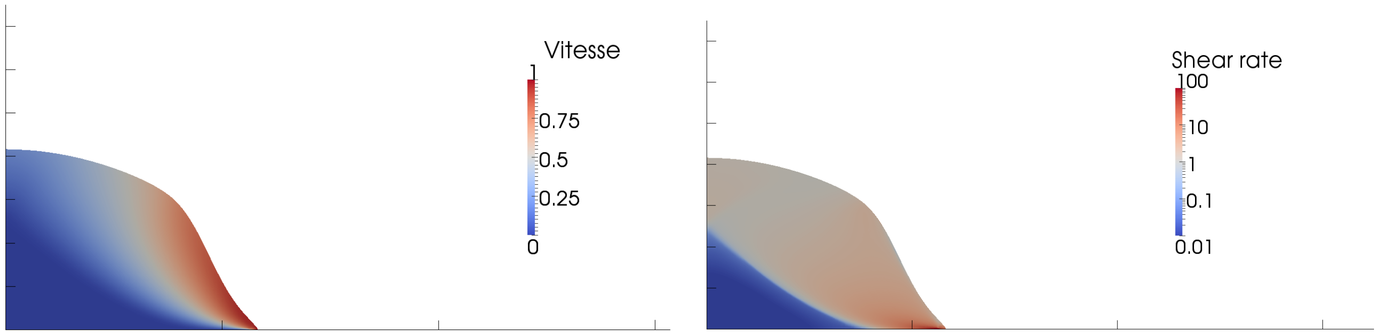

(a) Velocity field v

(b) Shear rate $|| \dot{\gamma} ||$

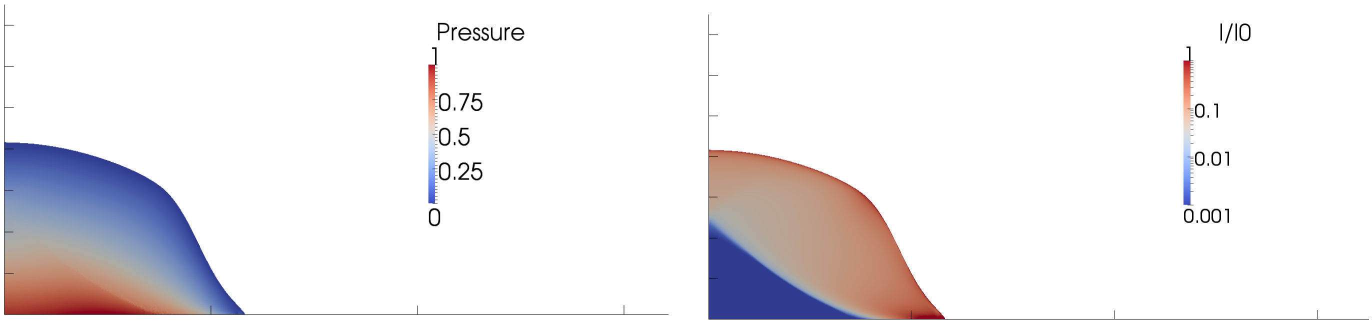

(c) Pressure p

(d) I/I_0

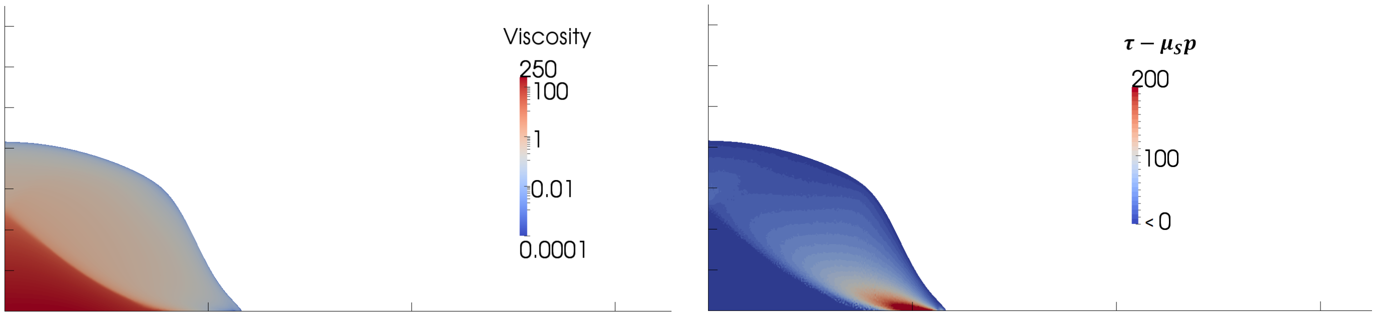

(e) Effective viscosity η_{eff}

(f) $\tau - \mu_S p$

Figure 84: Screen-shots on several physical fields during a granular collapse with $a = 1.42$, plotted at time $\bar{t} = 1$

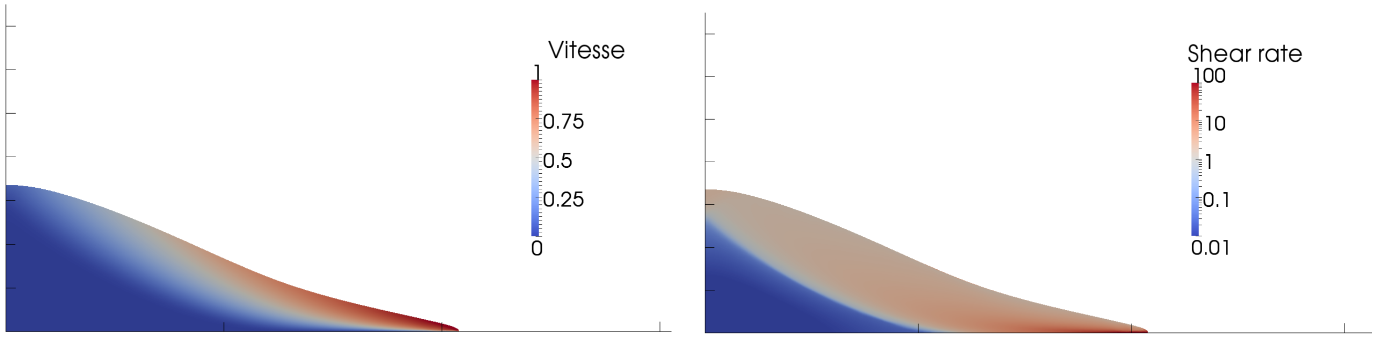

(a) Velocity field v

(b) Shear rate $|| \dot{\gamma} ||$

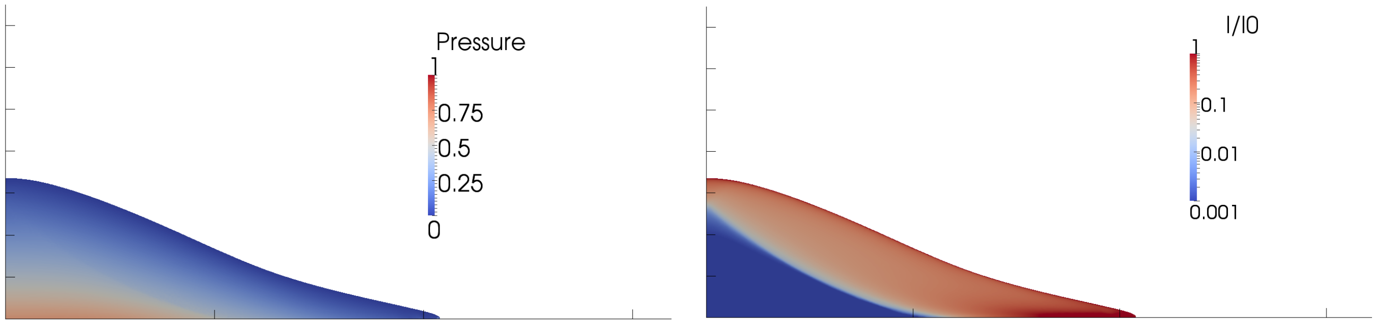

(c) Pressure p

(d) I/I_0

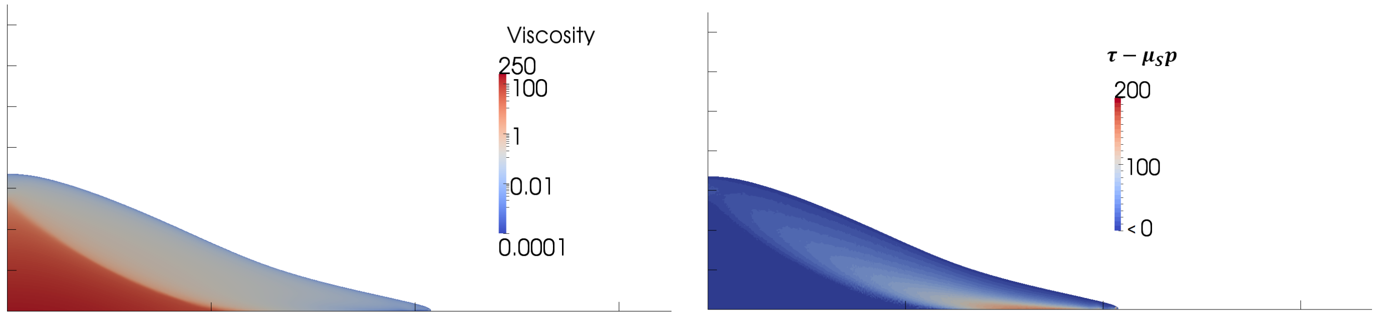

(e) Effective viscosity η_{eff}

(f) $\tau - \mu_S p$

Figure 85: Screen-shots on several dimensionless physical fields during a granular collapse with $a = 1.42$, plotted at time $\bar{t} = 2$

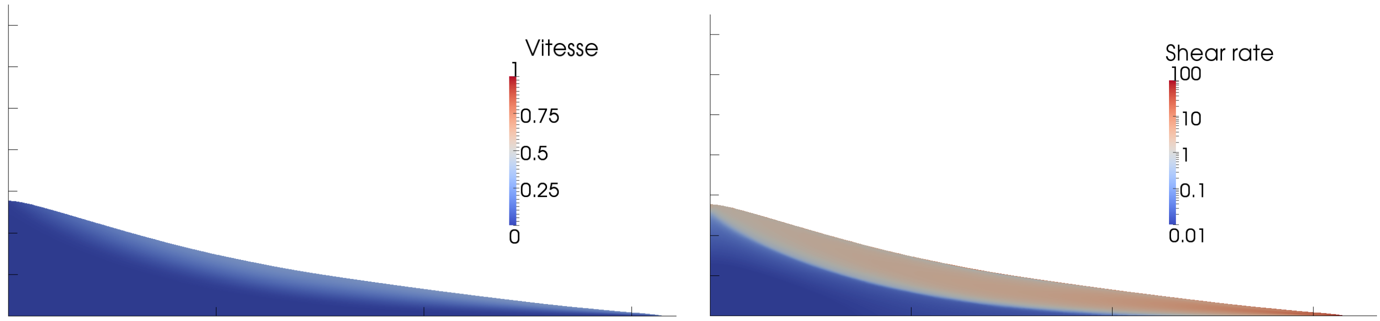

(a) Velocity field v

(b) Shear rate $|| \dot{\gamma} ||$

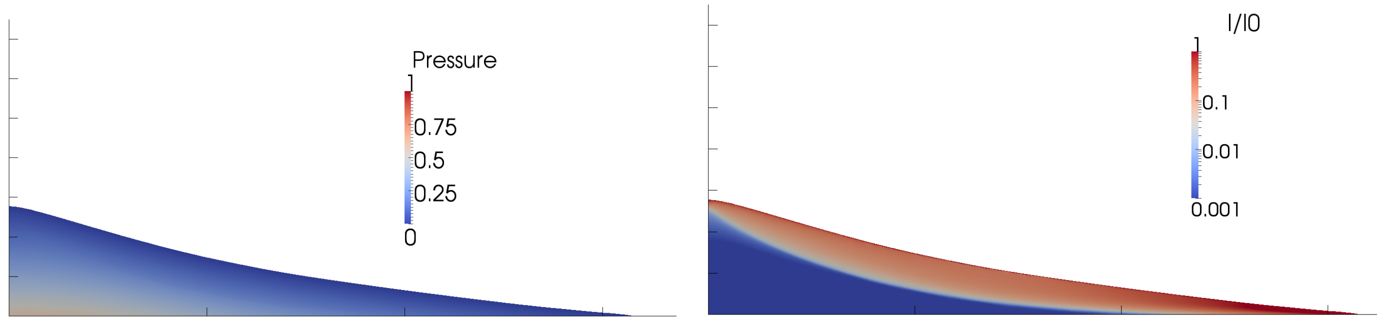

(c) Pressure p

(d) I/I_0

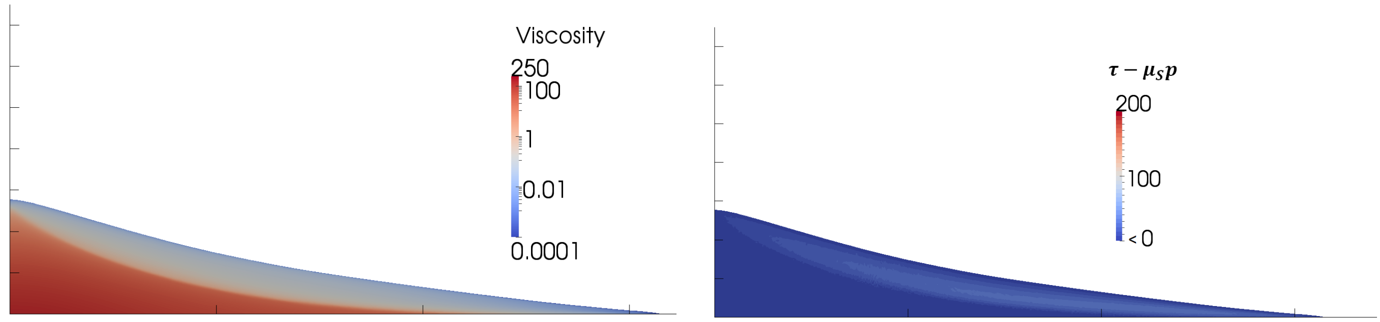

(e) Effective viscosity η_{eff}

(f) $\tau - \mu_S p$

Figure 86: Screen-shots on several dimensionless physical fields during a granular collapse with $a = 1.42$, plotted at time $\bar{t} = 4$

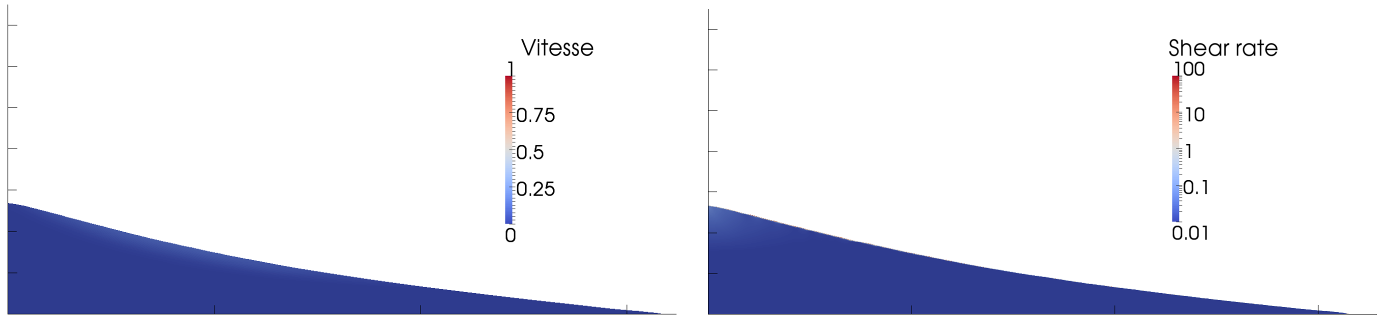

(a) Velocity field v

(b) Shear rate $|| \dot{\gamma} ||$

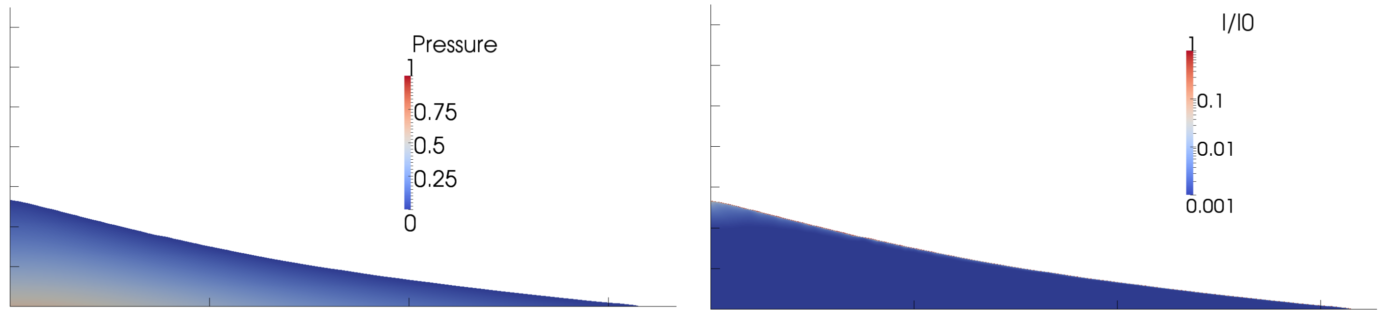

(c) Pressure p

(d) I/I_0

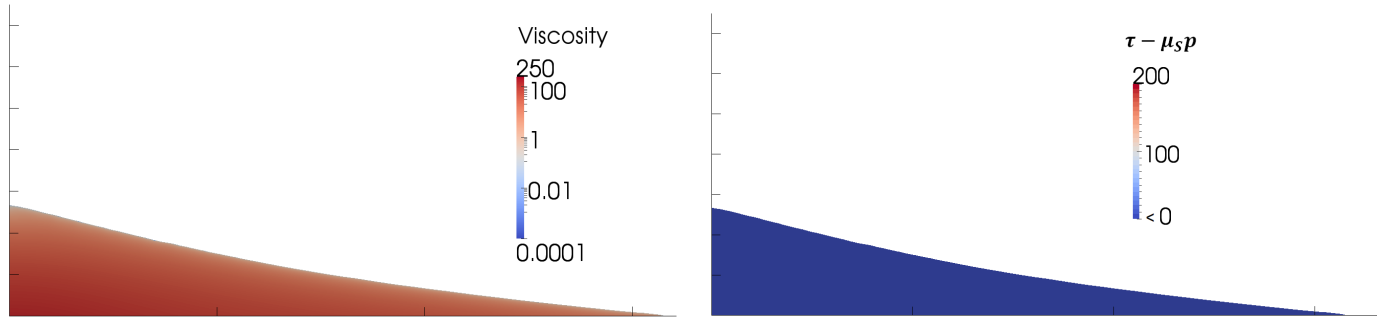

(e) Effective viscosity η_{eff}

(f) $\tau - \mu_S p$

Figure 87: Screen-shots on several dimensionless physical fields during a granular collapse with $a = 1.42$, plotted at time $\bar{t} = 6$

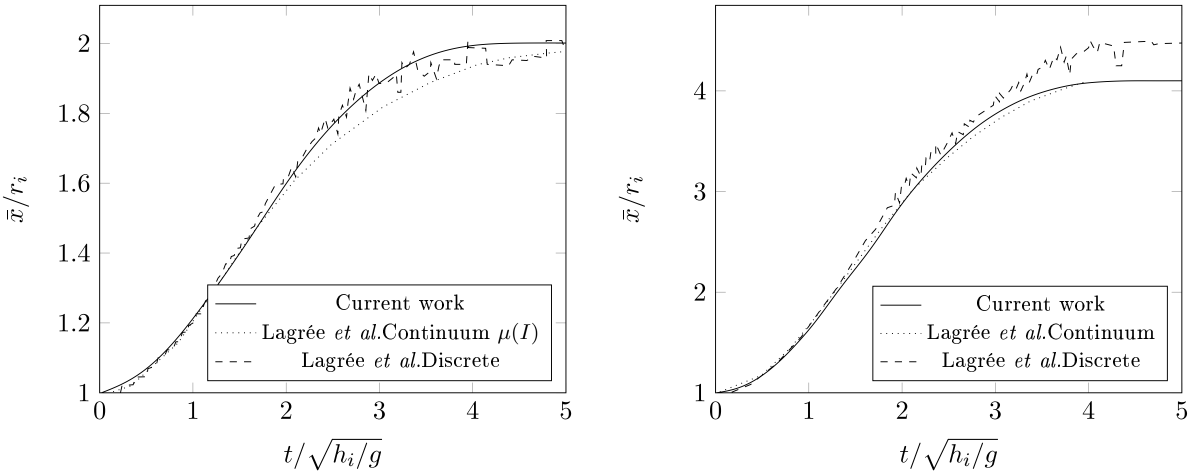

(a) $a = 0.5$

(b) $a = 1.42$

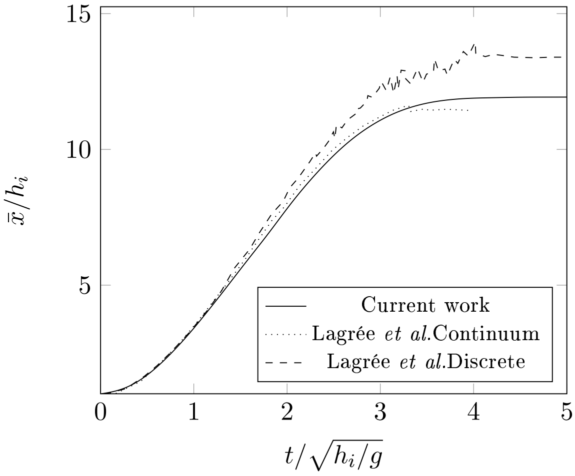

(c) $a = 6.26$

Figure 88: Dimensionless position of the front according to dimensionless time for granular collapses with different aspect ratios ($a = 0.5, 1.42$ and 6.26)

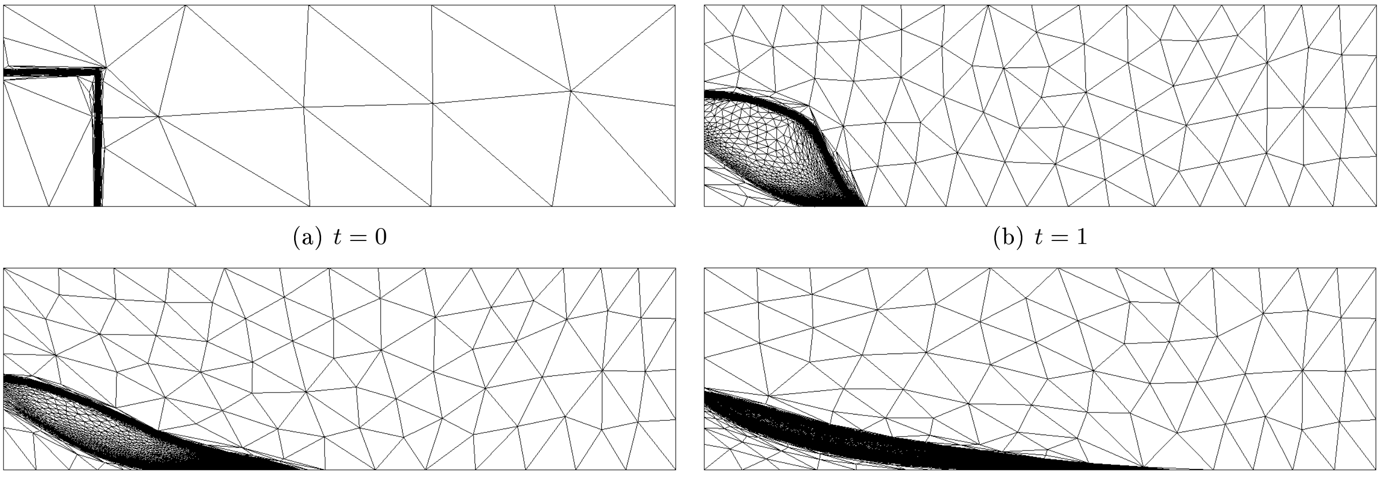
(a) $t = 0$

(b) $t = 1$

(c) $t = 2$

(d) $t = 4$

Figure 89: Anisotropic adaptive mesh at different instants ($t = 0, 1, 2$ and 4) for a granular collapse flow with initial aspect ratio $a = 1.42$

Sensitivity to minimum shear rate

Figure 90 and 91 compare the effect of the minimum shear rate ($|| \dot{\gamma} ||_{min}$) which goes from 10^{-6} to 1 onto, respectively, the dimensionless position of the front according to dimensionless time and the final dimensionless granular profiles. The results show approximately the same curves for $|| \dot{\gamma} ||_{min}$ under 10^{-2}. Thus, choosing $|| \dot{\gamma} ||_{min}$ to 10^{-2} is sufficient to obtain relevant results.

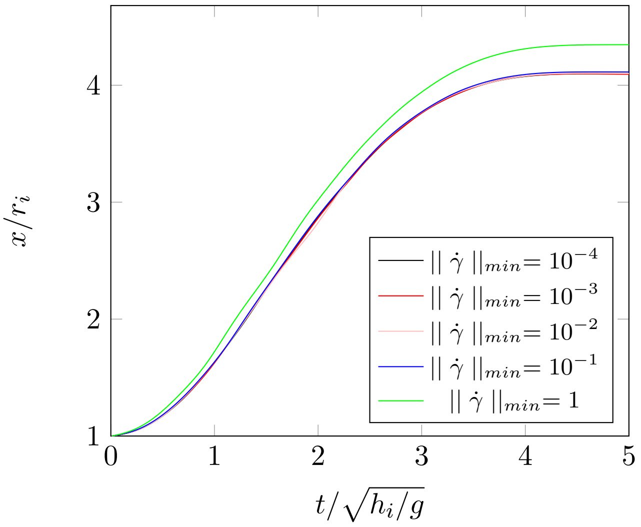

Figure 90: Sensitivity analysis to $|| \dot{\gamma} ||_{min}$ of dimensionless position of the front vs. dimensionless time for a granular collapse with $a = 1.42$

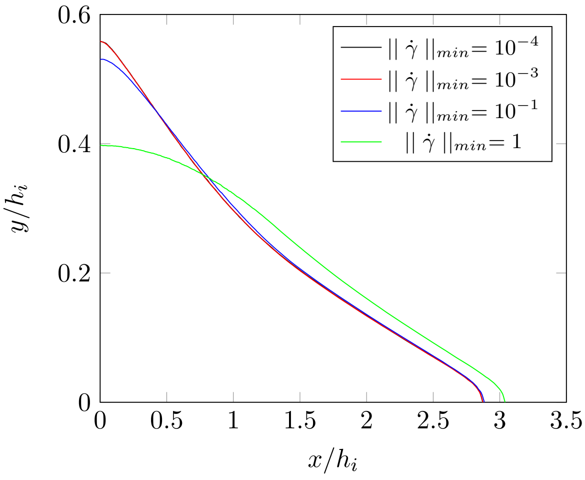

Figure 91: Sensitivity analysis to $|| \dot{\gamma} ||_{min}$ of final granular profiles after granular collapses ($a = 1.42$)

Sensitivity to minimum viscosity

Figures 92 and 93 show the influence of the minimum viscosity (η_{min}) onto, respectively, relative (t, x) plots and dimensionless final height profiles. First, the results show that the acceleration step is well-predicted and is weakly independent of the minimum viscosity. However, differences appear during the deceleration step. Indeed, considering a too large η_{min} leads to a more viscous fluid, tending to a shorter arrest than for a fluid with low η_{min}. However, the obtained results do not evolve when $\eta_{min} \leq 10^{-4}$ (differences between $\eta_{min} = 10^{-4}$ and $\eta_{min} = 10^{-5}$ computations are indistinguishable). Thus, the choice for η_{min} to 10^{-4} is relevant.

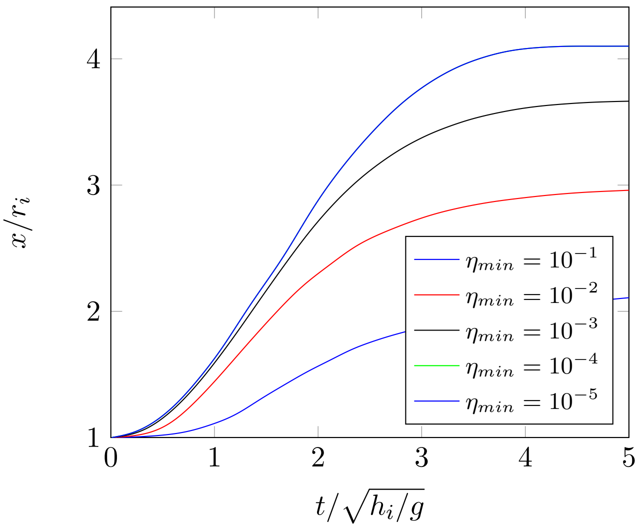

Figure 92: Sensitivity analysis to η_{min} by plotting dimensionless position of the front according to the dimensionless time during a granular collapse with $a = 1.42$

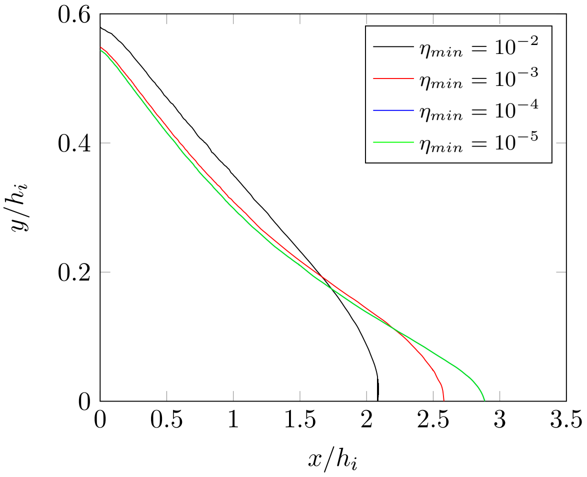

Figure 93: Final granular profiles after granular collapses ($a = 1.42$) with different η_{min}

In conclusion, the choice of regularization parameters is important as it can affect the granular final shape. However, considering highly plastic regions leads to convergence problems, with large viscosity jumps. Thus, a compromise must be determined. In the previous numerical simulation, it has been shown that choosing $|| \dot{\gamma} ||_{min} = 10^{-2}$ and $\eta_{min} = 10^{-4}$ give accurate results.

4.3.1.4 Flow sensitivity to rheological constants

In this section, influence of the rheological parameters (μ_S, $\Delta\mu$, I_0 and d) is studied. Thus, different numerical collapses are performed with different rheological parameters. In this work, the initial aspect ratio is fixed at $a = 1.42$.

Static friction coefficient μ_S

First, the influence of μ_S is studied. Four collapses are performed with different μ_S: $\mu_S = 0.32, 0.42, 0.52$ and 0.62. Figure 94 illustrates the final profiles. It is observed that static friction coefficient changes drastically the final shape of the flow. Indeed, from $\mu_S = 0.52$ to 0.62, the run-out distance is 20% larger.

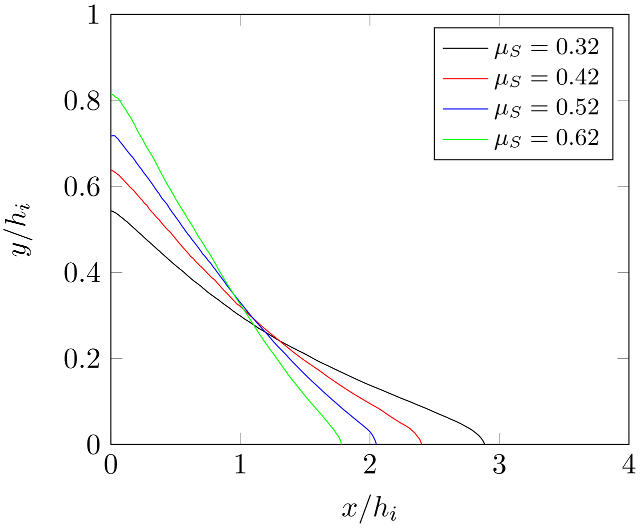

Figure 94: Final profiles after granular collapses ($a = 1.42$) with different μ_S

Moreover, the same analysis has been performed with a granular collapse with $a = 10$. Figure 95 illustrates the final profiles of the flow. The same conclusion as for $a = 1.42$ is performed: the static friction coefficient has a strong influence on the run-distance of the flow.

Thus, figure 96 illustrates the run-out distance according to μ_S for the two granular collapses. It is observed that the run-out distance follows a power-law curve according to μ_S. The exponent is found approximately to -1.2 for both flows, which is closely consistent with the scaling obtained from a crude energy argument (see equation 4.3).

Finally, figure 97 illustrates effective viscosity of the flow at $\bar{t} = 1$, for collapses with different μ_S. It is observed the unyielded regions increase close to free-surface (flow front and close to the symmetrical wall) as μ_S increases, but also the creation of shear-banding regions, leading to a reduced spreading of the granular material. The occurrence of shear bands was theoretically predicted by Barker *et al.*[69].

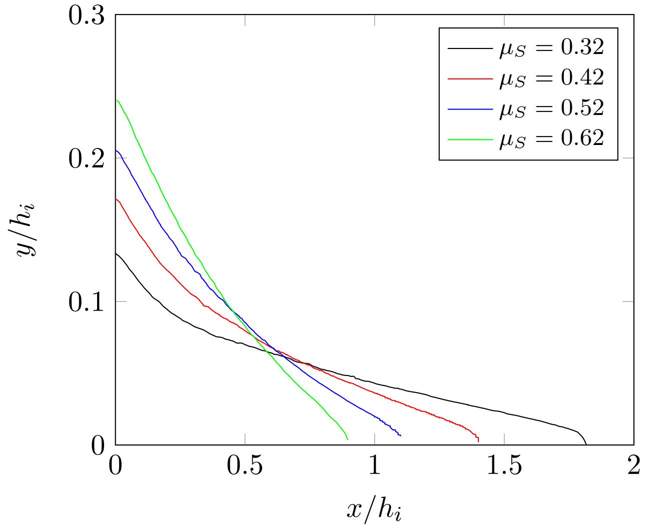

Figure 95: Final profiles after a granular column ($a = 10$) for different μ_S

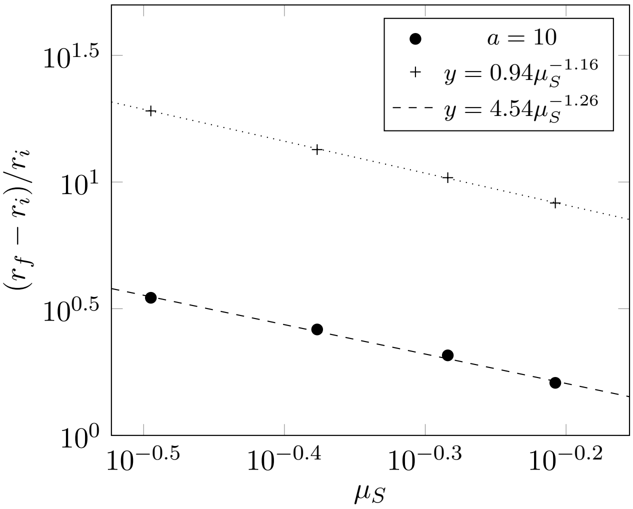

Figure 96: Dimensionless run-out of the flow according to the static friction coefficient μ_S

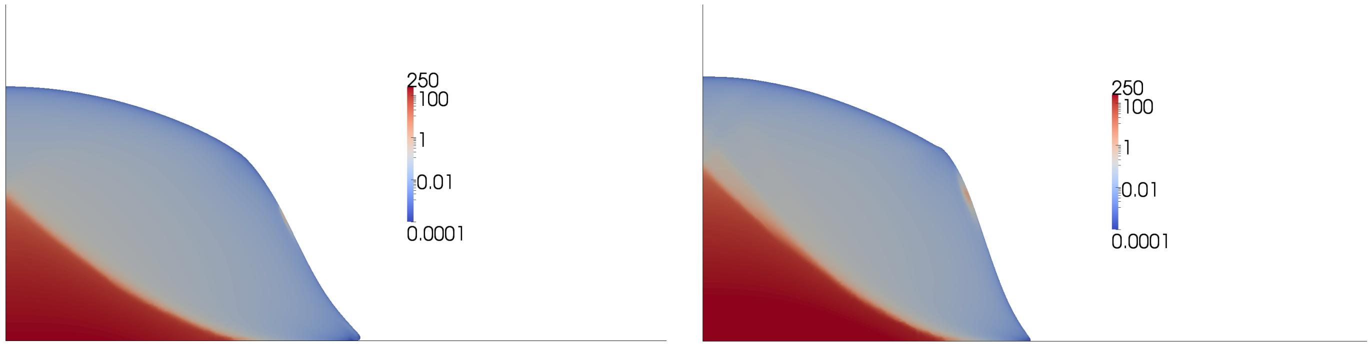

(a) $\mu_S = 0.32$

(b) $\mu_S = 0.42$

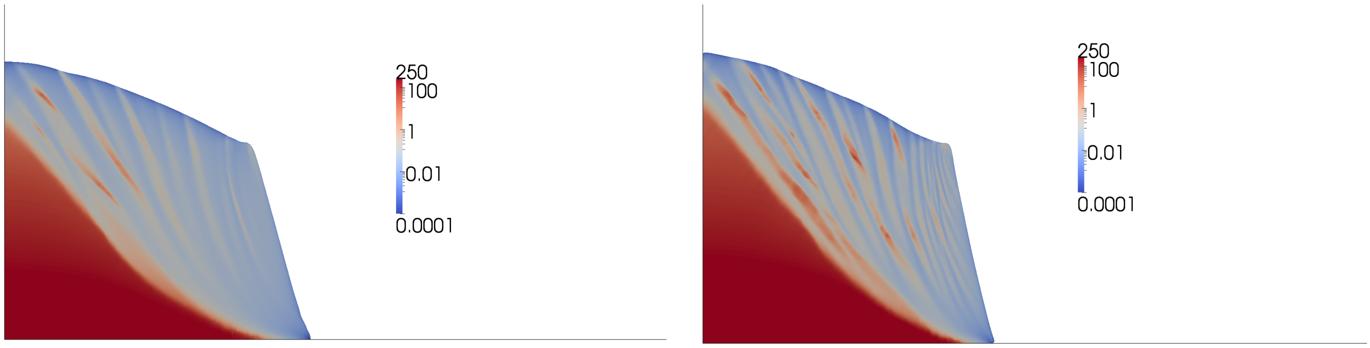

(c) $\mu_S = 0.52$

(d) $\mu_S = 0.62$

Figure 97: Effective viscosity of the granular material at time $\bar{t} = 1$

Influence of μ_F

Then, the influence of μ_F is studied. Thus, granular collapses with different $\Delta\mu$ ($\Delta\mu = \mu_F - \mu_S$) are performed and run-out distances are compared. In these simulations, μ_S is fixed to 0.32. Figure 98 illustrates the final granular profiles after the collapse. It is observed that the final height measured on the symmetry plane is independent of μ_F and remains constant. However, the difference deals with the run-out distance, which increases as μ_F decreases. Such a behavior is expected, as the inertial number is large in the vicinity of the front flow.

The evolution of the front position during the simulation (figure 99) shows that only the deceleration stage depends on μ_F, and not the acceleration one. By analyzing curves 98 and 99, μ_F acts at the end of the flow, leading to elongate (low μ_F) the final granular profile, while remaining the maximum height constant.

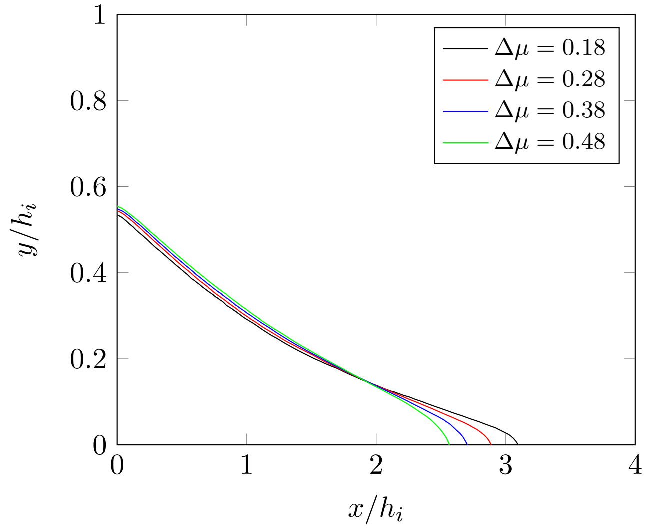

Figure 98: Final profiles for a column with initial aspect ratio $a = 1.42$ for different values of dynamic friction coefficient $\Delta\mu = 0.18, 0.28, 0.38$ and 0.48

Then, the same analysis has been performed for a granular collapse with higher a ($a = 10$) (figure 100). The same conclusion as for a lower a, is made.

Finally, figure 101 illustrates dimensionless run-out of the granular flow according to the $\Delta\mu$, for two granular collapses with $a = 1.42$ and 10. It is observed that the dimensionless run-out distance follows a power-law curve. Moreover, $\Delta\mu$ has a stronger impact on the run-out distance for low a. However, influence of $\Delta\mu$ on the run-out distance remains lower than the one for μ_S (relative impact four times lower).

Influence of I_0

Finally, influence of I_0 is studied. Three granular collapses with different I_0 ($0.04, 0.4$ and 4) are performed. Figure 102 shows the evolution of dimensionless front position during the simulation for the different collapses. It is observed that the flow spreads further for large I_0 granular collapses, which is expected.

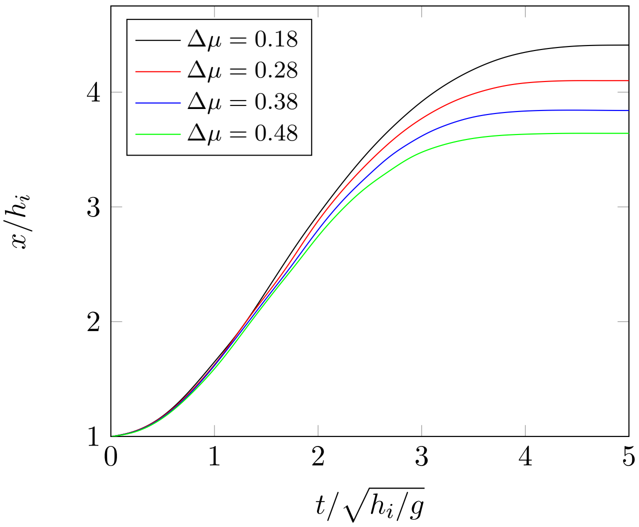

Figure 99: Dimensionless position of the front according to dimensionless time with initial aspect ratio $a = 1.42$ for different values of dynamic friction coefficient $\Delta\mu = 0.18, 0.28, 0.38$ and 0.48

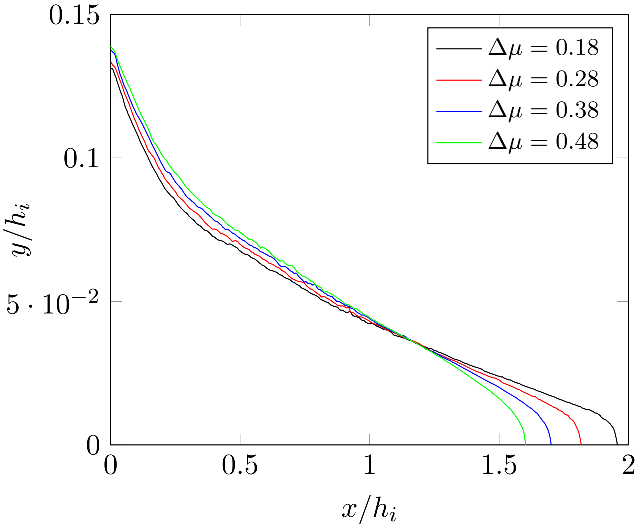

Figure 100: Final profiles after a granular collapse ($a = 10$) for different $\Delta\mu$

Indeed, a low I_0 leads to a fast transition between quasi-static and dense regimes, inducing thus smaller unyielded regions. Thus, it is expected that the granular material spreads further as I_0 increases, as obtained in the numerical simulations.

Figure 103 illustrates dimensionless run-out distance according to I_0, which follows a power-law curve with exponent 0.11. Thus, it is found that I_0 has a negligible influence on the granular dynamics (influence ten times less important than μ_S) for the chosen set of parameters. Let us remark that the influence of I_0 should be larger for large aspect ratios flows as such flows would become more inertial, this point is discussed further.

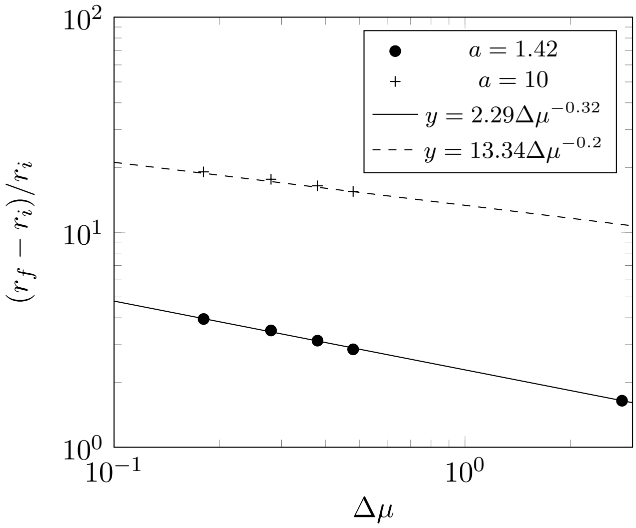

Figure 101: Dimensionless run-out distance according to $\Delta\mu$

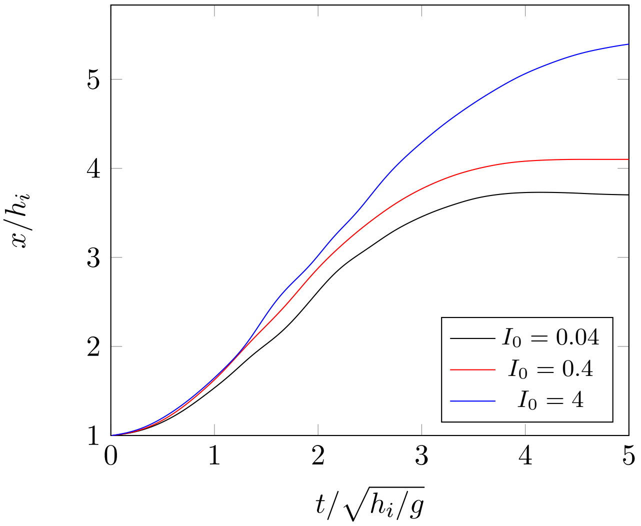

Figure 102: Dimensionless position of the front according to dimensionless time with initial aspect ratio $a = 1.42$ for different values of $I_0 = 0.04, 0.4$ and 4

In conclusion, we performed two-dimensional granular collapses with granular materials having different rheological properties (μ_S, μ_F and I_0). The analysis of each parameter shows that the predominant feature impacting the final run-out distance is μ_S. Then, it is observed that μ_F has also a small influence (approximately four times less than μ_S), particularly during the deceleration stage. Finally, I_0 has a negligible influence compared to μ_S (ten times less), for low h_i.

4.3.1.5 Influence of the aspect ratio

In this section, two-dimensional granular collapses with different aspect ratios are performed.

Figure 104 shows the normalized flow front position according to a. As obtained in Lube *et al.*[64], a

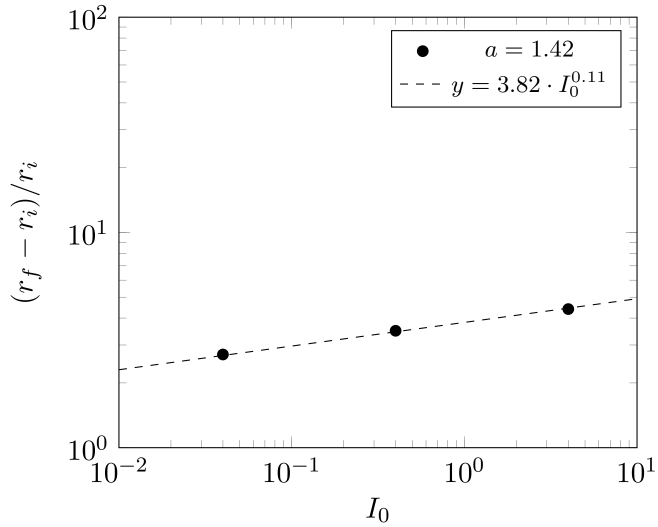

Figure 103: Dimensionless run-out distance according to I_0

linear curve is found for low a (lower than 7). Moreover, the power-law curve with exponent 0.7 is found for large a (larger than 7):

$$\frac{r_f - r_i}{r_i} \approx \begin{cases} 1.72\ a^{0.97} & a \leq 7 \\ 2.96\ a^{0.69} & a \geq 7 \end{cases} \tag{4.17}$$

The same results as obtained by Lagrée *et al.*[13] have been found, namely a limit between linear and power-law regimes $a_c \approx 7$, and a power-law exponent of 0.7 . In the experimental work conducted by Lube *et al.*[64], the same type of curves has been found. They fitted, however, a power-law exponent of 2/3 and a lower critical aspect ratio. This difference could be explained by the choice of the numerical rheological parameters (μ_S, typically) and maybe by the static and non-local effects that have not been introduced in the model, while they could influence the granular dynamics in unyielded regions.

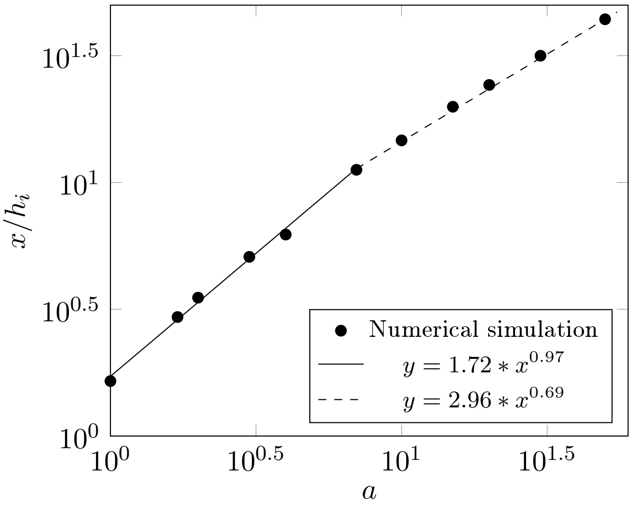

Figure 104: Dimensionless run-out distance according to a for two-dimensional granular collapses

In order to explain the two observed power-law regimes, we propose to confirm the theory proposed by Larrieu *et al.*[70], who suggested that, for large enough a, an extra-dissipation of some of the (vertical) kinetic energy of the fall is dissipated when the grains impact on the base, therefore not converted into horizontal kinetic energy.

Figures 105, 106 and 107 show relative (with respect to initial potential energy) energy partition (kinetic, potential, mechanical and dissipated energies) during a granular collapse of, respectively $a = 1.42$, $a = 10$ and $a = 50$. As expected, both the kinetic energy part and final dissipated energy increase with aspect ratio. For low aspect ratio, one notices that the maximum kinetic energy is reached a time $t \simeq \sqrt{2h_i/g}$, which is the impact time for a free fall. For large aspect ratios, the maximum kinetic energy is much larger and reached earlier, then decreases quickly until $t \simeq \sqrt{2h_i/g}$, while the dissipated energy jumps quickly.

It suggests that the extra-dissipation indeed occurs during the impact, which is confirmed on figures 108, 109 and 110 that show the volume fraction of flowing regions (non zero velocity) during a collapse for, respectively, $a = 1.42$, $a = 10$ and $a = 50$. Indeed, the graphs show that for large a, nearly the whole volume is flowing, including the bottom center region, inducing the measured extra-dissipation. Figure 111 shows the complex height profiles formed during a granular column collapse with $a = 50$, plotted for different times. At the free fall time $t \simeq 1.5\sqrt{h_i/g}$, a crater and a crest are formed, creating a wave that is advected away for the subsequent times, and then spreads away at late times, the crest being damped in the inner direction. This complex flow is divided in dense and inertial regions, forming respectively the top and bottom of the advected wave, as shown on figure 112.

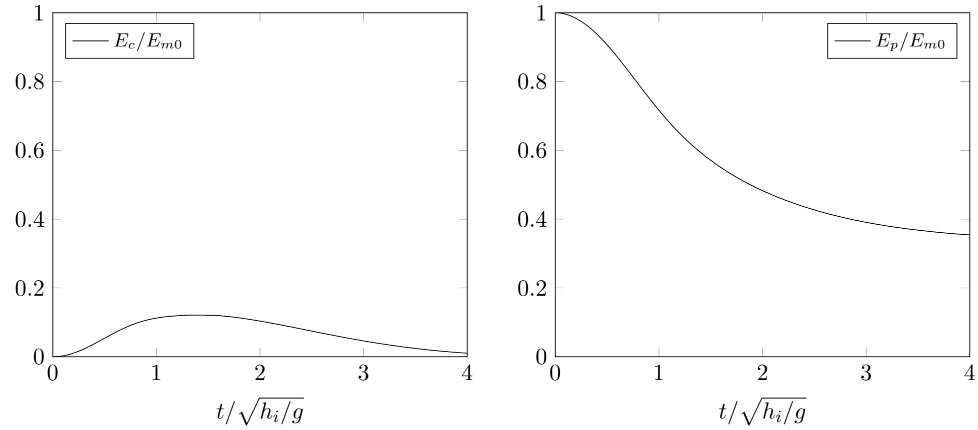

(a) Kinetic energy (b) Potential energy

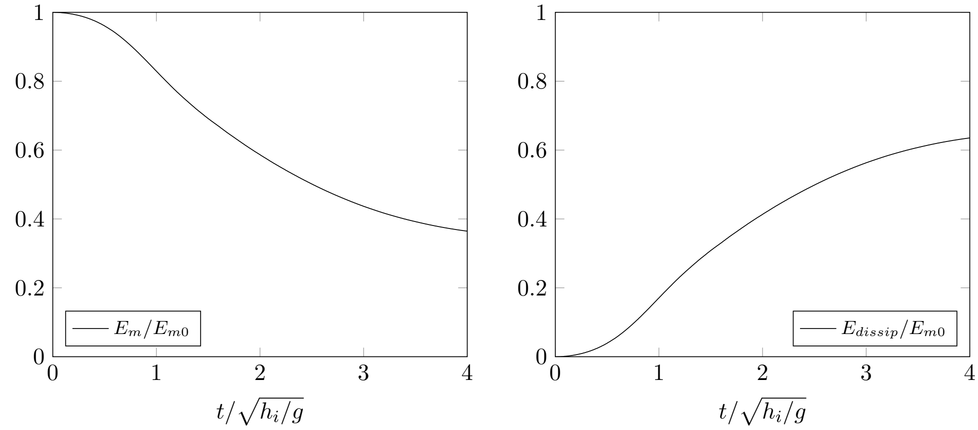

(c) Mechanical energy (d) Dissipated energy

Figure 105: Relative energy partition during a granular collapse with $a = 1.42$

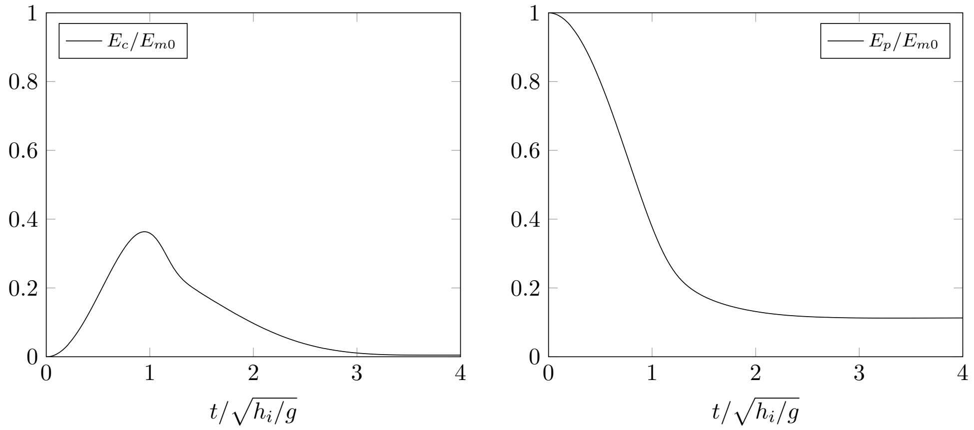

(a) Kinetic energy

(b) Potential energy

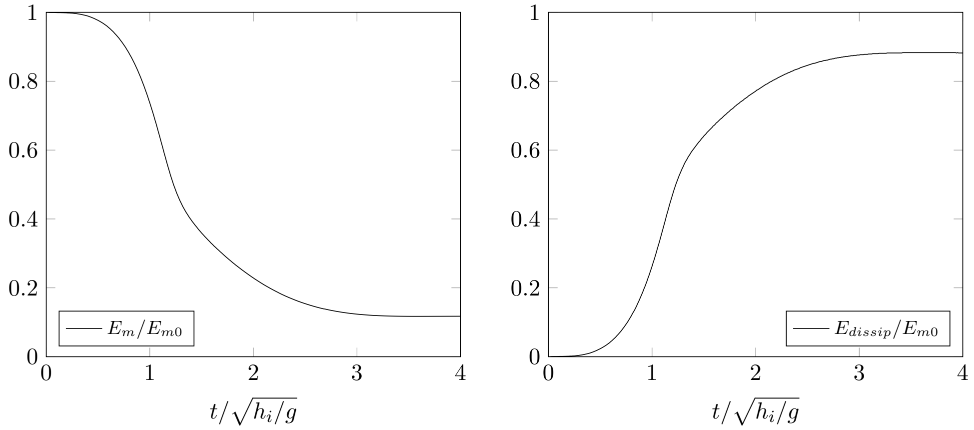

(c) Mechanical energy

(d) Dissipated energy

Figure 106: Relative energy partition during a granular collapse with $a = 10$

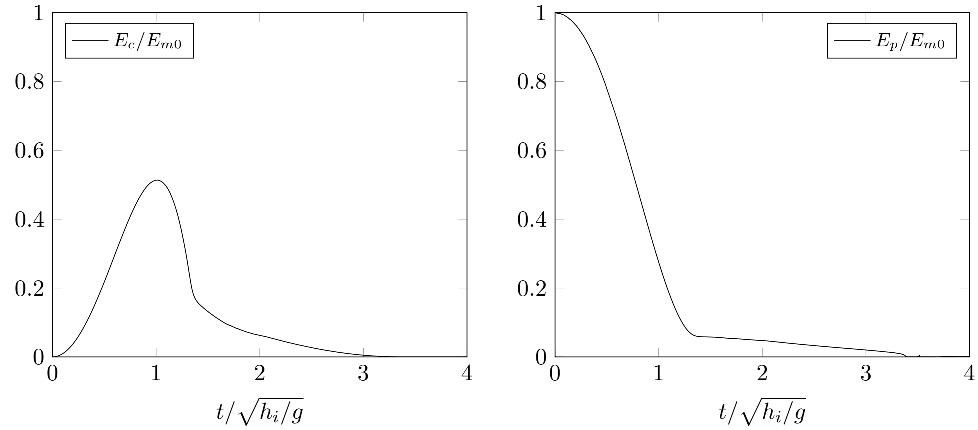

(a) Kinetic energy

(b) Potential energy

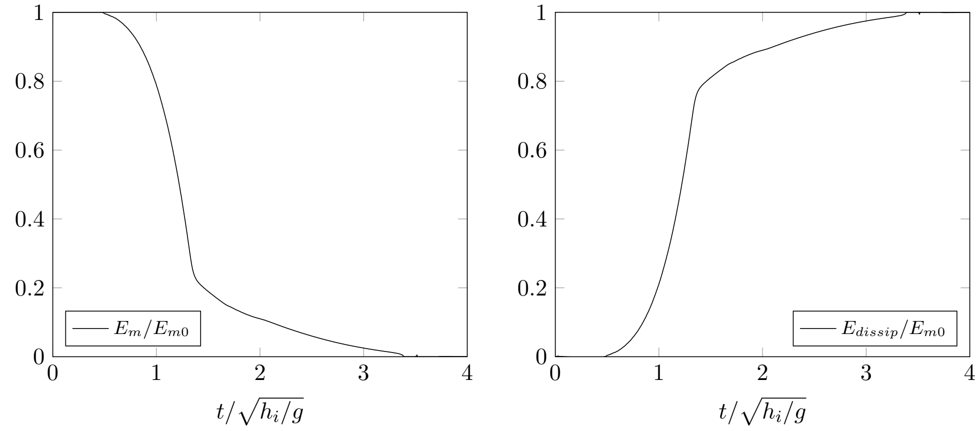

(c) Mechanical energy

(d) Dissipated energy

Figure 107: Relative energy partition during a granular collapse with $a = 50$

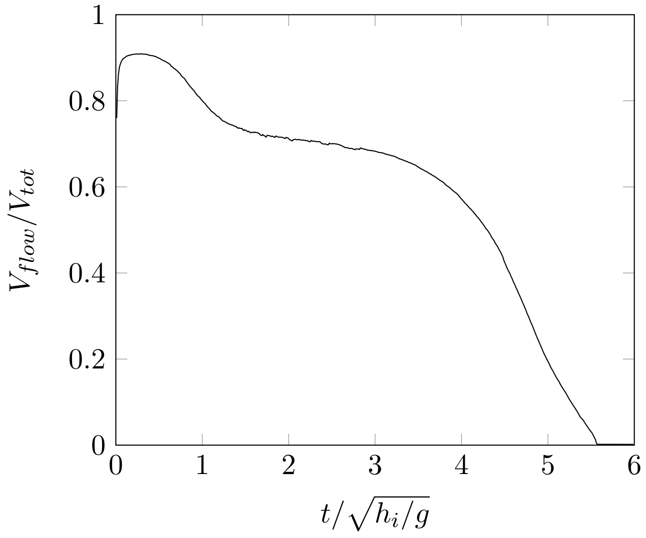

Figure 108: Volume fraction of flowing regions (non zero velocity) during a collapse for $a = 1.42$

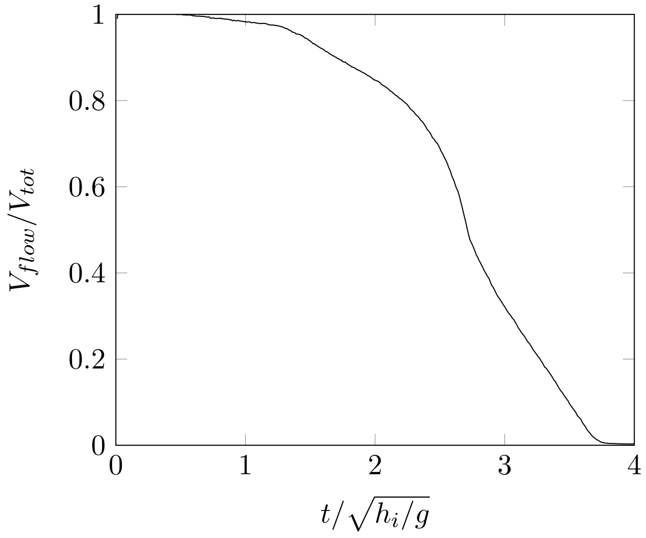

Figure 109: Volume fraction of flowing regions (non zero velocity) during a collapse for $a = 10$

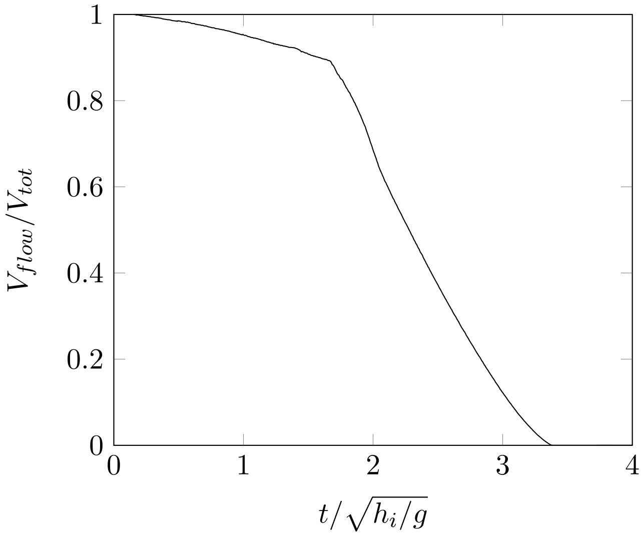

Figure 110: Volume fraction of flowing regions (non zero velocity) during a collapse for $a = 50$

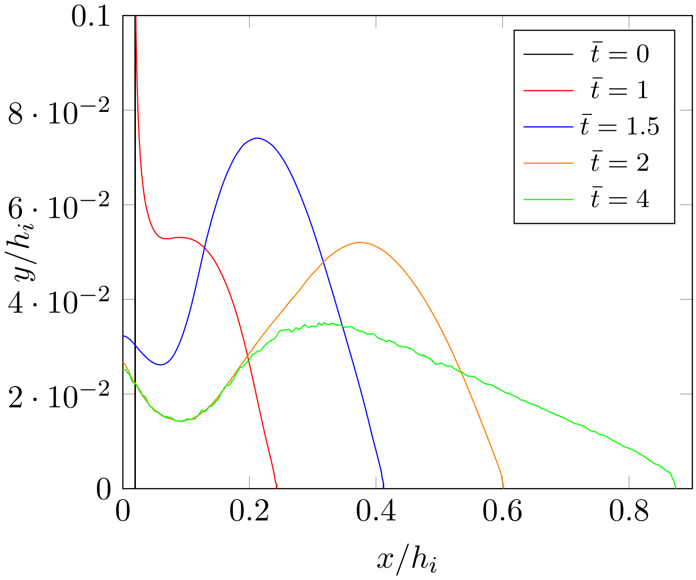

Figure 111: Height profiles during a granular column collapse with $a = 50$, plotted for different non-dimensional times $\bar{t} = t/\sqrt{h_i/g}$

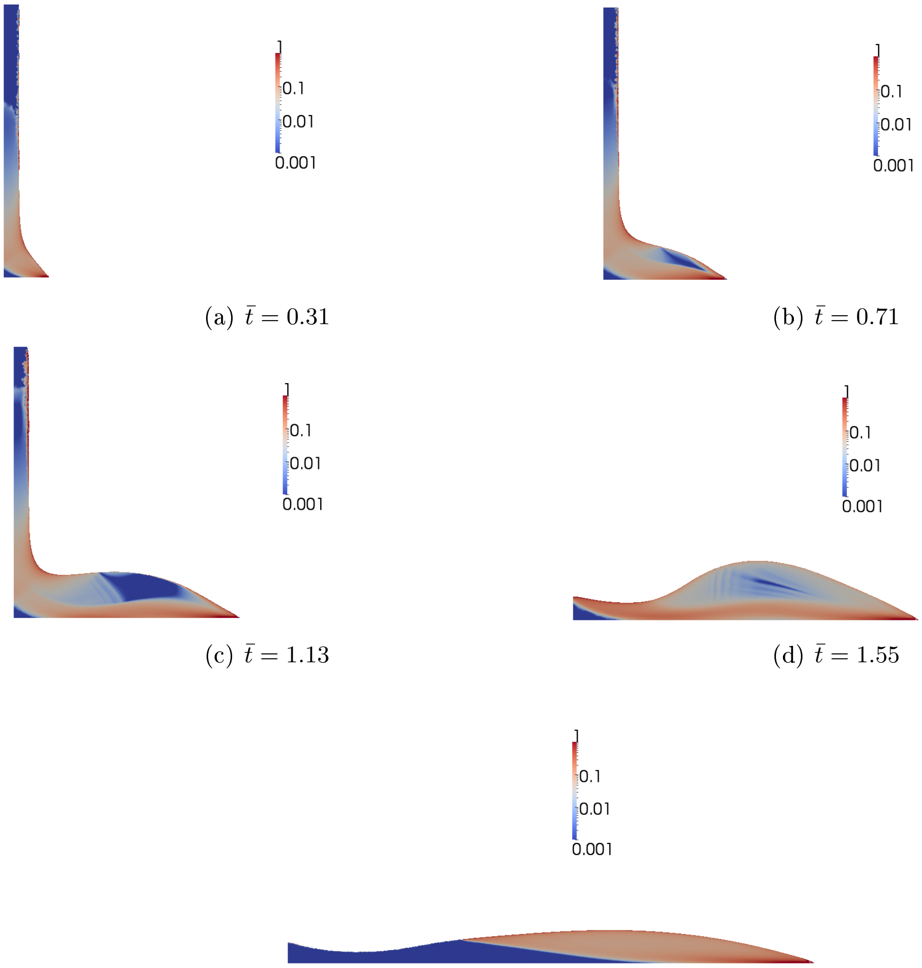

(a) $\bar{t} = 0.31$

(b) $\bar{t} = 0.71$

(c) $\bar{t} = 1.13$

(d) $\bar{t} = 1.55$

(e) $\bar{t} = 2.19$

Figure 112: Dense vs. inertial regions for different non-dimensional times $\bar{t} = t/\sqrt{h_i/g}$, plotted as I/I_0 for a granular collapse with $a = 50$

4.3.1.6 Flow features close to arrest

In this section, we introduce a method for the determination of granular flow arrests, as the chosen regularization method does not ensure a strict flow stop at long times, but rather a slow creep. We then study how flow stops for small and large aspect ratios a, and show that the last moving region before stop is close to the center for small a, whereas it is located at the front for large a.

As shown for Bingham flows, we expect to find the time for flow stop when the stress is smaller than $\mu_S p$ everywhere in the flow domain. However, as the pressure p depends on the flow geometry, there exist some regions (typically close to the free surface) where $\mu_S p$ is arbitrary small. Consequently, in these regions, the effective viscosity tends to the regularized value η_{min}, whereas stress close to the surface could occur from potential (for slow flows) or kinetic (for fast flows) energy. For example, when checking figure 87 we notice that the front flow does not satisfy the stress criterion in the two last elements, due to our method to avoid the triple point/line singularity. However, when plotting $\int_{\Omega_f} \parallel \bar{\dot{\gamma}} \parallel \Omega_f$ at different instants (see figure 113) we notice that the mean shear rate increases, corresponding to the flow start, then it reaches a maximum, followed by a plateau. Finally, it decreases drastically down to a finite plateau value [1]. We then choose the corresponding time as the flow stop time.

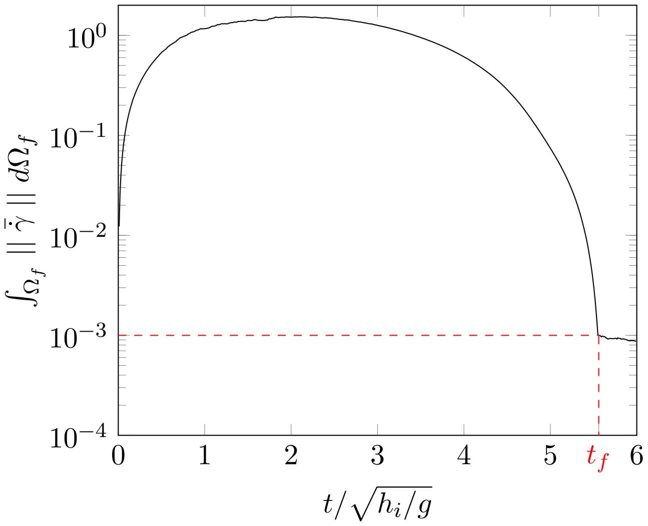

Figure 113: Evolution of mean shear rate during a granular collapse with $a = 1.42$

Influence of rheological constants on arrest time

For the same collapse, it is observed that the arrest time of the flow depends strongly on μ_S: the higher μ_S, the sooner the flow arrest, and the lower the run-out distance (see figure 114.a). Moreover, it is observed that $\Delta\mu$ has a smaller influence: the larger $\Delta\mu$, the sooner the flow arrest, and the lower the run-out distance (see figure 114.b). For larger aspect ratios, the arrest time is much less dependent on rheology, as the free fall time controls the global flow duration.

Influence of the aspect ratio

---

[1] This finite plateau scales inversely with η_{min}

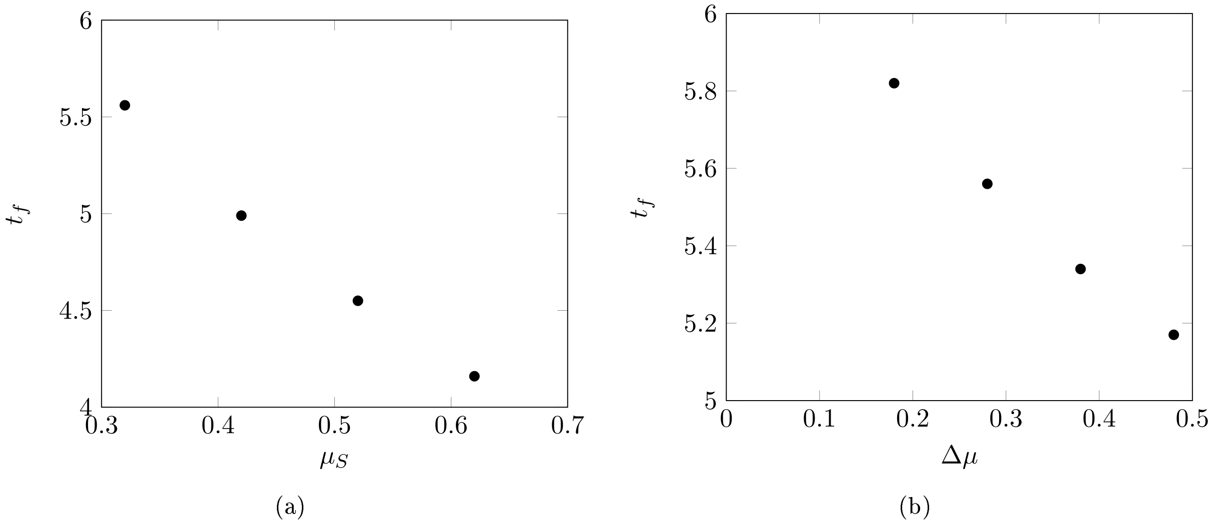

(a)

(b)

Figure 114: Variation of arrest time with rheological constants: (a) Influence of μ_S ; (b) Influence of $\Delta\mu$

When varying the aspect ratio from small to large, according to the transition value a_c, we observe two types of flow arrests. First, for small aspect ratio, the flow consists of a first excursion of the edges, that stops before the global arrest, followed by a rearrangement of the surface, close to the symmetry plane (see shear rates plots on figure 115). For large aspect ratio, the flow spreads from the edges until the arrest (see figure 116), because the kinetic energy is concentrated in these zones.

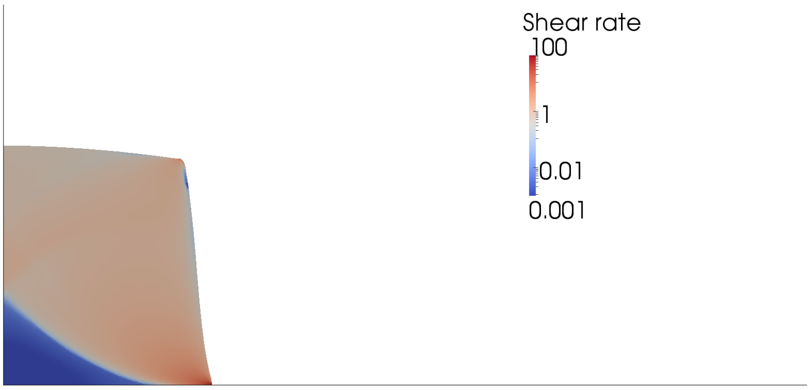

(a) $\bar{t} = 0.5$

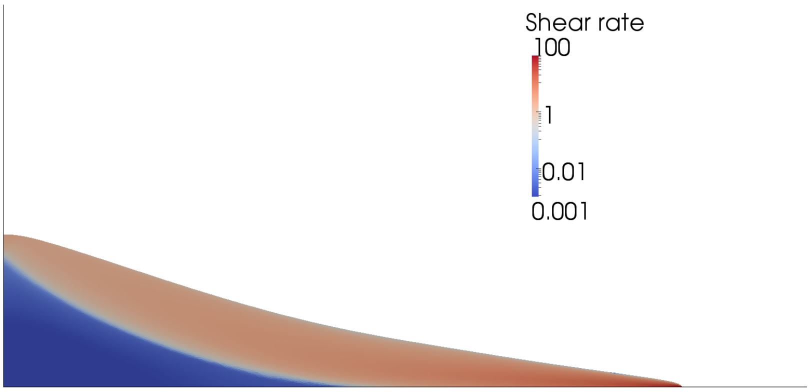

(b) $\bar{t} = 3$

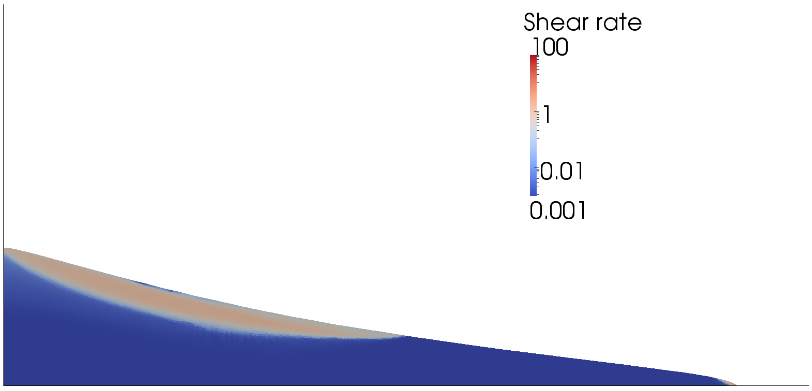

(c) $\bar{t} = 5$

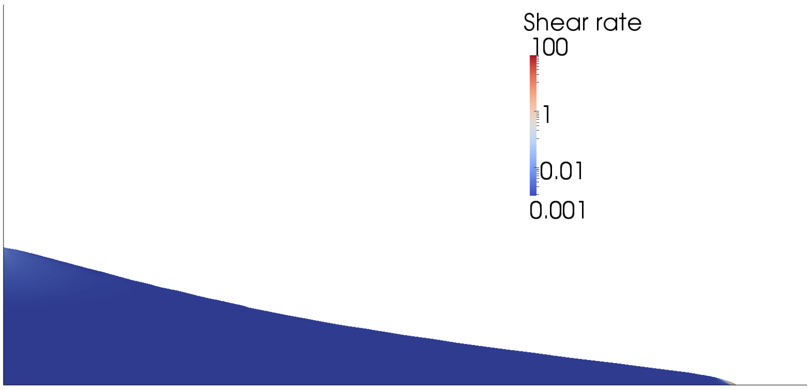

(d) $\bar{t} = 6$

Figure 115: Shear rate for a granular collapse with $a = 1.42$ plotted at several instants

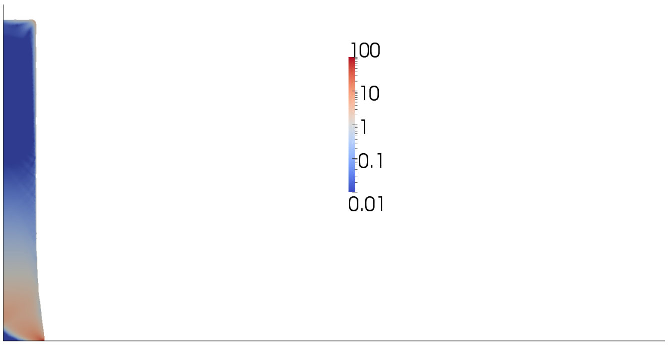

(a) $\bar{t} = 0.25$

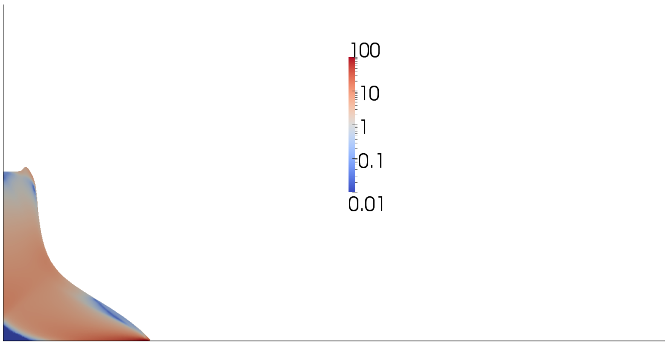

(b) $\bar{t} = 1$

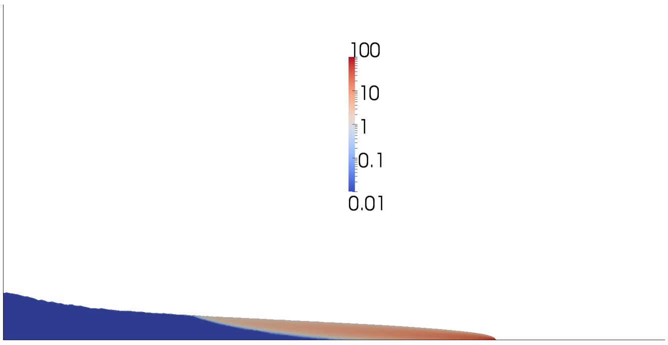

(c) $\bar{t} = 3$

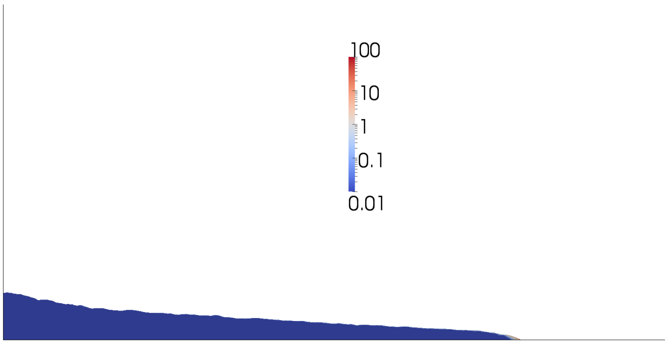

(d) $\bar{t} = 5$

Figure 116: Shear rate during a granular collapse with $a = 10$, plotted at several instants

4.3.1.7 Master curves for granular collapses

As introduced at the beginning of this chapter, the work of Lube *et al.*[64] pointed that for any rheology and geometrical features, the flow follows a same curve, representing the relative run-out distance $(r - r_i)/(r_f - r_i)$ according to the relative time $\bar{t}/t_f$, where r_f is the time made by the flow to reach its final position.

Figure 117 illustrates this curve for granular collapses ($a = 10$) with different μ_S. It is observed that the run-out distance follows a curve nearly independent of μ_S. Slight differences are observed, particularly, the acceleration is slower as μ_S increases.

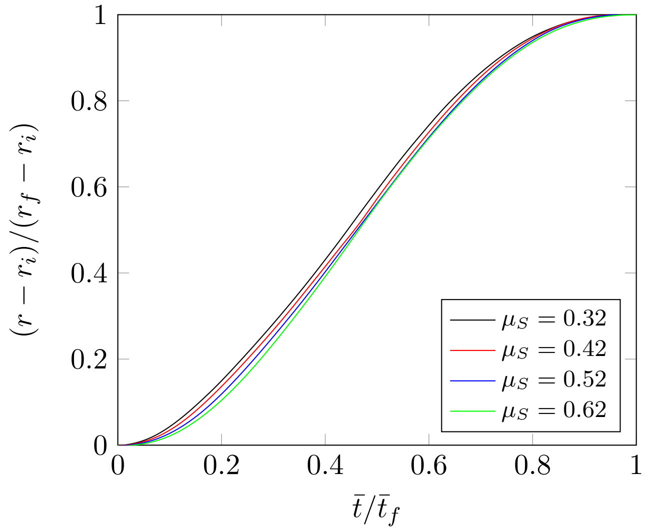

Figure 117: Run-out distance according to dimensionless time for granular collapses for $a = 10$ with different μ_S

Figure 118 illustrates the same curve for granular collapses with different $\Delta\mu$. This analysis shows that $\Delta\mu$ has an even smaller influence on the granular dynamics.

Lube *et al.*[64] outlined that the granular dynamics is independent of geometrical and rheological flow features, by demonstrating that granular materials follow a same curve (relative run-out distance according to relative time). However, several differences are outlined by performing granular collapses with different μ_S and $\Delta\mu$, as illustrated in curves 117 and 118. Thus, this work suggests, according to the $\mu(I)$ theory, that rheological constants influence the granular dynamics, contrary to Lube *et al.*[64]. Alternatively, we could conclude that the materials used in Lube *et al.*[64] were not rheologically different, as suggested by Balmforth and Kerswell [63].

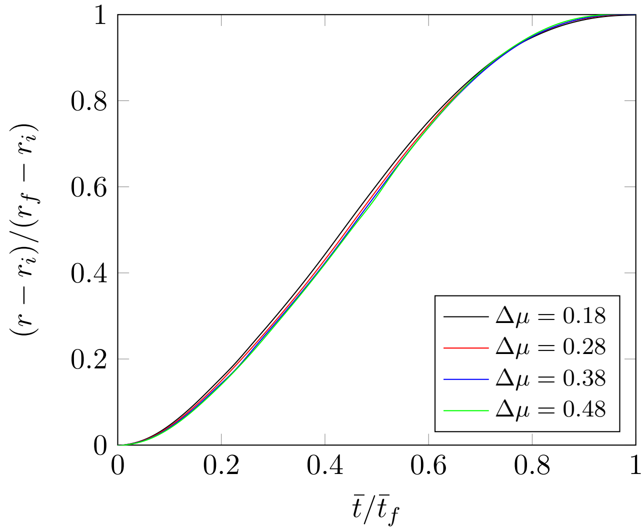

Figure 118: Run-out distance according to dimensionless time for granular collapses for $a = 10$ with different $\Delta\mu$

4.3.1.8 Conclusion

In this part, we performed two-dimensional granular collapses with materials exhibiting different rheological features, but also with different a. First, multiphase $\mu(I)$ rheology flows have been validated with results of Lagrée *et al.*[13] obtained with discrete methods (DEM). Then, the influence of rheological features has been analyzed. It has been shown that μ_S is the dominant rheological parameter that drives the flow.

Then, the influence of a has been studied. The two regimes observed in Lube *et al.*[64] have been found: a linear regime for low a, and a power-law one for high a. Moreover, we found that the $\mu(I)$ model can predict a quasi universal relative time-distance curve.

4.3.2 Three-dimensional granular collapses

4.3.2.1 Problem statement

Then, the model developed in this work is extended to three-dimensional granular collapses. The geometry of the problem is illustrated in figure 119. A cylindrical granular column with initial height h_i and radius r_i is considered. The computations are performed in a rectangular domain (with two symmetry planes) of height H in z direction and length L in both x and y directions.

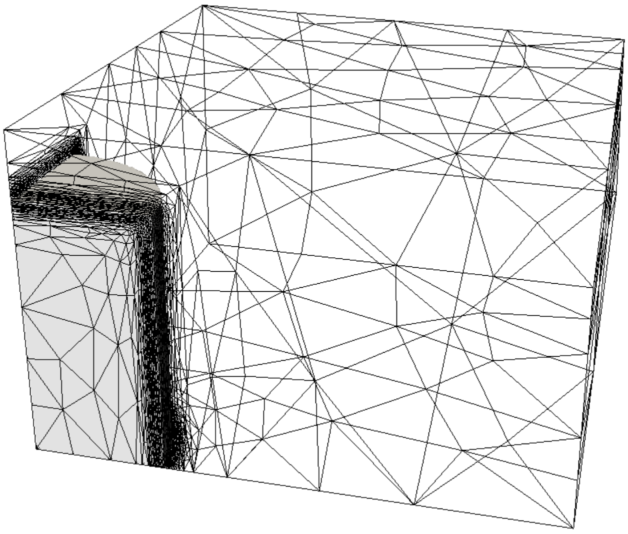

Figure 119: Initial granular column and adaptive mesh of a three-dimensional granular collapse simulation

Symmetry conditions are applied on the two lateral faces. The pressure is set to zero on the other faces except at the bottom one, where no-slip conditions are applied. As detailed in the previous section, one needs to set slip zones upstream the flow front. Figure 120 illustrates the proposed method to identify these zones. First, elements cut by zero-isovalue of the Level-Set function, but also located onto the bottom surface, are determined, creating a surface called Γ_i. Then, a new field ψ_m is created, by removing from $\Omega_f \cap \Gamma_b$ the surface Γ_i (figure 120.c):

$$\psi_m = \begin{cases} 1 & \text{if } x \in (\Omega_f \cap \Gamma_b) \setminus \Gamma_i \\ 0 & \text{elsewhere} \end{cases} \tag{4.18}$$

The last step consists of setting a slip boundary condition to the nodes belonging to the determining the nodes where the granular material is allowed to slip (figure 120). Finally, ψ_n is computed, aiming to determine minimum of ψ_m of all the connected elements to a specific node:

$$\psi_n = \underset{\Omega}{min} \quad (\psi_m) \tag{4.19}$$

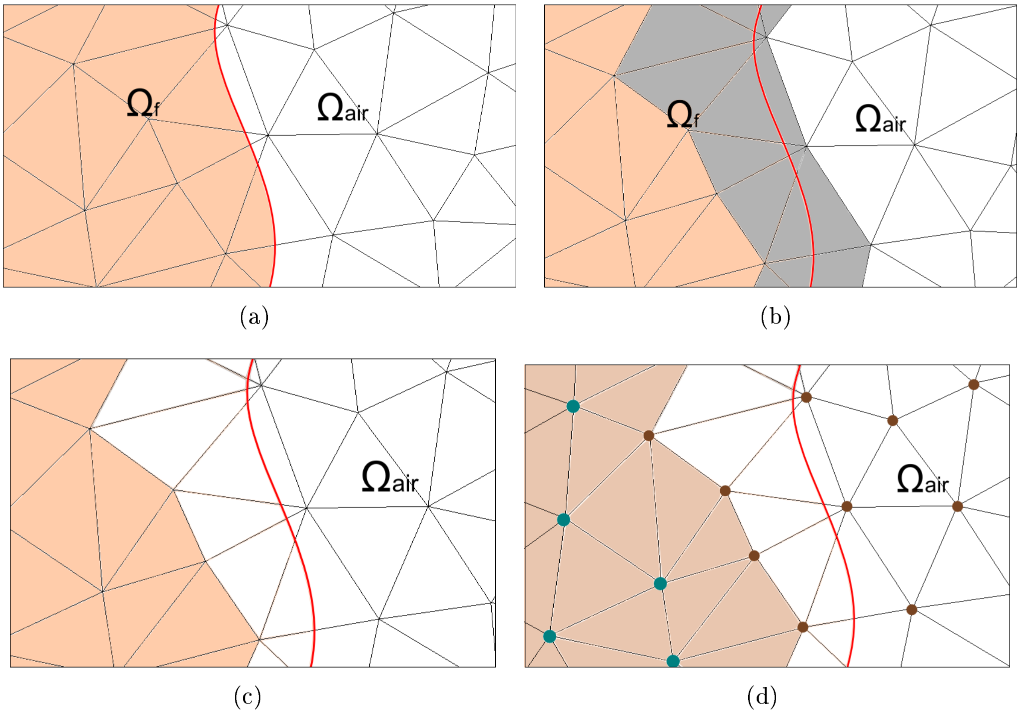

(a) (b) (c) (d)

Figure 120: Steps required to determine regions where the granular material is allowed to slip: (a) The interface between the two domains (red): granular material (orange) and air (white) ; (b) Localization of the region where elements are cut by the interface (gray) ; (c) Subtraction of the gray region from granular domain ; (d) Determination of nodes located into the granular area where slip boundary conditions is applied (nodes in brown)

4.3.2.2 Flow sensitivity to rheological constants

In this part, the influence of $\mu(I)$ parameters on the final run-out distance is analyzed. Thus, dimensionless run-out distances according to μ_S, $\Delta\mu$ and I_0 are plotted.

Figure 121 illustrates the dimensionless final run-out distance according to μ_S. As observed for two-dimensional granular collapses, the granular material spreads further for low μ_S. Moreover, the obtained curve follows a power-law regime with exponent -0.7 according to μ_S. Thus, it is found that the impact of μ_S onto the spreading is less strong than for 2D collapses (where the power-law exponent was $\simeq -1.2$). This suggest that the covered surface (proportional to a in 2D and a^2 in 3D) is likely to depend on $1/\mu_S$.

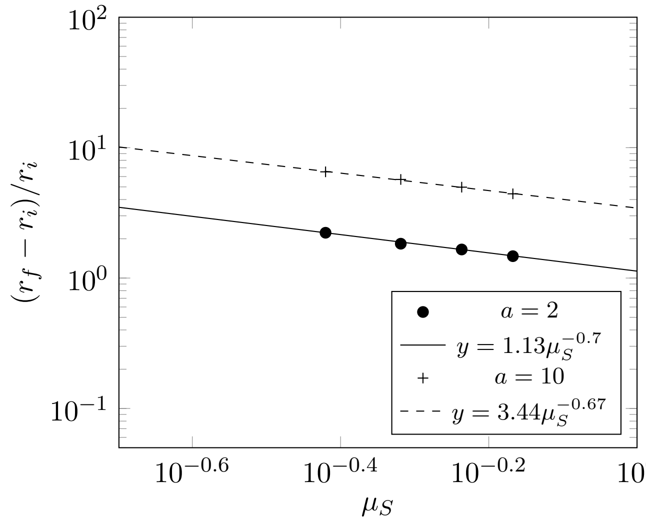

Figure 121: Dimensionless final run-out distance according to μ_S after three-dimensional collapses

Figure 122 illustrates dimensionless final run-out distance according to $\Delta\mu$. As observed for two-dimensional granular collapses, the granular material spreads further when $\Delta\mu$ is lower. Moreover, it is observed that the curve follows a power-law with exponent -0.21. Thus, as for two-dimensional granular collapses, μ_S has a stronger influence (three times more) than μ_F.

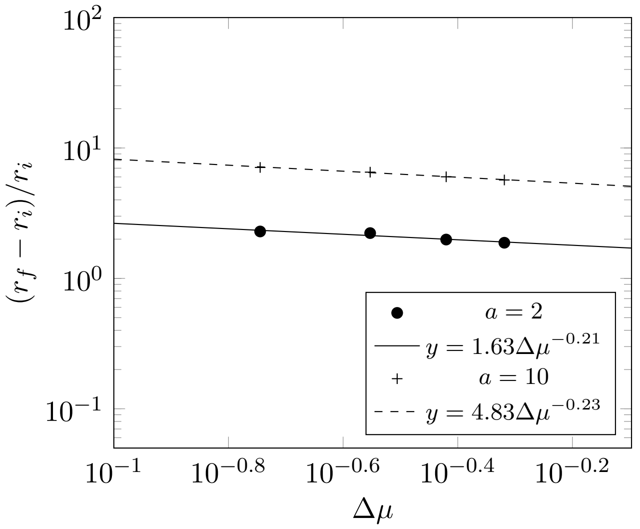

Figure 122: Dimensionless run-out of the flow according to $\Delta\mu$ after three-dimensional granular collapses

Finally, figure 123 illustrates dimensionless run-out distance according to I_0. As observed for two-dimensional granular collapses, the granular material spreads further when I_0 is lower. Moreover, it is observed that the curve follows a power-law with exponent 0.08 on I_0. Thus, influence of I_0 is negligible compared to the one of μ_S (ten times smaller), at least for small h_i.

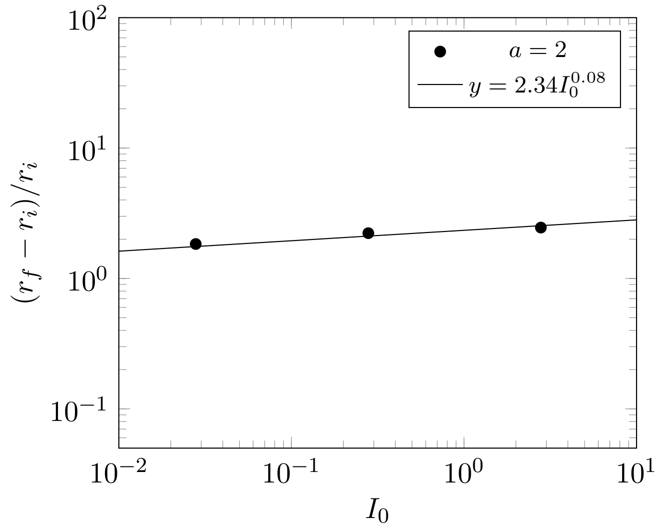

Figure 123: Dimensionless run-out distance according to I_0 after three-dimensional collapses

4.3.2.3 Influence of the aspect ratio

Now, three-dimensional granular collapses with different a are performed. In the computations, the parameters of Jop *et al.*[2] are taken for the description of granular rheology: $\mu_S = 0.38$, $\Delta\mu = 0.28$, $I_0 = 0.279$, $\rho_f = 2500 kg \cdot m^{-3}$, $d = 0.54 mm$.

Figure 124 illustrates dimensionless position of the final front according to a. It is observed that for large aspect ratios ($a > 2.7$), the granular dynamics follows a power-law curve with exponent 0.54, and for low aspect ratios ($a < 2.7$), a linear regime is found, which has also been observed in two-dimensional granular collapses. Thus, the critical aspect ratio has been found equal to $a_c = 2.7$:

$$\frac{r_f - r_i}{r_i} = \begin{cases} 1.2\ a & \text{if } a < 2.7 \\ 1.93\ a^{0.54} & \text{if } a > 2.7 \end{cases} \tag{4.20}$$

Figures 125 and 126 illustrate the flow shape during granular collapses with $a = 2$ and 7. In figure 126, a granular chute is occurring at the beginning of the flow, leading to a more dissipative impact than for a granular collapse with low a (figure 125), as explained previously.

4.3.2.4 Influence of initial column height

Now, the purpose consists in analyzing the influence of h_i on the flow dynamics, for a fixed rheology and a fixed aspect ratio. To do so, r_i is set 10 times larger than previously ($r_i = 0.2m$), leading to proportionally larger h_i for the analysis of dimensionless run-out distance curve according to a. Figure 127 illustrates this curve, by comparing with the previous curve obtained for granular collapses with $r_i = 0.02$ m (illustrated in figure 124). We observe that granular collapses with same a and higher h_i leads to a larger run-out distance.

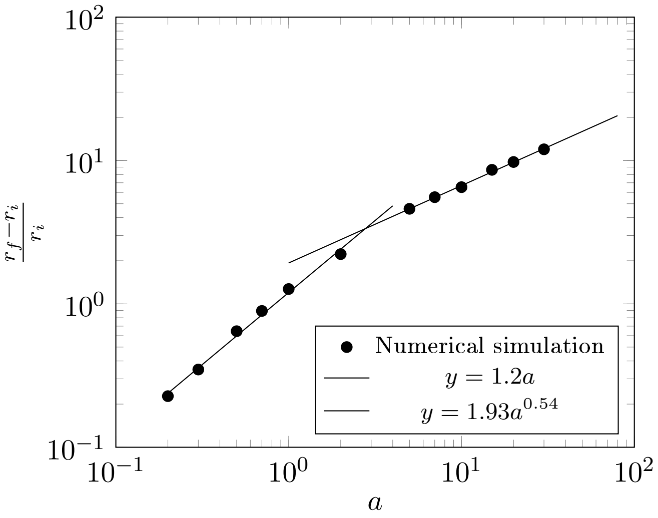

Figure 124: Dimensionless run-out distance according to a after three-dimensional granular collapses

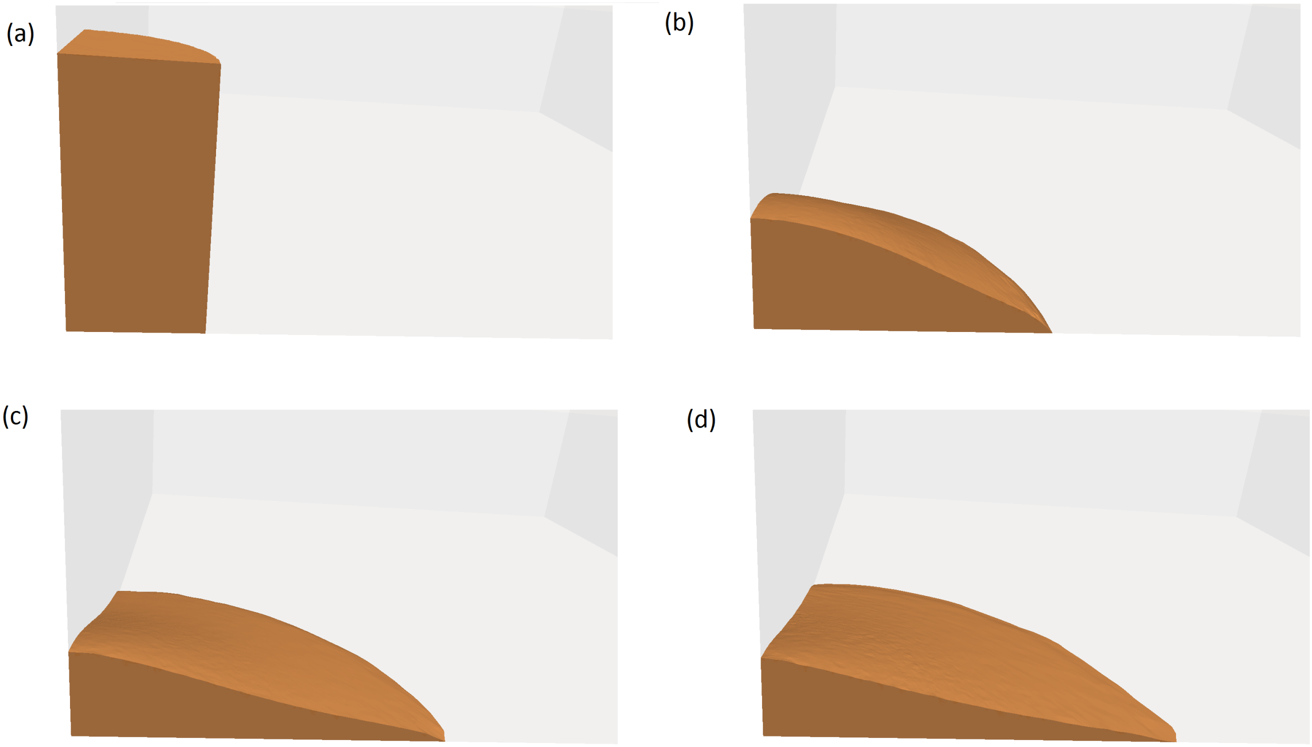

Figure 125: Flow profiles illustrated at several instants during a three-dimensional collapse with $a = 2$: (a) $t = 0s$; (b) $t = 0.1s$; (c) $t = 0.15s$; (d) $t = 0.23s$

We propose to explain this result by the fact that the velocity field varies as $\sqrt{h_i}$, leading $\| \dot{\gamma} \|$ to vary as $1/\sqrt{h_i}$. Furthermore, the pressure may be approximated by a linear function of h_i. Finally, the inertial number I varies as $1/h_i$. A similar trend can be deduced by considering that the ration between grain

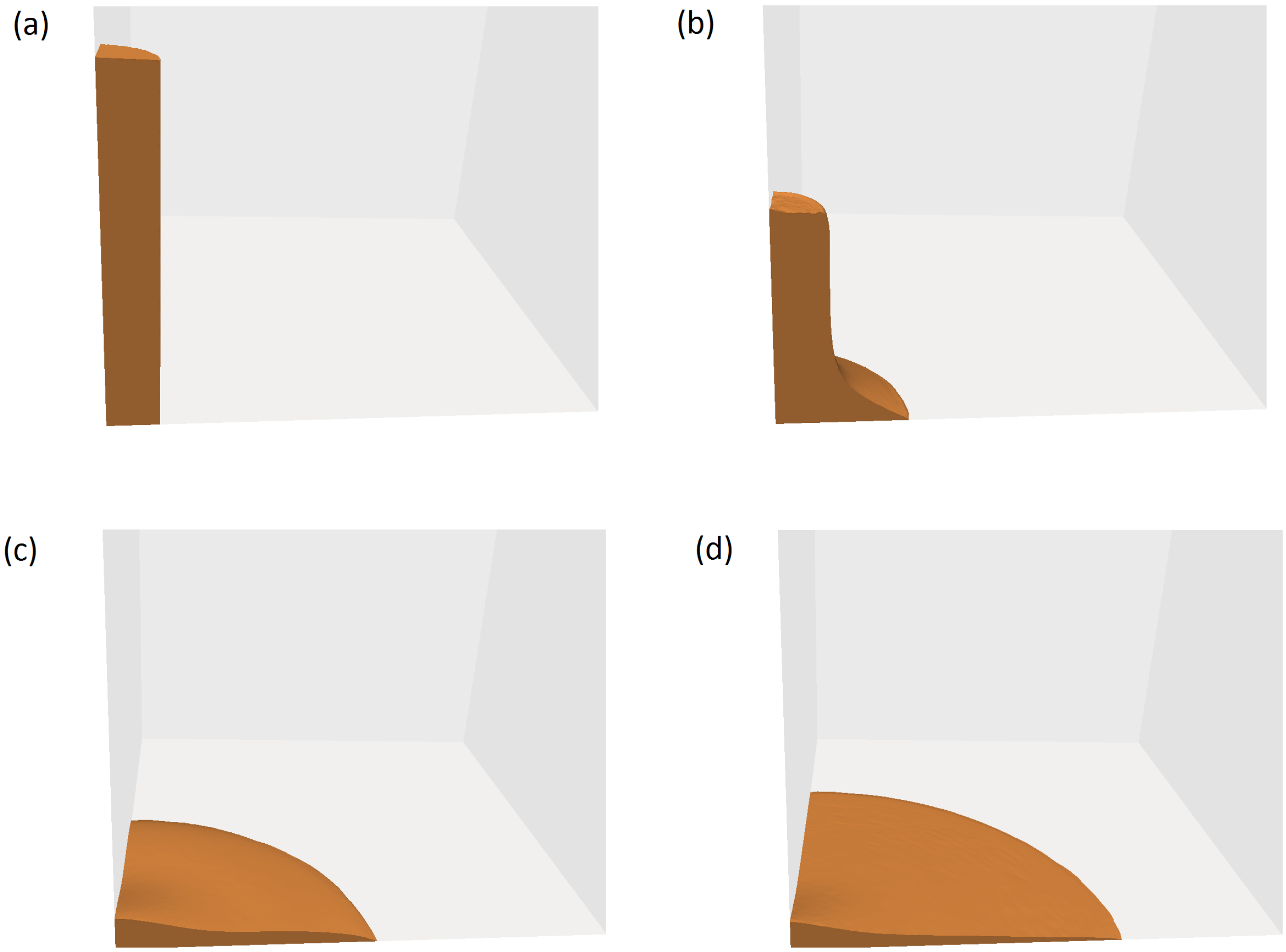

Figure 126: Profiles at different instants of a 3D granular column collapse with initial aspect ratio $a = 7$: (a) $t = 0s$; (b) $t = 0.1s$; (c) $t = 0.21s$; (d) $t = 0.33s$

diameter and characteristic length h_i scales as $1/h_i$ for a fixed grain diameter. Thus, increasing h_i leads to less friction, inducing a larger granular spreading. This explanation is confirmed in figure 128, where the inertial number fields are plotted for $a = 10$ and two different (by a factor 10) h_i for two different (by a factor $\sqrt{10}$) times. As we can see, the global shapes are similar and the proposed scalings can be retrieved, sustaining our argument.

4.3.2.5 Master curve

Figure 129 shows the relative run-out distance according to relative time during granular collapses for different aspect ratios a. Three different dynamics are observed. For low a (lower than a_c), a slow and late acceleration stage is observed.For larger a, the front position increases linearly after the acceleration. For very elongated columns (a>20), a wave is formed during the collapse. As observed in two-dimensional collapses, the chute column is occurring, leading to a wave formation. The constant velocity front flow is taking most of the flow time. Comparing to the sensitivity analysis to rheological parameters, performed in the 2D section, we observe here a similar sensitivity to aspect ratio a, but the effect is more pronounced as

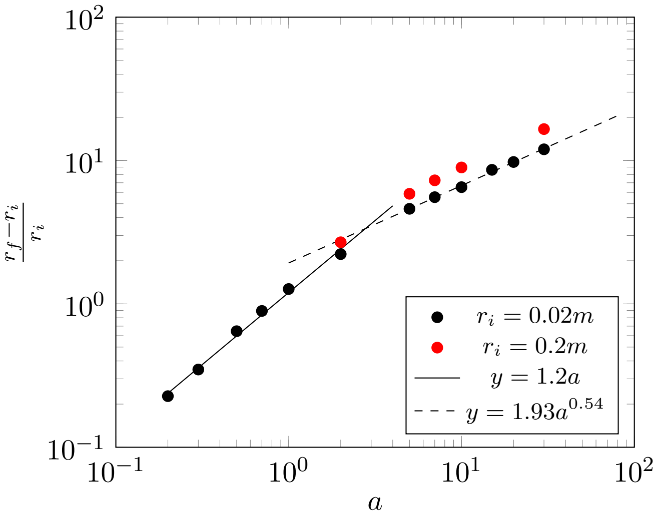

Figure 127: Dimensionless final run-out distance according to a after three-dimensional granular collapses and influence of h_i

geometry is more likely to vary than rheological parameters in experimental works. These results confirm that the $\mu(I)$ model can predict the nearly universal curve proposed in the experimental literature.

Moreover, figure 130 illustrates dimensionless run-out distance according to dimensionless time during granular collapses with different h_i and fixed a. It is shown that the granular dynamics for the two collapses are very close. To conclude this analysis, the granular dynamics is more dependent on a than h_i.

4.3.2.6 Conclusion

In this section, three-dimensional numerical simulations of granular collapses have been performed. As observed for two-dimensional collapses, granular flows exhibit two different dynamics, depending on a. For low a, dimensionless run-out distance follows a linear curve according to a, and for higher a, a power-law curve with exponent 0.5. In Lajeunesse *et al.*[61], the same flow regimes have been observed. Then, influence of rheology has been studied. As for two-dimensional collapses, the dominant parameter driving the granular flow is μ_S. Then, influence of initial column height has been studied. It has been observed a larger run-out distance for larger h_i, underlying the influence of the inertial regime on the spreading.

(a) $h_i = 0.2$m (b) $h_i = 2$m

Figure 128: Dense vs. inertial regimes region for time $t = \sqrt{h_i/g}$, plotted as I/I_0 for granular collapses with $a = 10$ and different h_i

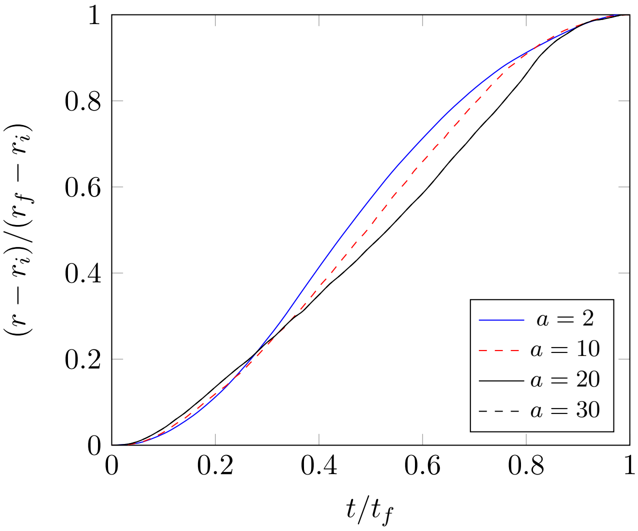

Figure 129: Dimensionless run-out distance according to dimensionless time during granular collapses with different a

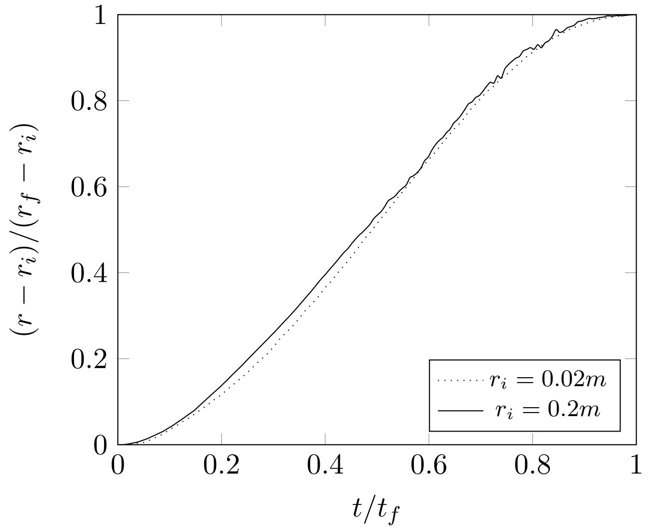

Figure 130: Dimensionless run-out distance according dimensionless time for columns spreading with different initial radius

4.3.3 Numerical studies for 3D granular chutes

During ingot casting process, it has been outlined that three methods are used in industry (figure 2) to initially place powder bags. The most investigated one consists in hanging powder bags by ropes in the mold. Thus, they burn due to high temperatures induced by the metal entering into the mold, leading to the powder chute. Consequently, we focus now on the dynamics of 3D granular chute dynamics (onto a solid and sticky substrate, at first).

Figure 131 illustrates the problem statement. We consider a granular column with initial height h_i and radius r_i, released from a height h_r. In this configuration, we define a new dimensionless number a_r, corresponding to the ratio between $h_i + h_r$ to r_i:

$$a_r = \frac{h_i + h_r}{r_i} \tag{4.21}$$

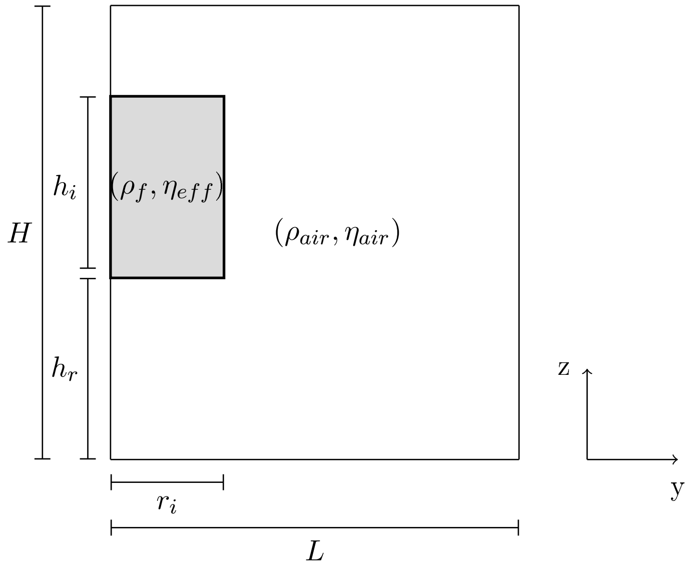

Figure 131: Problem statement of a granular chute from height h_r - Cut in the (y, z) plane

This flow problem is split into two parts. The first one consists of a free chute before impacting the bottom surface. The second one consists of the granular impact and spreading onto the solid substrate. During the chute, all the potential energy is transformed into kinetic energy, leading to the analytical computation of the velocity field. Therefore, the numerical resolution of the granular chute may be avoided, leading to the reduction of computational times. Thus, the purpose consists in transforming the problem into a granular spreading with imposed initial velocity v_{impact}:

$$v_{impact} = \sqrt{2gh_r} \tag{4.22}$$

Thus, the time of the granular chute is computed such as:

$$t_{chute} = \sqrt{\frac{2h_r}{g}} \tag{4.23}$$

Then, the new problem statement is shown in figure 132. No-slip boundary conditions are applied onto the bottom surface. Furthermore, symmetry conditions are applied onto (x, z) and (x, y) planes. Moreover, the computational domain is opened, leading to apply zero-pressure conditions in the other sides.

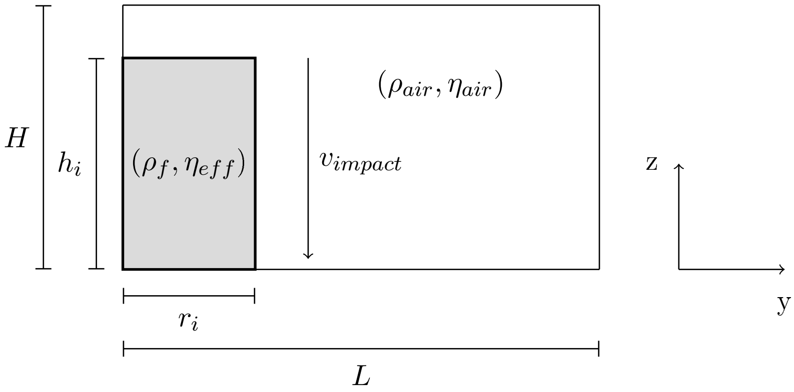

Figure 132: Problem statement of granular chutes from a collapse point of view

4.3.3.1 Run-out analysis

In this part, final run-out distances after granular chutes for the same rheological parameters as Jop *et al.*[2] are analyzed. Thus, several granular chutes with different a and a_r are performed, aiming to determine the dynamics of granular chutes. In the following numerical simulations, r_i is fixed to 2.5cm.

Curves illustrated in figure 133 show the dimensionless run-out of the flow according to a_r. The black curve represents the run-out distance after a granular collapse ($h_r = 0$, thus $a = a_r$). Moreover, colored curves are representing this dynamics for granular collapses with fixed a and several a_r.

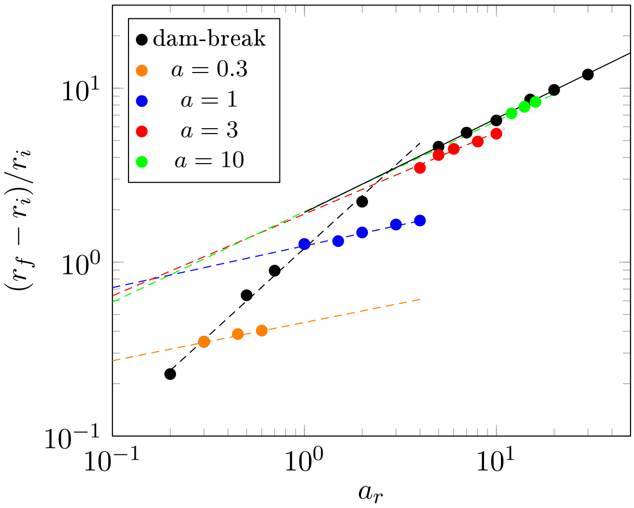

Figure 133: Dimensionless final run-out distance according to a_r, after granular chutes with different a

First, it is observed that for a given granular column aspect ratio a, the initial fall helps to spread further, as expected. Moreover, when a is large enough, the collapse power-law exponent tends to 0.54 (obtained in the previous section):

$$\frac{r_f - r_i}{r_i} = \begin{cases} 1.24 \cdot a_r^{0.24} & \text{for } a = 1 \\ 1.89 \cdot a_r^{0.47} & \text{for } a = 3 \\ 1.95 \cdot a_r^{0.52} & \text{for } a = 10 \end{cases} \tag{4.24}$$

Consequently, for large enough a, the dominant parameter to ensure a good spreading is a_r. For low aspect ratios, it is less useful to drop the granular material from a given height.

Now, the dynamics of granular chutes with fixed a_r and different a is analyzed: we performed four granular chutes with different h_i. Figure 134 illustrates the problem statement. The first case, illustrated in figure 134(a), corresponds to a granular collapse ($a_r = a$). In the other simulations, granular chutes with fixed a_r and different a are investigated. Moreover, r_i is fixed ($r_i = 2.5$ cm), inducing h_i and h_r to vary.

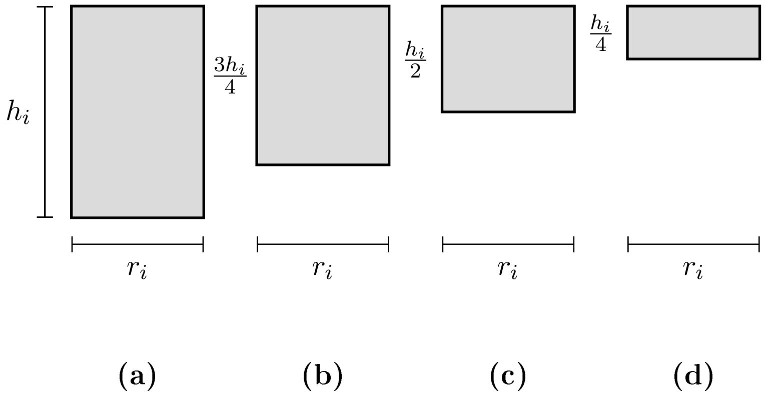

Figure 134: Study of influence of granular volume fraction for granular collapses with fixed a_r : (a) $a = 4$, (b) $a = 3$, (c) $a = 2$ and (d) $a = 1$

Figure 135 illustrates the dimensionless final run-out distance according to a after granular collapses with $a_r = 4$. It is observed that the run-out distance increases as a increases. However, if we now consider the covered surface (which is proportional to $r_f^2 - r_i^2$) with respect to the needed volume (proportional to ar_i^3) of granular material, we notice that it is more efficient to spread 1/4 of the volume ($a = 1$) from a sufficient height than to perform a dam-break of the initial volume ($a = 4$).

4.3.3.2 Energy analysis

In figure 136 an energy partition is computed for granular chutes with fixed $a = 4$ (which correspond to the "large enough" aspect ratio mentioned in the previous paragraph) and different a_r ($h_i = 10$cm and $r_i = 2.5$cm). We can see that the final dissipated energy is proportional to a_r, while the radius of the surface of spreading varies closely like $a_r^{0.5}$. We can then conclude that the surface of spreading varies nearly linearly with a_r, for large enough a.

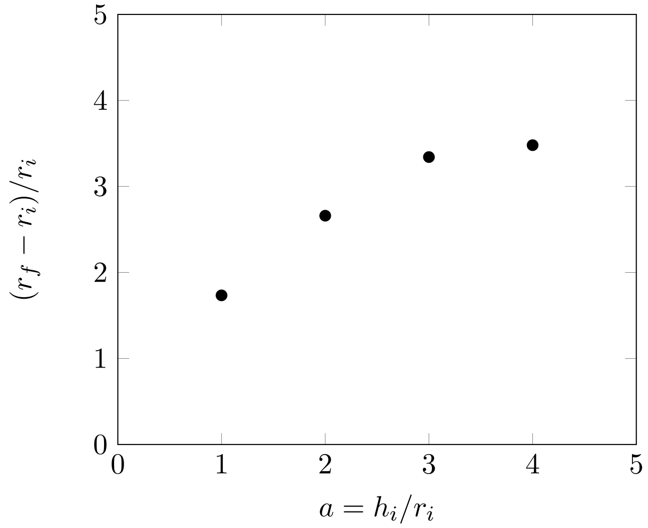

Figure 135: Dimensionless run-out of the flow according to $a = h_i/r_i$ for $a_r = 4$

In figure 137 an energy partition is computed for granular chutes with fixed $a_r = 4$ and different aspect ratios a ($r_i = 2.5$cm). We can see now that the final dissipated energy is approximately proportional to a, contrarily to the surface of spreading (see previous paragraph and figure 135 that saturates with a. This result confirms the previous one: to maximize the spreading, one needs to play on the height of the fall, for a large enough aspect ratio.

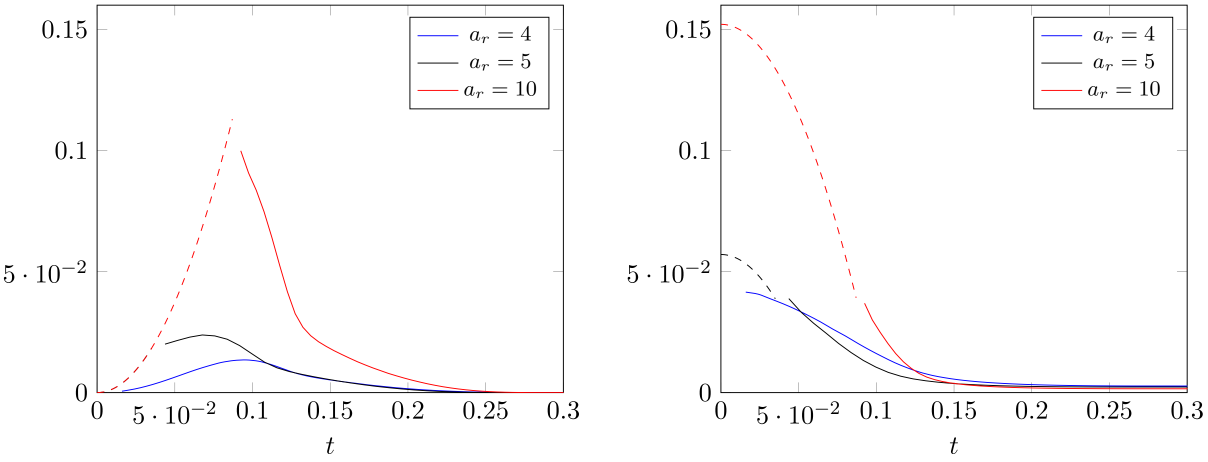

(a) Kinetic energy (b) Potential energy

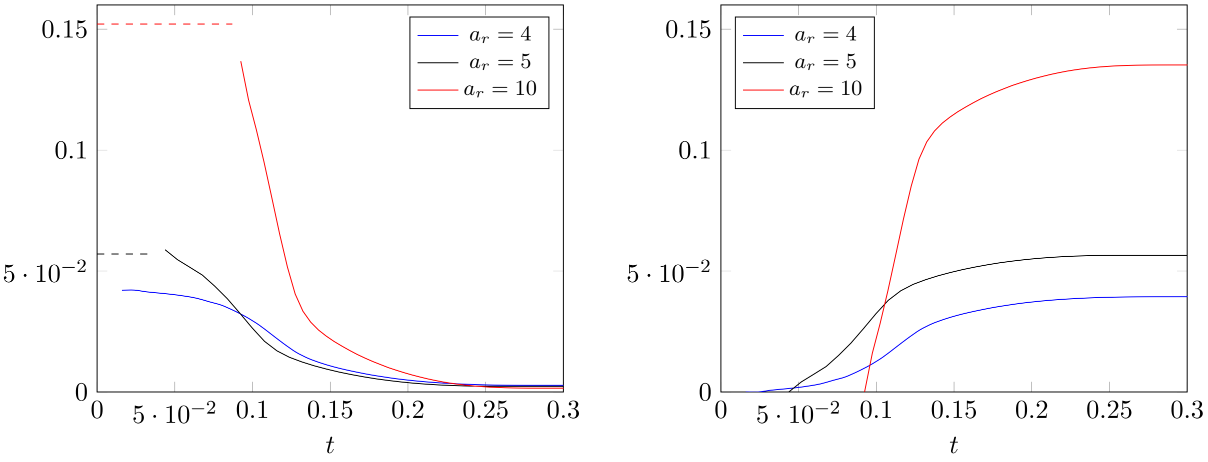

(c) Mechanical energy (d) Dissipated energy

Figure 136: Energy partition during granular chutes with $a = 4$ and different a_r

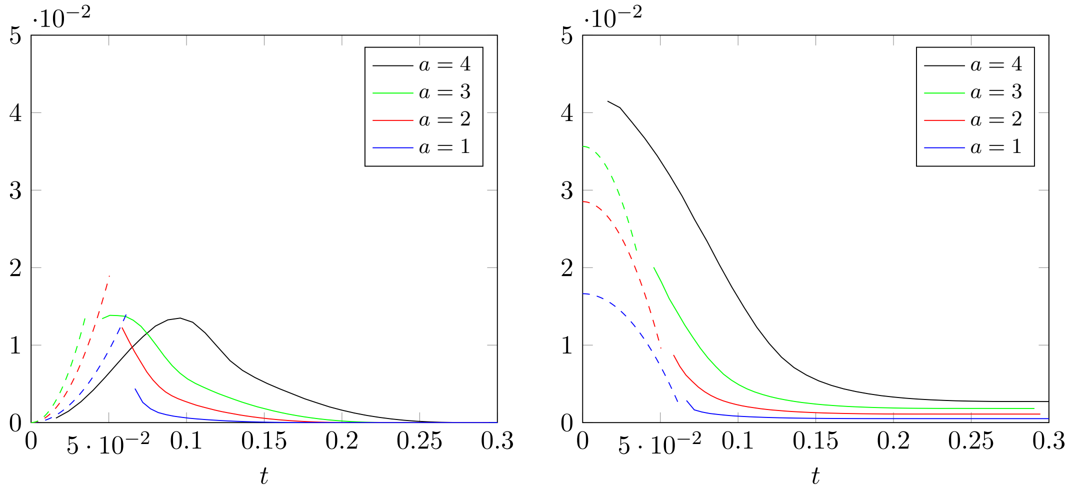

(a) Kinetic energy

(b) Potential energy

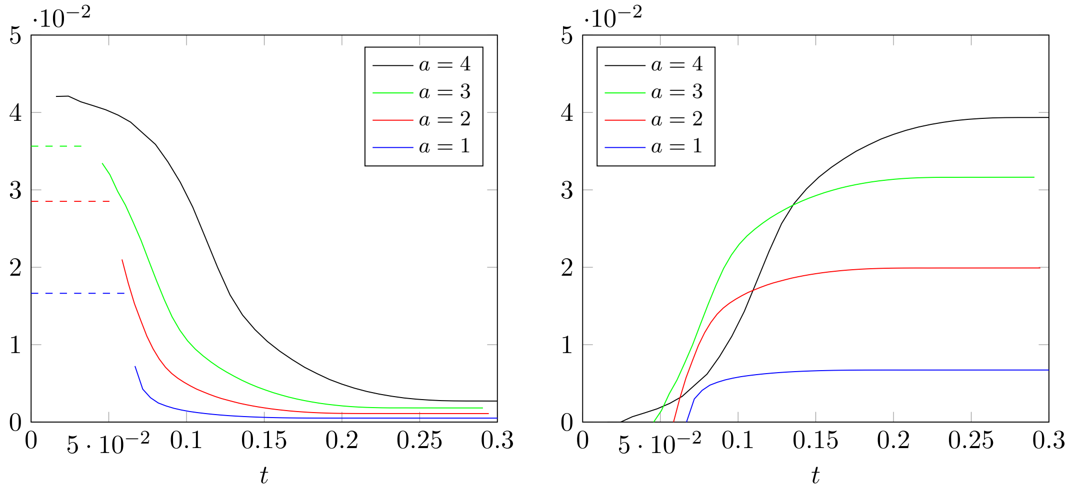

(c) Mechanical energy

(d) Dissipated energy

Figure 137: Energy partition during granular chutes with $a_r = 4$ and different a

4.4 Conclusion

This chapter aimed to validate the use of $\mu(I)$ rheology for describing granular flows. Thus, a new formulation, based on the finite element method, has been proposed. Momentum and mass equations have been solved and stabilized using VMS, and a Bercovier-Engelman regularization method has been used in order to take into account the granular behavior. This model has been validated onto granular collapses in two and three dimensions, by comparing with experimental works conducted by Lube *et al.*[64] and Lajeunesse *et al.*[61].

For two-dimensional granular collapses, it has been observed a good agreement with the results of Lagrée *et al.*[13]. Moreover, the influence of geometrical and rheological parameters on flow features has been discussed (μ_S, $\Delta\mu$, I_0 and a). Thus, it has been shown that the static friction coefficient μ_S corresponds to the most dominant rheological parameter for the flow dynamics. Moreover, we displayed the well-know curve representing the dimensionless position of the front according to the initial aspect ratio, and found the two different regimes evidenced by Lube *et al.*[64]: a linear one, and a power-law one with exponent 2/3.

In this chapter, we also performed new three-dimensional granular collapses. Different aspect ratios for the initial column have been considered and we found the two regimes evidenced by the experiments of Lajeunesse *et al.*[61]: a linear regime for very small aspect ratios and a power-law regime with exponent 1/2 for larger aspect ratios. We also proved that the $\mu(I)$ rheology is predictive with respect to the experimental work. We also underlined an additional aspect ratio effect: grain diameter vs. column height.

Finally, for some test cases, we provided a "rule of thumb" to maximize the surface of spreading for a falling granular column, using the $\mu(I)$ model.

f

Chapter 5

Industrial application: mold powder in ingot casting processes

Contents

Résumé en français

Ce chapitre est consacré à la validation du modèle basé sur la rhéologie $\mu(I)$, aux écoulements de poudres dans un contexte industriel, sans échanges thermiques.

Dans un premier temps, la dynamique des poudres industrielles est étudiée par la réalisation d'essais expérimentaux d'effondrement de colonnes ainsi que de chutes et étalements sur un substrat solide. Dans cette étude, deux poudres industrielles ont été sélectionnées par leurs différentes caractéristiques intrinsèques. La première, Thermotect M20-10, est une poudre noire très fine et cohésive. La seconde, G Izy-109, se présente sous forme de granulés marrons plus grossiers.

Tout d'abord, des essais d'effondrement de grains sur substrat solide sont menés. Le dispositif expétimental consiste en un tube cylindrique rempli de grains, que l'on soulève très rapidement. Le dispositif expérimental est tout d'abord validé sur des matériaux granulaires usuels (sucre, sable et polenta), et les distances parcourues observées ont été comparées avec celles de [61]. Ensuite, les essais sont reconduits sur des effondrements de colonnes des deux poudres industrielles sélectionnées. Il a été observé que la poudre G Izy-109 suit la même dynamique que les matériaux granulaires usuels. En effet, la distance parcourue adimensionnée suit bien une courbe loi de puissance pour de grands rapports d'aspect. En revanche, la poudre Thermotect M20-10 ne suit pas la même dynamique, due à une forte cohésion. Cependant, il est observé qu'au plus le rapport d'aspect de la colonne est grand, au plus la distance parcourue se rapproche d'une loi puissance, ce qui peut être expliqué par une énergie de cohésion négligeable devant l'énergie de chute de la colonne. Enfin, ces lois puissances sont retrouvées par la simulations numériques.

Ensuite, des essais de chute de colonnes de poudre ont été menés sur un substrat solide. Le nombre adimensionnel a_r est défini comme le rapport entre hauteur maximale de chute (somme entre hauteurs de lâcher et de la colonne) et du rayon initial de la colonne. Il a été montré que les effondrements de colonnes posées sur un substrat solide vont plus loin que si elles sont lâchées d'une certaine hauteur à même a_r.

La seconde partie de ce chapitre est consacrée à la simulation numérique de l'écoulement de poudre industrielle sur du métal en fusion statique, par l'utilisation du logiciel Thercast. Une formulation Level-Set permettant l'écoulement de trois fluides a été proposé. Plusieurs analyses ont été menées et ont conduit à des premières pistes pour l'optimisation du procédé.

Dans un premier temps, nous avons comparé l'influence de la couche de métal sur l'étalement. Ainsi, moins d'energie sera dissipée si le moule est faiblement rempli, ce qui entraînera un meilleur étalement.

Enfin, l'écoulement de la poudre aux parois du moule est également étudié. Ainsi, il est observé un meilleur recouvrement de la surface du métal après l'impact de la poudre aux parois. En effet, celles-ci vont pousser la poudre sur les côtés, et ainsi permettre le recouvrement près des coins du moule.

Finalement, l'influence du nombre de sacs de poudre a été analysé. Pour un volume de poudre donné, il a été observé un meilleur recouvrement de la surface du métal si un seul sac de poudre est dispoé dans le moule.

5.1 Introduction

In the previous chapter, we focused on the numerical simulation of granular collapses and validated the proposed model with benchmarks from the literature. Now, the purpose consists in proposing a few test cases on industrial applications. Thus, collapses and chutes of industrial powders onto liquid metal will be performed and analyzed.

Before studying the flow of metal in ingot casting process, powders are conditioned into bags, placed in the mold according to several ways. Thus, they may be deposited at the bottom surface, raised onto a cardboard box, or hanged with ropes at different levels of the mold (figure 2).

The hot liquid metal is then filling the mold, leading to burn the bags due to the high temperatures involved, and allowing the powder to spread onto the metal ingot surface.

This chapter deals with industrial applications involving industrial powder flows, without thermal fluxes. The $\mu(I)$ rheology is adopted.

First, experimental and numerical powder collapses are performed, then, the use of a static liquid metal substrate is considered. Finally, the influence of number of bags, dispositions and shapes, but also the effects of lateral walls of the mold will be discussed.

5.2 Industrial powder collapse

In this section, a preliminary work consists in validating the $\mu(I)$ rheology for the dynamics of industrial powders.

Thus, three-dimensional experimental powder collapses are performed. Then, the obtained results are compared with the results of Lajeunesse *et al.*[61]. Finally, numerical collapses are performed in order to validate the model for industrial powder flows, and a sensitivity analysis to rheological parameters is then conducted.

5.2.1 Experimental collapses

5.2.1.1 Methods

Granular collapses

The experimental set-up used to perform granular collapses is illustrated in figure 138: a polyvinyl chloride (PVC) cylindrical tube, with height h_i and radius r_i, is disposed onto a plane surface. The granular material is allowed to spread thanks to the removal of the tube in the fastest possible way (in order to reduce its impact on the flow dynamics).

Granular chutes

The experimental set-up used to perform granular chutes is illustrated in figure 139. Now, the PVC tube is linked to a stand, and placed at a height h_r from the bottom surface. The granular material is blocked with a solid plug, placed under the tube. Then, the fall and spreading are triggered by removing the plug in the fastest possible way.

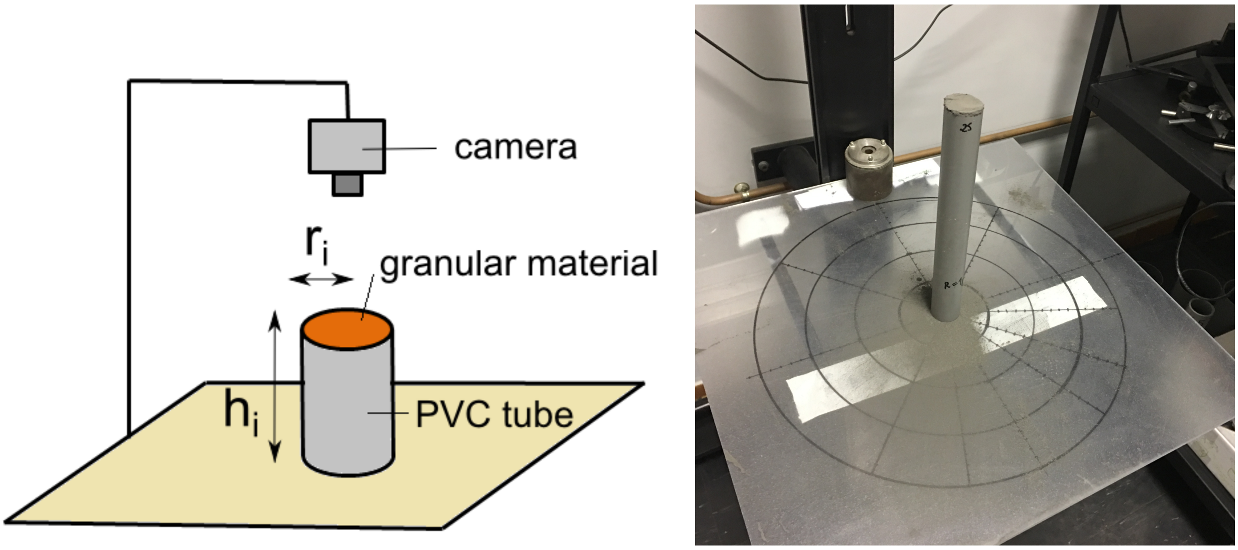

(a) (b)

Figure 138: Experimental setup for granular collapse experiments

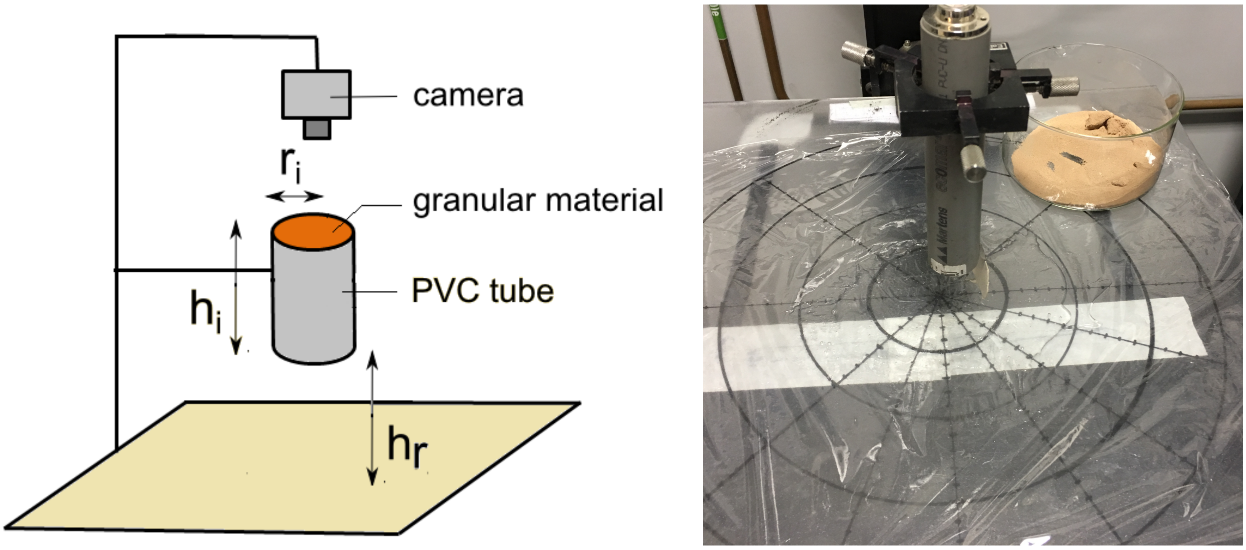

(a) (b)

Figure 139: Experimental setup for granular chute experiments

The final front position is determined by taking a picture of the final deposit from the top, and then, by offsetting it with the ImageJ software in order to neglect grains dispersion. Final run-out distance is computed as: $r = \sqrt{S\,\pi}$, where S is the surface computed using ImageJ.

5.2.1.2 Granular materials

Usual granular materials

First, the experimental setup is validated with collapses onto a solid substrate with usual granular materials (polenta, sugar and sand). Then, the obtained results are compared with the ones of Lajeunesse *et al.*[61].

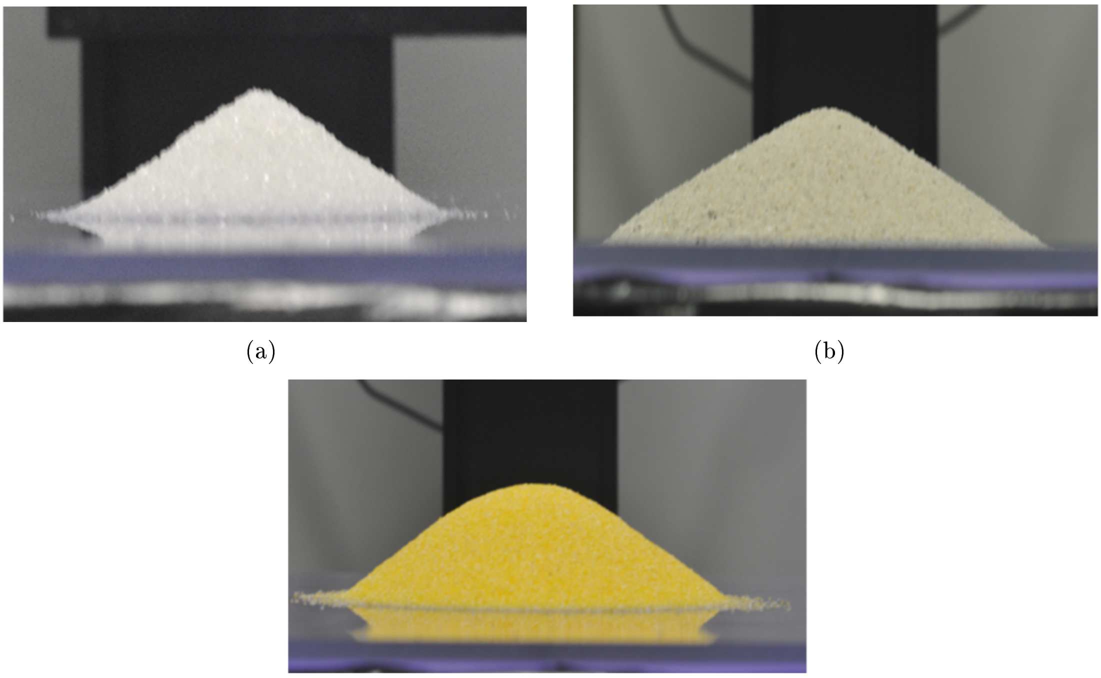

(a)

(b)

(c)

Figure 140: Deposit profiles of sugar, sand and polenta

Repose angles and static friction coefficients of the different materials, obtained using a static pile, are given in table 2.

	Repose angle	static friction coefficient
Sugar	$26\ ^{o}$	0.43
Sand	$29\ ^{o}$	0.47
Polenta	$33.5\ ^{o}$	0.53

Table 2: Repose angles and static friction coefficients of sugar, sand and polenta

Industrial powders

Two industrial powders, with different internal properties, have been selected. The first material is a black powder, called "Thermotect M20-10", which is mostly composed of silicon (SiO_2), alumina (Al_2O_3) and carbon (more than 20%) . The second one, called "G-Izy 109", consists of a brown granular material, and is mostly composed of SiO_2, CaO and Al_2O_3. Rheological features of these powders are summarized in table 3.

	Thermotect M20-10	G-Izy 109
Repose angle	36^o	29^o
Static friction coefficient μ_S	0.73	0.55
Mean diameter d	$3.2 \cdot 10^{-5}$	$2 \cdot 10^{-4}$
Apparent density ρ	625	550

Table 3: Rheological features of Thermotect M20-10 and G-Izy 109

5.2.1.3 Estimation of run-out distance

Collapses

As mentioned before, the experimental set-up is first validated with usual granular collapses, and the obtained results are compared with the ones of Lajeunesse *et al.*[61]. Sugar, polenta and sand are considered and several collapses with different aspect ratios a are conducted. The obtained dimensionless run-out distances according to a are illustrated in figure 141. For the several granular collapses, the two regimes are observed. For polenta and sand (materials with the larger μ_S), the exponents corresponding to the two regimes are found very close from the ones shown in [61]. For sugar (material with the lower μ_S), the exponent obtained for the power-law curve is larger (figure 141.a) than the ones obtained for sand and polenta (figures 141.b and 141.c). Thus, two regimes are observed, but the exponent of the power-law curve seems to depend on μ_S, as it decreases for large values. In the future, it would be interesting to study the influence of granular rheology onto the dynamics for large a.

As introduced in the previous chapter (figure 76), the theoretical dimensionless run-out distance may be obtained with the critical aspect ratio, as a conic deposit is obtained. In figures 141.a, 141.b and 141.c, it is observed that theoretical critical run-out distance (equation 4.3) is lower than the one obtained in experimental works.

Figure 141.d illustrates numerical collapse simulations of sand, sugar and polenta obtained using the identified μ_S and arbitrary values for I_0 and $\Delta\mu$ (taken from Jop *et al.*). The influence of μ_S outlined in the previous chapter, is observed, as the run-out distance is larger for low μ_S. By comparing these results with the experimental ones, several differences are observed. Indeed, a larger run-out distance for the polenta is noticed in our experiments, which is not conform with μ_S values. This difference may be explained by some uncertainties in our experimental protocol, confirming the global results of Lube *et al.*, Lajeunesse *et al.*and other papers.

In conclusion, experimental work conducted with sugar, polenta and sand, show the same dynamics as the one observed in the literature, which validates the investigated setup for the study of industrial powder collapses and chute.

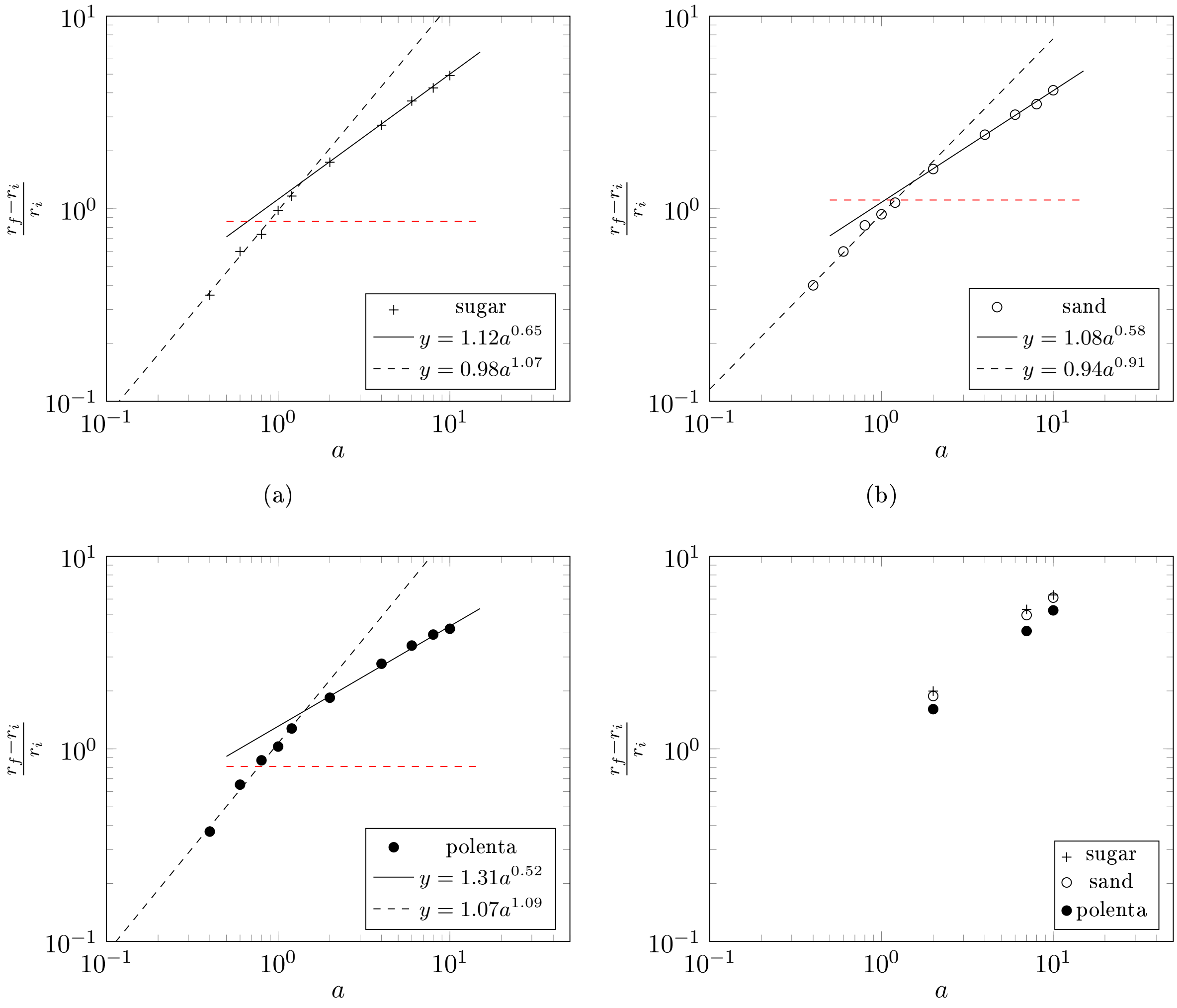

(a) (b) (c) (d)

Figure 141: Run-out distance obtained for experimental and numerical granular collapses, and by considering different granular materials: (a) Sugar collapses ; (b) Sand collapses ; (c) Polenta collapses ; (d) Numerical results

Now, industrial powder collapses are performed and studied. As mentioned previously, two industrial powders have been chosen for these experiments.

First, the spreading of the coarsest industrial powder, called G-IZY 109, is investigated. The results, illustrated in figure 142, show the same dynamics as for usual granular experiments, with the appearance of the power-law regime (with exponent 0.54) at large a.

Then, the spreading of the finest one, called Thermotect M20-10, is carried out, and figure 142 shows the granular dynamics. It is observed that the dimensionless run-out approaches the power-law regime only for large a. Indeed, the material exhibits several heterogeneities at low a. This result is explained by the small size of the grains (order of ten microns), that should induce non negligible cohesion. Thus, we may assume the existence of another yield, which changes the powder dynamics, where cohesion dominates. Large aspect ratio collapses imply larger potential energy, that may overcome the cohesion energy, which tends to a final run-out close to the dry granular theoretical curve.

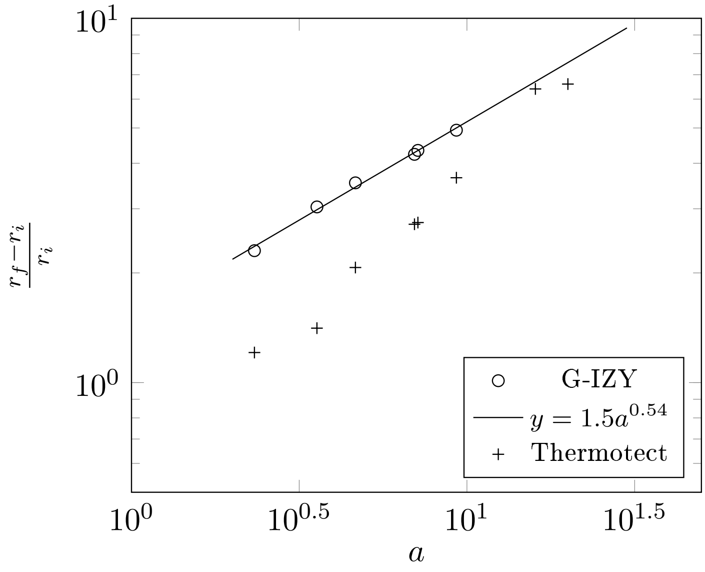

Figure 142: Dimensionless run-out distance according to the aspect ratio, obtained with industrial powders collapse

Figure 143 compares the experimental dimensionless run-out distance of Thermotect M20-10 with the numerical one. In the numerical simulations (where μ_S was identified previously and arbitrary values for I_0 and $\Delta\mu$ were taken from Jop *et al.*), the power-law regime is observed, with a larger exponent 0.6. For low a, the numerical curve does not fit the experimental data. However, the same observation as done before is verified, and the experimental run-out distances are in agreement with the numerical curve for large a.

Figure 144 compares dimensionless run-out distances of experimental G-Izy collapses with the numerical results. A good agreement between the two methods are found for large a.

In conclusion, granular collapses with the two industrial powders show different dynamics. For the coarsest powder (G-Izy 109), the observed dynamics is the same as for dry granular materials. However, the one observed for the finest powder (Thermotect M20-10) is different for low a, and is due to a larger cohesion. Moreover, the results obtained with the numerical simulations are relevant as experimental run-out distances

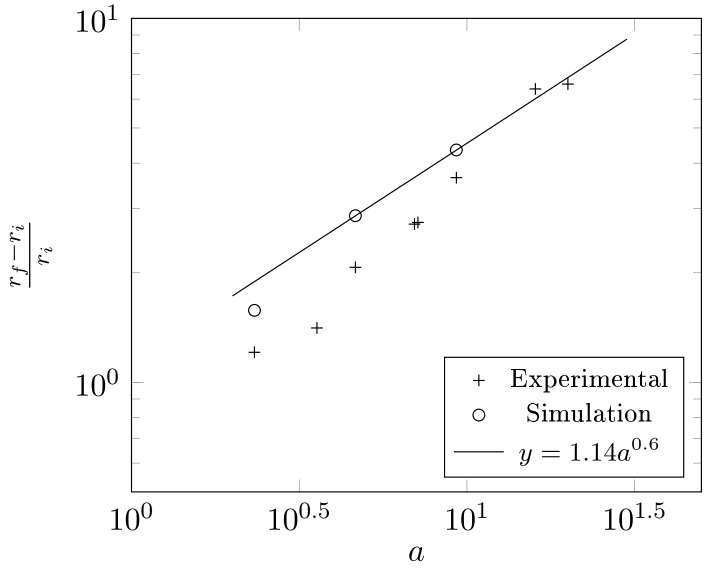

Figure 143: Dimensionless run-out distance according to a after a Thermotect collapse and comparison with numerical simulation

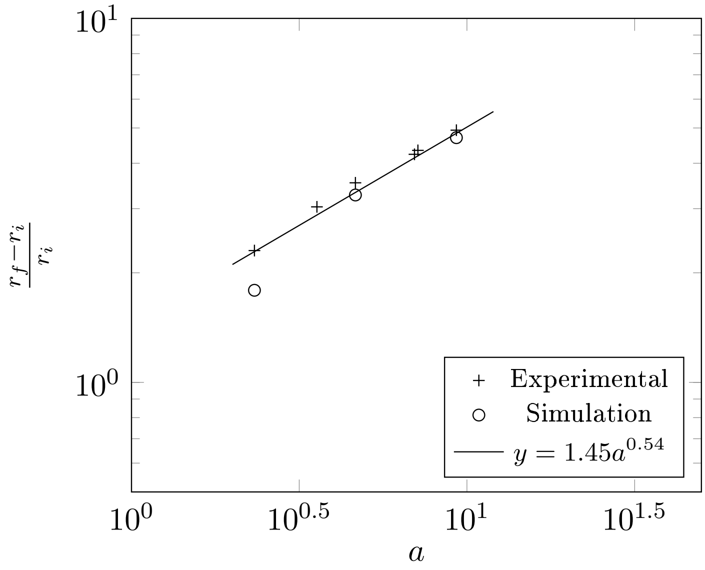

Figure 144: Dimensionless run-out distance according to a after a Gizy collapse and comparison with numerical simulation

obtained for large a fits the curves. Thus, the $\mu(I)$ rheology is validated for describing industrial powder collapses. However, further studies must be conducted in order to take into account cohesion.

Powder chutes

Now, the purpose consists in determining industrial powder chute dynamics onto a solid substrate. We recall the dimensionless number a_r, defined in the previous chapter, and corresponding to the ratio between $h_i + h_r$ and r_i:

$$a_r = \frac{h_i + h_r}{r_i} \tag{5.1}$$

First, experimental industrial chutes are investigated by using G-Izy powder (deposit shape illustrated in figure 145). Figure 146.a shows dimensionless run-out distance according to a_r, and for several a. First, it is observed that the global behaviour is consistent with our previous theoretical conclusions using the $\mu(I)$ model: the spreading behaves as a power-law for sufficiently large aspect ratio, increasing up to the collapse curve for a given a_r. For chute experiments, we notice that large aspect ratios $a = 8$ and $a = 10$ do not discriminate significantly for large a_r, which should be due to a dispersion in our experimental protocol.

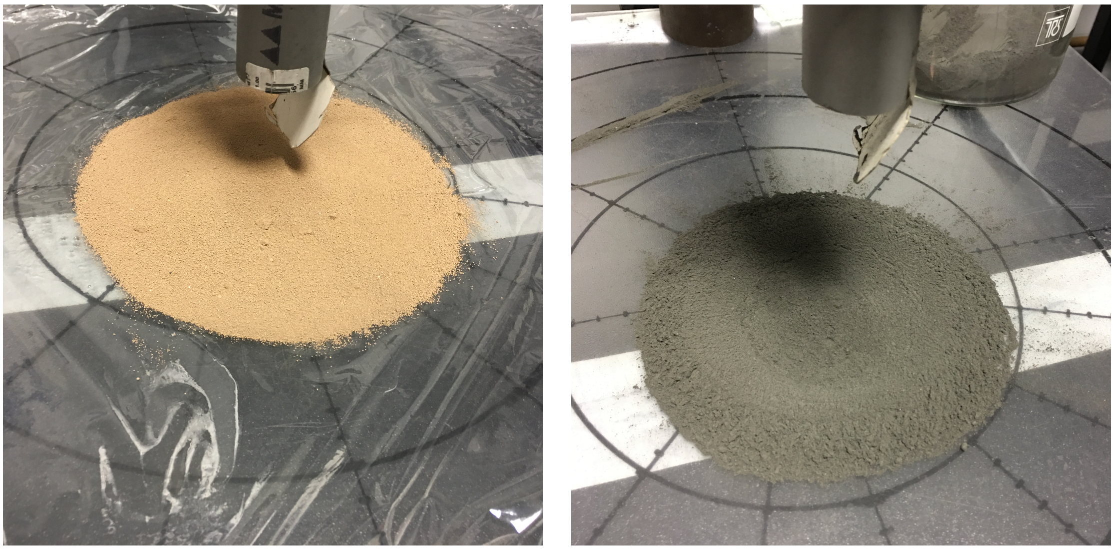

(a) G-Izy 109

(b) Thermotect M20-10

Figure 145: Deposit shape after granular chutes of industrial powders

Then, the influence of the bottom substrate is studied. Thus, a sticky substrate is created with a polyethylene film covered by a silicone layer. Figure 146.b compares the dimensionless-run-out distance after the chute of a G-Izy column, by considering different substrate. It is shown that the basal friction of the substrate has a slight influence on the run-out distance of the flow.

Then, the same experiments have been conducted with the Thermotect powder. The same observations as done with G-Izy powder are made.

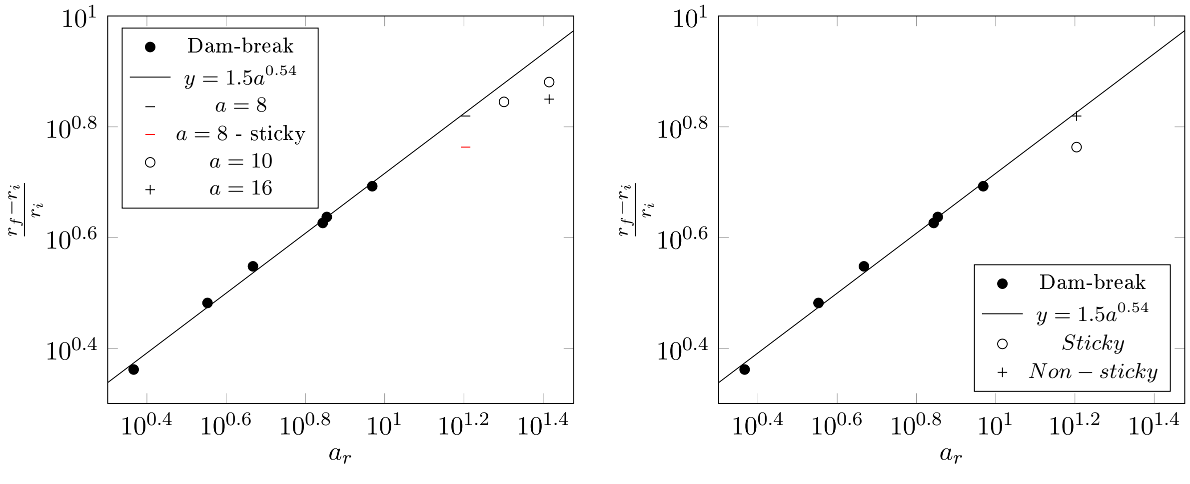

(a) (b)

Figure 146: Dimensionless run-out distance according to a_r, obtained after G-izy column chute and spreading: (a) Influence of a ; (b) Effect of the kind of substrate for a column chute with $a = 8$

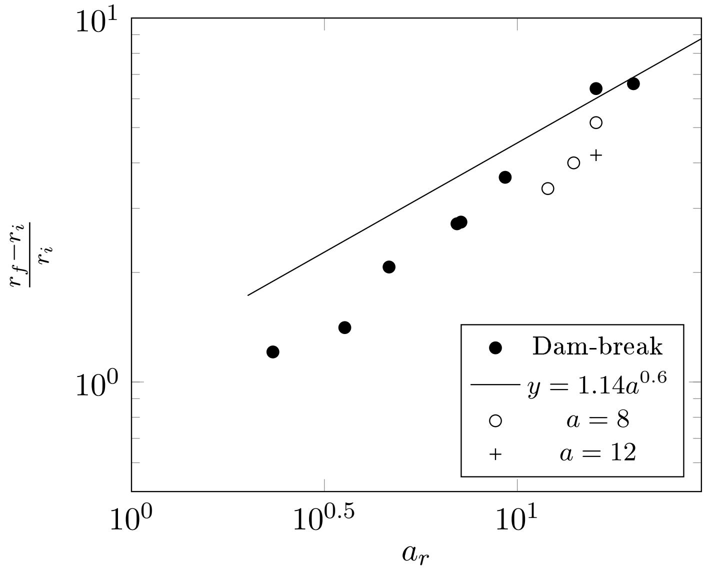

Figure 147: Dimensionless run-out distance according to a_r, obtained for Thermotect M20-10 chutes

5.2.2 Numerical simulations of powder chute

Finally, figure 148 compares dimensionless run-out after a G-Izy chute between experiments and numerical simulations. We can observe that a reasonable agreement is obtained for most of the cases.

In conclusion, the purpose of this section was to extend the $\mu(I)$ rheology to industrial powder flows. Thus, experimental powder collapses and chutes have been conducted to analyze the flow dynamics. Then,

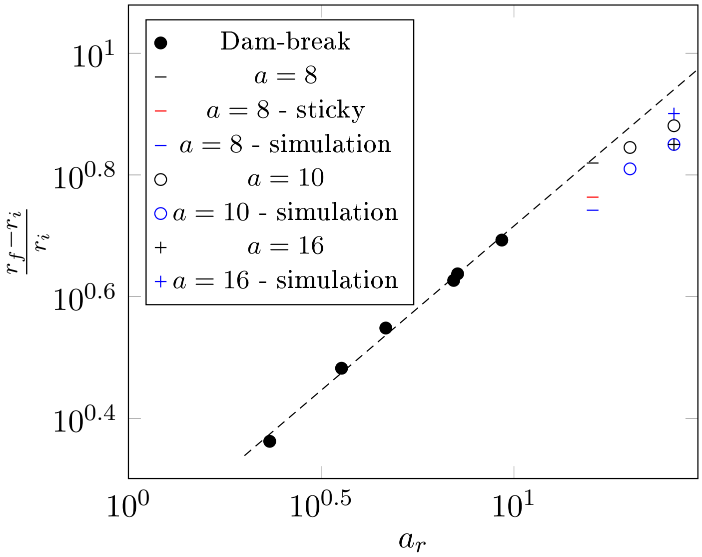

Figure 148: Dimensionless run-out distance according to a_r, obtained after G-izy chute simulations

numerical simulations have been performed using a $\mu(I)$ rheology, which confirm the dominant role of μ_s on the dynamics and a second order influence of other parameters.

5.3 Numerical simulation of powder flow onto molten metal

During this thesis, the proposed model for the simulation of granular flows has been implemented by Transvalor into the Thercast software, aiming to model casting processes. Now, we propose to simulate granular flows onto liquid metal by using this software, and to discuss on the influence of several industrial features, such as wall effects, liquid metal layer, or number of bags.

5.3.1 Problem statement

The problem statement of the powder chute onto liquid metal is illustrated in figure 149. A mold, with height H_i and radius R_i, is filled with liquid metal at height h_m from the bottom. A powder cylindrical bag, with volume V_b, is placed at a height h_r from the molten metal. In the simulations, no-slip boundary conditions are assumed on the mold walls.

Finally, density and viscosity of the liquid metal are set respectively to $\rho_m = 7 \cdot 10^3 \ kg \cdot m^{-3}$ and $\eta_m = 10^{-2} \ Pa \cdot s$.

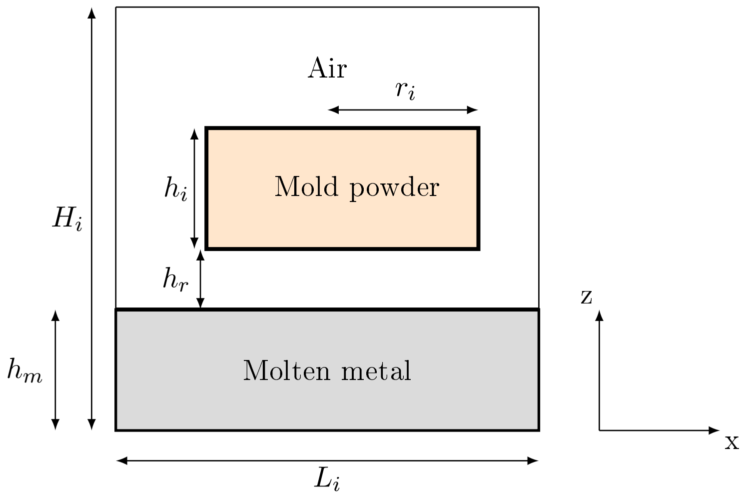

Figure 149: Problem statement of powder flow onto liquid metal

5.3.2 Three materials flow

5.3.2.1 Problem statement

As shown in figure 149, three fluids are flowing. Therefore, the simulation of the full process requires the resolution of a flow that takes them into account. Thus, the Level-Set formulation introduced in chapter 2 must be extended.

Figure 150 illustrates a three-fluids flow problem. Fluids 1, 2 and 3 cover respectively computational domains Ω_1, Ω_2 and Ω_3, localized in the Ω domain. Each fluid has its own features, denoted respectively as ρ_1, ρ_2, ρ_3 for the density, and η_1, η_2, η_3 for the viscosity. Then, two interfaces are defined: Γ_{13} and Γ_{23}.

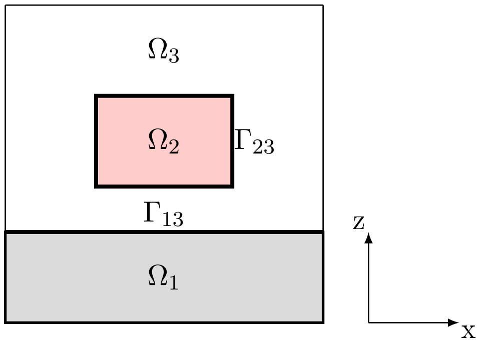

Figure 150: Computational domain of a three-fluids flow problem

5.3.2.2 Interfaces capturing

Then, we need to capture the two interfaces Γ_{23} and Γ_{13} . Thus, two Level-Set functions α_{23} and α_{13} are defined and correspond to the signed distance function to the corresponding interface.

Therefore, two following Level-Set functions are defined such that:

$$\alpha_{23}(x) = \left\{ \begin{array}{lll} & d(x,\Gamma_{23}) & ,x \in \Omega_2 \\ - & d(x,\Gamma_{23}) & ,x \in \Omega_3 \cup \Omega_1 \\ & 0 & ,x \in \Gamma_{23} \end{array} \right. \tag{5.2}$$

and

$$\alpha_{13}(x) = \left\{ \begin{array}{lll} & d(x,\Gamma_{13}) & ,x \in \Omega_1 \\ - & d(x,\Gamma_{13}) & ,x \in \Omega_2 \cup \Omega_3 \\ & 0 & ,x \in \Gamma_{13} \end{array} \right. \tag{5.3}$$

5.3.2.3 Mixing laws for physical properties

First, we need to take into account the fluid properties onto the computational domain. In this configuration, two mixing steps are performed. In a first time, the purpose consists in mixing fluid 2 and 3 properties by using a Heaviside function $H_{23}(x)$, and leading to the mixing density ρ_{23} and viscosity η_{23}:

$$\left\{ \begin{array}{l} \rho_{23} = \rho_2 H_{23}(x) + \rho_3 \left(1 - H_{23}(x)\right) \\ \eta_{23} = \eta_2 H_{23}(x) + \eta_3 \left(1 - H_{23}(x)\right) \end{array} \right. \tag{5.4}$$

with $H_{23}(x)$ defined such as:

$$H_{23}(x) = \left\{ \begin{array}{ll} 1 & \text{if } x \in \Omega_2 \\ 0 & \text{if } x \in \Omega_3 \end{array} \right. \tag{5.5}$$

Then, density ρ_{23} and viscosity η_{23}, are mixed with the properties of fluid 1 (ρ_1, η_1) by the use of an other Heaviside function $H(x)$, defined such as:

$$H(x) = \left\{ \begin{array}{ll} 1 & \text{if } x \in \Omega_1 \\ 0 & \text{if } x \in \Omega_2 \cap \Omega_3 \end{array} \right. \tag{5.6}$$

leading finally to the final density ρ and viscosity η:

$$\left\{ \begin{array}{l} \rho = \rho_1 H(x) + \rho_{23} \left(1 - H(x)\right) \\ \eta = \eta_1 H(x) + \eta_{23} \left(1 - H(x)\right) \end{array} \right. \tag{5.7}$$

5.3.2.4 Interfaces tracking

Then, we need to compute the two interfaces during the simulation. The same procedure as for a two fluid flows is performed. First, the two Level-Set functions are filtered in the vicinity of the interface, and are now denoted as $\hat{\alpha}_{23}$ and $\hat{\alpha}_{13}$. Finally, two convective auto-reinitialization equations are solved in order to ensure the transport of the two filtered Level-Set functions. By defining α such as the vector $(\alpha_{23}, \alpha_{13})$ containing the two Level-Set functions, the transport of the Level-Set functions leads to the resolution of the following system:

$$\frac{\partial \hat{\alpha}}{\partial t} + (v + \lambda U).\nabla \hat{\alpha} = \lambda s(\hat{\alpha}) \cdot \left(1 - \left(\frac{\hat{\alpha}}{E}\right)^2\right) \tag{5.8}$$

5.3.3 Discussion on the liquid metal layer

In this part, the influence of liquid metal height is studied. Figure 151 illustrates problem statements of the two considered benchmarks. A powder cylinder with height $h_i = 25$cm and radius $r_i = 5$cm is placed at $h_r = 25$cm from the metal surface.

First, the liquid metal height is chosen sufficiently large in order that the perturbation of the liquid substrate does not reach the bottom of the mold, and thus, $h_m = 15$cm (figure 151). Finally, the length of the mold are taken very large in order that the powder never reaches it.

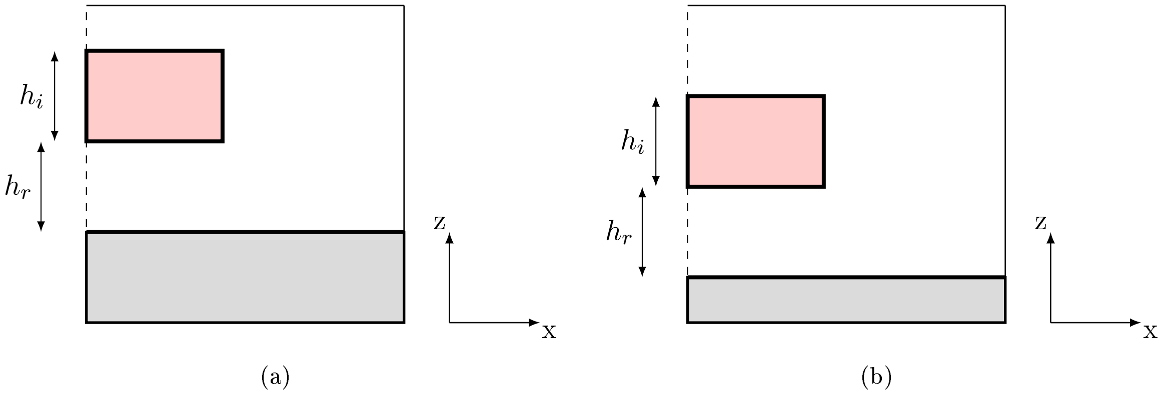

Figure 151: Spreading onto liquid metal and analysis of its height

Figure 152 illustrates the powder flow onto liquid metal at several instants. Before $t = 0.3$, the powder chute is observed. Then, the impact velocity onto the metal layer leads to the creation of a crater. Finally, the powder stops with $r_f \approx 30.8$cm.

Then, a thinner layer of liquid metal is considered ($h_m = 2$ cm), as shown on figure 151.b . Moreover, we recall that h_r and h_i are taken as in the previous case. Figure 153 shows the powder spreading at several instants. In this configuration, the crater formed by the impact is less deep, probably due to a lower dissipation in the liquid metal. Moreover, the run-out distance is larger: $r_f \approx 31.7$cm.

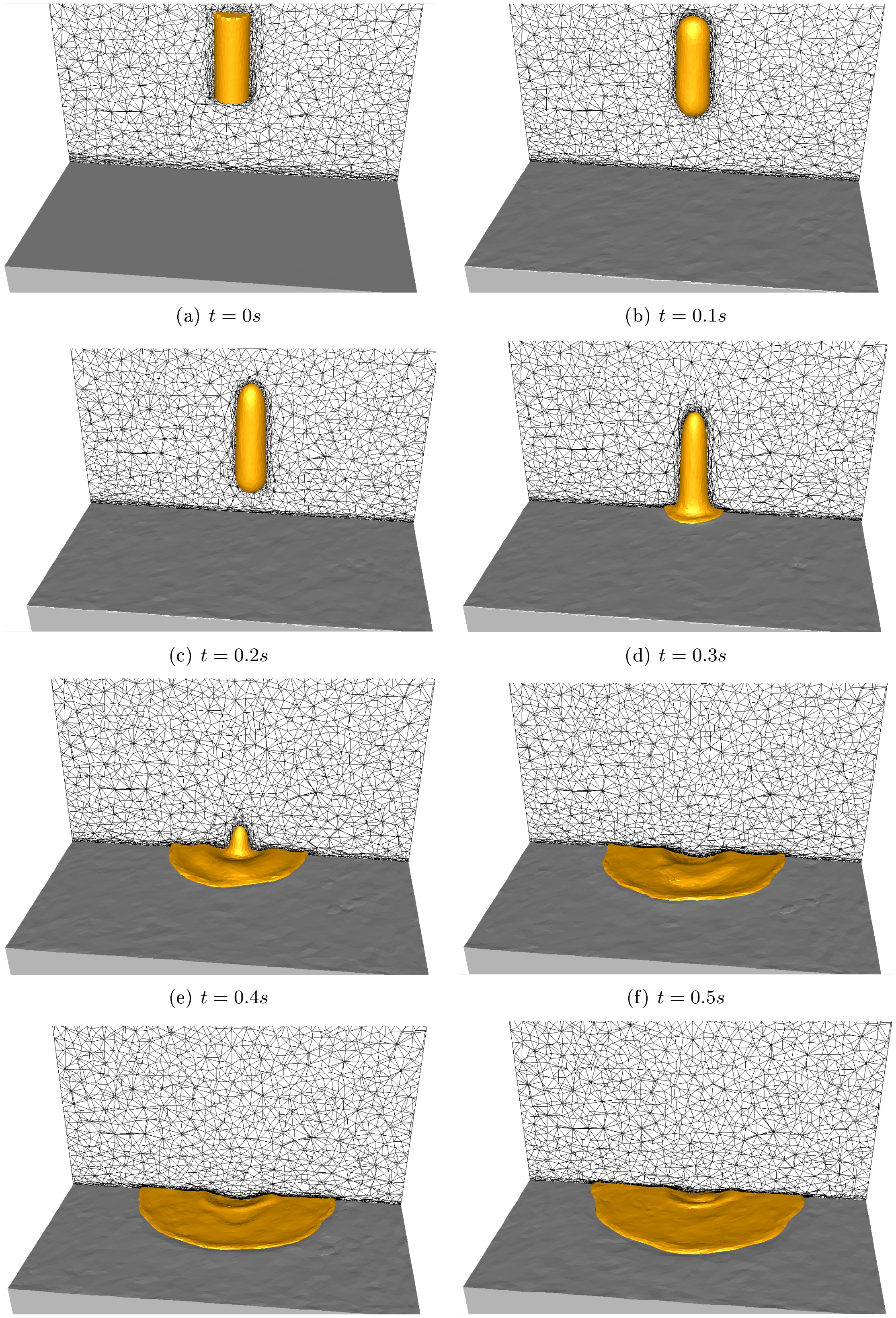

(a) $t = 0s$

(b) $t = 0.1s$

(c) $t = 0.2s$

(d) $t = 0.3s$

(e) $t = 0.4s$

(f) $t = 0.5s$

(g) $t = 0.6s$

(h) $t = 0.7s$

Figure 152: Chute and spreading of a G-Izy column onto liquid metal

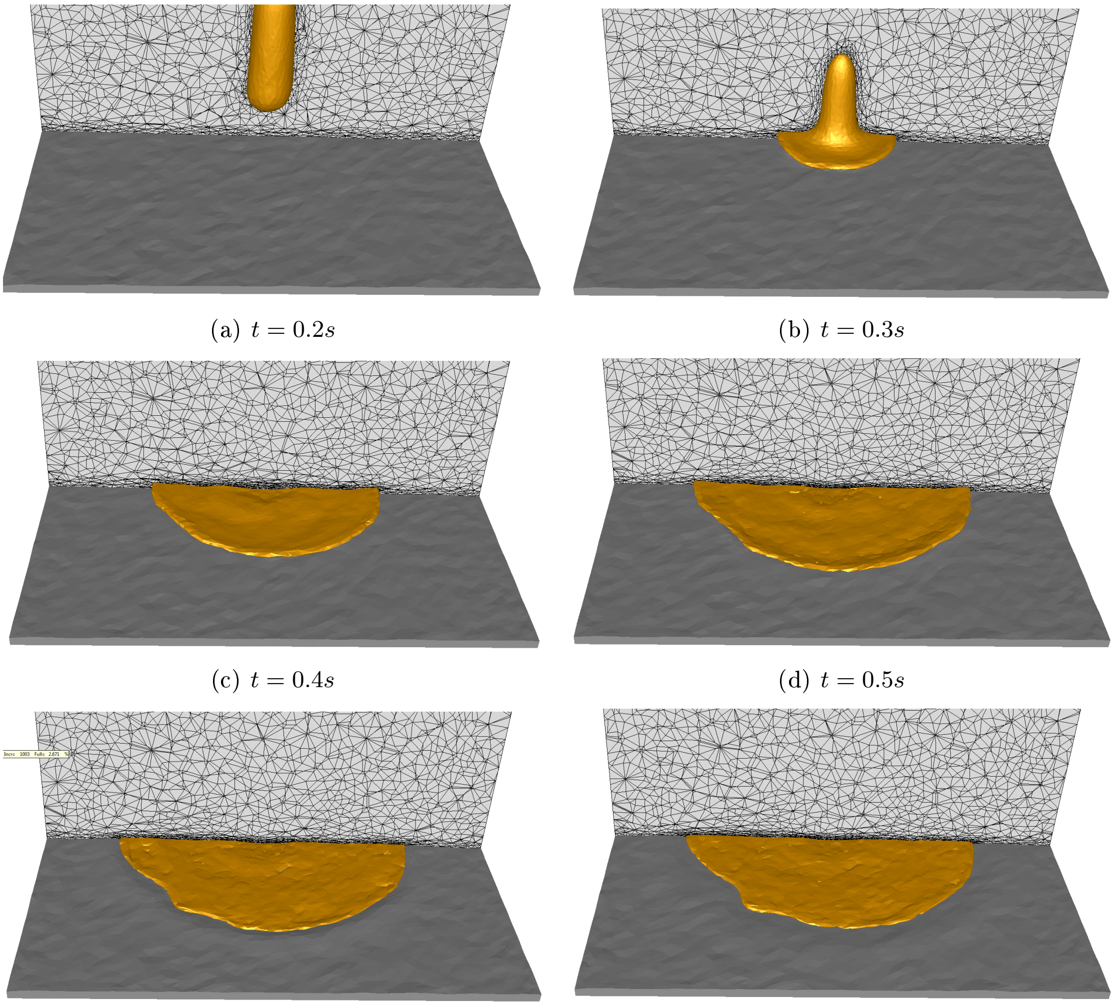

(a) $t = 0.2s$

(b) $t = 0.3s$

(c) $t = 0.4s$

(d) $t = 0.5s$

(e) $t = 0.6s$

(f) $t = 0.7s$

Figure 153: Chute and spreading of a G-Izy column onto a thin layer of liquid metal

5.3.4 Walls effects

Now, we analyze the effects of the mold walls onto the powder spreading. We consider now a cylindrical powder bag with aspect ratio equal to 5 ($r_i = 5$ cm and $h_i = 25$ cm, thus, $V_b = 1.96$ L). Furthermore, the mold is assumed to be filled at 15 cm from the bottom. The bag chutes at a height $h_r = 25$ cm from the metal surface, as for the previous numerical simulations.

The configuration of this study is built by using the results obtained in the previous simulation (with $h_m = 15$ cm). Indeed, the purpose consists in taking adequate mold lengths for the analysis of walls influence. Thus, the circumscribe square of the circle with radius $r_f = 30.8$ cm is traced, leading to the computation of half of its diagonal value $r_c = 0.523$. Finally, we compute $R_i = (r_c + r_f)/2$, as shown on figure 154. The circumscribe square (in red) to the circle of radius R_i corresponds to the basis geometry of the considered mold. Thus, $L_i = 52.3$cm.

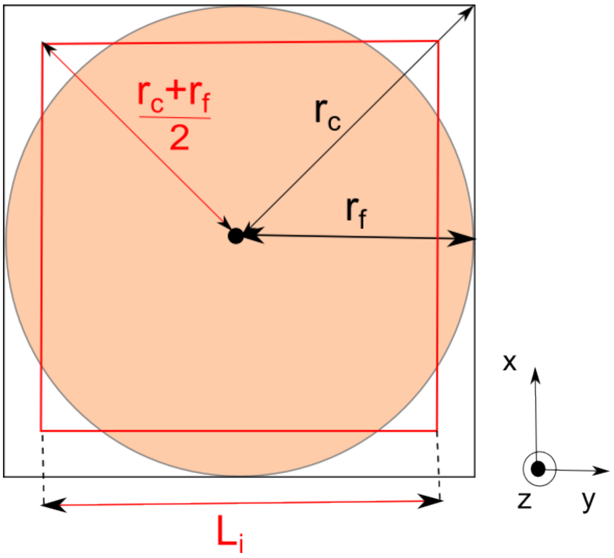

Figure 154: Computation of the mold dimensions for the analysis of wall effects

Figure 155 illustrates the powder front moving onto the liquid metal at several instants. After impacting the wall, the powder moves in the wall direction, and finishes to cover entirely the metal surface. At $t = 0.65$s, the powder is very close to reach wall corners, as figure 155.f illustrates, as the liquid substrate drags the front powder flow up to the mold corners.

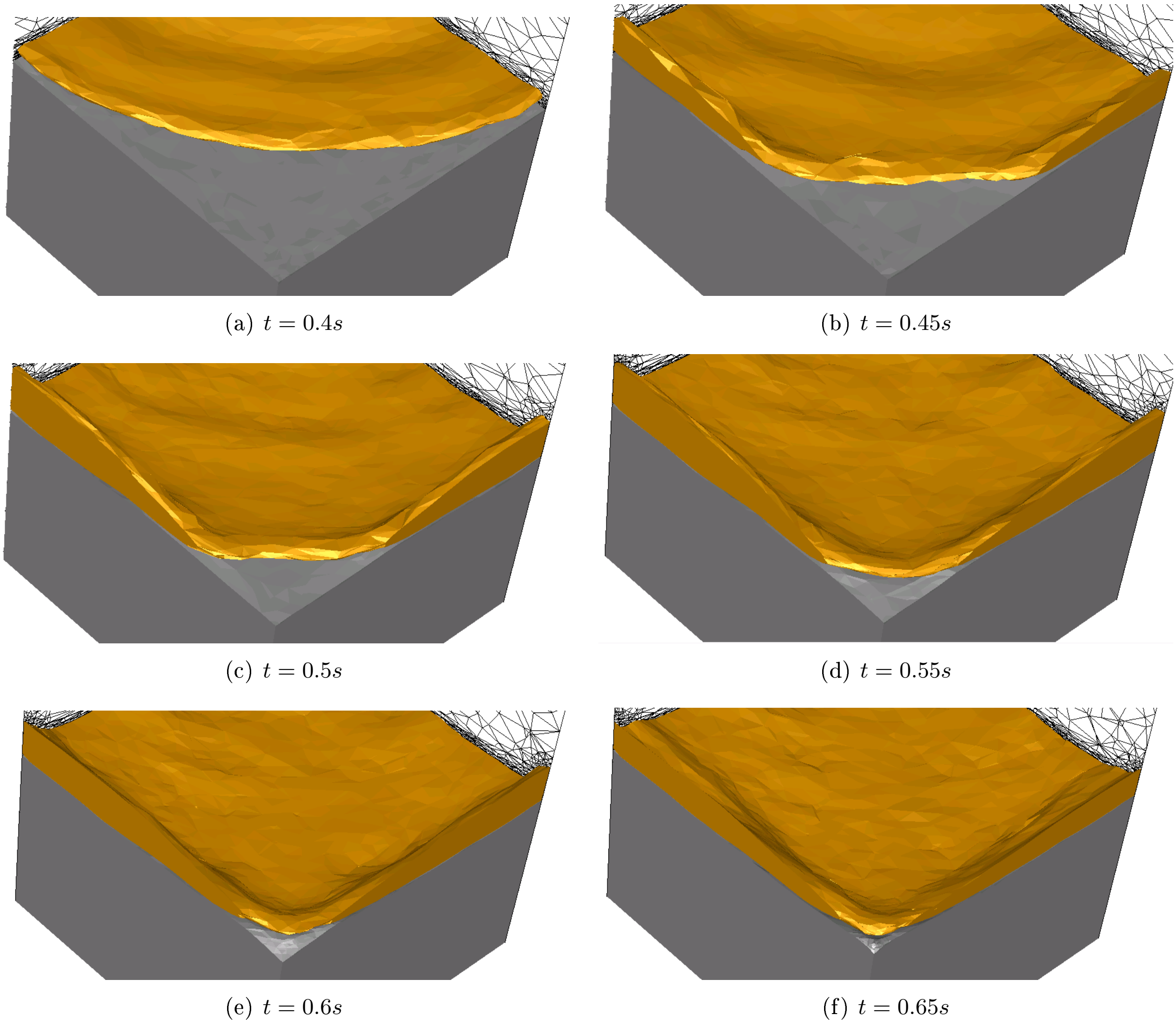
(a) $t = 0.4s$ (b) $t = 0.45s$

(c) $t = 0.5s$ (d) $t = 0.55s$

(e) $t = 0.6s$ (f) $t = 0.65s$

Figure 155: Powder front advancing to the mold corner, illustrated at several instants

5.3.5 Influence of the number of bags

Now, the goal is to analyze the influence of the number of bags deposited into the mold, and how it affects the powder spreading near the walls.

Geometry and initial disposition of the powder bags into the mold are illustrated in figure 156. The same mold ($L_i = 52.3$cm and $H_i = 80$cm), and the same powder volume as used in the previous analysis, are considered. However, the granular column is split into four smaller ones, by dividing initial radius and height by two. Powder flow onto liquid metal is illustrated in figure 157. It is observed a weaker spreading than by considering one granular column. Indeed, the powder does not cover the full metal surface, which even leads to the powder decovering in several regions. This difference may be explained by a stronger dissipative energy induced by the liquid metal, contrarily to what was concluded from the chute on a solid surface.

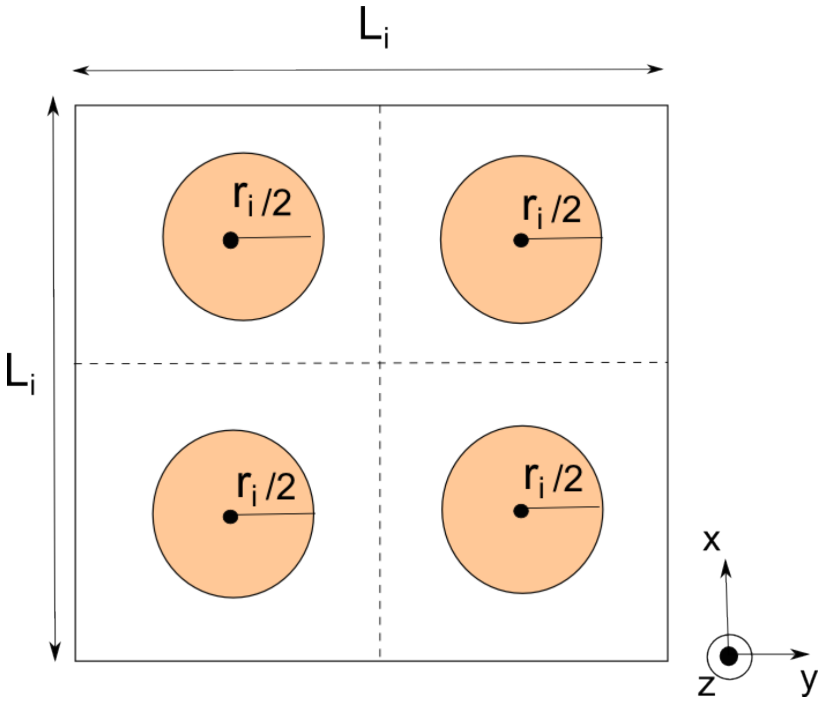

Figure 156: Mold dimensions and initial bags disposition for the study of the influence of number of bags

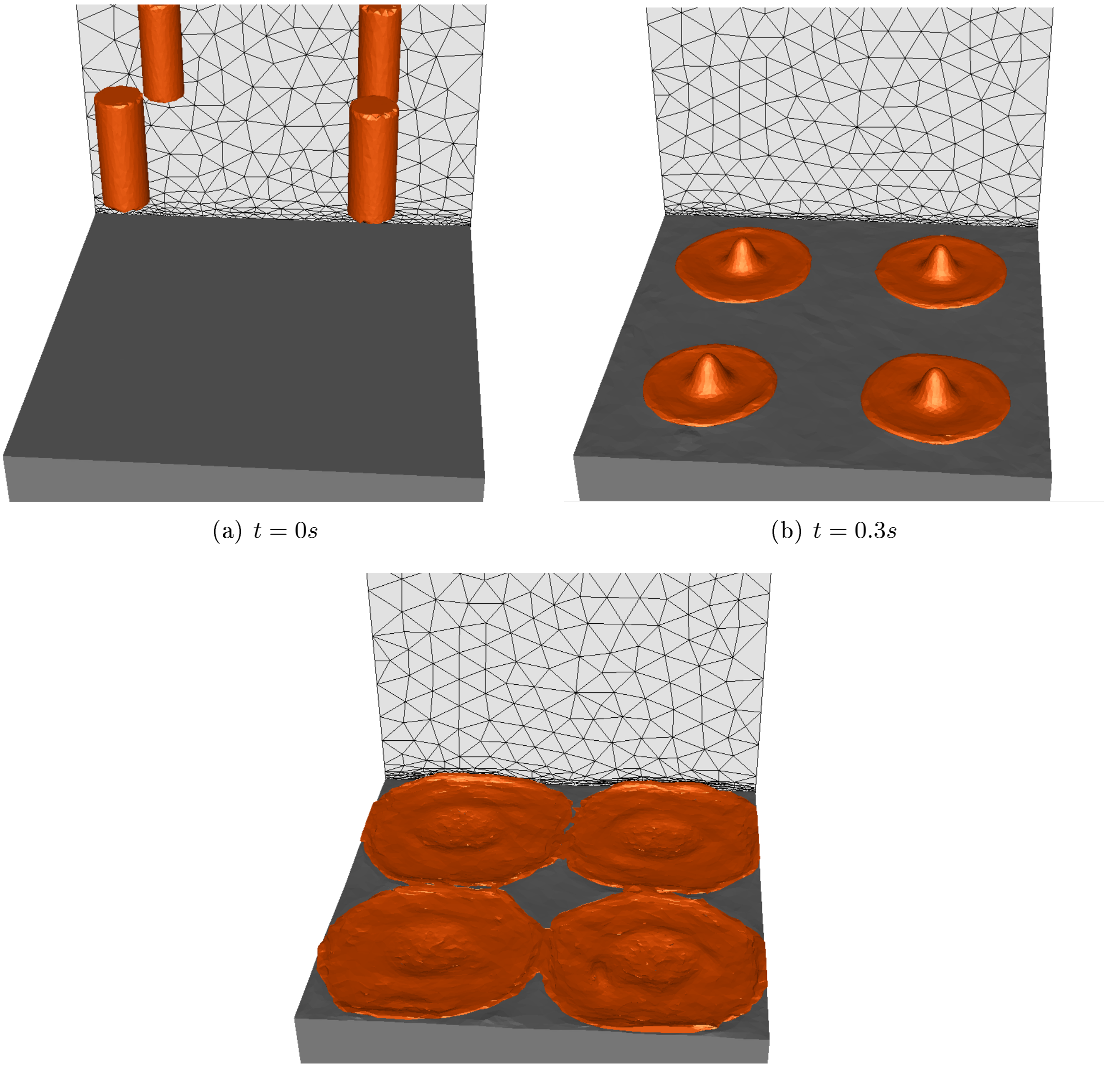

(a) $t = 0s$

(b) $t = 0.3s$

(c) $t = 0.4s$

Figure 157: Chute and spreading of four granular columns onto liquid metal

5.3.6 Conclusion

In this section, we performed numerical industrial powder chutes onto static liquid metal, by using the Thercast software. Several casting features are discussed, such as the height of liquid metal, spreading at mold corners and number of bags.

Some improvements for a better powder spreading are thus proposed. First, it has been observed that the liquid layer has an influence onto the powder run-out distance. Indeed, a lower h_m leads to soften the powder chute, and thus, to decrease the crater depth formed by the impact and finally, to increase the run-out distance of the powder.

Then, the spreading at the corner mold has been also analyzed. It has been observed that the powder moves in the mold walls directions, leading to cover a larger surface than without considering any walls.

Thus, walls have a strong influence on the powder spreading, and may increase the run-out distance of powder.

Finally, splitting a bag into smaller ones leads to a worse spreading. Thus, it would be more interesting for metallurgists to deposit just one bag into the mold, in order to optimize the powder spreading.

5.4 Conclusion

In this chapter, the purpose consisted in simulating industrial powder chutes onto a solid substrate and a static liquid metal. First, experimental collapses and chutes of industrial powders have been performed in order to analyze the relevance of $\mu(I)$ rheology for describing these flows. For the coarsest powder, the same dynamics as determined in [61] has been found. For the finest one, it has been observed a strong cohesion between grains inducing a bad spreading, which tends to disappear as a increases, and thus leading to obtain the same dynamics as [61].

Then, industrial powder chutes onto liquid metal have been performed by using the industrial software Thercast. Several industrial features have been discussed, leading to the process optimization. Finally, it has been observed that liquid metal height, walls and number of powder bags influence a lot the spreading quality.

Chapter 6

Conclusion and perspectives

Contents

Résumé en français

Pour conclure, l'objectif de cette thèse était de fournir un modèle continu pour simuler l'étalement des poudres de couverture qui protègent le métal de l'air durant le procédé de coulée en lingotière. Une formulation éléments finis a ainsi été proposée afin de simuler les écoulements multiphasique de matériaux granulaires. Une méthode Level-Set a été utilisée pour capturer et suivre l'interface au cours du temps. Les équations de Navier-Stokes ont été résolues avec une approche variationelle multi-échelle, couplée à une adaptation de maillage anisotrope. Dans un premier temps, nous avons traité les écoulements de Bingham, qui présentent de fortes non-linéarités aux interfaces. Le modèle proposé permet donc de résoudre ces écoulements hautement plastiques. Puis, la formulation a été étendue aux écoulements de granulaires en 2D et 3D, décrits par la rhéologie $\mu(I)$. L'influence de plusieurs paramètres rhéologiques est étudiée, montrant que le coefficient de frottement statique est le paramètre dominant l'écoulement. Puis, l'influence de la géométrie a été étudiée. Nous retrouvons bien la dynamique prédite par la littérature expérimentale.

Finalement, nous avons appliqué la rhéologie $\mu(I)$ aux écoulements de poudres industrielles. Enfin, des chutes de colonnes de poudre sur du métal liquide statique ont été simulées, donnant des premières pistes pour l'optimisation du procédé.

Numériquement, il serait intéressant de proposer une formulation exacte [42], afin de simuler les arrêts de l'écoulement. Concernant le procédé industriel, la prochaine étape sera de simuler le changement de phase de la poudre, ainsi que le suivi inclusionnaire dans le métal en fusion. Il serait également intéressant d'étudier la pertinence de la rhéologie $\mu(I)$ pour d'autres types d'écoulement. Enfin, ce formalisme éléments finis peut être étendu à d'autres types de fluides complexes, comme les fluides thixotropes.

6.1 Conclusion

The final objective of this thesis was to provide numerical tools for modeling the spreadng of industrial powders by a continuous approach. Suitable constitutive equations of certain behaviors representative of granular materials were chosen according to their numerical and physical relevance. For dry granular materials, the $\mu(I)$ rheology is able to characterize the different regimes (quasi-static, dense and collisional), representative of the dynamics of this type of material.

Finally, we chose yield stress fluids to characterize the understanding of partially wet granular materials. Although other phenomena exist to characterize this type of material, these types of fluids have been privileged because they represent a numerical challenge, especially for free surface flows and due to the strong non-linearities.

We proposed and developed a finite element formulation for the resolution of multiphase flows of materials obeying the chosen constitutive models. Interface capture and tracking was performed using a Level-Set method. The signed distance field is first truncated around the interface to improve stability, convected over time, but also reset. Then, momentum and mass equations are solved, and stabilized by a variational multiscale approach. In addition, the behavior of the fluid was taken into account by a regularization method. Finally, an anisotropic mesh adaptation method was proposed to increase accuracy. In the case of non-Newtonian flows, the mesh has been adapted in zones with strong variations in level-set field gradients, velocity but also effective viscosity (in order to capture the yielded / unyielded transition).

It has been shown that this method has great potential for the simulation of highly plastic flows. Indeed, for Bingham flows, it is possible to consider very large viscosity jumps thanks to the VMS method and mesh adaptation where very fine and stretched meshes are considered in the transition zones.

Finally, we simulated the flow of dry granular materials in two and three dimensions by the $\mu(I)$ rheology. We have dealt with the case of granular column collapses. First, we compared the $\mu(I)$ model with the discrete simulations of Lagrée *et al.*[13], that showed good agreement. Finally, we studied the influence of different rheological parameters on spreading. Thus, it has been observed that static friction coefficient μ_S is the dominant parameter in the flow. Finally, the influence of the geometry of the column was discussed. We found the same dynamics observed in the experimental literature: a linear regime for low aspect ratios and a power law regime for large aspect ratios. In addition, a study of the influence of the initial height was carried out, and greater spreading.

Finally, we applied the $\mu(I)$ rheology to the flow of industrial powders. In a first step, the objective was to validate the $\mu(I)$ rheology to describe the flows of powder, with collapse and collapse experiments that we carried out. Thus, it is observed that the granuar material follows the same dynamics as the $\mu(I)$ rheology. On the other hand, the finest powder tends towards this dynamic for large aspect ratios, due to a negligible cohesion between grains over the flow energy. Finally, simulations of powder chute on liquid metal were performed with the software Thercast, commercialized by Transvalor, in order to give first ways to optimize the process.

6.2 Perpectives

6.2.1 Improvement of numerical methods

In this thesis, the behavior of the non-Newtonian fluids was introduced into the equations of fluid mechanics by a regularization method. However, some limitations of the method appear, due in particular to the fact that the flow never stops. This can cause more uncertainties in the calculation of the material arrest time. In this perspective, it would be interesting to use an exact method, as proposed by Roquet *et al.*[42].

To mathematically translate non-deformed zones that are not defined below the threshold, we solve a constrained system energy minimization problem that $|| \dot{\gamma} ||$, using the augmented Lagrangian method, coupled with the Uzawa algorithm. These methods are very powerful, because they are able to model very precisely the unyielded zones of the fluid. Roquet *et al.*[42] solved single-phase flows of Bingham fluids using this approach. Very promising results have been obtained by the authors.

It would be interesting to extend this method first to the multiphase flows of Bingham fluids. However, careful attention must be paid to the robustness of this method, since it may appear very expensive in computing time, if it is not well adapted to the problem under consideration.

Finally, it would also be interesting to propose an exact formulation for the $\mu(I)$ model, based on the same method of resolution. However, an additional difficulty is introduced, with the appearance of a nonlinear term in pressure, and which, if we do not take it into account, can totally degrade the quality of the solution. In order to simulate such a flow, it would be interesting to validate the model on a Bagnold profile, for which we have an analytical solution, and where it would be interesting to study the robustness of the calculations as well as the speed of convergence.

6.2.2 Ingot casting process

As part of the industrial project COMCEPT, this model has been applied to the prediction of the spreading of the cover powders used during the ingot casting process. All the developments numerically related to this thesis work were introduced by the company Transvalor in the Thercast software.

In this thesis, we simulated the spreading of industrial powder on a static bath of liquid metal, without considering the heat exchanges. We have evaluated the influence of different parameters representative of the industrial process: thickness of the liquid metal layer, spreading in the corners of the ingot mold, influence of the number of bags. It would be interesting to continue further studies on the influence of these parameters in order to determine the best arrangement of powder bags for a given ingot mold.

The prospects of the COMCEPT project then consist in considering the thermal exchanges induced by the filling of the metal in the ingot mold, and in particular to take into account the phase change of the powder, which occurs after spreading. Finally, the last numerical perspective is to numerically simulate this process dynamically (ie, considering the filling of the ingot mold). Indeed, the powder can penetrate into the molten metal, due mainly to the strong tubulences generated by the entry of the metal, creating inclusions in the final product. Post-doctoral work is in progress and aims to propose a criterion of removal of the powder, and also focuses on the inclusion monitoring during the process, in order to finally predict the final position of the inclusions.

Finally, it would be interesting to extend this model to mold powders used in continuous casting.

6.2.3 Extension to other type of flows for the $\mu(I)$ rheology

It could be also interesting to use our solver to test the pertinence of the $\mu(I)$ model to other types of flows. For example, the drag and lift of an object immersed in a sheared granular medium could be computed.

6.2.3.1 Extension to other non-Newtonian flows

In this work, we proposed and implemented numerical methods for the resolution of non-Newtonian fluid flows. We began by treating the flows of threshold fluids, and more particularly of Bingham fluids, by the numerical challenge that occurs because of the strong non-linearities observed specifically at the interfaces. We then extended our method to flows of dry granular materials (obeying the $\mu(I)$ model), since during the casting process, the powder is always considered in its granular state during spreading.

This model can nevertheless be extended to the flow of other non-Newtonian fluids, such as thixotropic fuids. The simulation of the flow of the latter was the subject of a Master internship within the Computing and Fluids team.

6.2.3.2 Thixotropic fluids

The behavior of a thixotropic fluid is characterized by the evolution of its microstructure over time and the reversibility of this evolution. Indeed, when the fluid is heavily sheared, the behavior approximates that of a Newtonian fluid. At rest, a change in the microstucture of the fluid will take place over time, drastically increasing the viscosity of the fluid (which is not due to the existence of a flow threshold. New convection-reaction equation appears in the problem, and corresponds to the evolution over time of the fluid structure parameter λ:

$$\frac{\partial \lambda}{\partial t} + v \cdot \nabla \lambda + \alpha \lambda \mid\mid \dot{\gamma} \mid\mid = \frac{1}{T_0} \tag{6.1}$$

T_0 corresponds to a time of restructuring of the material considered and α is a constant of the system. For $\lambda = 0$, the fluid is not structured at all, and the effective viscosity tends towards the plastic viscosity. When λ tends to infinity, the fluid is structured, and the effective viscosity tends to infinity. As in the case of Bingham fluids, the divergence of this viscosity should be limited, and methods similar to those used for Bingham or $\mu(I)$ flows should be developed and tested.

Bibliography

[1] F. Da Cruz, S. Emam, and M. e. a. Prochnow, “Rheophysics of dense granular materials: Discrete simulation of plane shear flows,” *Physical Review E*, vol. 72, 2005.

[2] P. Jop, O. Pouliquen, and Y. Forterre, “A constitutive law for dense granular flows,” *Nature*, vol. 441, pp. 727–730, 2003.

[3] B. Andreotti, Y. Forterre, and O. Pouliquen, *Les milieux granulaires : Entre fluide et solide.* EDP Sciences, 2011.

[4] N. Vriend, J. Mc Elwaine, C. Keylock, M. Ash, P. Brennan, and B. Sovilla, “High resolution radar measurements of snow avalanches,” *Geophysical Research Letters*, vol. 40, pp. 727–731, 2013.

[5] A. Gupta, A. Katterfeld, B. Soeteman, and S. Luding, “Discrete element study mixing in an industrial sized mixer,” *Proc. World Congress Particle Technology 6, Nuremberg*, 2010.

[6] Y. Forterre and O. Pouliquen, “Flows of dense granular media,” *Annual Review of Fluid Mechanics*, vol. 40, pp. 1–24, 2008.

[7] S. Luding, “Granular matter: So much for the jamming point,” *Nature Physics*, vol. 12, pp. 531–532, 2016.

[8] G. MiDi, “On dense granular flows,” *The European Physical Journal E*, vol. 14, pp. 341–365, 2004.

[9] P. Coussot, “Rheophysics of pastes: a review of microscopic modelling approaches,” *Soft matter*, vol. 3, pp. 528–540, 2007.

[10] P. Coussot, “Yield stress fluid flows : A review of experimental data,” *Journal of Non-Newtonian Fluid Mechanics*, vol. 211, pp. 31 – 49, 2014.

[11] N. Zainali, A. annd Tofighi, M. Shadloo, and M. Yildiz, “Numerical investigation of newtonian and non-newtonian multiphase flows using isph method,” *Computer methods in applied mechanics and engineering*, vol. 254, pp. 99–113, 2013.

[12] I. Ionescu, A. Mangeney, F. Bouchut, and O. Roche, “Viscoplastic modeling of granular column collapse with pressure-dependent rheology,” *Journal of Non-Newtonian Fluid Mechanics*, vol. 219, pp. 1–18, 2015.

[13] P.-Y. Lagree, L. Staron, and S. Popinet, "The granular column collapse as a continuum : validity of a two-dimensional navier-stokes model with a i rheology," *Journal of Fluid Mechanics*, pp. 1–31, 2011.

[14] C. Hirt and B. Nichols, "Volume of fluid (vof) method for the dynamics of free boundaries," *Journal of Computational Physics*, vol. 39, pp. 201–225, 1981.

[15] S. Mosso, C. Garasi, and R. Drake, "A smoothed two- and three-dimensional interface reconstruction method," *Computing and Visualization in Science*, vol. 12, pp. 365 – 381, 2009.

[16] D. Anderson, G. Mcfadden, and A. Wheeler, "Diffuse-interface methods in fluid mechanics," *Annual review of fluid Mechanics*, vol. 30, pp. pages = 139–165, 1998.

[17] S. Osher and J.-A. Sethian, "Fronts propagating with curvature dependent speed: algorithms based on hamilton-jacobi formulations," *Journal of Computational Physics*, vol. 79, pp. 12–49, 1988.

[18] S. Osher and R. Fedkiw, "Level- set methods: An overview and some recent results," *Journal of Computational Physics*, vol. 169, pp. 463–502, 2001.

[19] H. Ji, D. Chopp, and J. Dolbow, "A hybrid extended finite element/level set method for modeling phase transformations," *International journal for numerical methods in engineering*, vol. 54, pp. 1209–1233, 2002.

[20] M. Sussmann and E. Puckett, "A coupled level set and volume-of-fluid method for computing 3d and axisymmetric incompressible two-phase flows," *Journal of Computational Physics*, vol. 162, pp. 301–337, 2000.

[21] D. Enright, R. Fedkiw, J. Ferziger, and I. Mitchell, "A hybrid particle level set method for improved interface capturing," *Journal of Computational Physics*, vol. 183, pp. 83–116, 2002.

[22] L. Ville, L. Silva, and T. Coupez, "Convected level set method for the numerical simulation of fluid buckling," *International journal for Numerical methods in Fluids*, vol. 66, pp. 324–344, 2011.

[23] E. Olsson and G. Kreiss, "A conservative level set method for two phase flow," *Journal of Computational Physics*, vol. 210, pp. 225–246, 2005.

[24] A. Bonito, J.-L. Guermond, and S. Lee, "Numerical simulations of bouncing jets," *International Journal for Numerical Methods in Fluids*, vol. 80, pp. 53–75, 2015.

[25] M. Khalloufi, Y. Mesri, R. Valette, E. Massoni, and E. Hachem, "High fidelity anisotropic adaptive variational multiscale method for multiphase flows with surface tension," *Computer methods in Applied Mechanics and Engineering*, vol. 307, pp. 44–67, 2016.

[26] T. Hugues, "Multiscale phenomena: Green's functions, the dirichlet-to-neumann formulation, subgrid scale models, bubbles and the origin of stabilized methods," *Computer methods in applied mechanics and engineering*, vol. 127, pp. 387–401, 1995.

[27] T. Hugues, G. Feijoo, L. Mazzei, and J. Quincy, “The variational multiscale method - a paradigm for computational mechanics,” *Computer methods in applied mechanics and engineering*, vol. 166, pp. 3–24, 1998.

[28] T. Hugues, G. Scovazzi, P. Bochev, and A. Buffa, “A multiscale discontinuous galerkin method with the computational structure of a continuous galerkin method,” *Computer methods in applied mechanics and engineering*, vol. 195, pp. 19–22, 2006.

[29] K. Nakshatrala, D. Turner, K. Hjelmstad, and A. Masud, “A stabilized mixed finite element method for darcy flow based on a multiscale decomposition of the solution,” *Computer methods in applied mechanics and engineering*, vol. 195, pp. 33–36, 2006.

[30] E. Hachem, S. Feghali, R. Codina, and T. Coupez, “Immersed stress method for fluid-structure interaction using anisotropic mesh adaptation,” *International journal for numerical methods in engineering*, vol. 94, pp. 805–825, 2013.

[31] G. Scovazzi, “Lagrangian shock hydrodynamics on tetrahedral meshed: a stable and accurate variational multiscale approach,” *Journal of Computational Physics*, vol. 231, pp. 8029–8069, 2012.

[32] E. Castillo and R. Codina, “Stabilized stress-velocity-pressure finite element formulations of the navier-stokes problem for fluids with non-linear viscosity,” *Computer methods in applied mechanics and engineering*, vol. 279, pp. 554–578, 2014.

[33] E. Hachem, B. Rivaux, T. Kloczko, H. Digonnet, and T. Coupez, “Stabilized finite element method for incompressible flows with high reynolds number,” *Journal of Computational Physics*, vol. 229, pp. 8643–8665, 2010.

[34] R. Codina, “Comparison of some finite element methods for solving the diffusion-convection-reaction equation,” *Computer methods in applied mechanics and engineering*, vol. 156, pp. 185–210, 1998.

[35] R. Khurram and A. Masud, “A multiscale/stabilized formulation of the incompressible navier–stokes equations for moving boundary flows and fluid–structure interaction,” *Computational Mechanics*, vol. 38, pp. 403–416, 2006.

[36] R. Codina and J. Principe, “Dynamic subscales in the finite element approximation of thermally coupled incompressible flows,” *Intenational Journal for Numerical Methods in Fluids*, vol. 2007, pp. 707–730, 2007.

[37] T. Coupez, “Metric construction by length distribution tensor and edge based error for anisotropic adaptive meshing,” *Journal of Computational Physics*, vol. 230, pp. 2391–2405, 2011.

[38] G. Jannoun, E. Hachem, J. Veysset, and T. Coupez, “Adaptive time-step with anisotropic meshing for unsteady convection-diffusion problems,” *Applied Mathematics Modelling*, vol. 39, pp. 1899–1916, 2015.

[39] G. Kunert and R. Verfurth, “Edge residuals dominate a posteriori error estimates for linear finite element methods on anistropic triangular and tetrahedral meshes,” *Numerische Mathematik*, vol. 86, pp. 283–303, 2000.

[40] M. Cruchaga, D. Celentano, and T. Tezduyar, “Collapse of a liquid column : numerical simulation and experimental validation,” *Computational Mechanics*, 2007.

[41] T. Coupez and E. Hachem, “Solution of high-reynolds incompressible flow with stabilized finite element and adaptive anisotropic meshing,” *Computer methods in applied mechanics and engineering*, vol. 267, pp. 65–85, 2013.

[42] N. Roquet and P. Saramito, “An adaptive finite element method for bingham fluid flows around a cylinder,” *Computer methods in applied mechanics and engineering*, vol. 192, pp. 3317–3341, 2003.

[43] Y. Liu, N. Balmforth, S. Hormozi, and D. Hewitt, “Two-dimensional viscoplastic dambreaks,” *Journal of Non-Newtonian Fluid Mechanics*, 2016.

[44] A. Syrakos, G. C. Georgiou, and A. N. Alexandrou, “Solution of the square lid-driven cavity flow of a bingham plastic using the finite volume method,” *Journal of Non-Newtonian Fluid Mechanics*, vol. 195, pp. 19–31, 2013.

[45] H. Zhu, N. S. Martys, C. Ferraris, and D. D. Kee, “A numerical study of the flow of bingham-like fluids in two-dimensional vane and cylinder rheometers using a smoothed particle hydrodynamics sph based method,” *Journal of Non-Newtonian Fluid Mechanics*, vol. 165, pp. 362–375, 2010.

[46] D. Vola, L. Boscardin, and J.-C. Latche, “Laminar unsteady flows of bingham fluids : a numerical strategy and some benchmark results,” *Journal of Computational Physics*, vol. 187, pp. 441–456, 2003.

[47] C. Faria and J. Karam-Filho, “A regularized-stabilized miwed finite element formulation for viscoplasticity of bingham type,” *Computers and Mathematics with Applications*, vol. 66, pp. 975–995, 2013.

[48] M. Bercovier, “a finite-element method for incompressible non-newtonian flows,” *Journal of Computational Physics*, vol. 36, pp. 313–326, 1980.

[49] T. Papanastasiou, “Flows of materials with yield,” *Journal of Rheology*, vol. 31, pp. 385–404, 1987.

[50] I. Frigaard and C. Nouar, “On the usage of viscosity regularisation methods for visco-plastic fluid flow computation,” *Journal of Non-Newtonian Fluid Mechanics*, vol. 127, pp. 1–26, 2005.

[51] A. Aposporidis, E. Haber, M. Olshanskii, and A. Veneziani, “A mixed formulation of the bingham fluid flow problem : Analysis and numerical solution,” *Compuuters methods in applied mechanics and engineering*, vol. 200, pp. 2434–2446, 2011.

[52] A. Syrakos, G. Georgiou, and A. Alexandrou, “Performance of the finite volume method in solving regularised bingham flows : Inertial effects in the lid-driven cavity flow,” *Journal of Non-Newtonian Fluid Mechanics*, vol. 208-209, pp. 88–107, 2014.

[53] S. Frey, F. S. Silveira, and F. Zinani, "Stabilized mixed approximations for inertial viscoplastic fluid flows," *Mechanics Research Communications*, vol. 37, pp. 145–152, 2010.

[54] P. Neofytou, "A 3rd order upwind finite volume method for generalised newtonian fluid flows," *Advances in Engineering Software*, vol. 36, pp. 664–680, 2005.

[55] D. L. Tokpavi, A. Magnin, and P. Jay, "Very slow flow of bingham viscoplastic fluid around a circular cylinder," *Journal of Non-Newtonian Fluid Mechanics*, vol. 154, pp. 65–76, 2008.

[56] S. Riber, R. Valette, Y. Mesri, and E. Hachem, "Adaptive variational multiscale method for bingham flows," *Computers and Fluids*, vol. 138, pp. 51–60, 2016.

[57] N. J. Balmforth, R. V. Craster, P. Perona, A. C. Rust, and R. Sassi, "Viscoplastic dam breaks and the Bostwick consistometer," *Journal of Non-Newtonian Fluid Mechanics*, vol. 142, pp. 63–78, 2007.

[58] G. Matson and A. Hogg, "Two-dimensional dam break flows of Herschel–Bulkley fluids: The approach to the arrested state," *Journal of Non-Newtonian Fluid Mechanics*, vol. 142, pp. 79–94, 2007.

[59] D. Vola, F. Babik, and J.-C. Latche, "On a numerical strategy to compute gravity currents of non-newtonian fluids," *Journal of Computational Physics*, vol. 201, pp. 397–420, 2004.

[60] L. Staron, P.-Y. Lagrée, P. Ray, and S. Popinet, "Scaling laws for the slumping of a bingham plastic fluid," *Journal of Rheology*, vol. 57, 2013.

[61] E. Lajeunesse, A. Mangeney-Castelnau, and J. Vilotte, "Spreading of a granular mass on a horizontal plane," *Physics of fluids*, vol. 16, 2004.

[62] G. Lube, H. Huppert, R. Stephen, J. Sparks, and M. Hallworth, "Axisymmetric collapses of granular columns," *Journal of Fluid Mechanics*, vol. 508, pp. 175–199, 2004.

[63] N. Balmforth and R. Kerswell, "Granular collapse in two dimensions," *Journal of Fluid Mechanics*, vol. 538, pp. 399–428, 2005.

[64] G. Lube, H. E. Hupper, R. Sparks, and A. Freundt, "Collapses of two-dimensional granular columns," *Physical review*, vol. 72, 2005.

[65] S. Dunatunga and K. Kamrin, "Continuum modeling and simulation of granular flows through their many phases," *Journal of Fluid Mechanics*, 2015.

[66] L. Minatti and E. Paris, "A sph model for the simulation of free surface granular flows in a dense regime," *Applied Mathematical Modelling*, vol. 39, pp. 363–382, 2015.

[67] G. Chambon, R. Bouvarel, and D. e. a. Laigle, "Numerical simulations of granular free-surface flows using smoothed particle hydrodynamics," *Journal of Non-Newtonian Fluid Mechanics*, vol. 166, pp. 698–712, 2011.

[68] J. Chauchat and M. Medale, “A three-dimensional numerical model for dense granular flows based on the $\mu(i)$ rheology,” *Journal of Computational Physics*, vol. 256, pp. 696–712, 2013.

[69] T. Barker, D. Schaeffer, P. Bohorquez, and J. Gray, “Well-posed and ill-posed behaviour of the $\mu(i)$-rheology for granular flows,” *Journal of Fluid Mechanics*, vol. 779, pp. 794–818, 2015.

[70] E. Larrieu, L. Staron, and E. J. Hinch, “Raining into shallow water as a description of the collapse of a column of grains,” *Journal of Fluid Mechanics*, vol. 554, pp. 259–270, 2006.

Résumé

Cette thèse traite de la modélisation et des méthodes numériques pour la simulation d'écoulements de fluides non-Newtoniens, et particulièrement, de matériaux granulaires. Une application de ce travail concerne les poudres de couverture utilisées pour protéger thermiquement le métal de l'air dans le procédé de coulée en source d'alliages métalliques. Ces poudres sont conditionnées dans des sacs disposés dans la lingotière, qui brûlent suite aux fortes chaleurs engendrées, et permettant son écoulement sur la surface du métal. Ainsi, la simulation numérique apparaît comme un puissant outil pour l'optimisation du procédé, et notamment, de l'étalement de ces poudres.
Dans ce travail, une formulation éléments finis a été proposée pour modéliser l'écoulement multiphasique des matériaux granulaires dans un formalisme de la mécanique des milieux continus. Les équations associées sont résolues via des schémas numériques stabilisés, couplés avec la méthode Level-Set pour capturer et suivre le profil du matériau granulaire au cours de la simulation. Dans un premier temps, les outils numériques ont été testés sur des cas d'écoulements de fluides de Bingham, où les fortes non-linéarités sont traitées par une méthode de régularisation. Puis la formulation est étendue aux écoulements de granulaires secs, dont le comportement piezzo-dépendent est traduit par la loi $\mu(I)$. Le modèle a été validé sur des cas d'effondrement de colonnes de grains, et une étude de sensibilité aux conditions aux limites et constantes physiques du modèle est proposée.
Enfin, des cas industriels de chutes de poudres sur substrats solide et métal fondu ont été menés, amenant à des premières pistes pour l'optimisation du procédé de coulée en lingotière.

Mots Clés

Matériaux granulaires, rhéologie $\mu(I)$, fluides de Bingham simulation numérique, méthodes éléments finis, coulée en lingotière

Abstract

This thesis is devoted to the modeling and numerical methods for the simulation of non-Newtonian flows, and focuses particularly on granular materials flows. This work is applied to molten powders aiming to ensure metal thermal protection from the air in ingot casting process of metallic alloys. These powders are conditionned into bags disposed into the mold, which burn due to high temperatures, and allowing the powder spreading onto the metal surface. Thus, numerical simulation appears as a powerful tool for the process optimization, and especially, for the powder spreading.
In this work, a finite element formulation has been proposed for the modeling of granular multiphase flows by a continuum approach. The associated equations are solved using stabilized numerical schemes, coupled with the Level-Set method to capture and follow the granular profile during the simulation. First, the numerical tools have been implemented for Bingham flows, by using regularization a method. Then, the formulation was extended to dry granular flows, by the use of the $\mu(I)$ rheology constitutive model for describing its pressure-dependent behavior. The model has been validated on granular collapses, and a sensitivity analysis to boundary conditions and physical constants has been proposed.
Finally, industrial cases of powder chutes onto both solid and liquid metla substrates have been conducted, leading to preliminary solutions for the optimization of ingot casting process.

Keywords

Granular materials, $\mu(I)$ rheology, Bingham fluids, numerical simulation, finite element methods, ingot casting process